Optical Properties of Venusian Clouds

Joanna Victoria Egan

Submitted in accordance with the requirements for the degree of

Doctor of Philosophy

The University of Leeds

School of Chemistry

School of Chemical and Process Engineering

December 2024

I confirm that the work submitted is my own, except where work which has formed part of jointly authored publications has been included. My contributions, and those of other authors to this work, have been explicitly indicated below. I confirm that appropriate credit has been given within the thesis where reference has been made to the work of others.

In Chapter 2: Overview and validation of models:

- Initial development of PCM models and implementation of meteoric input functions into the PCM was performed by Dr Wuhu Feng. Additional development was performed by Joanna Egan.
- New chemistry was predicted by Professor John Plane for addition to the PCM by Wuhu Feng and Joanna Egan.
- Fe PCM runs were performed by Dr Wuhu Feng. Sulphur PCM runs were performed by Joanna Egan. All analysis of PCM data was performed by Joanna Egan.
- Development and testing of SOCRATES-Venus was performed by Joanna Egan under the supervision of James Manners.
- The 1D coagulation and sedimentation modelling was developed, performed, and described by Professor John Plane.

Chapter 3: Photochemical and radiative transfer modelling of OSSO is based upon a co-authored publication:

> Egan, J. V., Feng, W., James, A. D., et al. (2025). Is OSSO a significant contributor to the unknown UV absorber in Venus' atmosphere? *Geophysical Research Letters*, 52, e2024GL113090. https://doi.org/10.1029/2024GL113090

All authors had the opportunity to edit and provide comments on the paper and all authors approved the submitted paper manuscript. Contributions of the authors are as follows:

- Joanna Egan: PCM model development, SOCRATES model development, model running (PCM and SOCRATES), analysis, writing.
- Wuhu Feng: PCM model development, including initial addition of new chemistry and implementation of meteoric input functions to the code.
- Alexander James: supervision, significant proof-reading and editing.
- Daniel Marsh: supervision.
- James Manners: Initial SOCRATES model development, supervision.
- Franck Lefevre, Sebastien Lebonnois, Aurelien Stolzenbach: Initial PCM development.
- John Plane: Quantum chemistry calculations, prediction of absorption cross-sections and rate constants, and descriptions thereof.

In Chapter 4: Laboratory studies of ferric chloride ($FeCl_3$):

- All laboratory work and analysis was performed by Joanna Egan.
- Development of the fitting algorithm was carried out by Joanna Egan from examples by Dr Daniel Stone.

In Chapter 5: Photochemical and radiative transfer modelling of $FeCl_3$:

- Quantum chemistry calculations and prediction of absorption cross-sections and rate constants were performed and described by Professor John Plane.
- Initial development of the PCM and implementation of meteoric input functions into the PCM was performed by Dr Wuhu Feng. Additional development was performed by Joanna Egan.
- Fe PCM runs were performed by Dr Wuhu Feng using code provided by Joanna Egan.
- The 1D coagulation and sedimentation modelling was developed, performed, and described by Professor John Plane.

Appendix A details work by Professor John Plane to calculate the absorption cross-sections and rate coefficients for the iron chemistry introduced to the PCM. This work is included for validation of the iron chemistry described in Chapter 5.

The work was supervised by Professor John Plane, Professor Daniel Marsh, Dr Wuhu Feng, Professor Benjamin Murray, and Dr Alexander James.

Acknowledgements

There are so many people without whom I could never have made it this far. I'd like to thank my primary supervisor, John Plane, for his support and guidance throughout my PhD, and for sharing his invaluable advice and knowledge over the past four years. I'd also like to thank the rest of my supervisors, Wuhu Feng for his coding expertise, Dan Marsh for his advice and insights into atmospheric modelling, and Ben Murray for the opportunity to expand my labwork skills with the Ice Nucleation group, even though none of that work made it into this thesis!

The atmospheric chemistry group at Leeds has been an invaluable source of support and advice, throughout the years, in particular Tasha Aylett, Marcin Kupilas, and Tom Mangan, who lent many a sympathetic ear through the inevitable rough spots of a PhD. However, the largest thanks must go to Sandy James, who has been so generous with his time, advice, and expertise in science, academia, and life, and for whom no question has ever been too simple or too outlandish to be worth his time and consideration. As the group has grown over the years, with the notable additions of Katie, Caitlin, and Bianca, it has been wonderful to be part of a thriving research environment, and I look forward to seeing all that they will achieve over the coming years. Outside the group, I am eternally grateful to Dave Fogarty and Ben Cooper for their generosity with their equipment and skills, and to all of the technicians across the School and Stores, without whom laboratory work would be impossible.

The funding and training for my PhD studentship came through the EPSRC CDT in Aerosol Science. Without the tireless work of the core team, particularly Jonathan Reid, Rachael Miles, Kate Loutit, Yaelle Hartley, and Ka Man Kam, I would never have had the opportunity to undertake this PhD, let alone produced work I am so proud of. In addition, the supportive atmosphere of the CDT and the camaraderie engendered amongst Cohort 2 during the training has been invaluable. The CDT also made it possible for me to carry out two months of work with James Manners at the Met Office and the University of Exeter, and I am immensely grateful for his supervision and guidance, and for the warm welcome I received from the Exeter Exoplanet Theory group.

On a more personal note, no-one ever said doing a PhD would be easy, but it has been made so much better by the unwavering support of my family and friends. At the risk of making these acknowledgements longer than the rest of the thesis, it would seem remiss not to list at least some of them by name.

My family: Mum, Dad, Alan, and Alex, not only have you helped shape me and encourage me to become the person I am today, you have always been there for whatever was needed, whether a lift across the country, a midnight video call, or just a hug. Beri, you've been the greatest friend I could ever have asked for. One day, I hope to believe in myself as much as you believe in me. I wouldn't be here without you.

Evan, Ruby, Q, Jen, Harriet, and Louise, being friends with you has been a delight and a wonderful escape from everyday life, whether for a coffee-and-complaining session, a snowy weekend getting away from it all in Northumberland, or an ill-advised impromptu hike up an unexpectedly tall hill, you have all kept me sane throughout an absolutely mad four years. To Jess, Hetty, Scarlett, Molly, and Lucy, who have always met my academic achievements with a mixture of pride and the baffled certainty of a foregone conclusion, thank you for your faith across the years, it means the world. Morgan, I hope you'd be proud of me.

Abstract

The cause of the inhomogeneous absorption observed in the Venusian clouds at near-ultraviolet wavelengths has been a significant question in the field of Venusian research for decades. Many possible chemical species have been proposed as the cause of the so-called "unknown UV absorption", but none have been conclusively proven to be able to explain the observations. In this work, two candidates are considered: OSSO and ferric chloride ($FeCl_3$).

Cis-OSSO and *trans*-OSSO, two isomers of S_2O_2, are expected to be produced in the Venusian mesosphere by the third body recombination reaction of two SO molecules. Their combined predicted absorption cross-sections have been reported to provide a good match to the spectrum of the unknown absorber, but 1D models suggest only low concentrations would be produced. 3D chemical and dynamical modelling was carried out to investigate the concentrations of OSSO likely in the Venusian atmosphere. The injection of additional SO from ablation of meteoric material was also modelled. The resulting concentrations were used in a radiative transfer model (SOCRATES), and the OSSO found to be able to explain less than 1% of the observed near-UV absorption.

$FeCl_3$ has been proposed to explain the absorption if present in the micron-radius cloud droplets. However, representative absorption spectra of $FeCl_3$ are not available in the literature. Laboratory experiments to measure the absorbance of ferric chloride in sulphuric acid were performed, and the absorption spectrum measured over time. The resulting spectra were used in the SOCRATES model, and the observations satisfactorily reproduced by 2 – 3 wt% $FeCl_3$ in the sub-micron ("mode 1") cloud droplets. By comparison with the predicted chemical formation and accumulation of $FeCl_3$ in the atmosphere from the reaction of Fe ablated from cosmic dust with gas-phase HCl and Cl, ~40 % of the observed absorption can be explained by $FeCl_3$.

Table of contents

Acknowledgements v

Abstract vii

Table of contents ix

List of Tables xi

List of Figures xiii

List of abbreviations xxvii

1. Introduction: the Venusian unknown UV absorber 1

1.1 Statement of the problem 1

1.2 Overview and terminology of Venus 3

1.3 Clouds 23

1.4 UV absorption overview 39

1.5 Sulphur 59

1.6 Iron 64

1.7 Conclusions 68

2. Overview and validation of models 69

2.1 Venus PCM 69

2.2 SOCRATES 90

2.3. 1D coagulation and sedimentation modelling 118

3. Photochemical and radiative transfer modelling of OSSO 121

3.1 Introduction 121

3.2 Existing PCM chemistry 126

3.3 Quantum chemistry calculations 130

3.4 Meteoric injection 141

3.5 New chemistry results 141

3.6 Photochemical modelling results 143

3.7 SOCRATES results 150

3.8 Conclusions 153

4. Laboratory studies of ferric chloride ($FeCl_3$) 155

4.1 Overview and justification 155

4.2 Initial experiments 156
4.3 Change of absorption over time for $FeCl_3$ in an HCl/H_2SO_4 mixture 163
4.4. Identification of the reaction product as ferric sulphate 168
4.5 Investigation of further reaction of ferric sulphate 172
4.6 Molar absorptivity measurements of iron chlorides and sulphates 176
4.7 Concentration calculations using non-linear fitting 182
4.8 Temperature-dependent rates 193
4.9 Conclusions 197
5. Photochemical and radiative transfer modelling of $FeCl_3$ 199
5.1 Introduction 199
5.2 Chemical modelling 199
5.3 SOCRATES reflectance calculations 208
5.4 Validation of $FeCl_3$ absorbance cross-section 216
5.5 Estimated meteoric sources of $FeCl_3$ 217
5.6 Conclusions 220
6. Conclusions and future work 221
6.1 Conclusions 221
6.2 Future work 223
A. Iron chemistry predictions – J.M.C.Plane 227
A1 Iron chemistry in the Venus PCM 227
References 235

List of Tables

Table 1.1. A summary of successful space missions to Venus.....**13**

Table 1.2. From Esposito et al. (1983); Satoh et al. (2015). Venus standard cloud model. Values appear to be taken directly from Knollenberg and Hunten (1980).....**24**

Table 1.3. From Knollenberg and Hunten (1980). Particle distributions of the modes at different altitudes. Knollenberg and Hunten note that a log-normal distribution did not provide a fit for particles larger than 20 μm. Precloud layers and boundaries between the main cloud layers are shaded for readability.....**28**

Table 1.4. Photographs from Rossow et al. (1980) and descriptions and cartoons of the contrast features they show.....**44**

Table 2.1. List of observations and models included in Figures 2.6 – 2.9.....**75**

Table 2.2. Observations of key species plotted in Figures 2.11 and 2.16 – 2.25. The wavelength region of observations is given with the instrument name if it is not already included therein.....**84**

Table 2.3. Wavelength limits and widths of the 280 SOCRATES-Venus spectral bands.....**96**

Table 2.4. Mass weighting of the cloud modes. r is the geometric mean radius of the log-normal distribution, σ_g the geometric standard deviation and k_{mass} the fraction of the total cloud in that region that is in that mode. Heights refer to the centres of the layers. Layers are approximately 2 km thick, clouds do not have gaps between the layers.....**115**

Table 2.5. Number density and size distribution values used to calculate the single scattering aerosol properties. Number densities are calculated to approximate the mass weightings in Table 2.4, averaged across the atmosphere.....**116**

Table 3.1. Summary of the nomenclature used to refer to the first four isomers of S_2O_2 in the current literature.....**122**

Table 3.2. Sulphur chemistry in r3188 of the Venus PCM.....**126**

Table 3.3. Molecular properties and heats of formation (at 0 K) for the stationary points on the singlet and triplet potential energy surfaces for the dimerization reaction SO + SO (the singlet surface is illustrated in Figure 3.5), and for the SSO, SO_2 and ClSO products formed in the reactions of *cis*-OSSO with CO, O and Cl atoms (Section 3.3.2 and Figure 3.7 – 3.9).....**131**

Table 3.4. Molecular properties and heats of formation (at 0 K) for SSO, SO_2, and ClSO products and stationary points on the PESs for the reactions of *cis*-OSSO with CO, O and Cl (Figures 3.7 – 3.9).....**135**

Table 3.5. Reactions and rate coefficients describing S_2O_2 chemistry that has been added to the Venus PCM. Recombination reactions, marked with [a], have rates defined by Equation 3.1 .....**137**

Table 3.6. Photolysis rates of S_2O_2 isomers and ClSO that have been added to the Venus PCM..**138**

Table 3.7. Changes to the chemistry scheme from the released PCM version 3188.....**139**

Table 4.1. Concentrations of H_2SO_4, HCl, and $FeCl_3$ in each sample.....**164**

Table 4.2. Resulting concentrations of $FeCl_3$ in different concentrations of sulphuric acid.....**169**

Table 4.3. Resulting concentrations of $Fe_2(SO_4)_3$ in different concentrations of sulphuric acid..**169**

Table 4.4. Concentrations of $Fe_2(SO_4)_3$ and H_2SO_4 in each sample.....**172**

Table 4.5. Resulting concentrations of $FeCl_3$ in different concentrations of hydrochloric acid...**176**

Table 4.6. Resulting concentrations of $Fe_2(SO_4)_3$ in different concentrations of sulphuric acid..**176**

Table 4.7. Concentration of solutions for temperature-dependent experiments.....**193**

Table 5.1. Fe chemistry in the Venus PCM.....**200**

Table 5.2. Percentage of required $FeCl_3$ to account for all absorption in the four test cases (Figure 5.18, rows) available from meteoric iron in the different regions and with and without coagulation (columns).....**219**

Table A.1. Reaction enthalpies (at 0 K) for the additional reactions of Fe species predicted in this work that are included in the Venus PCM. The reader is referred to Table 5.1 (page 200) for a full list of reactions and references.....**228**

Table A.2. Molecular properties of the Fe-containing molecules illustrated in Figures A.1 and A.2, calculated at the B3LYP/6-311+g(2d,p) level of theory.....**229**

List of Figures

Figure 1.1. Images of Venus a) at 630 nm, showing most of the dayside of Venus and recorded by the spacecraft MESSENGER during its approach (NASA/JHU/APL, 2007a, 2007b) and b) at 365 nm, recorded by the Venus Monitoring Camera on the Venus Express orbiter, showing the southern polar region (ESA/MPS/DLR/IDA, 2008; Svedhem et al., 2007)...**1**

Figure 1.2. A section of Plate I from Ross (1928). A series of UV photographs of Venus taken in 1927. While the resolution is poor, bright regions near the poles (top and bottom of each disc) and generally darker low latitudes are apparent.....**2**

Figure 1.3. From Pérez-Hoyos et al. (2018). Measured optical properties (circles) of the Venusian UV absorber calculated from spectra recorded by MASCS/MESSENGER during its 2007 Venus gravity assist manoeuvre compared to prior values (triangles) from Pollack et al. (1980) (imaginary refractive index) and Haus et al. (2016) (normalised optical depth).....**2**

Figure 1.4. Diagram of orbital and rotational periods of Venus. The passage of time to each position (#) in Earth days and Venus solar and sidereal days and years are shown in the table in the upper right corner. Positions with integer values of solar or sidereal days and years are in bold in the table. The diagram is from above the Venusian northern pole. Venus follows an anticlockwise orbit and a clockwise rotation. The red cross and dashed line show a fixed point on the surface and normal to that surface. The combination of the orbit and rotation mean that midday at the cross occurs in positions 1 and 5 in panel a), just over half a Venusian year apart, with the planet having completed less than half a rotation (sidereal day). After one Venusian year, the planet returns to its original position relative to the sun (panel b, position 8) at the top of the diagram. Midday occurs again at position 9 (panel c) after just over a Venusian year, and the planet completes one full rotation (sidereal day) when the planet has returned to its initial orientation (dashed line vertically downwards in the diagram) in position 10 (panel d), after just over two solar days and one year.....**4**

Figure 1.5. The locations of the morning and evening terminators on a) Venus and b) a simplified Earth, ignoring axial tilt, viewed from above their northern poles. The shaded regions show the nightside of the planets. The green dot indicates an observer, stood at the morning terminator (at a previous point in time, they would have been on the nightside of the planet before it rotated to its current position) as the sun rises over the a) western or b) eastern horizon. When the planets are projected to equirectangular latitude-longitude plots, or latitude-local time plots, the local time axis is reversed for Venus.....**5**

Figure 1.6. Temperature profiles and atmospheric layers of a) Earth (Pielke, 2024) and b) Venus (Yung & DeMore, 1999). The green area in panel b) shows the variation in mesopause height between the dayside and nightside of the planet.....**6**

Figure 1.7. From Seiff et al. (1979). Temperature profiles measured by the four Pioneer Venus probes, along with extended profiles for the North and Day probes above 65 km (from probe deceleration measurements) and day and nightside IR sounding. A shape change at ~270 K can be seen, as can the divergence of the North probe temperature profile from the other three.....**8**

Figure 1.8. From Seiff et al. (1979). All four probes measured the same pressure profile below 30 km (top line) but diverge above that. Clear divergence of the North probe from the others is seen, but some variation between the Large (Sounder), Day, and Night probes is also present.....**9**

Figure 1.9. From Ignatiev et al. (2009). Predicted dependence of dayside cloud top height ($\tau = 1$) on wavelength. Peak of near-UV absorption and near-IR wavelengths are indicated for clarity.....**10**

Figure 1.10. From Haus et al. (2014). Zonal average temperature field from Venus Express (VIRTIS-M) observations. The cold collar is apparent as the two low temperature areas in the high latitude regions.....**12**

Figure 1.11. From Esposito et al. (1983); Satoh et al. (2015). The standard cloud model of Venus with altitudes, pressures, and mean particle sizes for the different modes indicated.....**23**

Figure 1.12. Best fit reported sizes of the smallest mode in the upper clouds (Knollenberg & Hunten, 1980), the smallest mode in the upper haze reported by Luginin et al. (2016) and the upper haze distribution reported by Kawabata et al. (1980). All populations are scaled to a maximum *n(r)* value of 20 cm^{-3} μm^{-1} for straightforward comparison of their shapes. **25**

Figure 1.13. Figure from Knollenberg and Hunten (1980) showing the LCPS measured distribution (bars) with mode 2 particle distribution measured by the instrument (dash-dotted line), and reconstructed mode 2 distribution once instrumental broadening had been removed (dotted line). Much of the mode 1 size distribution is below the limit of detection of the LCPS, so the tail of a log-normal distribution is fitted to the lower size bins (dashed line), resulting in a mean mode 1 diameter lower than the lower limit of detection of the instrument. The data shown is for the upper precloud layer, not the upper clouds, and is included here purely for illustration of the fitting and deconvolution of the data.....**27**

Figure 1.14. Adapted from Seiff et al. (1979). Stability of the atmosphere measured during Pioneer Venus descent. Negative values indicate instability. The middle clouds are the most statically unstable region of the atmosphere measured. Stability increases at the middle-lower cloud boundary, and then decreases again in the lower cloud. The y-axes have been inverted from the original plot. The surface is now towards the bottom of the plot.....**31**

Figure 1.15. Adapted from Counselman et al. (1980). Equatorward (a) and eastward zonal (b) wind velocity measured by the four Pioneer Venus probes. Zonal winds are westward, and therefore are negative. Equatorward winds are offset horizontally for clarity. The upper, middle, and lower clouds are shown in grey. Boundaries between cloud regions occurred at slightly different heights at the different probe locations; the regions shown are for the Large probe.....**31**

Figure 1.16. From Knollenberg and Hunten (1980). Size distribution for modes 1, 2, and 3 at 54.2 km. The right hand of the figure shows the large particle sizes. A log-normal distribution is unable to fit the largest detected sizes of the particles.....**32**

Figure 1.17. From Knollenberg and Hunten (1980). A long, thin particle, such as a crystal, can occult several range 2 detector elements (shown above for clarity), resulting in detection and accurate sizing of the particle. The same particle fails to occult 62.5% of any range 3 element and so is not detected.....**38**

Figure 1.18. From Murray et al. (1974). Left: photographs taken from Earth in a) 1966 and c) 1967 showing feature known as the "Y": the dark horizontal band across the centre of the disc, broader at the left-hand edge; and the “reverse-C”: bright limbs and dark centre seen at the evening terminator. Right, photographs taken by Mariner 10 in 1974, showing b) a similar Y feature and e) a pattern which, when projected onto a sphere (d) to mimic a view of the evening terminator, produced a similar pattern to the reverse-C.....**40**

Figure 1.19. Adapted from Pérez-Hoyos et al. (2018). Calculated UV absorption (dashed black line) and uncertainty (shaded area) compared to four candidates for the unknown UV absorber. While some provide a better fit than others, none can provide the correct slope at 0.4 – 0.5 μm.....**42**

Figure 1.20. From Yamazaki et al. (2018). Images from the Akatsuki UV Imager at 283 nm, looking at SO_2 absorption (left) and 3 minutes later, at 365 nm, looking at the unknown UV absorption (right).....**43**

Figure 1.21. From Travis et al. (1979a). Photographs from the Pioneer Venus cloud photopolarimeter, taken at 365 nm. A and B, taken a day apart, show the Y feature. It recurred 3 days later, shown in panels C, D, and E (each one day apart). Cloud motion is right to left.....**49**

Figure 1.22. From Travis et al. (1979a). Morning (A) and evening (B) regions photographed by the Pioneer Venus cloud polarimeter at 365 nm.....**50**

Figure 1.23. From Titov et al. (2012). Images taken by the VMC on Venus Express. The south pole is approximately in the white triangle between the images. The morning (a) and evening (b) terminators. The morning is characterised by streaky clouds, also visible in the southern part the evening terminator. The mottled, patchy patterns around the equatorial region of the evening terminator may indicate greater convection and turbulence.....**51**

Figure 1.24. From Markiewicz et al. (2014). Left: Intensity phase functions of glory patterns at (top to bottom): 365 nm (UV), 513 nm (visible), and 965 nm (near-IR) and right: glory images at the corresponding wavelengths. The glory is most prominent in the UV image, but superimposed contrasts from the inhomogeneous NUV absorption introduce additional complexity.....**55**

Figure 1.25. From Markiewicz et al. (2014). Intensity phase curve observations at 965 nm with predicted phase functions for (top curve) droplets of radius 1.2 μm with varied real refractive index, and (bottom curve) droplets with best fit refractive index 1.48 and varied radius. The two curves are offset vertically for clarity.....**56**

Figure 1.26. From Petrova (2018). For droplet radius 1.4 μm, the fit to observed data (red) is improved when the real refractive index is set to 1.48 and absorbing mode 1-size particles are included in the droplets.....**57**

Figure 1.27. From Hapke and Graham (1989). Top left: Reflectance of S_2O at 77 K. Top right: Reflectance of polysulphur oxide (PSO) at 195 K. Reflectance spectra at 400 – 600 nm were also provided at 77 K and 295 K with only minor changes in shape. Bottom: Absorbance of polysulphur oxide thin film at room temperature.....**60**

Figure 1.28. From Hapke and Graham (1989). The reflectance spectra of unirradiated, UV-irradiated (by exposure to a Hg-Xe lamp for 30 minutes), and X-ray irradiated (by exposure to a commercial x-ray tube for 2 minutes) flowers of sulphur at 77 K.....**61**

Figure 1.29. An overview of the sulphur chemistry in the Venusian atmosphere. Reactions are from the Venus PCM (Chapters 2 and 3). S_2O_2 is a combination of *cis*- and *trans*-OSSO, and cyclic-S_2O_2. Collision partners are indicated on arrows. *hv* indicates photolysis, *M* indicates thermal decomposition after collision with a third body, usually CO_2. .....**62**

Figure 1.30. SO_2 observations above and below the cloud deck. A decrease of 3 – 4 orders of magnitude is seen between observations above and below the cloud base.....**63**

Figure 1.31. From Kuiper (1969). Reflectance spectra of anhydrous (top) and hydrated (bottom) ferric chloride.....**64**

Figure 1.32. From Zasova et al. (1981). Predicted albedo of $FeCl_3$ in sulphuric acid cloud droplets (dashed line) compared to the observed Venusian albedo (solid line). "mkm" in the x-axis label means "μm".....**65**

Figure 1.33. From Saunders et al. (2012). UV absorbance spectrum of MSP analogues in sulphuric acid with time after the addition of the particles.....**66**

Figure 1.34. From Jiang et al. (2024). The combination of acid ferric sulphate and rhomboclase to produce the best fit (gold) to the measured spectrum of the unknown UV absorber (MASCS-2007: Pérez-Hoyos et al. (2018), ABCE-2020: Lee et al. (2022)).....**67**

Figure 2.1. 2D heatmap of zonal average PCM temperatures compared to temporal and zonal average of radio occultation measurements from Venus Express and Akatsuki (contours) (Ando et al., 2020).....**70**

Figure 2.2. Zonal average PCM temperature at a) 0 – 30°, b) 30 – 60°, c) 60 – 80°, and d) 80 – 90° latitude compared to observations and models (Ando et al., 2020; Mahieux et al., 2023b; Seiff et al., 1979). Insets show the cloud region (48 – 78 km) in more detail.....**71**

Figure 2.3. PCM global average cloud particle mass loading compared to measurements from the LCPS (Knollenberg & Hunten, 1980).....**73**

Figure 2.4. Comparison of observations of zonal wind in the a) upper clouds, b) upper-to-middle clouds and c) lower clouds with zonally averaged PCM modelled winds. As the observation heights are often somewhat imprecise, a range of model heights is included on each plot.....**78**

Figure 2.5. Comparison of observations of meridional wind in the a) upper clouds, b) upper-to-middle clouds and c) lower clouds with zonally averaged PCM modelled winds. Wind direction is set such that northward (southerly) winds are positive in both hemispheres, i.e., poleward flow in the southern hemisphere is negative.....**80**

Figure 2.6. Instantaneous PCM-modelled meridional winds at 60 km altitude. The black dashed line (0°) indicates midnight, the white dashed lines (± 180°, just visible at the edges of the plot) is midday.....**81**

Figure 2.7. Instantaneous zonal wind measurements from the four Pioneer Venus probes (Counselman et al., 1980) and Venera 8 – 10 and 12 – 14 during descent (Kerzhanovich & Limaye, 1985), along with the PCM profiles at each of their latitudes and local times, and the VIRA model.....**82**

Figure 2.8. Comparison of instantaneous Pioneer Venus probe-measured meridional winds with the VIRA model and PCM profiles at the same latitudes and local times (Counselman et al., 1980; Kerzhanovich & Limaye, 1985).....**82**

Figure 2.9. Initial molar (volume) mixing ratios of key species in the 78-level model.....**83**

Figure 2.10. Initial molar (volume) mixing ratios of key species in the 90-level model.....**84**

Figure 2.11. Initial and final mixing vmr of key species compared to observations.....**88**

Figure 2.12. Diagram of the levels and layers in SOCRATES. Adapted from Manners et al. (2022a).....**93**

Figure 2.13. The contributions of each of the fluxes to the upward and downward flux at each level. For clarity, fluxes are shown on an angle to allow for separation of incident and reflected fluxes. The fluxes are calculated on levels while T_i, T_{0i}, and R_i are properties of the layer.....**95**

Figure 2.14. a) An example of the longitude-averaged temperature profiles at a given latitude (0°) and their average. The variation between timesteps is less than the width of the lines. b) Some example average temperature profiles at different latitudes. c) The average, minimum, and maximum temperature for all latitudes and range of temperatures provided in the SOCRATES lookup table to account for all possible conditions.....**98**

Figure 2.15. a) Spectral line intensities and UV cross-sections from HITRAN, and calculated for *cis*-OSSO, *trans*-OSSO, and cyclic-S_2O_2, b) k coefficients per band for the gases in the spectral file generated by SOCRATES, c) modelled flux absorbed by each individual gas in the model. Note: $FeCl_3$ is not included in this model run.....**101**

Figure 2.16. a) Modelled vmr profile of CO_2 and observations, b) the absorbed and scattered flux due to CO_2 compared to total absorbed flux and TOA incident solar and outgoing fluxes. **103**

Figure 2.17. a) Modelled vmr profile of CO and observations, b) the absorbed flux due to CO compared to total absorbed flux and TOA incident solar and outgoing fluxes.....**104**

Figure 2.18. a) Modelled vmr profile of N_2 and observations, b) the scattered flux due to N_2 compared to total absorbed flux and TOA incident solar and outgoing fluxes.....**105**

Figure 2.19. a) Modelled vmr profile of H_2O and observations, b) the absorbed flux due to H_2O compared to total absorbed flux and TOA incident solar and outgoing fluxes.....**106**

Figure 2.20. a) Modelled vmr profile of SO_2 and observations, b) the absorbed flux due to SO_2 compared to total absorbed flux and TOA incident solar and outgoing fluxes.....**107**

Figure 2.21. a) Assumed vmr profile of H_2S from Eymet et al. (2009), and observations, b) the absorbed flux due to H_2S compared to total absorbed flux and TOA incident solar and outgoing fluxes.....**108**

Figure 2.22. a) Modelled vmr profile of HCl and observations, b) the absorbed flux due to HCl compared to total absorbed flux and TOA incident solar and outgoing fluxes.....**109**

Figure 2.23. a) Assumed vmr profile of HF from Eymet et al. (2009) and observations, b) the absorbed flux due to HF compared to total absorbed flux and TOA incident solar and outgoing fluxes.....**110**

Figure 2.24. a) Modelled vmr profile of OCS and observations, b) the absorbed flux due to OCS compared to total absorbed flux and TOA incident solar and outgoing fluxes. Observations from Oyama et al. (1980) are an upper limit, not detections.....**111**

Figure 2.25. a) Predicted HDO vmr, calculated by modelled H_2O vmr profile scaled by a factor of 0.0144 (Eymet et al., 2009) and observations, b) H_2O/HDO ratio compared to observations, c) the absorbed flux due to HDO compared to total absorbed flux and TOA incident solar and outgoing fluxes.....**112**

Figure 2.26. The total impact of N_2 and CO_2 Rayleigh scattering on the TOA spectrum.....**113**

Figure 2.27. Total flux absorbed due to H_2O-H_2O and CO_2-CO_2 continuum absorption compared to the TOA solar and reflected flux spectrum.....**113**

Figure 2.28. Volume mixing ratios of the four cloud modes with altitude. Mixing ratio here refers to the total mole fraction of liquid H_2SO_4 and H_2O.....**116**

Figure 2.29. Modelled effect of aqueous sulphuric acid modes 1, 2, 2' and 3 cloud particles on the TOA spectrum. All modes have a scattering effect on the spectrum.....**117**

Figure 2.30. Real and imaginary components of the refractive index of 75 wt% sulphuric acid. **118**

Figure 2.31. Vertical profiles of temperature (solid line, PCM model daytime average at the equator) and eddy diffusion coefficient (K_{zz}, dashed line) from Krasnopolsky (2007, 2012).....**118**

Figure 3.1. Adapted from Frandsen et al. (2016). Diagrams of the four relevant S_2O_2 isomers considered in this thesis. Oxygen atoms are shown in red, sulphur atoms in yellow. Isomer numbers are indicated in labels. Table 3.1 details the nomenclature in use for these isomers in the literature.....**121**

Figure 3.2. Comparison of the literature OSSO spectra with those of this work. Solid lines are *cis*-OSSO spectra, dashed lines are *trans*-OSSO. Spectra from Frandsen et al. (2016) and Frandsen et al. (2020) and this work are plotted on the primary axis and compare cross-section values. Spectra from Wu et al. (2018) and Pérez-Hoyos et al. (2018) are plotted on the secondary axis (blue) as the authors did not report cross-sections, only absorbance. In the case of the spectrum from Pérez-Hoyos et al. (dotted line), this absorbance is normalised to maximum of 1.0 and is a combination of both *cis*- and *trans*- isomers.....**125**

Figure 3.3. Variation of global mean a) SO_2, b) SO, c) H_2O, and d) OCS over 9.0 Vd in the out-of-the-box PCM run.....**129**

Figure 3.4. Variation of global mean trigonal-S_2O_2 in the out-of-the-box PCM run.....**130**

Figure 3.5. Potential energy surface (singlet spin multiplicity, zero-point energies included) for the reaction SO + SO (the triplet surface is not shown here to maintain clarity – see Figure 3.6). Calculations are at the w1bd level of theory (Barnes et al., 2009).....**133**

Figure 3.6. Potential energy surface of triplet spin multiplicity for the reaction SO + SO. Calculated at the w1bd level of theory (Barnes et al., 2009).....**133**

Figure 3.7. Potential energy surface for the reaction *cis*-OSSO + CO (singlet spin multiplicity), calculated at the w1bd level of theory (Barnes et al., 2009).....**136**

Figure 3.8. Potential energy surface for the reaction *cis*-OSSO + O (triplet spin multiplicity), calculated at the w1bd level of theory (Barnes et al., 2009).....**136**

Figure 3.9. Potential energy surface for the reaction *cis*-OSSO + Cl (doublet spin multiplicity), calculated at the w1bd level of theory (Barnes et al., 2009).....**136**

Figure 3.10. Absorption cross-sections versus wavelength: *cis*-OSSO and *trans*-OSSO calculated using EOM-CCSD theory (Goings et al., 2014) with the aug-cc-pVQZ basis set; cyclic-S_2O_2 and ClSO calculated with TD-B3LYP theory and the 6-311+g(2d,p) level of theory (Frisch et al., 2016).....**138**

Figure 3.11. Variation in global mean a) SO_2, b) SO, c) H_2O, and d) OCS concentration for the new chemistry PCM run.....**142**

Figure 3.12. Variation in global mean a) SO_2, b) SO, c) H_2O, and d) OCS concentration for the SO MIF PCM run.....**142**

Figure 3.13 Comparison of PCM modelled vmr to observations for a) SO_2, b) SO, c) H_2O, and d) OCS. Model results are averaged from -30° – 30° latitude. Dayside (nightside) is defined as the 140° longitude centred on the subsolar (antisolar) point to prevent capturing terminators. Observations of OCS by Oyama et al. (1980) constitute an upper limit on OCS concentration due to the limit of detection of the instrument. Dayside (blue) and nightside (red) results are plotted after 9.0 Venus days for the three runs, the longitude-averaged profiles are for the SO MIF run only.....**144**

Figure 3.14. Vmr profiles of the three S_2O_2 isomers in different latitude bands and local times. An average is taken across 140° centred on the subsolar or antisolar points to avoid capturing the terminators in dayside and nightside averages, respectively.....**146**

Figure 3.15. Column abundance of S_2O_2 from 59 km to TOA. The black dashed line indicates local midnight (which is at the break of the plot), midday is the white dashed line. Morning and evening terminators are clear at 270 and 90°, with an abrupt change in concentration due to photolysis. The column density on the nightside is approximately an order of magnitude higher than the dayside.....**147**

Figure 3.16. Net production and loss of a) *cis*-OSSO, b) *trans*-OSSO, and c) cyclic-S_2O_2 compared to modelled and steady-state concentrations, and d) – f) contribution of each loss mechanism to the total loss of each isomer with altitude. Photolysis is taken to be constant through the atmosphere. The excellent agreement between black (PCM modelled concentration) and grey (steady state) lines shows the model has reached steady state. **148**

Figure 3.17. Low-latitude (30°S – 30°N latitude) dayside (subsolar point ± 70° longitude) a) *cis*-OSSO and b) *trans*-OSSO concentrations for the standard chemistry scheme, Sensitivity Test 1 and Sensitivity Test 2 (see text for details).....**150**

Figure 3.18. SOCRATES modelled TOA reflectance for PCM concentrations of OSSO and various scalings. See the text for interpretation of these scalings.....**151**

Figure 3.19. Contributions of each of the four absorbing species below 600 nm to the modelled TOA absorption. To ensure contributions are visible, the scaled version which best reproduces the absorption near 350 nm (*cis*-OSSO and cyclic-S_2O_2 are scaled by a factor of 800, *trans*-OSSO by a factor of 1600) is used.....**152**

Figure 3.20. Required PCM S_2O_2 scalings in each case of the sensitivity study to approximately reproduce the TOA reflectance.....**153**

Figure 4.1. Normalised absorption spectrum measured by the MASCS instrument on MESSENGER during its 2007 gravity assist manoeuvre (Pérez-Hoyos et al., 2018) and the absorption spectrum of $FeCl_3$ in ethyl acetate (Aoshima et al., 2013).....**155**

Figure 4.2. a) Measured real refractive index of 1 wt% $FeCl_3$ in 75wt% sulphuric acid. Photographs of the solution over time b – e) before mixing, or f – i) after inverting to mix. The solution becomes a paler yellow over time, but the supernatant remains yellow even after its refractive index becomes consistent with H_2SO_4 on day 10. The volume of the sample decreases as small portions are taken for spectroscopy over time. The volume of the precipitate increases over time.....**157**

Figure 4.3. 1% $FeCl_3$ in 75 wt% sulphuric acid shortly after the solution was made up. Black and pale yellow arrows indicate some dark and light particles.....**158**

Figure 4.4. $FeCl_3.6H_2O$ (yellow, left) and anhydrous $FeCl_3$ (black, right). The anhydrous form is highly hygroscopic and absorbs ambient water from the air. This is apparent as the yellow staining on the filter paper to the top right of the anhydrous sample.....**159**

Figure 4.5. 1% $FeCl_3$ in 75 wt% sulphuric acid one day after mixing. a) The particles have settled to the bottom of the flask, leaving a translucent liquid. b) Particles are pale, either yellow or white.....**159**

Figure 4.6. The average of four measured absorption spectra of $1.44 \pm 0.12 \times 10^{-4}$ M $FeCl_3$ in $1.70 \pm 0.14 \times 10^{-2}$ M sulphuric acid. Variation between repeats is within the thickness of the line.....**161**

Figure 4.7. Cloud droplet predicted HCl concentration using a PCM HCl mixing ratio profile and Henry's law coefficients reported by Williams and Golden (1993) at 60 wt% sulphuric acid (orange) and extrapolated to 80 wt% (blue).....**162**

Figure 4.8. The average of four measured absorption spectra of $2.3 \pm 0.2 \times 10^{-4}$ M $FeCl_3$ in a solution of $<0.2847 \pm 0.0007$ M HCl and 12.45 ± 0.02 M H_2SO_4. Variation was within the thickness of the line.....**162**

Figure 4.9. Change in the measured absorbance spectrum of sample 0C from both sets of samples with time. The reader is referred to Table 4.1 (page 164) for concentrations.....**165**

Figure 4.10. Spectra over time for all samples in set N23. HCl concentration decreases from top to bottom, initial $FeCl_3$ concentration roughly increases from left to right. The reader is referred to Table 4.1 (page 164) for interpretation of concentrations.....**166**

Figure 4.11. Spectra over time for all samples in set A24. HCl concentration decreases from top to bottom, initial $FeCl_3$ concentration increases from left to right. The reader is referred to Table 4.1 (page 164) for interpretation of concentrations.....**167**

Figure 4.12. Measured spectra relative to stock acids for a) $FeCl_3$ and b) $Fe_2(SO_4)_3$. The Fe concentration in the samples is plotted against absorbance at several wavelengths (c, d) and any concentrations that do not obey a linear relationship are shown as crosses and excluded from the calculation of absorptivity. Linear regression lines are fitted through the solid points.....**170**

Figure 4.13. Calculated molar absorptivity of Fe for $FeCl_3$ (yellow) and $Fe_2(SO_4)_3$ (blue). Samples at similar sulphuric acid concentrations are plotted together for comparison...**171**

Figure 4.14. Measured absorption spectra at different H_2SO_4 concentrations over time. The reader is referred to Table 4.4 (page 172) for precise concentrations.....**173**

Figure 4.15. Average absorbance spectrum over time for each sample.....**174**

Figure 4.16. A model to show qualitatively how the observed change in shape of the spectrum in Figure 4.15 can be produced with two absorbing species. Dashed lines are the absorption due to the $FeSO_4^+$ analogue, dotted lines are due to the $Fe(SO_4)_2^-$ analogue, solid lines are the sum.....**175**

Figure 4.17. All measured spectra of $FeCl_3$ in HCl. For concentrations of samples and dilutions, the reader is referred to Table 4.5 (page 176).....**177**

Figure 4.18. 1st and 3rd columns: measured absorbance spectra with stock acid spectrum removed. 2nd and 4th columns: concentration against absorbance for each sample, with a linear regression line fitted through the points. $FeCl_3$ concentrations of samples are as shown in Table 4.5 (page 176).....**178**

Figure 4.19. Calculated absorptivities of $FeCl_3$ in different concentrations of HCl. Shaded areas indicate the uncertainties in the absorptivity from the fitting process. The large uncertainty in the 10.44 M sample is due to non-linearity of absorbance with concentration (see Figure 4.18d).....**179**

Figure 4.20. All spectra with stock H_2SO_4 spectra removed. The absorbances of samples at particular wavelengths are plotted in the right-hand column, with a linear regression fitted to the points.....**181**

Figure 4.21. Calculated molar absorptivities of $Fe_2(SO_4)_3$ in different concentrations of H_2SO_4. Shaded regions show uncertainties. Inset: absorptivity at given wavelengths against sulphuric acid concentration.....**182**

Figure 4.22. Example fitting programme results. The measured spectrum (grey line) is fitted by least squared minimisation to produce a total spectrum (black, dashed line). Components fitted to the spectrum with concentrations of $>10^{-8}$ M are plotted (different colours) with uncertainties from the fitting programme (shaded regions). The reader is referred to Table 4.5 (page 176) for interpretation of the Cl spectrum names. The SO_4 spectrum is the $Fe_2(SO_4)_3$ spectrum at the closest available H_2SO_4 concentration (Samples 77 and 79 for N23 and A24 samples respectively, see Table 4.6, page 176).....**184**

Figure 4.23. Fitted concentration of iron chlorides and sulphate over time for all samples. Shaded areas show uncertainties.....**186**

Figure 4.24. Calculated rate of reaction of $FeCl_3$ for first-order (blue) and second-order (green) kinetics for each sample. The A samples are not shown due to their low Fe concentration. The first-order plots show better agreement, so the reaction is concluded to be first-order in $FeCl_3$.....**190**

Figure 4.25. Diagram of low temperature apparatus. The Labplant control box is connected to the immersion probe and temperature probe (this connection is not shown for clarity). Cooling is turned on and off automatically to maintain the set point temperature. The Labplant RP100CD cools a bath of propylene glycol in a dual-skinned vacuum flask. A small beaker is suspended from the rim of the flask using a clamp (not shown for clarity). The beaker and flask both contain propylene glycol. The sample cuvette(s) are placed within the small beaker. The beaker can be removed easily to access the samples, then lowered back into the flask.....**194**

Figure 4.26. Room temperature sample in an unstoppeded cuvette after 1 day. Large numbers of bubbles, presumably HCl, have nucleated in the solution.....**195**

Figure 4.27. Arrhenius plot of the rate constant for the conversion of $FeCl_3$ to $Fe_2(SO_4)_3$. The reader is referred to Table 4.7 (page 193) for concentrations. For clarity, while $1/T$ and $\ln(k_{obs})$ are fitted, k_{obs} and T are shown on secondary axes).....**196**

Figure 5.1. Reactions of neutral (gold) and charged (blue) Fe-containing species added to the PCM (Table 5.1). Meteoric ablation (green) provides a source of Fe and Fe^+. Black lines and reactants indicate neutral chemistry, red lines and reactants indicate reactions involving charged species. Collision partners are indicated on arrows. *M* indicates thermal decomposition after collision with CO_2, e^- is electron uptake, and *hv* indicates absorption of a photon. Solid lines indicate reactions that have been measured experimentally, dashed lines indicate predicted reaction rates.....**202**

Figure 5.2. Global mean vmrs of all a) charged and b) neutral iron species after 3.0 Venus days. **203**

Figure 5.3. Calculated absorption cross-sections for the $FeCl_3.CO_2$ cluster and $FeCl_3$ in the gas phase, and $FeCl_3$ in liquid H_2SO_4 using Time-Dependent Density Functional Theory (Scalmani et al., 2006). See Appendix Section A1.2 for details of the calculation of these spectra.....**204**

Figure 5.4. The change in global mean total $FeCl_3$ a) column density and b) number density with time over the 3.0 Venus days of model run.....**204**

Figure 5.5. Vertical slices through the atmosphere at different local times and at the start, middle, and end of the first day of the model run, and after each subsequent day.....**205**

Figure 5.6. Total $FeCl_3$ column abundance across the model run. White dashed line indicates local midday, black lines indicate midnight, which is at the break of the map projection.....**206**

Figure 5.7. The size distribution (radius *r*) of MSP particle number density, *N*, as a function of altitude, after running the 1D model with coagulation for 20 000 Earth days.....**207**

Figure 5.8. $FeCl_3$ number density in MSPs with and without coagulation of particles.....**208**

Figure 5.9. The calculated imaginary refractive index of a solution of an initial concentration of 1 wt% $FeCl_3$, based on measurements of 2×10^{-3} to 10×10^{-3} wt%.....**210**

Figure 5.10. SOCRATES modelled reflectance for different initial concentrations of $FeCl_3$ in all cloud modes.....**211**

Figure 5.11. SOCRATES modelled reflectance for different concentration of $FeCl_3$ in a) mode 1, b) mode 2, c) mode 2', and d) mode 3 cloud droplets only. In each case, all other cloud modes are sulphuric acid.....**211**

Figure 5.12. 2-nm resolution imaginary refractive index spectra of solutions of 1 wt% initial $FeCl_3$ concentration calculated from the measured absorption spectra of sample N23 0C (see Table 4.1 (page 164) for initial concentrations) on different days.....**213**

Figure 5.13. SOCRATES modelled reflectance for different modelled initial concentrations of $FeCl_3$ for spectra measured after a) 1 day, b) 4 days, c) 9 days, and d) 18 days in mode 1 cloud droplets. In each case, all other cloud modes are modelled as sulphuric acid.....**214**

Figure 5.14. Best fit initial $FeCl_3$ concentrations for the four spectra in mode 1 from comparison of SOCRATES model results to observations.....**214**

Figure 5.15. Dominant fitted components in sample N23 0C day 4 calculated using the fitting algorithm described in Section 4.7.....**215**

Figure 5.16. The SOCRATES model results using spectral fit results for ferric chloride species only.....**216**

Figure 5.17. Time-Dependent Density Functional Theory calculated absorption cross-sections for the $FeCl_3.CO_2$ cluster and $FeCl_3$ in the gas phase, and $FeCl_3$ in liquid H_2SO_4. See Appendix Section A1.2 for details of the calculation of these spectra.....**217**

Figure 5.18. Global average number density of $FeCl_3$ equal to 2.5 wt% of the total cloud particles (purple); 2.5 wt% of mode 1 throughout the clouds (blue), or only above 60 km (orange); and 1.75 wt% of mode 1 above 60 km (green); compared to 1D model (Figure 5.8), with (red) and without (black) coagulation and sedimentation.....**218**

Figure 6.1. Measured molar absorptivity spectrum (per total fitted concentration of Fe, red) of a solution of $FeCl_3$ in 76.5(5) wt% H_2SO_4 with small amounts of HCl. Best fit to MESSENGER observations was for an initial 2 – 3 wt% $FeCl_3$ in the cloud droplets. Partial reaction to form ferric sulphate ions has occurred. When the ferric sulphate contribution is removed by the fitting algorithm, the absorptivity of the chloride contribution only can be calculated (blue). The best fit to MESSENGER observations was for 1.5 – 2 wt% $FeCl_3$. Spectra are reported in both molar absorptivity (primary axis) and cross-section (secondary axis).....**222**

Figure A.1. Molecular geometries calculated at the b3lyp/6-311+g(2d,p) level of theory: (a) FeCl; (b) $FeCl_2$; (c) $FeCl_2.H_2O$; (d) $FeCl_3$; (e) $FeCl_3.CO_2$; (f) $FeCO_3$; (g) $FeCO_3.CO_2$; (h) FeO_2; (i) HOFeCl; (j) $OFeCO_3$; (k) OFeCl.....**232**

Figure A.2. Molecular geometries calculated at the b3lyp/6-311+g(2d,p) level of theory: (a) FeO^+; (b) FeO_2^+; (c) $FeO^+.CO_2$; (d) $Fe^+.CO_2$; (e) $Fe^+.(CO_2)_2$; (f) $FeO^+.(CO_2)_2$.....**233**

Figure A.3. Absorption cross-sections of FeCl, $FeCl_2$, $FeCO_3$, $FeCO_3.CO_2$ and $OFeCO_3$, calculated using Time-Dependent Density Functional Theory with the 6-311+g(2d,p) basis set.....**234**

List of abbreviations

Abbreviation	Term	Description
A24	-	The set of H_2SO_4/HCl/$FeCl_3$ samples produced in August 2024. See Table 4.1 for concentrations.
amu	atomic mass unit	Defined as $1/12^{th}$ the mass of carbon-12. The equivalent of a molar mass of 1 g mol^{-1}.
AU	Astronomical Unit	149 597 870 700 m. The approximate average distance between the Earth and Sun.
CCN	Cloud Condensation Nucleus/Nuclei	Small particles onto which a liquid phase can condense heterogeneously to form cloud particles.
CSHELL	Cryogenic Echelle Spectrograph	An instrument at NASA IRTF.
DLR	Deutsches Zentrum für Luft- und Raumfahrt	The German aerospace centre.
ESA	European Space Agency	Europe's intergovernmental space agency.
FIGS	Fabry-Perot Interferometer Grating Spectrometer	An instrument at the Anglo-Australian IR Telescope.
GCM	Global Climate Model	3D planetary models that aim to capture the dynamics and chemistry of a planetary atmosphere.
HITRAN	High Resolution Transmission	A database of molecular spectroscopic data. Available via Gordon et al. (2022).
HST/STIS	Hubble Space Telescope Imaging Spectrograph	The imaging system on the Hubble Space Telescope.
IAU	International Astronomical Union	An international non-governmental organisation focused on promoting and safeguarding astronomy and related science.
IDA	Institut für Datentechnik und Kommunikationsnetze	The Institude for Computer and Network Engineering at Technische Universität Braunschweig.
IPSL	Institut Pierre-Simon Laplace	An environmental science research consortium of nine laboratories in Lle-de-France.
IR	Infrared	The region of the electromagnetic spectrum from 750 nm – 1 mm.

IR1	1-μm camera	The 1-μm camera on JAXA's Akatsuki orbiter, imaging at 0.90, 0.97, and 1.01 μm.
IR2	2-μm camera	The 2-μm camera on JAXA's Akatsuki orbiter, imaging at 1.74, 2.26, and 2.32 μm.
IRTF	InfraRed Telescope Facility	NASA's IR telescope facility in Hawaii.
ISAV	-	A nephelometer (ISAV-A) and UV spectrometer (ISAV-S) on the Vega landers.
JAXA	Japan Aerospace Exploration Agency	The Japanese national air and space agency.
JCMT	James Clerk Maxwell Telescope	A sub-mm telescope in Hawaii.
JHU APL	Johns Hopkins University Applied Physics Laboratory	A research centre in Maryland, USA.
LCPS	Large probe Cloud Particle Size spectrometer	The optical particle sizing instrument on the Pioneer Venus Large probe. It recorded the measurements on which the Venus cloud model is based.
LSA	-	A particle size spectrometer on the Vega 1 and 2 landers.
MASCS	Mercury Atmospheric and Surface Composition Spectrometer	One of the instruments on MESSENGER, consisting of a UV-Visible spectrometer and a Visible-IR spectrograph.
MDIS	MESSENGER Dual Imaging System	A system of two cameras (wide angle and narrow angle) on MESSENGER.
MESMER	Master Equation Solver for Multi-Energy well Reactions	Code to perform kinetic calculations of predicted rate constants. Available via Glowacki et al. (2012).
MESSENGER	Mercury Surface, Space, Environment, Geochemistry and Ranging	A NASA spacecraft launched in 2004 to study Mercury from orbit.
MIF	Meteoric Input Function	The altitude dependent input flux of metal atoms or ions from ablated meteoric material.

mmr	Mass mixing ratio	Abundance of a species as a fraction of the total mass of air.
MPS	Max Planck Institute for Solar System Research	An astronomy and astrophysics research institute in Germany.
MSP	Meteoric smoke particles	The products of meteoric dust that has entered a planet's atmosphere and ablated.
N23	-	The set of H_2SO_4/HCl/$FeCl_3$ samples produced in November 2023. See Table 4.1 for concentrations.
NASA	National Aeronautics and Space Administration	United States of America government space agency.
NIMS	Near-Infrared Mapping Spectrometer	A spectrometer on Gallileo.
NUV	Near-Ultraviolet	Ultraviolet wavelengths just shorter than visible light (300 – 400 nm).
OCPP	Orbiter Cloud Photo-Polarimeter	The cloud polarimetry instrument on the Pioneer Venus Orbiter.
PCM	Planetary Climate Model	The name given to the Venus 3D atmospheric model developed at IPSL.
PES	Potential Energy Surface	A description of the energy of a system of molecules used to determine the lowest energy (most stable) state.
ppm	parts per million	Mixing ratio of 1×10^{-6}.
ppb	parts per billion	Mixing ratio of 1×10^{-9}.
PSO	Polysulphur Oxides	Sulphur-and-oxygen-containing molecules with atomic formule S_nO.
RRKM	Rice-Ramsperger-Kassel-Markus	A method of calculating reaction rates from the reaction PES using statistical rate theory.
SOCRATES	Suite Of Community Radiative Transfer codes based on Edwards and Slingo	The radiative transfer module designed for use with the Unified Model developed by the UK Met Office.
SOIR	Solar Occultation in Infrared	A solar occultation IR spectrometer on Venus Express, part of the SPICAV instrument.

SPICAV	Spectroscopy for the Investigation of the Characteristics of the Atmosphere of Venus	A suite of three spectrometers (SPICAV UV, SPICAV VIS-IR, and SPICAV SOIR) on Venus Express.
SSI	Solid State Imager	The camera on the Galileo space craft, with eight wavelength filters in the 350 – 1100 nm range
t d^{-1}	tonnes per Earth day	The standard unit meteoric flux is reported in. Units are in metric tonnes and Earth days, regardless of the planet being described.
TEXES	Texas Echelon-cross-Echelle Spectrograph	An instrument at NASA IRTF.
TOA	Top Of the Atmosphere	Used when referring to observations from above the atmosphere. It is refers to the highest level of an atmospheric model.
UV	Ultraviolet	Region of the electromagnetic spectrum between x-rays and visible light (10 – 400 nm).
UVI	Ultraviolet Imager	An imager on the Akatsuki orbiter which takes photographs at 283 and 365 nm.
UV-Vis	Ultraviolet-visible	A form of spectroscopy, generally using wavelengths of light between 800 and 200 nm.
Vd	Venus days	Venus solar days, equal to 116.75 Earth days.
VeGa VEGA Vega	Venera-Gallei	Two spacecraft, launched in 1984 to investigate both Venus and Halley's comet. Venera-Gallei is an anglicisation of Венера-Галлей, the Russian words for Venus and Halley.
VeRa	Venus Express Radio Science experiment	Radio science instrument for radio occultation, surface investigation, and gravitational field measurements on Venus Express.
VEx	Venus Express	ESA Venus orbiter, launched in 2005.
VIRA	Venus International Reference Atmosphere	A compilation of observations from the Pioneer Venus missions and earlier (VIRA 2 also includes Venera) and a model to generalise the observations (Keating et al., 1985; von Zahn & Moroz, 1985).
VIRTIS	Visible and Infrared Thermal Imaging Spectrometer	A spectrometer on Venus Express with three channels, split into Mapping (2 channels) and High-resolution (1 channel) (see below).

VIRTIS-H	Visible and Infrared Thermal Imaging Spectrometer - High resolution	The high resolution VIRTIS channel (2 – 5 μm).
VIRTIS-M	Visible and Infrared Thermal Imaging Spectrometer - Mapping	The visible (0.25 – 1 μm) and IR (1 – 5 μm) channels of the VIRTIS instrument, dedicated to mapping.
VMC	Venus Monitoring Camera	A camera on the Venus Express orbiter with four wavelength filters, centered at 365 nm, 513 nm, 965 nm, and 1.0 μm.
vmr	Volume mixing ratio	Abundance of a species as a fraction of the total moles of air. Due to the ideal gas law, molar fraction and volume fraction are equivalent.
w1bd	W1 theory with unrestricted coupled cluster and Brueckner Doubles	A method of estimating the energy of reactions and transition states.
wt%	weight percent	Mass fraction of a species in a solution as a fraction of the total mass of the solution.

1. Introduction: the Venusian unknown UV absorber

1.1 Statement of the problem

While broadly featureless at visible wavelengths (Figure 1.1a), distinct dark and bright regions are visible across the whole planet when Venus is viewed at near-ultraviolet (NUV) wavelengths (Figure 1.1b). These contrasts, which occur due to the presence of an absorbing species (or mixture of species) within the generally bright and reflective cloud layer, were first observed by Earth-based observation (Ross, 1928; Wright, 1927; Figure 1.2). They were initially assumed to be caused by sulphur in the atmosphere (Hapke & Nelson, 1975), but later space missions and ground-based observation found no indications of sulphur particles (Pollack et al., 1979; Ragent & Blamont, 1980). Various candidates for the cause of the absorption have been proposed since then (e.g Pérez-Hoyos et al., 2018, and references therein), but none have been conclusively proven to be the cause of the contrasts, and the identity of the so-called "unknown UV absorber" remains one of the largest open questions in the study of Venus to this day (Titov et al., 2018).

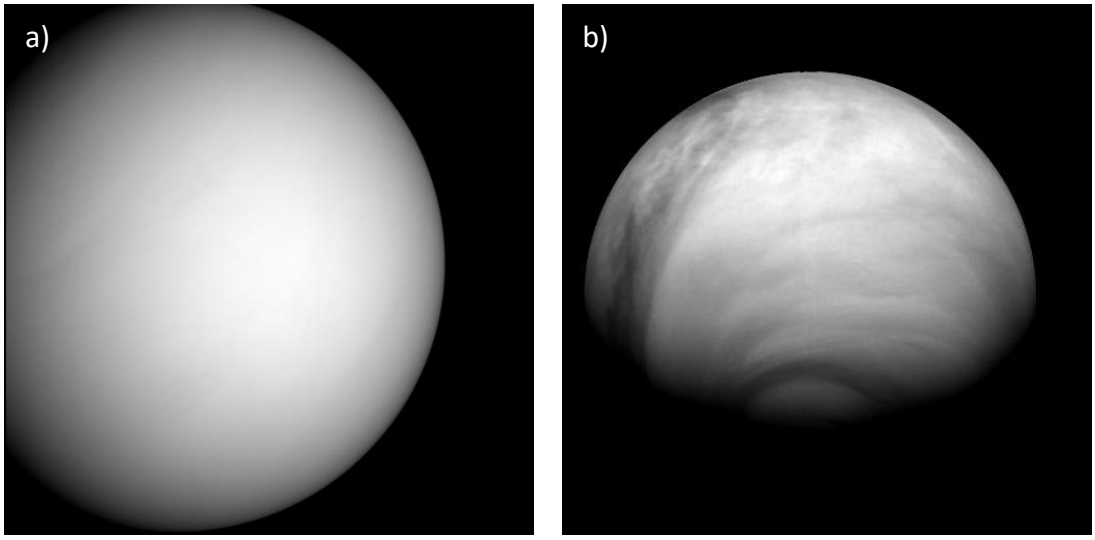

Figure 1.1. Images of Venus a) at 630 nm, showing most of the dayside of Venus and recorded by the spacecraft MESSENGER during its approach (NASA/JHU/APL, 2007a, 2007b) and b) at 365 nm, recorded by the Venus Monitoring Camera on the Venus Express orbiter, showing the southern polar region (ESA/MPS/DLR/IDA, 2008; Svedhem et al., 2007).

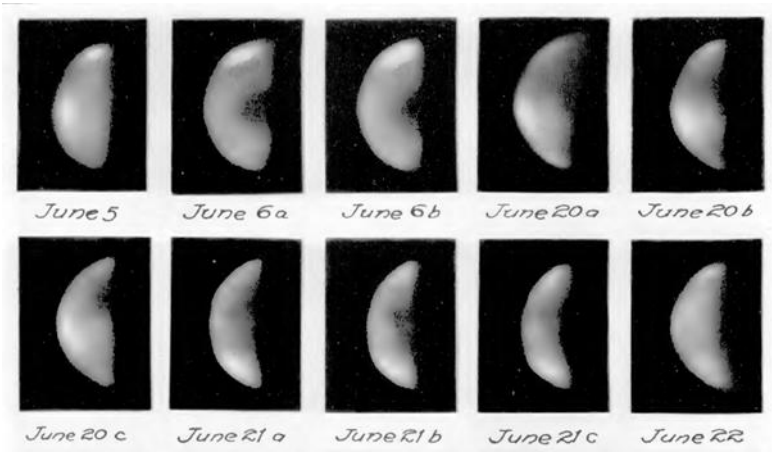

Figure 1.2. A section of Plate I from Ross (1928). A series of UV photographs of Venus taken in 1927. While the resolution is poor, bright regions near the poles (top and bottom of each disc) and generally darker low latitudes are apparent.

The planet is commonly imaged at NUV wavelengths by space missions, and spectra are occasionally recorded (Figure 1.3). The UV absorption is broad, centred at around 360 nm and extending from 300 – 500 nm and likely beyond (Pérez-Hoyos et al., 2018). The unknown species is a dominant contributor to the total absorbed solar energy (Titov et al., 2018), so accurate modelling of its properties, location, and variation are key to fully understanding the energy balance of Venus (Crisp, 1986).

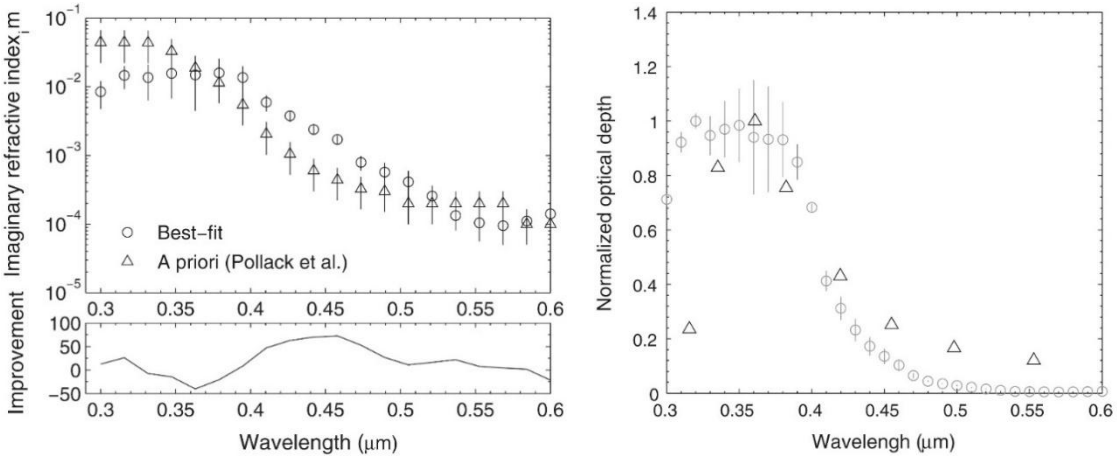

Figure 1.3. From Pérez-Hoyos et al. (2018). Measured optical properties (circles) of the Venusian UV absorber calculated from spectra recorded by MASCS/MESSENGER during its 2007 Venus gravity assist manoeuvre compared to prior values (triangles) from Pollack et al. (1980) (imaginary refractive index) and Haus et al. (2016) (normalised optical depth).

The main aim of this thesis is to make contributions to the identification of the unknown UV absorber by investigating two promising candidates: the combination of two isomers of disulphur dioxide, S_2O_2 (*cis- and trans*-OSSO, "OSSO" collectively), and ferric chloride ($FeCl_3$). An overview of Venus (Section 1.2), the clouds where the absorption originates (Section 1.3), and the observed absorption (Section 1.4) provide background to understand the problem before the two

candidates are discussed in more detail. Venusian sulphur chemistry is outlined in Section 1.5.2 and investigated through modelling work using 3D dynamical and photochemical modelling and 1D radiative transfer modelling (Chapter 3). Chapter 2 contains an overview of the models used. A combination of laboratory studies (Chapter 4) and modelling (Chapter 5) are used to investigate $FeCl_3$. The results are summarised, and potential future work discussed in Chapter 6.

1.2 Overview and terminology of Venus

While Venus is termed a "terrestrial planet", it differs from Earth in significant ways, and comparisons or use of Earth terminology to refer to Venus is often counterintuitive or unhelpful. Nevertheless, many terrestrial terms have been adopted and adjusted to apply to Venus in subtly different ways than their original meaning.

This section aims to lay out the fundamental Venusian properties and the terminology used to refer to them, and highlight where they differ from terrestrial definitions.

1.2.1 Rotation and orbit

Venus is the second planet from the sun, with a mean orbital radius of 0.72 AU, an orbital period (year) of 224.70 Earth days, and an orbital eccentricity of 0.0067, the lowest of any planet in the solar system. Venus's axial tilt is low, 2.64° from parallel to its orbital axis, so Venus has negligible seasonality (ESA, 2019).

Following the guidance set out by Commission 16 at the International Astronomical Union (IAU) General Assembly in 1970 (Hall, 1971), the north poles of planets were formally defined by the IAU Working Group on Cartographical Co-ordinates and Rotational Elements of the Planets and Satellites in 1979 (Davies et al., 1980) as the rotational poles "on the north side" (the same side as the Earth's north pole) of the invariable plane (the plane perpendicular to the angular momentum vector that passes through the centre of mass of the solar system). Davies et al. (1980) also formalised the definition of rotational direction relative to the north pole. Following their definition, the majority of the planets, including the Earth, have prograde rotation (anticlockwise when viewed from above their north pole). Conversely, Venus has a retrograde rotation (clockwise when viewed from above its north pole) (Davies et al., 1980; Hall, 1971).

Venus's rotation is very slow compared to other planets. Earth has a sidereal day (one axial rotation) of 23 hours and 56 minutes, a solar day (the time for the sun to return to the same point overhead) of 24 hours, and a year of 365.25 solar days (equivalent to approximately 366 sidereal days). By comparison, Venus has a sidereal day of 243.02 Earth days, a solar day of 116.75 Earth days, and a year of 224.70 Earth days (0.92 Venusian sidereal days, or 1.92 Venusian solar days) (ESA, 2019). Venus's orbit, rotation, and the resulting relationship between solar and sidereal days and the Venusian year are shown in Figure 1.4.

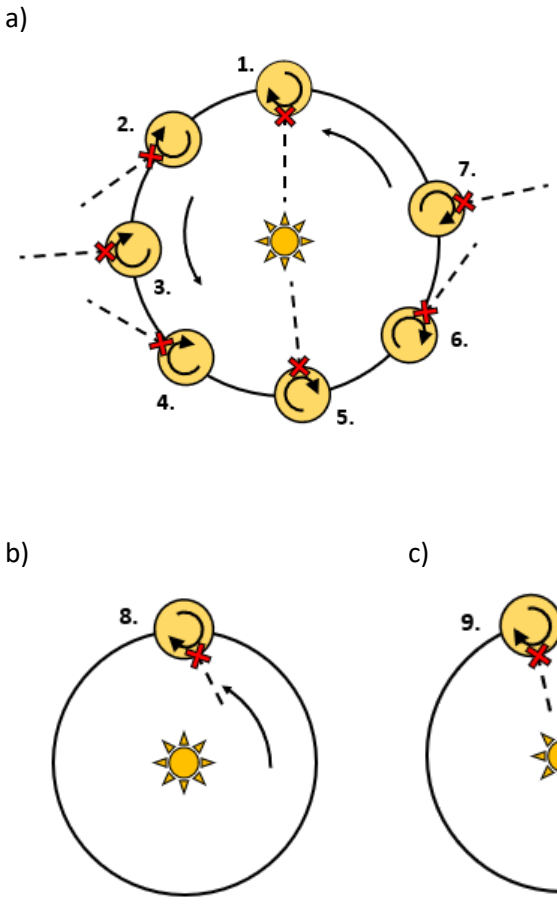

#	Earth day	Venus		
		Solar day	Sidereal day	Year
1	**0.0**	**0.00**	**0.00**	**0.00**
2	29.2	0.25	0.12	0.13
3	58.4	0.50	0.24	0.26
4	87.6	0.75	0.36	0.39
5	**116.8**	**1.00**	**0.48**	**0.52**
6	145.9	1.25	0.60	0.65
7	175.1	1.50	0.72	0.78
8	**224.7**	**1.92**	**0.92**	**1.00**
9	**233.5**	**2.00**	**0.96**	**1.04**
10	**243.0**	**2.08**	**1.00**	**1.08**

Figure 1.4. Diagram of orbital and rotational periods of Venus. The passage of time to each position (#) in Earth days and Venus solar and sidereal days and years are shown in the table in the upper right corner. Positions with integer values of solar or sidereal days and years are in bold in the table. The diagram is from above the Venusian northern pole. Venus follows an anticlockwise orbit and a clockwise rotation. The red cross and dashed line show a fixed point on the surface and normal to that surface. The combination of the orbit and rotation mean that midday at the cross occurs in positions 1 and 5 in panel a), just over half a Venusian year apart, with the planet having completed less than half a rotation (sidereal day). After one Venusian year, the planet returns to its original position relative to the sun (panel b, position 8) at the top of the diagram. Midday occurs again at position 9 (panel c) after just over a Venusian year, and the planet completes one full rotation (sidereal day) when the planet has returned to its initial orientation (dashed line vertically downwards in the diagram) in position 10 (panel d), after just over two solar days and one year.

The other large impact of the opposite direction (and slow speed) of rotation compared to Earth's is that the morning and evening terminators are swapped – the sun rises in the western sky on Venus, and the morning terminator is therefore the rightmost terminator when the illuminated disc is oriented with the north pole upwards. This difference in terminators is illustrated in Figure 1.5. For diagrams fixed in the reference frame of the planet (i.e., at fixed longitudes), the sun moves

from left to right across the figure. The opposite direction of rotation to the Earth's means that the prevailing zonal winds, which follow the planet's rotation, are westward. The telluric sign convention is generally used, where eastward winds are positive, so Venusian zonal winds are generally reported as negative. For figures fixed in the reference frame of the sun (i.e., at fixed local times), the planet's rotation and the zonal wind direction is from right to left.

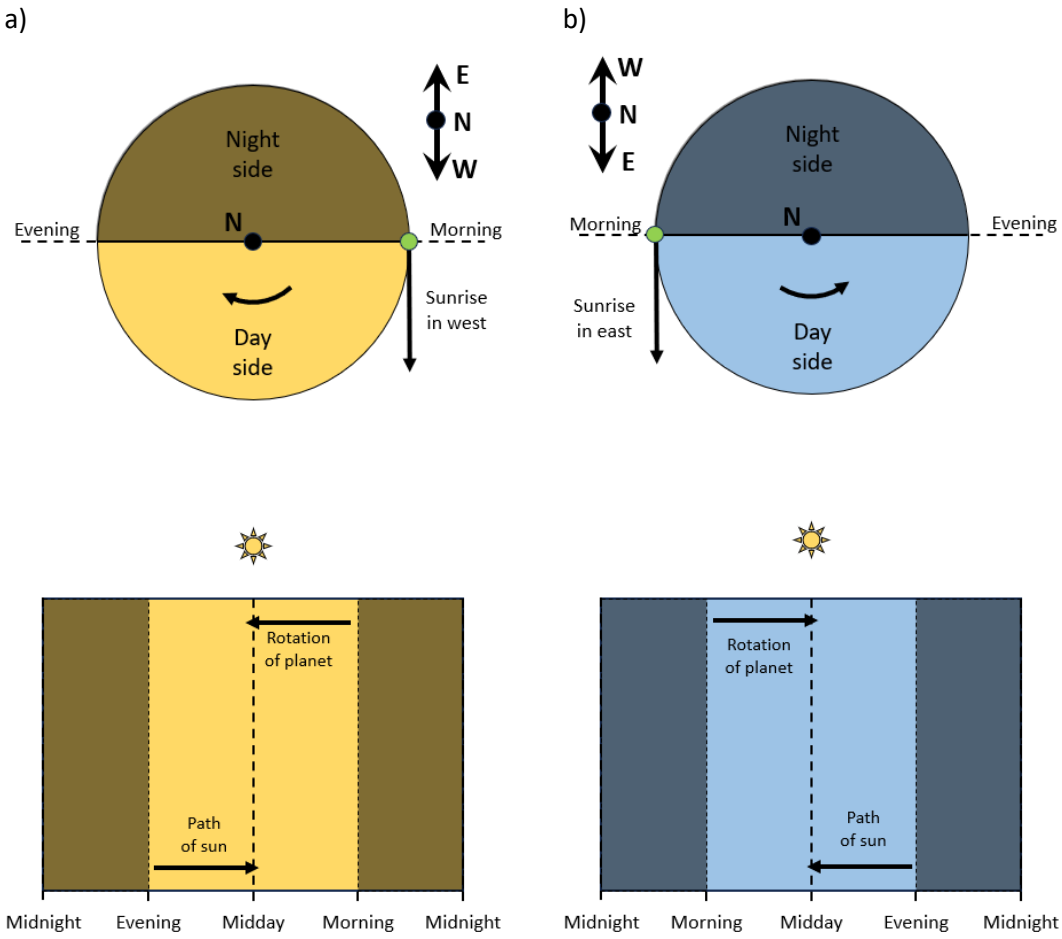

Figure 1.5. The locations of the morning and evening terminators on a) Venus and b) a simplified Earth, ignoring axial tilt, viewed from above their northern poles. The shaded regions show the nightside of the planets. The green dot indicates an observer, stood at the morning terminator (at a previous point in time, they would have been on the nightside of the planet before it rotated to its current position) as the sun rises over the a) western or b) eastern horizon. When the planets are projected to equirectangular latitude-longitude plots, or latitude-local time plots, the local time axis is reversed for Venus.

The slow rotation of the planet means that Venusian local solar time, which depends on solar zenith angle and uses a 24-hour Earth clock for ease of understanding, is not the same as the amount of time that passes at a given location between two local times. An observer with a sundial and stopwatch, stood stationary on the surface of Venus from, for example, 14:00 to 15:00 local time (as measured by the sundial), would need to stand for 4 Earth days, 20 hours, and 45 minutes (as measured by the stopwatch).

1.2.2 Atmosphere

As the best studied atmosphere is that of the Earth, the terminology used for atmospheres is generally derived from terms for the Earth's atmosphere, despite marked differences between it and the atmospheres of other planets. Figure 1.6 shows a comparison of the atmospheres of Earth and Venus (note the different ranges of temperature and altitude on the x- and y-axes).

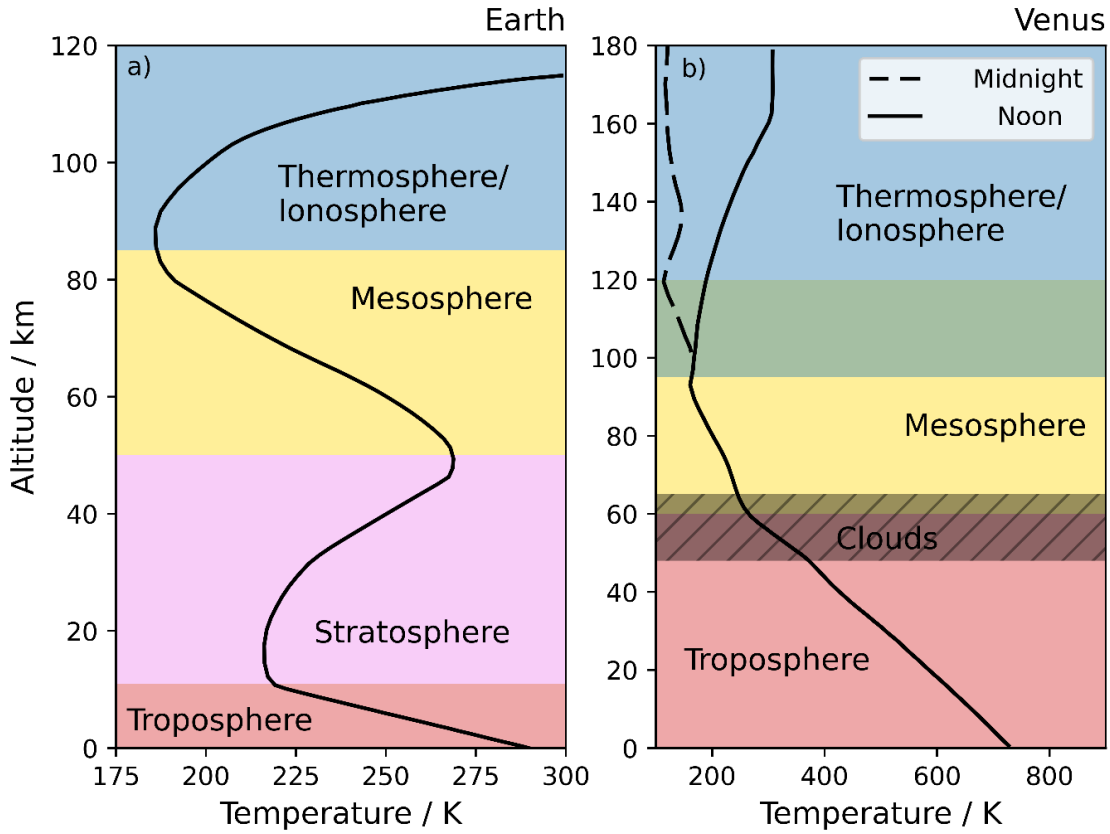

Figure 1.6. Temperature profiles and atmospheric layers of a) Earth (Pielke, 2024) and b) Venus (Yung & DeMore, 1999). The green area in panel b) shows the variation in mesopause height between the dayside and nightside of the planet.

The Earth's atmosphere is divided into levels based on the temperature profile. Nearest the surface (the troposphere), temperature decreases with height. Clouds in the Earth's atmosphere mostly occur within the troposphere, but some (such as cirrus, polar stratospheric clouds, or large thunder clouds) can reach into the lower stratosphere. The region above the Earth's troposphere is the stratosphere, a region where temperature increases with height, resulting in a stably stratified or layered region. Above the stratosphere, temperature decreases with height again in the mesosphere (or middle layer), to the thermosphere, where temperature increases with height again. Layers of high concentrations of ions exist in the thermosphere and the top of the mesosphere, so this region is considered to be part of the ionosphere. The boundaries of the layers, where temperature inversions exist, are known as the tropopause, stratopause, and mesopause.

The layers of Venus's atmosphere are named similarly. The Venusian troposphere is more extensive than Earth's, extending up to 60 km, compared to ~12 km on Earth. However, the

temperature profile of Venus does not increase with altitude until much higher in the atmosphere. The tropopause marks an inflection point in the temperature profile, not an inversion. Venus therefore has no stratosphere, though many works, particularly older or less specialist works, refer to the lower or whole mesosphere as a stratosphere (e.g., Rossow & Williams, 1979; Sohn, 2024; Yung & DeMore, 1982, 1999) in what appears to be an attempt to adapt terrestrial terminology to a planet it does not suit. The Venusian tropopause instead separates the troposphere from the mesosphere, as temperature continues to decrease to the mesopause. The slow rotation of Venus causes long days and nights and causes a strong diurnal temperature variation in the upper mesosphere and thermosphere. As can be seen in Figure 1.6b, the temperature minimum between the mesosphere and thermosphere/ionosphere occurs at approximately 95 – 100 km on the dayside of the planet, and 120 km on the nightside. This region is shown in green in Figure 1.6b to reflect the uncertainty and variable definitions of the location of the mesopause in the Venusian atmosphere.

The atmosphere on Venus is thick, with a surface pressure of 92 atm, and is composed predominantly of carbon dioxide (Taylor et al., 1997; von Zahn et al., 1983), causing a strong greenhouse effect (Tomasko et al., 1980b; Yung & DeMore, 1999) and an approximate surface temperature of 737 K (Seiff, 1983). It is cloaked in a thick layer of sulphuric acid clouds from the upper troposphere to the lower mesosphere (Blamont & Ragent, 1979; Knollenberg & Hunten, 1979a, 1979b, 1980; Ragent & Blamont, 1979, 1980; Young, 1973). The lack of diurnal temperature variation in the lower atmosphere is thought to be due to the high heat capacity of the thick atmosphere near the surface, and to rapid zonal winds which equilibrate the atmospheric temperature through the troposphere (Seiff, 1983; Seiff et al., 1979; Taylor et al., 1979).

The majority of the solar radiation incident upon Venus is absorbed in or above the upper clouds (Tomasko et al., 1980b), or below the clouds, with very little absorbed in the middle clouds (40 – 50 km) (Tomasko et al., 1980a). The zonal winds, reaching speeds of up to ~120 m s^{-1} in the upper clouds, are known as atmospheric superrotation – it takes the atmosphere only 4 – 5 days to complete a full rotation, more than 50 times faster than the surface rotation (Boyer, 1973; Counselman et al., 1979; Travis et al., 1979a). The rotation decreases the length of time the atmosphere spends being heated or cooled at a time, and redistributes the heat, flattening any diurnal temperature gradient that might form (Imamura et al., 2020).

Below the clouds, Seiff et al. (1979) found that the temperature profiles measured by four atmospheric probes during the Pioneer Venus mission (named North, Day, Night, and Large/Sounder probes, see Section 1.2.5 for details) descending in different locations at the same time (Figure 1.7), were very similar. The diurnal temperature variation below the clouds was no more than 1 – 2 K, and the maximum temperature difference between the profiles was 7 K, which occurred at 20 km. All of the probes detected warmer temperatures in the clouds (40 km to 53 km at the North probe site, 45 km to cloud top at the remainder of the sites) than would be expected

by extending the sub-cloud profile upwards. The North probe descended in a region known as the "cold collar" (Section 1.2.4), a bright band at around 60° latitude characterised by depressed cloud tops at low temperatures (Titov et al., 2018). Divergence of the temperature in the clouds from the below-cloud profiles indicated radiative heating in the clouds. The offset was found to be present, but weaker, on the nightside, suggesting contributions from both solar and surface radiation to the heating. All four probes detected a shape change in the temperature profile with altitude at 270 K (56 – 59 km), which Seiff et al. (1979) reported was indicative of a phase change in the clouds. They highlighted that 270 K is reported to be the approximate freezing point of 80% sulphuric acid (though it is more accurately the approximate melting point of sulphuric acid monohydrate), and the altitude coincides with the base of the upper cloud region.

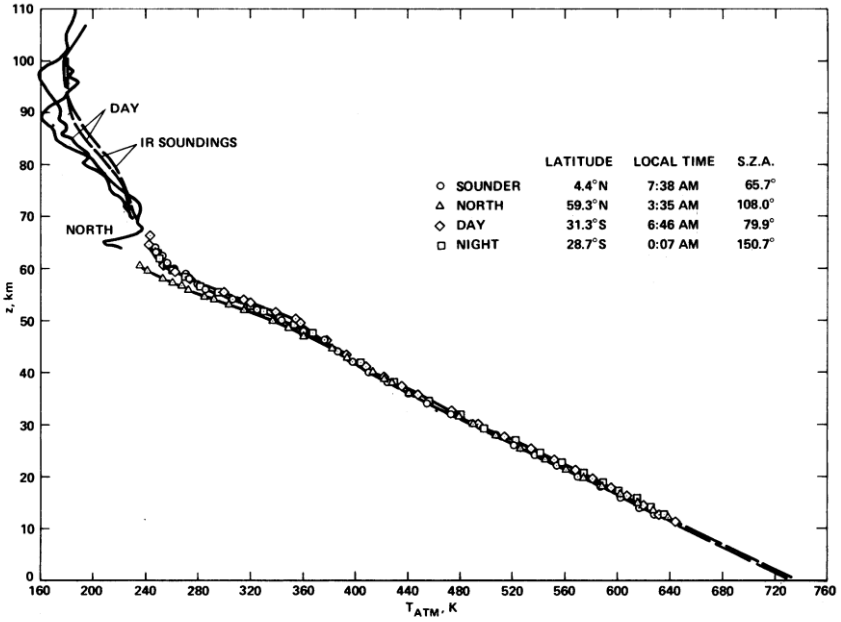

Figure 1.7. From Seiff et al. (1979). Temperature profiles measured by the four Pioneer Venus probes, along with extended profiles for the North and Day probes above 65 km (from probe deceleration measurements) and day and nightside IR sounding. A shape change at ~270 K can be seen, as can the divergence of the North probe temperature profile from the other three.

The diurnal pressure variations detected by the probes (Figure 1.8) were found to be similar to terrestrial pressure changes: the morning terminator exhibited higher pressures at the same altitude than the nightside. As for the temperature, the North probe profile of pressure against altitude differs from the other three probes in the clouds. Below 30 km, all probes measured the same pressure profile. Seiff et al. (1979) reported that the latitudinal differences and cyclostrophic balance were mostly sufficient to account for the variations between the North probe profile and the others. However, the differences between the Large and Day probe profiles (which were opposite the expectation from cyclostrophic flow) and the Day-Night probe profile differences required turbulent eddy activity.

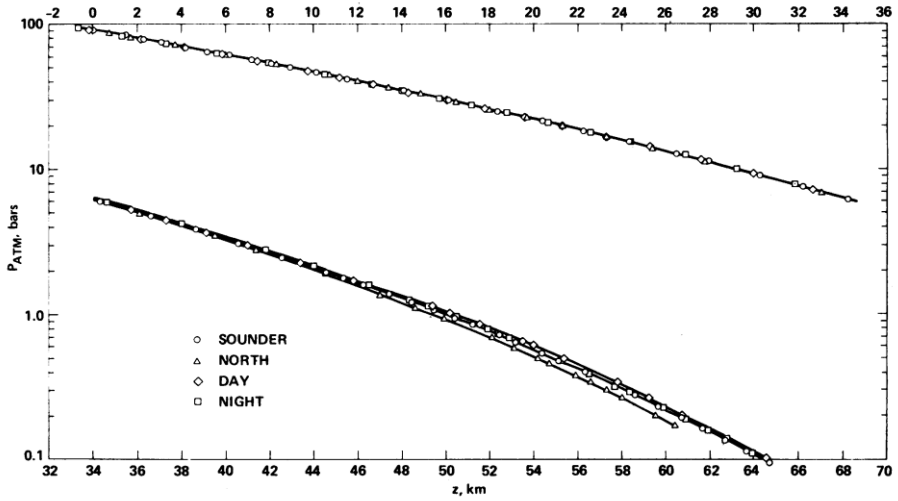

Figure 1.8. From Seiff et al. (1979). All four probes measured the same pressure profile below 30 km (top line) but diverge above that. Clear divergence of the North probe from the others is seen, but some variation between the Large (Sounder), Day, and Night probes is also present.

1.2.3 Clouds

1.2.3.1 Wavelength dependence of cloud tops

The majority of observations of the Venusian clouds are from above the atmosphere, whether by orbiters, flybys, or Earth-based measurements. A key location in a cloud is where the optical depth is equal to 1, often referred to as the cloud top (Crisp, 1986; Ignatiev et al., 2009; Young, 1973). The cloud optical depth at a given wavelength, $\tau(\lambda)$, is defined as the line integral of the attenuation coefficient, $\kappa(\lambda)$, through the cloud. Attenuation here is taken to be the sum of absorption and scattering, though either may also be used in isolation (Gary, 2003).

$$\tau(\lambda) = \int_0^L \kappa(\lambda)\, dl \tag{1.1}$$

If the optical thickness is small, the attenuation of light by the cloud is small, and light passes through the cloud ($\tau << 1$, "optically thin") and lower altitudes are visible through the cloud. An "optically thick" ($\tau >> 1$) cloud attenuates light strongly and is opaque, either bright if it is reflecting the light or dark if it is absorbing it. When observations of Venus are made from the top of the atmosphere (TOA) or beyond, the observed altitude is that where the clouds become optically thick. Absorption and scattering are both wavelength dependent, and therefore so is the optical thickness of the clouds. Viewing the atmosphere at different wavelengths therefore allows observations down to different altitudes.

The dayside ultraviolet, visible, and near-infrared (near-IR) cloud tops are at 70 – 75 km at low latitudes (Figure 1.9), becoming depressed in the polar regions (Ignatiev et al., 2009). This aligns well with the top of the upper clouds at 65 – 70 km and the upper haze which extends above that to ~90 km (Ragent et al., 1985). The UV opacity is due to the combination of reflected and absorbed light that makes up the unexplained contrasts seen in Figures 1.1 and 1.2. On the dayside, IR light is scattered back to space by the clouds or absorbed by carbon dioxide, which

makes up around 96.5% of the atmosphere, or by water vapour which is present in trace amounts (Ignatiev et al., 2009; von Zahn et al., 1983).

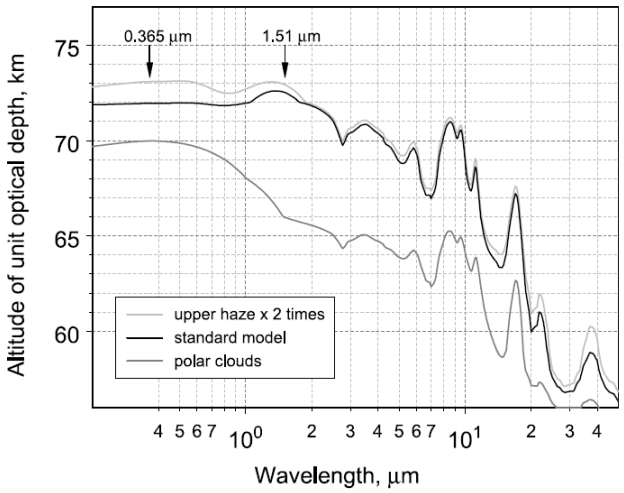

Figure 1.9. From Ignatiev et al. (2009). Predicted dependence of dayside cloud top height ($\tau = 1$) on wavelength. Peak of near-UV absorption and near-IR wavelengths are indicated for clarity.

On the nightside, the removal of the bright reflected sunlight results in narrow regions of the spectrum between absorption bands where near-IR radiation from near the surface and lower atmosphere can reach the TOA and be detected. These "transparency windows", which allow the atmosphere below the clouds (15 – 40 km) to be probed, were first detected in Earth-based observations (Allen & Crawford, 1984; Taylor et al., 1997). Further windows to the surface and lower clouds (0 – 50 km) were predicted by atmospheric models and observed by the Galileo spacecraft flyby (Taylor et al., 1997).

1.2.3.2 Regions of the clouds

Much of the terminology surrounding the clouds was developed in the 1980s following the Pioneer Venus and Venera missions (Kawabata et al., 1980; Knollenberg & Hunten, 1980) and follows the observations (and limitations thereof) from those missions. The clouds are generally split into three layers – upper, middle, and lower clouds – with some "pre-cloud layers" sometimes observed below the main cloud deck (Knollenberg & Hunten, 1980). Above and below the clouds are the upper and lower hazes.

The distinction between "cloud" and "haze" was originally one of particle size – the Pioneer Venus descent probes identified the larger particle sizes in the cloud layers and defined the regions based on particle number density down to the limit of detection of the instruments (~600 nm) (Knollenberg & Hunten, 1980). Kawabata et al. (1980) found that an additional layer of smaller particles – "haze" particles – was required above the clouds to explain observations from orbit. This distinction of larger particles being cloud particles, with smaller haze particles above has

shifted over time (Titov et al., 2018), and the upper haze is now taken to be the optically thin region above the main cloud deck, regardless of particle size (e.g., Luginin et al., 2016).

1.2.3.3 Cloud modes

Aerosols (including cloud particles) exist in distinct size populations, called "modes". The size distribution of the particles follows various standard distributions, such as a Gaussian distribution (Knollenberg & Hunten, 1979a):

$$n(r) = \frac{N_T}{\sqrt{2\pi}\sigma} exp\left(-\frac{(r - r_m)^2}{2\sigma^2}\right) \tag{1.2}$$

where N_T is the number density of particles, r_m is the mean radius, and σ the standard deviation of the distribution; a log-normal distribution (Knollenberg & Hunten, 1980):

$$n(r) = \frac{N_T}{r\sqrt{2\pi}\, ln\, \sigma_g} exp\left(-\frac{\left(\ln\left(\frac{r}{r_g}\right)\right)^2}{2\left(\ln \sigma_g\right)^2}\right) \tag{1.3}$$

where N_T is the number density of particles, r_g is the geometric mean radius, and σ_g the geometric standard deviation; or a modified gamma function, which can be applied to non-spherical particles (Kawabata et al., 1980; Petty & Huang, 2011):

$$n(r) = A\, r^{\frac{(1-3\nu_{eff})}{\nu_{eff}}} \exp\left(\frac{-r}{r_{eff}\nu_{eff}}\right) \tag{1.4}$$

where A is known as the intercept parameter, r_{eff} the effective radius, and ν_{eff} the effective variance.

Different sources use different shape distributions, though data could be well fitted by other distributions, e.g., log-normal and modified gamma distributions can have very similar shapes, though the parameters of the two distributions would be very different. Care must be taken when comparing reported distributions to consider the full shape of the reported distribution, not just the radius parameter.

1.2.4 The cold collar

Venus exhibits Hadley circulation at low- to mid-latitudes, with ascending branches at the equator and poleward flow at the cloud tops to around ±60° latitude, where downwelling and equatorward transport below the clouds form the return arm of the cell (Garate-Lopez & Lebonnois, 2018; Titov et al., 2018). The downwelling occurs in a region known as the "cold collar", a circumpolar ring found in each hemisphere from ~60 – 80°, characterised by depressed cloud tops and low temperatures compared to similar altitudes at lower latitudes (Figure 1.10) (Haus et al., 2014; Tellmann et al., 2009; Titov et al., 2018). The equatorward edge of the cold collar coincides with the zonal jets of the atmospheric super-rotation (Tellmann et al., 2009).

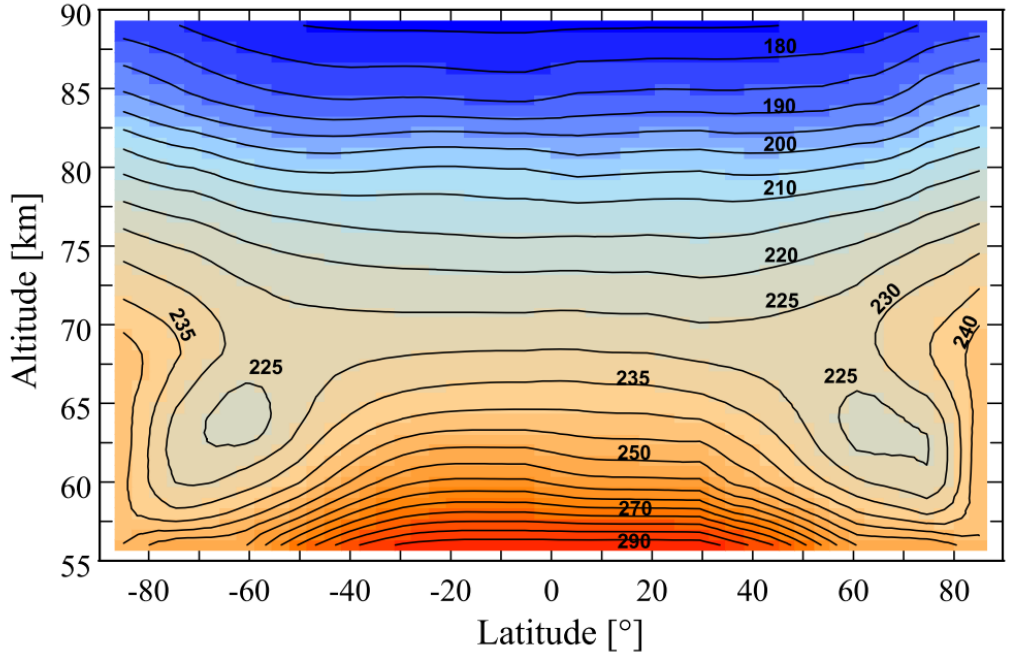

Figure 1.10. From Haus et al. (2014). Zonal average temperature field from Venus Express (VIRTIS-M) observations. The cold collar is apparent as the two low temperature areas in the high latitude regions.

Titov et al. (2018) proposed that the cold collar is radiative in origin, and reinforced by a feedback loop, wherein the sharp cloud top allows efficient radiative cooling of the cloud, reinforcing a stably stratified region above the cloud and preventing mixing of the warmer air above into the cloud, which maintains the cloud top. As the air descends following Hadley circulation, it is heated adiabatically, producing the higher temperatures below the cold collar. This is supported by the findings of Garate-Lopez and Lebonnois (2018), who were able to model a feature similar to the cold collar in the Venus Planetary Climate Model (PCM) with updated radiative transfer treatment and latitudinal cloud variations.

1.2.5 Mission overview

In addition to Earth-based observations, several successful missions to Venus, in the form of orbiters, atmospheric probes and descenders, and flybys, have contributed to the knowledge of the planet. A brief summary of each (successful) mission is provided in Table 1.1. The majority of the current understanding of the clouds comes from Pioneer Venus, Venera, and Vega probes and balloons, which provided the only *in situ* cloud measurements. Additional study of the upper clouds and haze had been performed by the Pioneer Venus, Venus Express, and Akatsuki orbiters. An overview of the *in situ* measurements is provided here.

Table 1.1. A summary of successful space missions to Venus.

#	Name	Mission type	Launch	Observations	Overview of relevant results	References
1	Mariner 2	Flyby	27 August 1962	14 December 1962	Evidence from the microwave radiometer that Venus has a hot surface (~400 K) with little diurnal difference. Thick, unbroken clouds at ~240 K were detected along with some CO_2 in the atmosphere. No magnetic field was detected, suggesting that Venus spun slowly or had a non-convective core.	JPL (1965); Sonett (1963)
2	Venera 4	Atmospheric probe (with landing capability) and carrier spacecraft	12 June 1967	18 August 1967	The probe was intended to deploy at 26 km altitude and descend to the surface. However, the high pressures and thick atmosphere meant it deployed early (~57 km), descended slowly, and was destroyed at 22 – 27 km altitude, ~22 atm pressure, and 270 – 280 °C. It detected a predominantly CO_2 atmosphere with N_2, atomic oxygen, and water vapour also present. No magnetic field was detected, and the possibility of a watery surface ruled out. Some strong winds and turbulence were detected at 40 – 50 km.	Harvey (2007c); Kerzhanovich et al. (1972); Vakhnin (1968)

3	Mariner 5	Flyby	14 June 1967	19 October 1967	Mariner 5 estimated temperatures of ~ 230 K at the cloud top, which it placed at around 60 – 70 km in a primarily CO_2 atmosphere. A planetary radius of 6056 ± 1 km was computed and used for altitude calculations. Agreement between the detected temperatures by Mariner 5 and Venera 4 (whereas they were at the time believed to have probed different regions of the atmosphere) prompted the realisation that Venera 4 had deployed higher than intended. Comparison between the results led to predicted surface conditions of 600 – 800 K and 30 – 105 atm.	Harvey (2007c); Jastrow (1968); Sagan (1969); Snyder (1967)
4	Venera 5 & 6	Atmospheric probes (with landing capability) and carrier spacecrafts	5 January 1969	17 May 1969	Venera 5 descended to ~16 km altitude, recording temperature and pressure of 327 °C and 27.5 atm at 18 km. Venera 6 descended to ~10 km altitude, and recorded temperature and pressure of 294 °C and 19.8 atm at 22 km. The two probes detected 93 – 97% CO_2 and small amounts of inert gases, nitrogen, oxygen, and water vapour. Average surface conditions of 96.2 atm and 769 K were predicted.	Avduevsky et al. (1970); Harvey (2007c)
			10 January 1969	18 May 1969		
5	Venera 7	Lander and carrier spacecraft	17 August 1970	15 December 1970	During descent, the full parachute deployed significantly before it was planned to, and then melted and detached, leaving the probe to fall to the surface. It measured temperature from 55 km to the surface and continued transmitting for 20 minutes on the surface. Surface temperature of 730 – 747 K were measured. Surface pressure was inferred to be 92 atm.	Avduevsky et al. (1971); Harvey (2007a)

6	Venera 8	Lander and carrier spacecraft	27 March 1972	22 July 1972	Venera 8 descended successfully on the dayside, while all previous descents had been on the nightside. It detected similar temperatures and pressures (741 ± 7 K and 90 ± 1.5 atm) to the nightside. Granite-like surface rock was detected. Photometers suggested that Venera 8 descended through cloud (thick from 65 – 50 km, thinner at 48 – 35 km) consistent with sulphuric acid. Surface light levels were low, with parallels drawn to an overcast Earth day. Strong winds, consistent with those inferred by UV photography, were detected in the upper clouds, decreasing to 1 m s^{-1} just above the surface.	Harvey (2007a); Marov et al. (1973)
7	Mariner 10	Flyby (gravity assist)	3 November 1973	5 – 13 February 1974	A series of UV photographs were taken, revealing details of the cloud-top contrasts. Radio sounding detected a thin and patchy upper cloud deck (up to 60 km) and a thicker lower cloud deck (35 – 52 km). The rapid motion of the upper clouds was apparent in the UV photographs. At the sub-solar point, polygonal structures associated with rising air were seen. Apparent layers in limb photographs and high concentrations of atomic oxygen compared to Mars suggested little mixing between the upper and lower atmosphere. A weak planetary magnetic field was detected.	Dunne and Burgess (1978)

8	Venera 9	Orbiters and landers	8 June 1975	20 October 1975 – ~22 March 1976* (orbiter) 22 October (lander)	The landers descended in brighter sunlight than Venera 8 had measured and were able to photograph the surface without additional lighting. Surface composition indicated basalt-like rocks. Surface conditions were 480 °C and 90 atm (Venera 9) and 465 °C and 92 atm (Venera 10). Backscattering nephelometers operated from 62 – 14 km and small angle nephelometers from 62 – 32/44 km (9/10). Strong scatter was detected from the main cloud at 62 – 49 km, with weaker scattering below. Venera 9 detected strong backscatter down to 20 km, but Venera 10 did not. Three cloud layers were apparent, with cloud properties varying with height. The orbiters measured cloud properties and found a cloud base at 30 – 35 km, with clouds extending up to 64 km. Venera 9 took UV photographs of the clouds. No such photographs from Venera 10 were released.	Harvey (2007b); Marov et al. (1980); Siddiqi (2018)
	Venera 10		14 June 1975	23 October 1975 – June 1976** (orbiter) 25 October 1975 (lander)		

9	Pioneer Venus 1 (orbiter)	Orbiter and atmospheric probes	20 May 1978	4 December 1978 – 8 October 1992 (orbiter)	The orbiter inferred atmospheric clearing over the north pole from IR measurements, took UV photos of cloud patterns to study the long- and short-term recurrence of the Y feature, reportedly observed lightning, and radar-mapped the surface in the northern hemisphere. In 1991, after a period of inactivity, it was reactivated to map the southern hemisphere and conduct radio occultations to measure temperature profiles in the clouds. The transport bus and four atmospheric probes detected a stable atmosphere except at 52 – 56 km and below 29 km. Diurnal temperature variation (15 – 20 K) was detected above 80 km. Zonal winds of ~130 m s^{-1} were reported at the cloud top, with speed decreasing below. The middle cloud was similar at all probe sites, while the upper, lower, and sub-cloud layers varied.	Donahue (1979); Jenkins (1995); Siddiqi (2018)
	Pioneer Venus 2 (four atmospheric probes and a transport bus)		8 August 1978	9 December 1978 (probes and transport bus)		
10	Venera 11	Flyby and landers	9 September 1978	25 December 1978	Atmospheric sulphur, iron, and chlorine were detected by x-ray fluorescence, and a 97% CO_2 atmosphere with most of the remainder being nitrogen was confirmed. The cloud base was identified at 48 – 49 km, and the lowest cloud level, 48 – 51 km, had distinct optical properties from the clouds above. Both Venera 11 and 12 landers carried microphones to listen for wind, thunder, and lightning. All three were reported, with Venera 11 reportedly recording up to 25 lightning strikes per second from a distant storm at one point during its descent.	Harvey (2007b); Siddiqi (2018)
	Venera 12		14 September 1978	21 December 1978		

11	Venera 13	Flyby and landers	30 October 1981	1 March 1982	The landers determined that the rocks were primarily basalt, basaltic rocks, and alkaline potassic salts. Primary chemical elements in the rocks were silicon, aluminium, iron, magnesium, calcium, potassium, and titanium. The UV intensity was measured during descent and three cloud layers were identified: dense above 57 km, thinner at 50 – 57 km, dense at 48 – 50 km. The majority of the UV flux was absorbed above 58 km. Temperatures of -100 °C at 90 km, increasing to -51 °C at 75 km were recorded. Water vapour concentrations were found to be generally small and variable, but were most concentrated in the clouds (40 – 60 km).	Harvey (2007b); Moroz et al. (1982)
	Venera 14		4 November 1981	5 March 1982		
12	Venera 15	Orbiters	2 June 1983	10 October 1983 – 5 January 1985	The primary mission of Venera 15 and 16 was radar mapping the surface in the northern regions, though atmospheric studies were also carried out. The emission spectrum of the planet was found to vary with latitude (e.g., the equatorial regions, poles, and polar collar exhibited different spectra). The clouds in the polar regions were found to be 5 – 8 km lower than in equatorial regions. The average surface temperature measured was 500 °C, though localised hotspots of 700 °C hotter than their surroundings, theorised to be volcanoes, were found.	Harvey (2007b); Moroz et al. (1986); Siddiqi (2018)
	Venera 16		7 June 1983	14 October 1983 – 13 June 198		

13	Vega 1	Flyby (gravity assist), landers, and atmospheric balloons	15 December 1984	11 June 1985 (lander) 11 June – 13 June 1985 (balloon)	A malfunction with the Vega 1 lander caused it to deploy surface experiments at ~18 km. During descent, the two landers detected sulphur, chlorine, iron, and phosphorus, and measured cloud particle sizes. Vega 2 found the phosphorus was predominantly in the lower clouds. The two balloons were released from the landers during descent and floated with the wind at around 54 km (535 mbar, 305 K) for ~two days. They found strong turbulence of up to 60 – 70 m s^{-1}, large vortices, and vertical winds of 1 – 3 m s^{-1}. No lightning was detected. The balloons travelled at around 15 m s^{-1} while the clouds were blown by zonal winds of 60 – 70 m s^{-1}.	Harvey (2007b); Sagdeev et al. (1986a); Siddiqi (2018)
	Vega 2		21 December 1984	15 June 1985 (lander) 15 June – 17 June 1985 (balloon)		
14	Magellan	Orbiter	4 May 1989	10 August 1990 – 13 October 1994	Magellan completed the surface radar mapping started by Venera 15 and 16. It found evidence of a volcanic surface with turbulent surface winds and estimated ~85% of Venus's surface is volcanic flows. It also conducted radio occultations of the atmosphere to produce temperature and pressure profiles.	Harvey (2007b); Jenkins (1995); Siddiqi (2018)
15	Galileo	Flyby (gravity assist)	18 October 1989	10 February 1990 – 17 February 1990+***	Galileo carried out violet and IR imaging during its flyby and gravity assist at Venus and mapped the lower atmosphere using near-IR transparency windows on the nightside. Galileo also searched for lightning during the flyby.	Belton et al. (1991); Johnson et al. (1991); Siddiqi (2018)

16	Cassini	Flyby (gravity assist)	15 October 1997	26 April 1988 24 June 1999	Cassini carried out two gravity assists at Venus and detected no lightning during either.	Gurnett et al. (2001); Siddiqi (2018)
17	MESSENGER	Flyby (gravity assist)	3 August 2004	5 June 2007	During its second gravity assist at Venus, MESSENGER took visible and IR images and spectra.	Pérez-Hoyos et al. (2018); Siddiqi (2018)
18	Venus Express	Orbiter	9 November 2005	11 April 2006 – 28 November 2014	Venus Express carried various spectrometers, radio occultation equipment, and a dedicated camera for studying the atmosphere. It mapped the temperature of the southern hemisphere and studied the southern polar vortex, which was found to be irregular and changeable. The same was assumed to be true of the northern polar vortex, though it could not be studied due to Venus Express's orbit. The long-term behaviour of the clouds was studied and the superrotation found to be variable and seemingly accelerating over the course of the mission.	ESA (2014a, 2014b); Siddiqi (2018)
19	Akatsuki	Orbiter	20 May 2010	7 December 2015 – April 2024	Akatsuki had numerous cameras at different wavelengths to study the atmospheric dynamics of Venus, along with radio occultation studies and a search for lightning. Evidence of atmospheric gravity waves was detected by IR imaging.	Fukuhara et al. (2017); Jones (2024); Nakamura et al. (2018); Siddiqi (2018)

20	Parker Solar Probe	Flyby (gravity assist)	12 August 2018	3 October 2018 26 December 2019 11 July 2020 20 February 2021 November 6, 2024	During its first two assists, the Parker Solar probe measured the magnetosphere. On its third gravity assist at Venus, it measured the depth of Venus' nightside ionosphere. The nightside surface of the planet was later imaged at 470 – 800 nm and oxygen airglow observed. It measured non-lightning generated Whistler waves, suggesting lighting may be less common than previously assumed. Additional surface imaging occurred during in November 2024.	Collinson et al. (2021); George et al. (2023); Johnson-Groh (2022); NASA (2018); Volwerk et al. (2021); Wood et al. (2022)
21	BepiColombo	Flyby (gravity assist)	20 October 2018	15/16 October 2020 11 August 2021	O^+ and C^+ ions were detected in Venus's induced magnetosphere and temperature measurements of the lower mesosphere were similar to those measured by earlier missions. NUV spectra of the clouds were recorded.	ESA (2018, 2020a); Hadid et al. (2024); Helbert et al. (2023); Lee et al. (2022)
22	Solar Orbiter	Flyby (gravity assist)	10 February 2020	27 December 2020	Eight Venus gravity assists will occur before orbital insertion. The magnetosphere was studied during its first flyby.	ESA (2020b, 2022); NASA Goddard Space Flight Centre (2020); Volwerk et al. (2021)

* End date unknown. On 22 March 1976, the mission was announced to have been "fulfilled" (Siddiqi, 2018).

** End date unknown. Siddiqi (2018) reports that it "continued transmitting data until at least June 1976" but this data does not appear to have been released.

*** Imaging continued until 17th February 1990. Other experiments were carried out later, but the end date is not apparent (Belton et al., 1991; Johnson et al., 1991).

The Venera 9 and 10 descenders carried nephelometers – instruments for measuring the concentration of aerosols by detection of the scattered light from a population – and were able to identify cloud layers by the increase in scattered light. However, to interpret particle properties from scattering alone requires assumptions about the distribution of particle sizes (Marov et al., 1980). The first direct measurements of particle size were taken by the Cloud Particle Size spectrometer on the Pioneer Venus Large probe (LCPS). The direct size measurements could then be combined with nephelometer data to predict the particle composition and shape (Knollenberg & Hunten, 1980; Ragent & Blamont, 1980).

The four Pioneer Venus descent probes were deployed to different locations simultaneously, sampling a range of latitudes and local times (Ragent & Blamont, 1980). The Large probe, also called the Sounder probe (Colin, 1979), descended in the equatorial region, dayside of the morning terminator (07:58 local time). The three small probes were named based on their locations: the Day probe, like the Large probe, descended on the dayside of the planet (06:46), though further south than the large probe. The Night probe also descended in the low- to mid-southern latitudes, but on the nightside (00:07), and the North probe descended on the nightside (03:35) at ~60°N, within the cold circumpolar clouds (cold collar).

Each of the probes carried a nephelometer that measured the intensity of backscattered (175°) light at 900 nm when incident upon aerosols in the atmosphere (Ragent & Blamont, 1979, 1980). The Large probe carried several more instruments than each of the small probes (Williams, 2018), including the LCPS, which was capable of measuring the sizes of individual particles from 0.6 – 490 μm diameter. The LCPS used an Optical Array Spectrometer to size the particles by counting the number of photodiode elements occluded by the particle's shadow. Telemetry bandwidth constraints limited the sizing to 1D and as such no shape information about the particles was returned. The combined nephelometer and particle size data produced a globally applicable first-order cloud model of particle size and inferred composition that provides the standard model that is still in use (Knollenberg & Hunten, 1980). The findings of the Pioneer mission that developed the standard model are summarised in Section 1.3.

The Vega (also styled VeGa and VEGA in different sources) landers were the first (and by virtue of being the last Venus descent craft, the only other) missions since Pioneer Venus to carry size spectrometers. Each had two size spectrometers: LSA and ISAV, and the latter also contained a nephelometer and photometer. The Vega descenders detected broadly similar clouds to Pioneer Venus, though the exact altitudes of features varied. The range of clouds sampled was more limited than for Pioneer Venus as the detections were contaminated with smoke from the explosion to jettison the heat shield above 57 km and the instruments stopped taking readings at 33 km (Krasnopolsky, 1989; Titov et al., 2018).

The Vega balloons also carried nephelometers, though the instrument on the Vega 2 balloon did not return data. Vega 1 therefore provided the only measuremeants of the horizontal variation of cloud scattering properties. Measuring at ~54 km altitude, it detected no particle free regions, though many small regions of fluctuations in the detected scattering were apparent, suggesting the clouds were not uniform. Correlation between measured vertical winds and changes in temperature and pressure suggested the balloon was carried up and down in the atmosphere. When this happened, scattering typically increased on descent, suggesting cloud density increased deeper into the clouds (Sagdeev et al., 1986b).

1.3 Clouds

1.3.1 Venus standard cloud model

While the upper layers of the atmosphere and clouds can be readily probed by remote measurements, either by spacecraft or from Earth, the lower clouds can primarily only be observed using *in situ* measurements. As such, the standard model of the Venus clouds described by Esposito et al. (1983) is primarily based on the findings of the Venera and Pioneer Venus atmospheric descents and has remained mostly unchanged since. This model is summarised in Table 1.2 and Figure 1.11, both from Satoh et al. (2015), and is unchanged from that published by Esposito et al. (1983), who adopted the values reported by Knollenberg and Hunten (1980). Prior to the *in situ* cloud measurements, the expectation from Earth-based observation of the clouds was a single narrow mode of concentrated sulphuric acid droplets with a Gaussian distribution of modal radius 1.05 μm and $\sigma = 0.26$ μm (Knollenberg & Hunten, 1980). The Pioneer Venus mission instead detected complex, multimodal and highly organised cloud layers (Knollenberg & Hunten, 1979a, 1980). Their findings, along with some proposed changes to the standard cloud model in the intervening years, are summarised here.

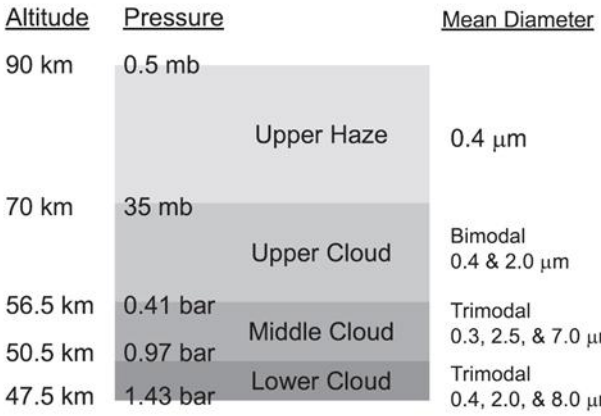

Figure 1.11. From Esposito et al. (1983); Satoh et al. (2015). The standard cloud model of Venus with altitudes, pressures, and mean particle sizes for the different modes indicated.

Table 1.2. From Esposito et al. (1983); Satoh et al. (2015). Venus standard cloud model. Values appear to be taken directly from Knollenberg and Hunten (1980).

Region	Altitude range / km	Optical depth (at 0.63 μm)		Mean diameter / μm	Average number density / cm^{-3}
Upper haze	70 – 90	0.2 – 1.0		0.4	500
Upper cloud	56.5 – 70	6.0 – 8.0	Mode 1: Mode 2:	0.4 2.0	1500 50
Middle cloud	50.5 – 56.5	8.0 – 10.0	Mode 1: Mode 2: Mode 3:	0.3 2.5 7.0	300 50 10
Lower cloud	47.5 – 50.5	6.0 – 12.0	Mode 1: Mode 2: Mode 3	0.4 2.0 8.0	1200 50 50

1.3.2 Cloud regions

1.3.2.1 Upper haze

The upper haze is an optically thin region above the main cloud deck, from approximately 70 – 90 km. It was not measured by the Pioneer Venus probes, which deployed around 61 – 65 km (Counselman et al., 1980), but was studied by remote sensing by the Venus Orbiter Cloud Photo-Polarimeter (OCPP) on the Pioneer Venus Orbiter (Kawabata et al., 1980). The OCPP found the cloud tops were consistent with concentrated sulphuric acid droplets with an effective radius of 1.05 μm (now termed "mode 2" particles), but the polarisation measured at the poles and morning terminator required smaller particles – a submicron haze overlying the planet (Taylor et al., 1979; Travis et al., 1979b). The haze optical thickness varied on the order of months by a factor of three, and the highest thickness was found to correlate with "exceptionally bright" polar clouds (Kawabata et al., 1980; Rossow et al., 1980; Travis et al., 1979b).

Kawabata et al. (1980) modelled the haze in layers, with a haze layer overlying a mixture of "haze" and "cloud" particles and reported that multiple scattering modelling provided the best agreement for a haze optical depth above the sulphuric acid (r_{eff} = 1.05 μm) clouds of between 0.2 and 0.5 at 935 nm (optical depth increases at shorter wavelengths), effective radius r_{eff} = 0.23 ± 0.04 μm, effective variance v_{eff} = 0.18 ± 0.1 (Kawabata et al. (1980) describe all particle distributions with modified gamma distributions), and real refractive index n = 1.45 ± 0.04 at 365 – 500 nm. The top of the haze layer was reported to be at ~4 mbar in the polar regions and lower (but not fully constrained) at low latitudes. The same trend was found for the cloud top.

More recent studies of the haze by the Venus Express and Akatsuki orbiters have found indications of larger particles present in the haze: Satoh et al. (2015) found mode 2 particles were required in

the haze layer to reproduce the phase function measured by the IR1 spectrometer on Akatsuki, and Luginin et al. (2016) reported a bimodal haze with effective radii of 0.12 ± 0.03 µm and 0.84 ± 0.16 µm and effective variances assumed to be 0.15, the equivalent of log-normal distributions with r_g = 0.08 ± 0.02 µm and 0.59 ± 0.11 µm and σ_g = 1.45. They found that the size distribution of the particles varied over time, sometimes appearing unimodal, though they put this down the detection limits of the SPICAV/SOIR (Spectroscopy for Investigation of Characteristics of the Atmosphere of Venus in its Solar Occultation in the InfraRed mode) instrument. The mode 1 particle size was found to be invariant with height, but mode 2 decreased in size with increasing altitude.

The size distributions reported for the upper haze populations are compared in Figure 1.12 with mode 1 in the upper clouds as reported by Knollenberg and Hunten (1980). Luginin et al. (2016) report a very narrow population with a smaller modal radius than Knollenberg and Hunten (1980) and Kawabata et al. (1980), who report similar modal radii but the haze distribution is narrower than mode 1 in the clouds. All populations are scaled to a maximum *n(r)* value of 20 cm^{-3} μm^{-1} for straightforward comparison of their shapes. The majority of the distributions reported by Kawabata et al. (1980) and Knollenberg and Hunten (1980), and all of the distribution reported by Luginin et al. (2016), are below the size limit of detection of the LCPS.

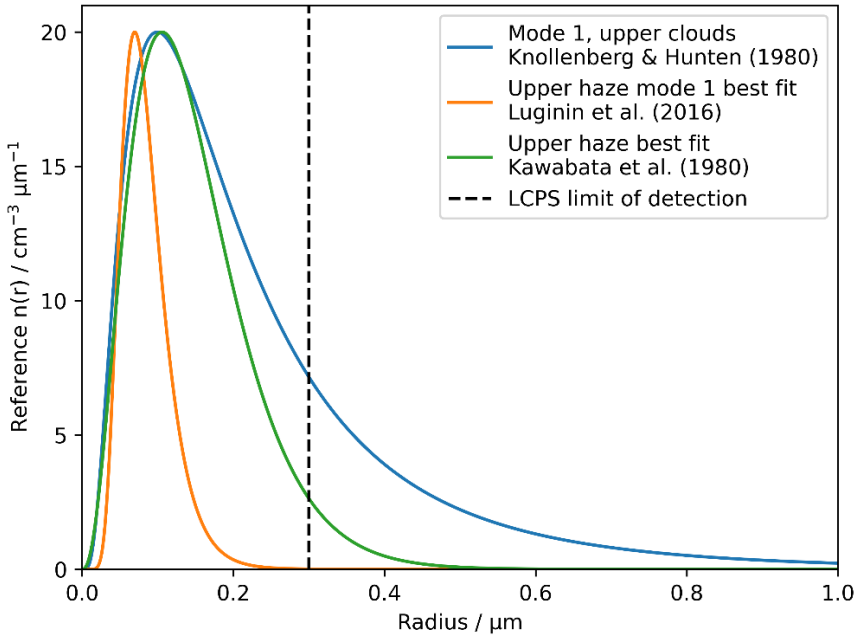

Figure 1.12. Best fit reported sizes of the smallest mode in the upper clouds (Knollenberg & Hunten, 1980), the smallest mode in the upper haze reported by Luginin et al. (2016) and the upper haze distribution reported by Kawabata et al. (1980). All populations are scaled to a maximum *n(r)* value of 20 cm^{-3} μm^{-1} for straightforward comparison of their shapes.

1.3.2.2 Upper clouds

The region referred to as the "upper cloud" by Knollenberg and Hunten (1979a, 1979b, 1980), and region D by Ragent and Blamont (1979, 1980) and Blamont and Ragent (1979), was detected

by both the Pioneer Venus probe backscattering nephelometers and the LCPS. The three small probes did not carry particle size spectrometers.

The Pioneer Venus Day, Large, and Night probes detected increased backscatter corresponding to an inhomogeneous cloud top at 63 km, 64 km, and 61.7 km, respectively, while the North probe deployed below the cloud top (Ragent & Blamont, 1979). As the upper cloud layer was detected by all four probes, it was assumed to be a global feature with a cloud top at 62 – 64 km and the LCPS data was taken to be generally representative of the clouds (Ragent & Blamont, 1980).

The LCPS detected a number density of 300 – 400 cm^{-3} of 0.6 – 4 μm diameter particles with low mass loading and a modal diameter of 1.2 μm (Knollenberg & Hunten, 1979b), assuming a unimodal distribution. However, as some layers in the upper clouds and all levels below were at least bimodal, the unimodal distribution was assumed to be due to the instrument failing to distinguish the modes. Knollenberg and Hunten (1979a, 1980) extended the profile of the ~2 μm particles detected in the middle cloud (see Section 1.3.2.3) upwards and identified two modes of particles in the upper clouds: mode 1, small sub-micron particles, and mode 2, just over 2 μm in modal diameter.

For both modes of particles, the number concentration, mass loading, and extinction coefficient were at a maximum at 60 km and decreased above and below that altitude. They reached a minimum at 56.5 km, in a region around 1 km thick detected by both the LCPS and nephelometers and interpreted as the transition between the upper cloud and the middle cloud below it (Blamont & Ragent, 1979; Knollenberg & Hunten, 1979a, 1979b, 1980; Ragent & Blamont, 1979, 1980).

The upper haze particles predicted by Kawabata et al. (1980) to be mixed into the upper cloud are too small for nephelometer detection (unless the number concentrations were very high), and most of the distribution would be below the 0.6 μm limit of LCPS detection (Figure 1.12). Ragent and Blamont (1980) found that while a real refractive index of 1.44 for solely the LCPS-detected particle distribution (assuming homogeneous, non-absorbing droplets) gave a good fit to the observations in the lower part of the upper cloud, the inclusion of Kawabata et al.'s predicted haze in the upper cloud meant that n = 1.44 matched the observations well across the entire upper cloud region. A real refractive index of 1.44 is consistent with concentrated sulphuric acid droplets. Seiff et al. (1979) noted that an apparent phase change at the lower boundary of the upper cloud (at ~57 km) coincided with a temperature of ~270 K, the melting point of 80% sulphuric acid.

Knollenberg and Hunten (1980) described the mode 2 particle distribution with a narrow Gaussian distribution (after correcting for instrumental broadening) and used a log-normal distribution for mode 1 to reasonably constrain the distribution below the LCPS minimum size detection (Figure 1.13). The size distributions throughout the cloud layers are summarised in Table 1.3. Satoh et al. (2015) reported that the bimodal upper clouds of the standard model were insufficient to explain

the observed phase function from the IR1 Akatsuki spectrometer channel and needed larger (mode 3) particles to replace some of the mode 2 particles in the model to reproduce observations.

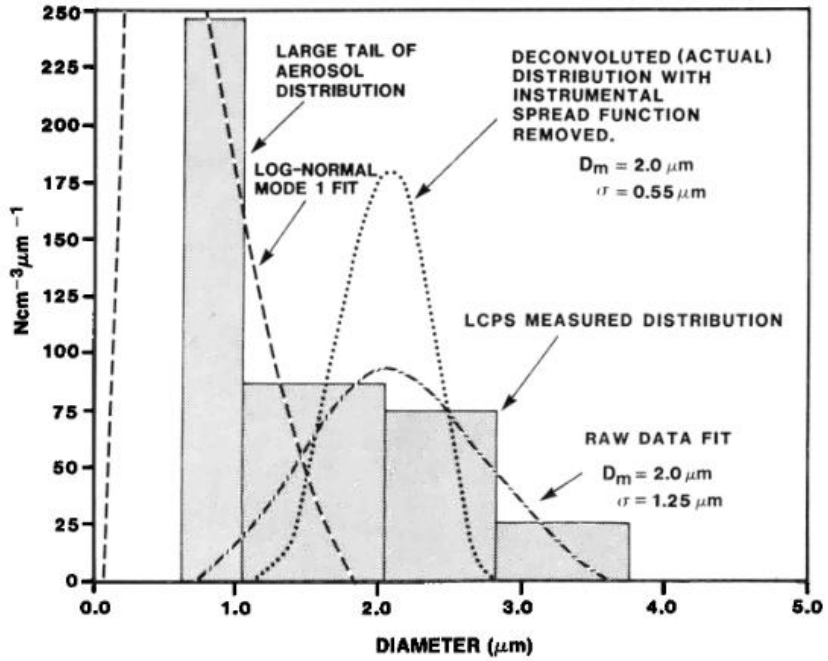

Figure 1.13. Figure from Knollenberg and Hunten (1980) showing the LCPS measured distribution (bars) with mode 2 particle distribution measured by the instrument (dash-dotted line), and reconstructed mode 2 distribution once instrumental broadening had been removed (dotted line). Much of the mode 1 size distribution is below the limit of detection of the LCPS, so the tail of a log-normal distribution is fitted to the lower size bins (dashed line), resulting in a mean mode 1 diameter lower than the lower limit of detection of the instrument. The data shown is for the upper precloud layer, not the upper clouds, and is included here purely for illustration of the fitting and deconvolution of the data.

Table 1.3. From Knollenberg and Hunten (1980). Particle distributions of the modes at different altitudes. Knollenberg and Hunten note that a log-normal distribution did not provide a fit for particles larger than 20 μm. Precloud layers and boundaries between the main cloud layers are shaded for readability.

		Mode 1 Log-normal distribution			Mode 2 Gaussian distribution			Mode 3 Log-normal distribution		
	Altitude range / km	N_T / n cm^{-3}	σ_g	$\overline{d_g}$ / μm	N_T / n cm^{-3}	σ / μm	$\bar{d}$ / μm	N_T / n cm^{-3}	σ_g	$\overline{d_g}$ / μm
	66.10 – 65.20	181	2.16	0.35	9	0.50	1.33			
	65.20 – 63.80	211	2.16	0.35	22	0.68	2.38			
	63.80 – 62.50	336	2.16	0.35	41	0.68	2.20			
Upper cloud	62.50 – 61.25	521	2.16	0.35	53	0.80	2.20			
	61.25 – 60.20	544	2.16	0.35	64	0.69	2.32			
	60.20 – 59.00	608	2.16	0.35	71	0.84	2.28			
	59.00 – 58.15	348	2.16	0.35	63	0.91	2.26			
	58.15 – 57.10	197	2.16	0.35	58	0.87	2.12			
T_{um}	57.10 – 56.20	54	2.16	0.35	29	0.82	2.38			
	65.20 – 55.40	69	2.16	0.35	30	0.74	2.54	17	1.25	7.40
	55.40 – 54.80	69	1.9	0.30	31	0.44	2.83	30	1.25	7.40
	54.80 – 54.30	69	1.9	0.30	30	0.49	2.73	37	1.25	7.40
Middle cloud	54.30 – 53.90	86	1.9	0.30	32	0.48	2.80	32	1.25	7.40
	53.90 – 53.25	72	1.9	0.30	38	0.55	2.70	50	1.26	7.28
	53.25 – 52.80	99	1.9	0.30	37	0.55	2.80	38	1.26	7.28
	52.80 – 52.30*	112	1.9	0.30	44	0.65	2.73	35	1.26	7.28

Middle cloud	52.30 – 51.70*	122	1.9	0.30	54	0.59	2.73	48	1.26	7.28
	51.70 – 51.10*	110	1.9	0.30	56	0.63	2.70	40	1.27	7.41
	51.10 – 50.60	121	1.9	0.30	52	0.68	2.70	39	1.27	7.41
	50.60 – 50.10	93	1.9	0.30	46	0.63	2.45	14	1.27	7.41
T_{ml}	50.10 – 49.70	144	1.80	0.35	14	0.60	1.70	15	1.27	7.41
Lower cloud	49.70 – 49.25	528	1.80	0.4	57	0.75	2.58	126	1.29	7.20
	49.25 – 48.75	563	1.80	0.4	71	0.60	2.73	177	1.29	7.20
	48.75 – 48.30	404	1.80	0.4	75	0.55	2.60	72	1.29	7.20
	48.30 – 47.75	233	1.80	0.4	59	0.66	2.14	33	1.29	7.20
Upper precloud	47.75 – 47.50	474	2.02	0.35	111	1.25	2.10			
Lower haze	47.50 – 46.45	128	1.70	0.28						
Lower precloud	46.45 – 46.30	179	1.80	0.30	34	0.85	2.90			
Lower haze	46.30 – 43.25	218	1.57	0.25						
	43.25 – 38.70	41	1.57	0.25						
	38.70 – 31.00	46	1.57	0.25						

** Reported altitude ranges have been corrected. Reported altitude ranges (52.80 – 51.30, 51.30 – 52.70, 52.70 – 51.10) duplicate altitudes, alternate between ascending and descending, and are significantly larger than the altitude ranges reported for the rest of the main cloud deck. The values in the table are corrected values, assuming typographical errors were made in the second digits to produce three non-overlapping altitude regions of 0.5 or 0.6 km depth.*

Knollenberg and Hunten (1979b) suggested that the behaviour of the clouds indicated a source of sulphuric acid, and perhaps mode 1 (which they attribute to sulphur, though that was later disproven (Pollack et al., 1979; Tomasko et al., 1979)) at the base of the upper clouds, likely linked to UV light to explain the lack of particle production deeper in the atmosphere. Esposito et al. (1979) reported that the sulphuric acid particle concentrations in the upper cloud could be photochemically produced from SO_2.

The probes also measured the wind speeds during descent. The zonal winds reached ~100 m s^{-1} at the cloud tops, the highest altitudes measured directly by the probes (Counselman et al., 1980; Counselman et al., 1979) consistent with the atmospheric super-rotation observed in the UV (e.g., Travis et al., 1979a). Regions of strong wind shear were detected at the base of the upper clouds (Counselman et al., 1980). The upper clouds were found to be statically stable against overturning (Seiff et al., 1979) with turbulent eddy mixing and turbulence consistent with trapped inertial gravity waves within the layer (Counselman et al., 1980). Horinouchi et al. (2020) reported that modelling showed atmospheric turbulent eddies were vital for the equatorward transport of angular momentum required to drive the observed super-rotation of the atmosphere.

1.3.2.3 Middle clouds

The boundary of the middle and upper clouds, inferred from a non-zero minimum in LCPS and nephelometer readings (Blamont & Ragent, 1979; Knollenberg & Hunten, 1979a, 1979b, 1980; Ragent & Blamont, 1979, 1980), coincides with the tropopause. Unlike the statically stable upper clouds, the middle cloud layer (50 – 55 km) was found to be unstable (Seiff et al., 1979, Figure 1.14), with a sharp increase in stability at the boundary of the middle and lower clouds, and a neutrally stable lower cloud region. The lower and middle cloud layers were predicted to be convective due to Large probe solar flux radiometer results (Tomasko et al., 1979). Travis et al. (1979b) reported observations in the UV of "bright- and dark-rimmed" convective cells in low- and mid-latitudes, organised into large-scale horizontal clusters (though Rossow et al. (1980) argued that the middle cloud layer should not be visible to the OCPP). No wind shear was detected in the middle clouds (Figure 1.15), consistent with a region of convective mixing (Counselman et al., 1980).

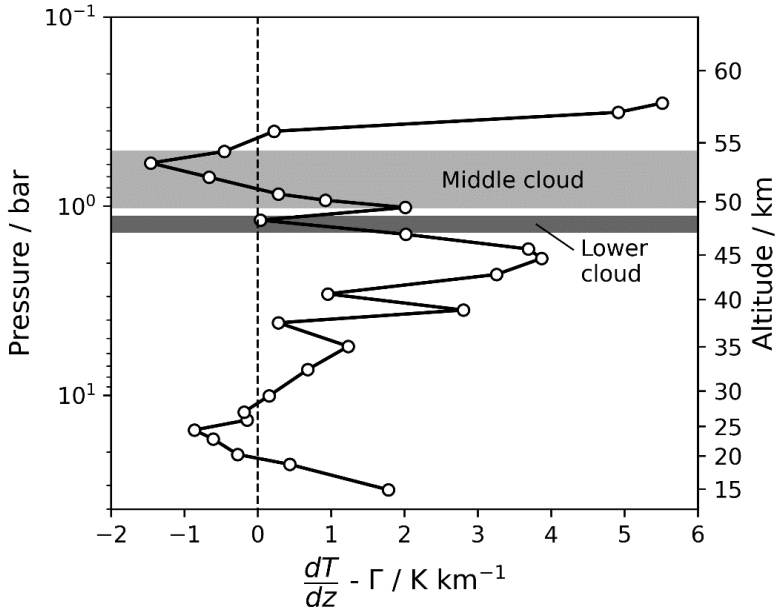

Figure 1.14. Adapted from Seiff et al. (1979). Stability of the atmosphere measured during Pioneer Venus descent. Negative values indicate instability. The middle clouds are the most statically unstable region of the atmosphere measured. Stability increases at the middle-lower cloud boundary, and then decreases again in the lower cloud. The y-axes have been inverted from the original plot. The surface is now towards the bottom of the plot.

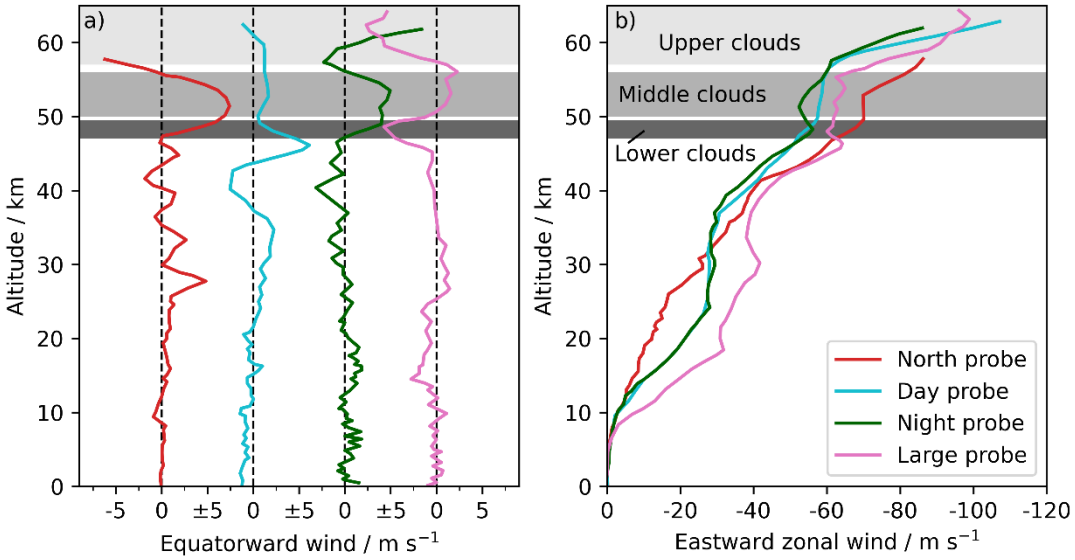

Figure 1.15. Adapted from Counselman et al. (1980). Equatorward (a) and eastward zonal (b) wind velocity measured by the four Pioneer Venus probes. Zonal winds are westward, and therefore are negative. Equatorward winds are offset horizontally for clarity. The upper, middle, and lower clouds are shown in grey. Boundaries between cloud regions occurred at slightly different heights at the different probe locations; the regions shown are for the Large probe.

The middle cloud region was detected by all four Pioneer Venus probes, with some small variations: the small probes all found that backscatter increased with decreasing altitude through the middle clouds, whereas the Large probe found that the backscatter remained approximately

constant (Blamont & Ragent, 1979). Nevertheless, as all probes detected it, it was inferred to be a global feature and the findings of the Large probe generalised to the whole planet (Ragent & Blamont, 1980).

Modes 1 and 2 were detected in the middle cloud by the LCPS, along with a small number of larger particles (5 – 25 μm diameter) referred to as mode 3 (Knollenberg & Hunten, 1979a, 1979b) (Figure 1.16). A decrease in mode 1 number density and an increase in mode 2 modal size made the two modes distinguishable (Knollenberg & Hunten, 1980). Mode 2 was best resolved in the middle cloud, being well described (once instrumental broadening was removed) by a modal diameter of 2.7 μm and standard deviation of less than 0.65 μm across the cloud. Most of this broadening was due to a change in the modal diameter with altitude – if only a single optical depth of mode 2 particles was considered (rather than the full 3 optical depths in the middle cloud), standard deviation was ~0.2 μm (Knollenberg & Hunten, 1979a).

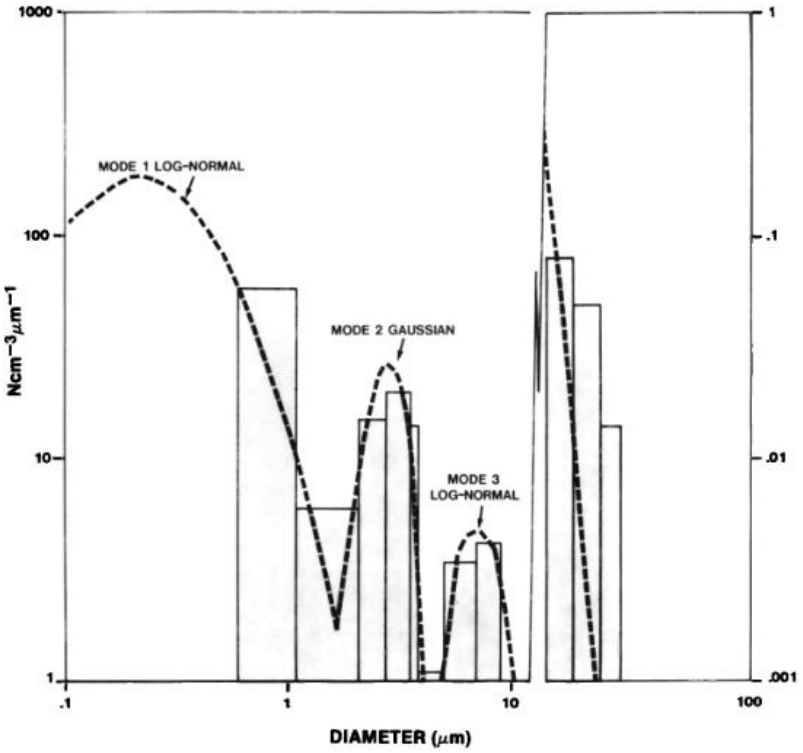

Figure 1.16. From Knollenberg and Hunten (1980). Size distribution for modes 1, 2, and 3 at 54.2 km. The right hand of the figure shows the large particle sizes. A log-normal distribution is unable to fit the largest detected sizes of the particles.

The mode 2 modal diameter grew rapidly across the transition from the upper to middle cloud to a diameter of 2.7 μm. The diameter fluctuated between 2.7 and 2.9 μm for a few kilometres before gradually decreasing again to ~2 μm at the boundary of the lower and middle clouds at 50.5 km (Knollenberg & Hunten, 1980). It was approximately monodisperse at each altitude and varied smoothly, indicating liquid droplets, rather than solid particles (Knollenberg & Hunten, 1979a). The larger size in the middle clouds for the mode 2 particles has led to them sometimes being labelled mode 2' (Tomasko et al., 1980b).

Poor counting statistics for the mode 3 particles made it difficult to draw reliable conclusions about the mode 3 distribution in the middle clouds, though Knollenberg and Hunten (1980) reported that they seemed to appear just below the upper-middle cloud transition.

Mode 3 particles had only a small number density, and the mode 1 particle number density was around an order of magnitude lower than in the upper cloud. This caused an overall decrease in total number density from top to bottom of the middle cloud, decreasing to ~100 cm^{-3} at the middle cloud base (Knollenberg & Hunten, 1979b, 1980; Ragent & Blamont, 1980). At the Large probe location, the extinction coefficient and mass loading did not change significantly throughout the middle cloud, despite the decrease in number density, due to the higher proportion of larger particles present than in the upper cloud. Number density, extinction coefficient, and mass loading all decreased to a minimum at the middle cloud base (50.5 km) (Knollenberg & Hunten, 1980).

Knollenberg and Hunten (1980) reported a good fit to the observations if all the particles were assumed to have equal refractive indices for n = 1.38 – 1.40. The nephelometers were not sensitive to the mode 1 particles, so their properties were assumed to be the same as in the upper clouds (Blamont & Ragent, 1979). If mode 3, the largest particles, were allowed to contain absorbing material or have non-spherical geometries (Section 1.3.3.3), they would be less backscattering than predicted for non-absorbing spheres, and the mode 2 (and mode 1) refractive index would be higher to compensate. The mode 2 particles remained consistent with concentrated sulphuric acid (Knollenberg & Hunten, 1979a).

1.3.2.4 Lower clouds

The lower cloud, located at around 48 – 50 km, was highly variable. It was detected by the Large and Night probes, was present but less prominent at the North probe location (the nephelometer data suggested that perhaps the top of the lower cloud was missing but the base was still present), and was absent at the Day probe location (Blamont & Ragent, 1979; Ragent & Blamont, 1979). This was supported by the data from the radiometers on the Day and Large probes: Ragent and Blamont (1980) reported that the Large probe data showed three distinct regions with different gradients corresponding to the upper, middle, and lower cloud regions, while the Day probe had only two different gradients apparent in the same altitude range, corresponding to the upper and middle clouds. More UV light also penetrated the lower atmosphere at the Day probe site than the Large probe site, likely due to the absence of the lower cloud.

The total number density remained approximately constant from the middle clouds, but mode 1 and mode 3 number densities increased by a factor of ~5. The larger size of mode 3 meant it dominated cloud properties, causing an increase in mass loading and extinction coefficient for the lower clouds (Knollenberg & Hunten, 1979b, 1980). They suggested that the variability in the lower cloud between locations could be due to mode 3 particles being a transient, rather than permanent, feature of the clouds (Ragent & Blamont, 1980).

As seen in Figures 1.14 and 1.15, the boundary between the middle and lower clouds at the Large probe location was marked by an increase in static stability. The lower cloud itself was found to be a region of neutral stability with strong wind shear at the base of the lower cloud (Counselman et al., 1980; Seiff et al., 1979).

Two thin (100 – 200 m) regions of higher particle size were detected by the LCPS, dubbed "pre-cloud layers" or "cloud filaments". They were found to be bimodal, consisting of mode 1 and 2 particles and were theorised to be either detached regions of the lower clouds (the upper pre-cloud layer) or newly condensed cloud particles (the lower pre-cloud layer) (Knollenberg & Hunten, 1980). The pre-cloud layers are not well understood, have been only rarely observed, and are generally not included in cloud models.

1.3.2.5 Lower haze

Below the main clouds, Knollenberg and Hunten (1979a, 1979b, 1980) reported that they detected mode 1 particles persisting down to ~31 km, with a maximum number density at 45 – 47 km. The nephelometers were not sensitive to mode 1 particles (Blamont & Ragent, 1979), but the day probe radiometer did detect UV extinction down to 24 – 28 km, which Ragent and Blamont (1980) suggested could indicate the lower haze was also present at other probe locations.

Titov et al. (2018) reported, citing Gnedykh et al (1987)[1], that the Venera 8 and Vega 1 and 2 descenders detected a haze of particles below the clouds to ~35 km. Data from the Vega probes suggested number densities of $5 \times 10^4 – 5 \times 10^5$ cm^{-3} for particles of radius < 0.25 μm and refractive index n = 2.

The Vega descenders detected phosphorus in the lower cloud and below, down to the lower limit of operation of the instrument (33 km). They did not detect a distinct lower cloud boundary, which may indicate the presence in only a few locations – Venera 8 alone may have detected a similar layer – of a phosphorus-containing cloud or haze below the main clouds (Krasnopolsky, 1989).

The temperature in the region below the main clouds is sufficiently high that not only would sulphuric acid evaporate, it would begin to decompose into SO_3 and H_2O, precluding this as the main constituent of the lower haze. The composition and existence of the lower haze are uncertain (Titov et al., 2018), and it is not included in the standard cloud model.

1.3.3 Cloud composition and formation

1.3.3.1 Mode 2

The mode 2 particles matched the expectation from Earth-based observations of clouds of predominantly ~2 μm diameter droplets of concentrated sulphuric acid (Knollenberg & Hunten,

[1] Paper is in Russian and unavailable (archive starts at 1996), though citations of what may be a translation also exist. Paper is detailed here: https://ui.adsabs.harvard.edu/abs/1987KosIs..25..707G/abstract
V. I. Gnedykh, L. V. Zasova, V. I. Moroz, B. E. Moshkin and A. P. Ekonomov. Vertical structure of the cloud layer of Venus at the Vega 1 and 2 landing sites. Cosmic Res. 25, 707 (1987), or Kosm. Issled. 25, 707 (1987) (In Russian).

1979b, 1980). The particles were found to be of the correct size in the upper clouds (the only region of the clouds penetrated by ground-based observations (Knollenberg & Hunten, 1979b), were consistent with liquid droplets and had refractive indices consistent with sulphuric acid in the upper and middle clouds (Blamont & Ragent, 1979; Ragent & Blamont, 1979, 1980), and in the lower clouds if the mode 3 particles were not required to have the same refractive index as the smaller modes (Ragent & Blamont, 1979). The mode 2 particles were readily traceable throughout the cloud system, with changes in size proposed to be due to the evaporation and recondensation of H_2O and H_2SO_4 vapour from and to the droplets (Knollenberg & Hunten, 1979b, 1980).

Recent observations (Markiewicz et al., 2014; Petrova, 2018; Petrova et al., 2015) suggest there may be traces of other component in mode 2. This is expanded upon in Section 1.4.3.

1.3.3.2 Mode 1

Knollenberg and Hunten (1979b) reported that, from Earth-based observations, it was assumed that the yellow colour of Venus was due to particles of elemental sulphur, which were expected to be detected in the upper clouds. Pollack et al. (1979) reported that sulphur would be unsuitable as mode 1 as the molecular structure (and therefore absorption spectrum) of sulphur is highly variable depending on its temperature (Young, 1977). Due to the low temperature in the upper clouds, elemental sulphur would not absorb at sufficiently long wavelengths to match the observations. This was supported by Ragent and Blamont (1980), who reported from nephelometry results that none of the particle modes detected were consistent with sulphur.

Knollenberg and Hunten (1979a, 1980) noted a strong correlation between mode 1 and mode 2 particle number concentrations in the upper and middle clouds: both reached a peak at ~60 km before decreasing gradually through the upper cloud followed by a sharp decrease at the upper-middle cloud boundary. They remarked that rapid changes in number density are often an indicator of proximity to a source or sink. That would therefore imply a source of mode 1 and 2 at 60 km, which Tomasko et al. (1979) identified as the location of strongest UV absorption. This could indicate that both mode 1 and 2 are chemically produced, possibly from a single parent vapour.

If mode 1 and 2 both grow from the same vapour, it would suggest that they are both sulphuric acid. However, in the lower clouds the mode 1 and 2 profiles diverged, with the number density of mode 1 increasing while the mode 2 profiles remained constant. The mode 1 profile was found to be more closely correlated with mode 3 in the lower clouds, suggesting it is not sulphuric acid at all altitudes (Knollenberg & Hunten, 1980).

Knollenberg and Hunten (1979a) theorised that mode 1 was a “polyparticle” aerosol composed of many different components, some volatile and some involatile, due to the similarity between the mode 1 distribution and that of terrestrial aerosols. They argued that the much higher particle number densities for mode 1 than seen for terrestrial aerosols was due to the lack of precipitation

on Venus. In the absence of rain, there is no "cleaning" of the atmosphere to remove the aerosol. They suggested that a portion of mode 1 could be formed by the recondensation of meteoric vapours. Venus would be expected to receive similar amounts of meteoric material to Earth (~40 tonnes per Earth day, t d^{-1}). This is supported by meteoric flux estimates of 31.0 ± 15.5 t d^{-1} by Carrillo-Sánchez et al. (2020). Knollenberg and Hunten (1979a) reasoned that such particles would be too small for detection by the LCPS (in accord with the findings of Frankland et al. (2017), who predicted a range of possible sizes of ablated and coagulated meteoric dust particles, all of which would be below the LCPS detection limit) but would be suitable condensation nuclei for the sulphuric acid cloud droplets. The idea of mode 1 being a mixture would appear to be supported by Gnedykh et al. (1987), who Titov et al. (2018) reported detected two distinct species within mode 1 in the Vega descent data: around 80% had refractive index n = 1.4 ± 0.1, consistent with sulphuric acid, but the remaining 20% were consistent with n = 1.7 ± 0.1, far too high for even concentrated sulphuric acid.

Knollenberg and Hunten (1980) proposed that, in the upper clouds, SO_3 (formed from gaseous SO_2) and water vapour recombine to form H_2SO_4 vapour. The reality may be somewhat more complex, with multiple reaction pathways, but the formation of sulphuric acid from water and SO_3 is broadly accepted (Krasnopolsky, 2012). Knollenberg and Hunten (1980) proposed that the vapour condenses onto mode 1 nuclei and the cloud droplets grow. The bimodality between modes 1 and 2 is due to the Kelvin effect: mode 1 are those particles below the critical size, while mode 2 are those that have overcome the activation energy required to reach critical size and can grow freely. In the middle clouds, the H_2SO_4 vapour is somewhat depleted. At the upper-middle cloud boundary, mode 2 grows from 2.2 to 2.7 μm over 1 km in altitude. The larger size in the middle clouds is often referred to as mode 2' (Tomasko et al., 1980b). Knollenberg and Hunten (1980) argued that away from the sulphuric acid source – which Krasnopolsky (2012) found to be at ~66 km – mode 2 outcompetes and grows at the expense of mode 1. The loss of sulphuric acid from mode 1 would account for mode 2 growth up to 2.5 μm, but growth beyond that would need to be from the condensation of sulphuric acid or water from the vapour phase. This growth by vapour deposition keeps the droplets large until the lower cloud, at which point the decrease in water vapour causes them to shrink again.

The mode 2 particles may collect additional mode 1 impurities by scavenging. When they reach sufficiently low altitudes that the droplets evaporate, these small mode 1 particles could fuse to form larger nuclei that, once brought back up to the upper clouds by updrafts, would be more favourable condensation nuclei, driving the growth of mode 1 (Knollenberg & Hunten, 1980).

1.3.3.3 Mode 3

Within the lower clouds, the mode 2 particles were 2.2 μm in size below the middle-lower cloud boundary, and decreased in size to ~1.9 μm at the base of the lower cloud (Knollenberg & Hunten, 1980). They were most clearly distinguishable at the top and bottom of the lower cloud, leading

Ragent and Blamont (1979) to theorise that the mode 2 particles grew into mode 3, and then reformed when mode 3 evaporated at the lower cloud base. However, further analysis of the data suggested that mode 3 and mode 2 could not be composed of the same material. Blamont and Ragent (1979) calculated a refractive index of 1.44 for modes 1 and 2 and 1.32 for mode 3, or 1.33 for all three, assuming spherical, inhomogeneous droplets. Values of ~1.33 are too low for concentrated sulphuric acid, as mode 2 is believed to be (Knollenberg & Hunten, 1980). The presence of mode 3 particles (2.5 – 19.5 μm in the lower clouds) would be expected to increase the measured scattering by a factor of ~10 (scattering from particles scales as radius^2 × concentration, and the mode 3 particles are a factor of 10 larger and a factor of 10 less abundant than mode 2 in the upper clouds), but only an increase of a factor of 2 – 3 was retrieved. The mode 3 particles were therefore required to have a smaller backscattering cross-section than expected for a non-absorbing sphere of their size (Ragent & Blamont, 1980). This could be achieved by making the particles non-spherical, or by including some absorbing material in the particles. For droplets of ~20 μm, Ragent and Blamont (1980) could not produce a significant change in the predicted backscatter, even for extremely strongly absorbing inclusions in sulphuric acid droplets. In addition, Knollenberg and Hunten (1980) and Ragent and Blamont (1980) reported that no absorption was detected in the lower clouds. Knollenberg and Hunten (1979a) reported having significant trouble fitting models to the mode 3 observations (Figure 1.16), again suggesting the need for non-spherical particles.

The strongest evidence for the non-spherical nature of the mode 3 particles comes from the overlap between two detection ranges of the LCPS. The LCPS sized particles by measuring how many detection elements were blocked by a particle as it passed through the detector (with each element needing to be 62.5% blocked to count as “occulted”). Different sizing ranges of the LCPS had different element sizes and therefore different particle size detection ranges: range 2 (5 μm elements, able to detect particles of 5 – 53 μm, split up into 10 channels for better size resolution) and range 3 (20 μm elements, able to detect particles of 16 – 181 μm, also split into 10 channels). Knollenberg and Hunten (1980) explained that as range 3 had a larger sampling volume than range 2, 50% more particles of the same size should have been detected in range 3 than in range 2 in the regions where they overlapped. However, from 48 – 56 km (the middle and lower clouds), 72 particles of 16 – 36 μm were detected in range 2, while only 3 particles of 16 – 35 μm were detected in range 3. Knollenberg and Hunten calculated a probability of “much less than 1%” for this to be purely due to random fluctuation. They instead drew parallels with issues faced by paired terrestrial instruments with different resolutions, which they reported tend to provide good agreement for liquid distributions, but not for snow crystals. They also reported that laboratory experiments with the flight spare instrument supported this conclusion.

Knollenberg and Hunten (1980) reasoned that spherical particles of 16.5 μm would easily occult 3 – 4 elements of the photodetector array of mode 2 and would likely occult at least 62.5% of a

larger mode 3 detector element, registering a detection in both cases. Range 3 may fail to detect some particles at this size if their shadows were not centred over the photodetector, but by 22 μm, spherical particles should be detected with 100% efficiency. For crystalline particles with a column, needle, or thin plate morphology, a long but narrow particle could easily occult several small detector elements (range 2) while failing to occult at least 62.5% of a range 3 element. The particle would therefore be detected in range 2, but not in range 3. This is demonstrated in Figure 1.17, reproduced from Knollenberg and Hunten (1980). They reported aspect ratios of 3:1 would be consistent with their observations, though other non-spherical morphologies would also be suitable. For a non-spherical particle, refractive indices of 1.3 – 2.0 could all be acceptable for mode 3.

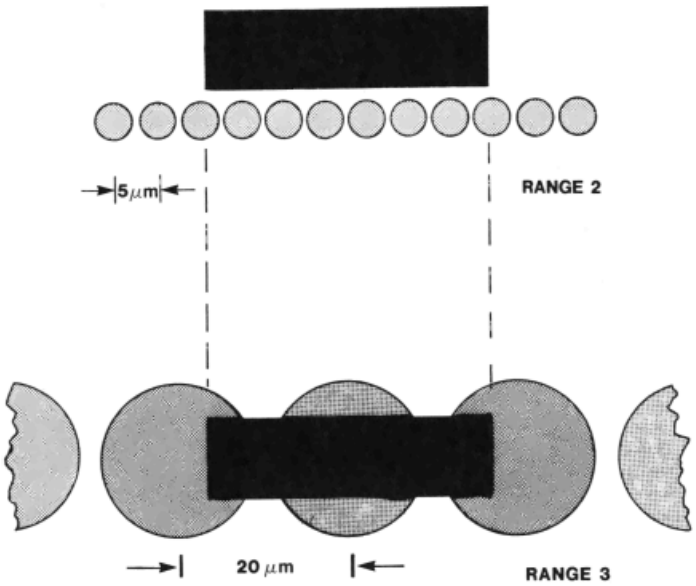

Figure 1.17. From Knollenberg and Hunten (1980). A long, thin particle, such as a crystal, can occult several range 2 detector elements (shown above for clarity), resulting in detection and accurate sizing of the particle. The same particle fails to occult 62.5% of any range 3 element and so is not detected.

An alternative solution was suggested by Toon et al. (1984): mode 3 was simply a long tail of the mode 2 distribution resulting from sizing and counting errors in the LCPS. For example, they suggested that, since the sample volume varied with particle size, and counts in different channels of the ranges were therefore weighted differently (for example, in range 2, they reported that a count in channel 1 was equivalent to 16 particles cm^{-3}, whereas in channel 2 it was 3 cm^{-3}), a larger particle that is misidentified as a smaller particle due to its shadow partially missing the detector elements introduced a counting error of a factor of 4 – 5. Alternatively, the smallest channel of range 2 could have been detecting particles below its supposed limit of detection (5 μm), increasing the number of large particles detected. They reported that, if they assumed these instrument errors occurred and corrected for them, the mode 3 particles were no longer a separate mode, but part of a broader mode 2. The correction decreased the number of large

particles detected and therefore the nephelometer data could be fitted with mode 2 particles of refractive indices consistent with sulphuric acid.

However, as an unforeseen consequence of their LCPS corrections, Toon et al. (1984) found that the required refractive index to fit the upper cloud in both Venera phase function data and Pioneer Venus nephelometer data increased to $n > 1.49$, significantly too high to be pure sulphuric acid. They proposed that 10% of the volume of the droplets could be a sulphur core with a sulphuric acid shell. While this was conclusively disproven – sulphur is not wetted by sulphuric acid and cannot be included in a droplet, only adhered to the surface (Young, 1983) – it does not preclude the possibility of other highly refractive impurities in the cloud droplets.

The identity of mode 3, if mode 3 is a true feature of the clouds and not an artefact of instrumental error as suggested by Toon et al. (1984), remains unknown. Common crystalline possibilities include chlorides or sulphates (Knollenberg & Hunten, 1980; Ragent & Blamont, 1980). Ragent and Blamont (1980) suggested a metallic ion could provide absorption (if mode 3 are required to be absorbing) before being vapourised at the lower cloud base and forming part of the lower haze. Knollenberg and Hunten (1980) suggested crystalline ferric chloride as mode 3. They found that $FeCl_3.6H_2O$ had the required vapour pressure, but not melting point (310 K) to be crystalline at lower cloud temperatures (>355 K). They proposed that the hexahydrate could be present in the middle clouds before forming anhydrous ferric chloride and water vapour on descent to the lower clouds.

Knollenberg and Hunten (1980) also argued that, as mode 3 particles were observed in regions of high wind shear, particles sampled by a vertical transection were formed in different locations and at different times. By analogy to terrestrial cirrus clouds, they argued that the mode 3 particles could form from the condensation of vapour to supercooled droplets, which rapidly crystallise. The crystals could grow further in supersaturated regions and sediment to lower levels over length scales of several kilometres. Cirrus clouds form at the base of shear zones such as Kelvin-Helmholtz instabilities. By analogy, they proposed that the upper-middle clouds boundary could be such a dynamical shear region.

1.4 UV absorption overview

Having been observed from Earth since the 1920s and photographed by Mariner 10 during its flyby in 1974 (Murray et al., 1974; Ross, 1928; Wright, 1927, Figures 2, 18), the UV contrasts had been studied over a long period of time and recurring patterns, such as the “Y” and “reverse C” features (Figure 1.18), were known before Venus orbiters were planned. This has informed mission payload planning, and UV imaging cameras have been a component of the payloads of the Pioneer Venus, Venus Express, and Akatsuki orbiters, providing many photographs of the UV contrasts over a long period of time.

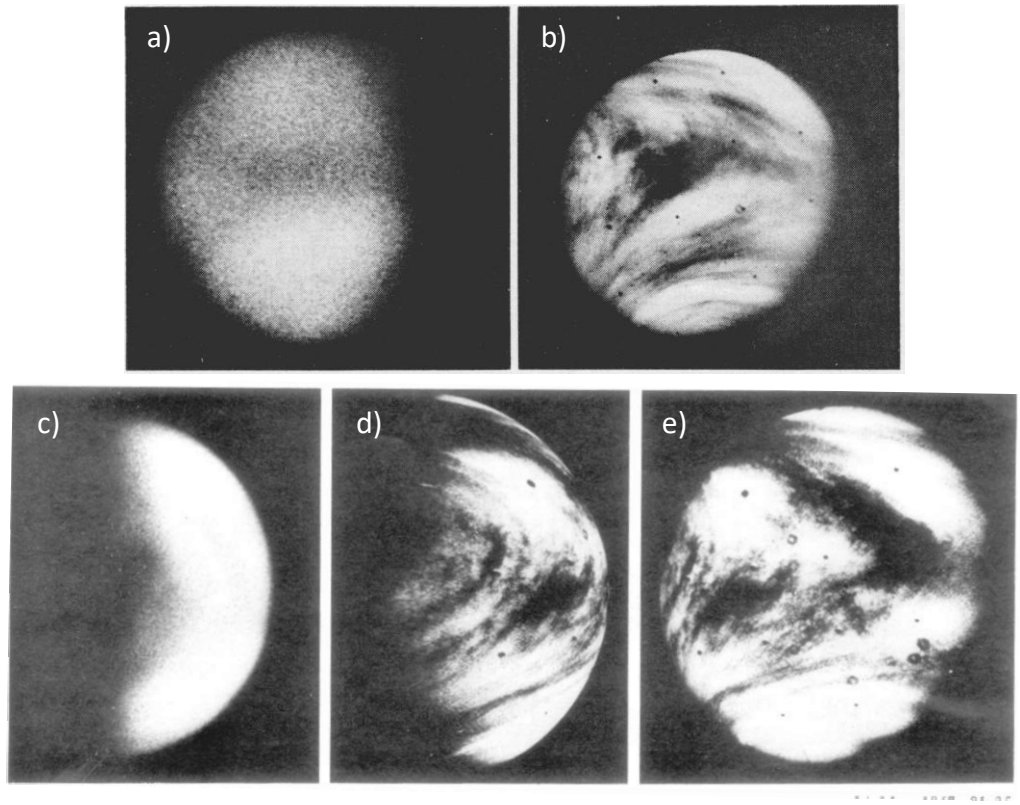

Figure 1.18. From Murray et al. (1974). Left: photographs taken from Earth in a) 1966 and c) 1967 showing feature known as the "Y": the dark horizontal band across the centre of the disc, broader at the left-hand edge; and the “reverse-C”: bright limbs and dark centre seen at the evening terminator. Right, photographs taken by Mariner 10 in 1974, showing b) a similar Y feature and e) a pattern which, when projected onto a sphere (d) to mimic a view of the evening terminator, produced a similar pattern to the reverse-C.

Mariner 10 had reported that the Y feature recurred with a period of around 4 days during its observations, consistent with the superrotation of the atmosphere at cloud-top heights (Murray et al., 1974). To study the long- and short-term variation of the UV patterns, the cloud photopolarimeter on the Pioneer Venus Orbiter took daily photographs at 365 nm of the Venusian upper clouds (Pollack et al., 1979; Travis et al., 1979a). The spectral albedo of Venus showed significant absorption from 300 to 520 nm, with marked contrasts (dark and light regions, rather than, for example, a uniform grey) visible at wavelengths below 400 nm. The observed cloud features are expanded on in Section 1.4.2.

The ratios of UV and visible light measured by the probes on descent imply that ultraviolet light is absorbed throughout the atmosphere, but visible light is only absorbed in the top ~15 optical depths (though Pollack et al. (1979) acknowledged that this could be an artefact of the filter used in the radiometer). Using data from the UV photometer on Venera 14, Ekonomov et al. (1984) also found that some UV absorption took place throughout the depths of the clouds, but that the majority of the absorption took place in the upper clouds (with 80% of the incident UV solar flux absorbed above 59 km) and most of the rest absorbed by 48 km. This primarily appears to have

been in the bottom part of the middle cloud and the lower cloud, as they found the region from 58 – 55 km had the lowest UV absorption coefficient by volume.

Taking the cloud top to be at an optical depth of $\tau = 4$ below the TOA, Pollack et al. (1979) modelled various potential absorbers, including sulphur dioxide, and small sulphur particles that had been the assumed cause of the absorption from Earth-based measurements (Knollenberg & Hunten, 1980). They also tested models of "meteoritic particle" cores in the sulphuric acid droplets, with carbonaceous matter, metallic iron, and magnetite used to simulate the cores. All of these, as well as sulphur were ruled out. Sulphur dioxide on the other hand was found to be a promising candidate, though it did not provide enough absorption above 55 km or at wavelengths longer than 350 nm.

Based on the cloud properties reported by Knollenberg and Hunten (1979a, 1979b), Blamont and Ragent (1979) and Ragent and Blamont (1979), Pollack et al. (1980) predicted the Venusian albedo with sulphur dioxide included using a 19 layer radiative transfer model. SO_2 absorption is dominant at 200 – 320 nm, but not beyond, resulting in their predicted albedo from the models being significantly too high at 350 nm and above. A second absorbing species (the unknown UV absorber) was therefore required. Pollack et al. compared their model results for the second absorber to spectra of solid iron and graphite, and gaseous Cl_2 and NO_2. They reported the best agreement for chlorine, though the known concentrations of Cl_2 on Venus were a factor of 50 too small to account for the absorption required.

1.4.1. UV absorption spectrum

To compare the absorption to potential candidates, Pollack et al. (1980) used a radiative transfer model to predict the absorber properties required to match the observations taken during the Pioneer Venus mission. Similar techniques of radiative transfer modelling to predict absorber properties from observations have been used since then to try to calculate the true spectrum of the unknown UV absorber (e.g., Haus et al. (2016) used Venus Express data, and Pérez-Hoyos et al. (2018) used MESSENGER data from its Venus flyby).

The radiative transfer models are highly sensitive to the position of the unknown UV absorber within the atmosphere, and so the modelled spectrum is strongly dependent on the assumptions about the nature of the absorber (for example, if it is a gas, an inclusion in mode 2 particles, part of mode 1, etc.) and its location. As such, variation between spectra predicted by different models and different datasets (Figure 1.3) is unavoidable until more is known about the absorber (Haus et al., 2016; Pérez-Hoyos et al., 2018; Pollack et al., 1980).

Pérez-Hoyos et al. (2018) calculated the normalised absorption of their modelled UV absorber and compared it to spectra of some previously proposed candidate species (Figure 1.19). Some of the plotted candidates, and a few other common candidates, are detailed in Sections 1.5 and 1.6.

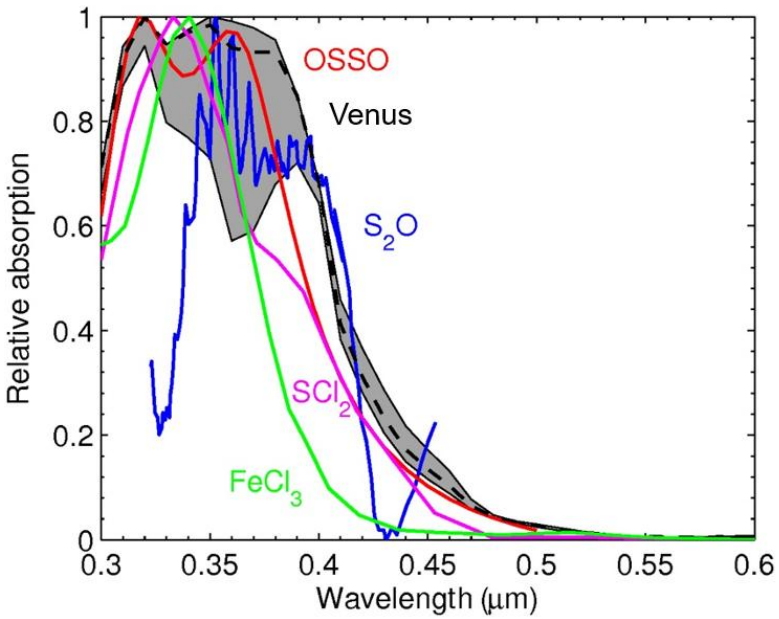

Figure 1.19. Adapted from Pérez-Hoyos et al. (2018). Calculated UV absorption (dashed black line) and uncertainty (shaded area) compared to four candidates for the unknown UV absorber. While some provide a better fit than others, none can provide the correct slope at 0.4 – 0.5 μm.

1.4.1.2 Relationship to SO_2

The Akatsuki Ultraviolet imager (UVI) took pairs of photographs at 283 nm and 365 nm, the absorption peaks of SO_2 and the unknown UV absorber respectively. The images were taken 3 minutes apart, and a pair of images was taken every two hours (Figure 1.20). The distribution of the unknown UV absorber appeared be broadly correlated with SO_2 with many of the same features, in particular the dark and bright streaks in the northern and southern polar regions. However, Yamazaki et al. (2018) noted that the detailed features are "quite different". They highlighted the overall greater brightness (see brightness scale) of the 365 nm image (Figure 1.36, right), greater contrasts, and the equatorial bright region which does not appear in the 283 nm image (Figure 1.36, left). From this they inferred that "the spatial distributions of SO_2 and unknown UV absorbers are governed by, at least partly, different chemical and/or dynamical processes", supporting claims that the unknown UV absorber is not a sulphur-based species. However, Pinto et al. (2021) highlighted that convection and upward transport of particulates such as elemental sulphur would decrease correlation between them and the gas they form from (SO_2). However, their photochemical models were one dimensional, so they could not predict the changes in horizontal distribution to verify this.

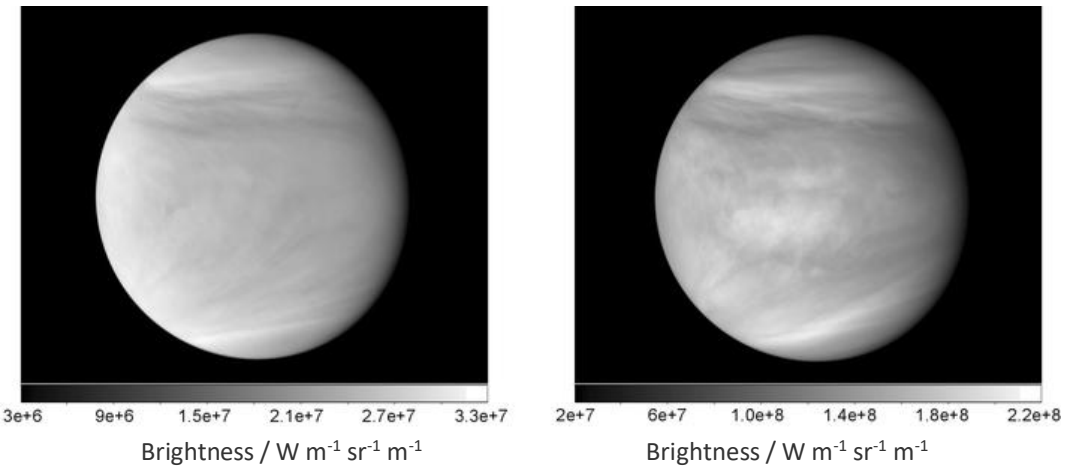

Figure 1.20. From Yamazaki et al. (2018). Images from the Akatsuki UV Imager at 283 nm, looking at SO_2 absorption (left) and 3 minutes later, at 365 nm, looking at the unknown UV absorption (right).

An alternative cause of the correlation is that the unknown UV absorber, which is generally assumed to only absorb above ~300 nm, is in fact absorbing at 283 nm as well. Lee et al. (2021) reported that their models of the unknown absorber could only reproduce the disc-integrated albedo phase curves obtained from Akatsuki UVI images if the unknown UV absorber absorbs more strongly at 283 nm than 365 nm by a factor of at least 2. If this is the case, predicted spectra of the unknown absorber (Figure 1.3, Figure 1.19) likely misrepresent the shape and strength of the UV absorption near and below 300 nm by attributing all of the observed absorption to SO_2.

1.4.2 2D observations

1.4.2.1 Recurring patterns and features

In Earth-based observations, the Y and reverse-C patterns (Figure 1.18) were observed to recur every 4 – 6 days. The Y feature, only observable from Earth when Venus was visible as a full disc, was readily observed by both Mariner 10 and Pioneer Venus to recur every ~4 days. Mariner 10 observed two recurrences of the Y during its brief period of observations. Pioneer Venus, by virtue of being in orbit and therefore able to take photographs over several months to years, was able to study the longer-term variations in the Y feature, and other recurring cloud features, with daily photographs to monitor the patterns and contrasts in the UV cloud tops. (Murray et al., 1974; Rossow et al., 1980; Travis et al., 1979a).

Table 1.4 contains pictures and descriptions of features identified by Rossow et al. (1980). Contrast in raw images was reported to be at most 30%, so all images were all processed to enhance the contrasts. The normalisation and enhancement vary between papers and datasets, and so the differences between published photographs are not indicative of changes in relative brightness of different features between different datasets. This will not have been helped by the digitisation of the original articles, which may also have altered the contrasts in the images (Murray et al., 1974; Rossow et al., 1980; Travis et al., 1979a). Cartoons accompany the photographs of each feature to highlight the feature being described without obscuring the image.

Rossow et al. (1980) assumed that cloud features were “dark objects on a bright background” and so the features are generally described as such. The automatic assumption when viewing black and white images is that highlights and shadows correspond to peaks and troughs respectively, the opposite of Rossow et al.’s descriptions. As the cause and location of the UV absorption is not known, it may be either case, or both.

Table 1.4. Photographs from Rossow et al. (1980) and descriptions and cartoons of the contrast features they show.

#	Image	Cartoon	Description
1	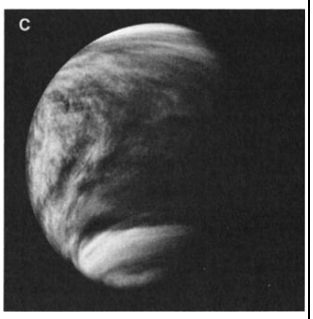		The **southern bright polar band** (white) and **cap** (light grey) are visible through the morning region. A **dark polar band** separates the bright band and cap. The northern bright polar band is not included in the cartoon. Due to viewing geometries, the northern polar cap is not visible.
2	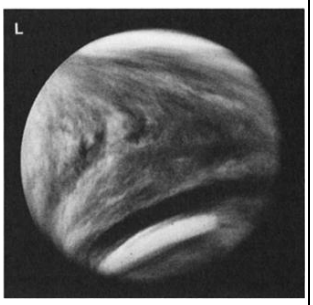		**Bright polar bands** are visible at the north and south of the planet. The southern polar cap (not included in the cartoon) is below the southern polar band and is generally darker than the bright polar bands.
3	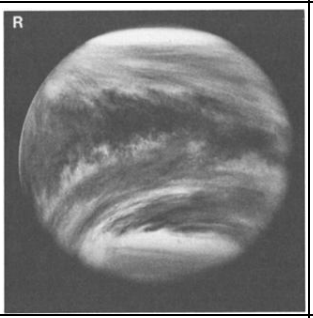		The southern **bright polar band**, with a ragged edge and "**bright streamers"** extending to mid-latitudes.
4	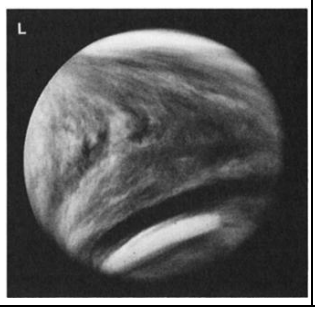		**Dark mid-latitude bands** are apparent in the northern hemisphere as a streaky, dark shadow, and in the southern hemisphere, where the band is much more pronounced.

5	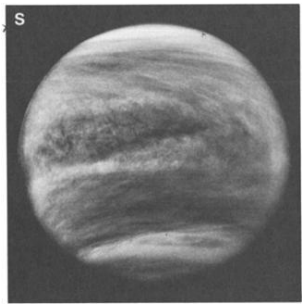		The **dark equatorial band** here is broader downstream (left) than upstream, coming to a point to the right of the centre of the disc. The equator is slightly above the centre of the disc as imaging is from above the southern hemisphere.
6	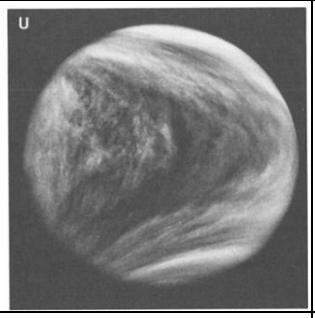		The **dark mid-latitude bands** (left side of disc) join the **equatorial band** (right of disc) to form the distinctive **Y shape**.
7	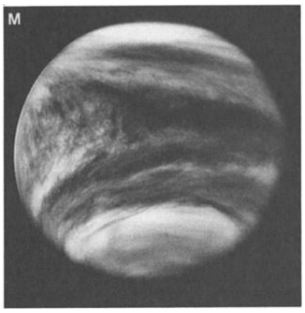		**Equatorial** and northern and southern **dark mid-latitude bands**. At the right of the disc, a **bright band** is visible in the southern hemisphere, separating the southern mid-latitude and equatorial dark bands.
8	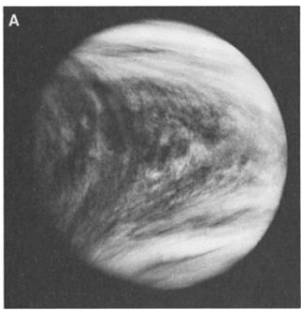	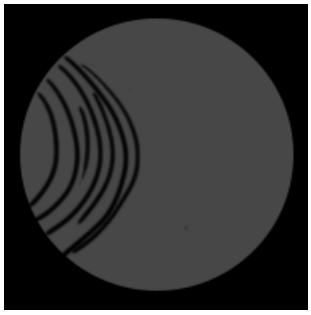	Large curved ("**bow-shaped**") features at the evening terminator, centred on the equator. Some form of bow-shaped features are present in almost all photographs. Travis et al. (1979a) clarify that “bow” is used to mean curved, not to invoke the bow-wave generated in front of a boat. Murray et al. (1974) term these “**bowlike waves**”.
9	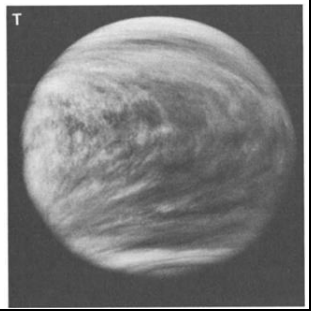		**Bow-shaped features** extending all the way across the disc, though less pronounced on the right-hand side than the left.

10	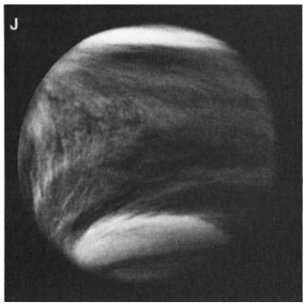	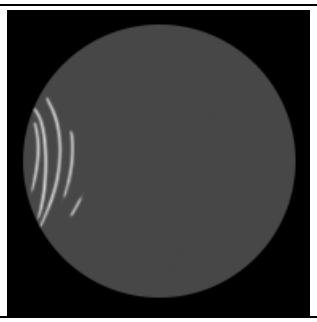	Small-scale **bow-shaped features** are visible on the left-hand edge of the disc.
11	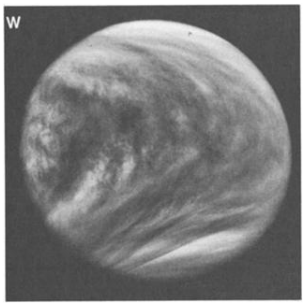	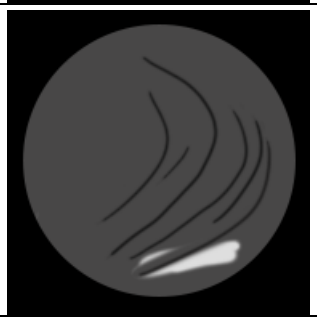	Planetary scale **bow-shaped features** reaching into polar latitudes are visible cutting across the **bright southern polar band**.
12	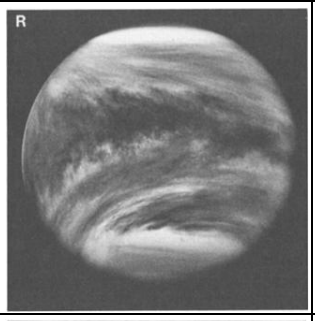		**Bow-shaped streaks** are visible almost parallel to the equator in the northern hemisphere.
13	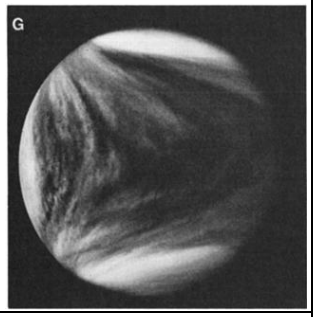	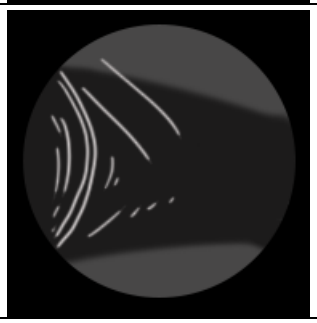	**Bow-shaped waves** on the left of the disc go from almost perpendicular to the equator to inclined to it at a shallow angle (right of disc).
14	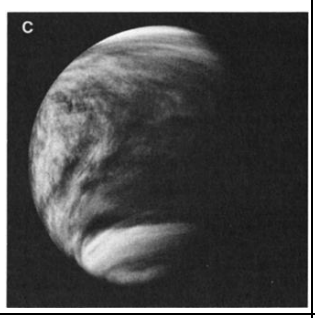		**Bright circum-equatorial belts** are visible in the northern hemisphere, cutting across the bow-shaped features on the left of the disc. The belts typically have a meridional width <100 km.
15	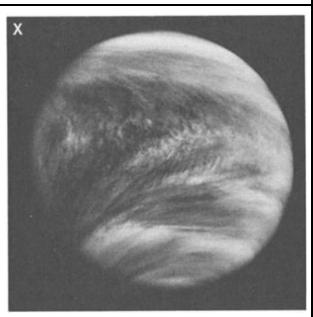		A "**wave train**" of nearly vertical dark and light lines is visible just to the lower right of the disc centre. Like the circum-equatorial belts, the wave trains cut through bow-shaped features and streaks.

16	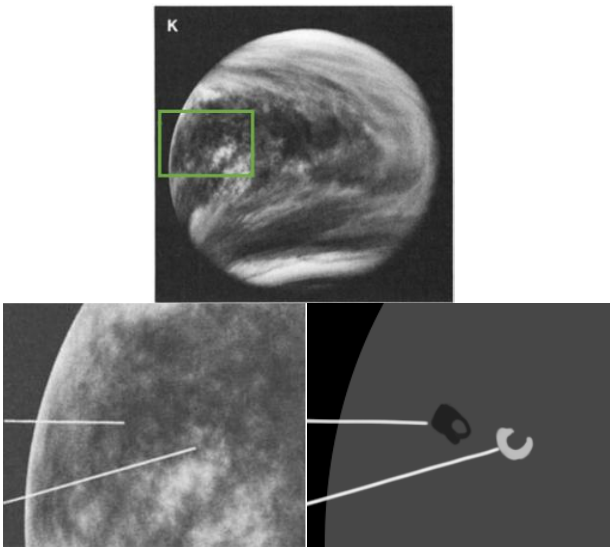	Top: a mottled region of convection is visible downstream of the subsolar point, indicated by a green box. Bottom: an enlarged view of the region indicated by the green box. White lines point to two examples of **convective cells**, one with a dark boundary and lighter centre (shown in black in the cartoon) and one with a bright boundary (shown in white in the cartoon). Murray et al. (1974) observed large convective cells (~280 km) persisting for several hours, but smaller cells (~170 km) did not.

Curved, "bow-like" features of various scales are present in most photographs taken in the UV and occur even when the majority of features in the equatorial regions are zonal (e.g., row 10 of Table 1.4). The features were found to be more visible in the afternoons and evenings, but were occasionally observed at the morning terminator (row 14, Table 1.4). The bow-like features generally (but not always, e.g., row 13, Table 1.4) exhibited the same inclination to the equator with latitude in a given photograph (e.g., rows 8 – 11, Table 1.4).

The Pioneer Venus mission began during a period of unusual polar brightness (Travis et al., 1979b), and as such the poles were much brighter than in Mariner 10 photographs, though this is not immediately apparent from the available images (as all presented photographs have been processed to maximise contrast). The poles are typically the brightest regions of images, with a dark polar band separating the bright polar band and cap in approximately half of the images recorded (Rossow et al., 1980). Some polar features were found to persist for a day or so, but rarely longer. Despite that, the overall appearance of the poles is fairly constant compared to the lower latitudes. While the viewing geometry from Pioneer Venus generally gives a better view of the southern hemisphere than the northern hemisphere, Rossow et al. (1980) claimed that these findings apply to both poles. There is no apparent correlation between the two poles with time – either can be particularly bright or dim, or vary in any of the usual ways, regardless of the form of the other. The bright polar band can be horizontal to the equator (Table 1.4, row 1) or tilted with respect to it (Table 1.4, row 2), and the transition to the mid latitudes can be smooth (Table 1.4, rows 1 and 2) or "whorl-like" (Table 1.4, row 3) (Rossow et al., 1980).

The thickest dark bow-shaped features make up the mid-latitude dark bands, which can be very distinctive, with high contrast, as in the southern mid-latitude band in Table 1.4, row 4, though they are more usually diffuse and poorly defined, as in the northern mid-latitude band in the same image (Rossow et al., 1980).

A similar dark band exists in the equatorial regions (±20°) (Table 1.4, rows 5 – 7). It is usually centred on the equator but can be slightly offset to either hemisphere. The combination of the viewing geometry (the orbiter photographed from a position over the southern hemisphere, and as such the equator is not central to the planetary disc in the photographs), the variable width of the band, and the diffuse edges make this difficult to identify in the images. The equatorial band has an average latitudinal width of 40° and is generally broader downstream (evening terminator, left of the planetary disc) than upstream. The downstream broadening, along with dark mid-latitude bands and bow-shaped features, forms the apex of the Y feature.

From assumed wind speeds of 100 m s^{-1}, Rossow et al. (1980) estimated the equatorial dark band spanned 120 – 280° in longitude. The mid-latitude and equatorial dark bands can exist parallel to one another, sometimes separated by a thin bright band (Table 1.4, row 7), or the mid-latitude bands can join the equatorial bands at the downstream end, forming the classical, symmetrical Y (Table 1.4, row 6). Table 1.4 row 7 shows a more asymmetrical Y, with the southern mid-latitude band and equatorial band both being present on the right-hand edge of the disc, producing a Y shape with a straight edge in the northern hemisphere and a curve in the southern hemisphere.

1.4.2.2 The Y feature

Travis et al. (1979a) reported on the observed behaviour of the Y feature by the Pioneer Venus imager over a period of three months. They found that the Y is produced by a combination of the upper haze near the terminators, sulphuric acid cloud, and UV absorption, and recurs every 4 – 5 days, consistent with the period of the atmospheric super-rotation in the upper clouds. However, Travis et al. highlighted that the specific features of the Y pattern change as it recurs.

Figure 1.21 shows two subsequent occurrences of the Y feature. The first, in panels A and B (a day apart) shows an “asymmetric Y feature”, which disappeared and reappeared 3 days later (panel C). Panels C, D, and E, each a day apart, show a more symmetric and elongated Y feature wrapping around the majority of the planet. Travis et al. (1979a) reported that it recurred once more, 4 days later, as a much shorter Y before becoming distorted and disappearing. It did not then recur for several weeks.

Figure 1.21 A is the same photograph as rows 2 and 4 of Table 1.4. The only differences are the paper it was published in, which highlights the differences in digitisation of the original papers.

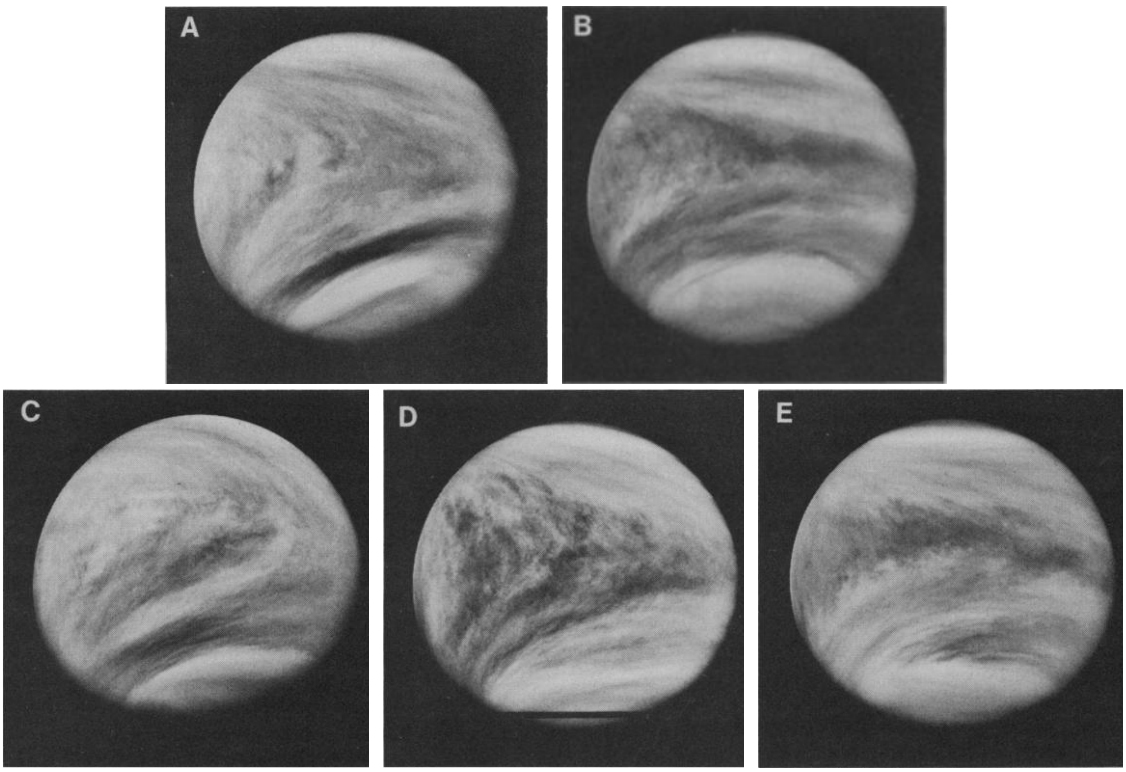

Figure 1.21. From Travis et al. (1979a). Photographs from the Pioneer Venus cloud photopolarimeter, taken at 365 nm. A and B, taken a day apart, show the Y feature. It recurred 3 days later, shown in panels C, D, and E (each one day apart). Cloud motion is right to left.

Table 1.4, row 13 shows a series of planetary-scale bow waves and an incredibly broad dark band, stretching from the north to south polar regions. This feature occurred during a period when Travis et al. (1979a) reported the Y feature was absent for several weeks. Rossow et al. (1980) found that the period when the Y did not appear consisted first of "highly asymmetric and distorted" patterns before the bow-shaped features in Table 1.4 row 13 appeared. Around a week later, an asymmetric Y feature (Table 1.4 row 7) appeared, recurring in a more symmetrical form every four days. Rossow et al. (1980) noted that, when the Y feature appeared or disappeared for a period of time, it underwent a "phase shift" – a particular point of the Y feature, for example the apex, would reappear in a different position rather than return to the same point on the disc. Their consideration of this in terms of phase was likely due to the OCPP taking photographs at the same time each day (its orbital period being 24 hours), so the photograph on the fourth day after the Y was apparent would show it in a different position. It would be equally correct to say that the period with which the Y recurred varied before it vanished. Rossow et al. (1980) described phase shifts in both directions – lengthening and shortening the period of time between recurrences. They proposed that the dark bands and bow-shaped features were produced at two different spatial scales, though they did not have a definitive proposal for the cause of the driving at these scales, and suggested that the interplay between the different scales that drive the rotation was responsible both for the phase shift of the Y feature and for its disappearance, which they theorised occurred when the phases of the bands and bow-shaped features became out of phase with one another.

1.4.2.3 Morning and evening terminators

Figure 1.22, panel A, taken just under a month after Figure 1.21, is of the afternoon and evening region in the absence of the Y feature. Figure 1.22, panel B, taken just under a month before Figure 1.21, in another period where the Y was absent for several weeks, shows the morning region. Travis et al. (1979a) reported that the photographs reflect the trend observed in the dataset of "generally higher contrasts" in the evening region than the morning region. This would seem to be referring to the presence of both UV bright and dark regions in close proximity on the evening terminator versus the more uniformly dark morning region. This may, however, be a peculiarity of the Pioneer Venus observation period, rather than a general rule: Figure 1.23 shows the morning and evening terminators as photographed by the Venus Monitoring Camera (VMC) on Venus Express (Titov et al., 2012). Titov et al. highlighted the general "streaky clouds" in the morning sector (Figure 1.23a) as compared to the more "turbulent" evening (Figure 1.23b), but each appears similar in the proportion of dark and light features. While the lower resolution of Figure 1.22 makes comparison difficult, the trend of streaky morning regions and patchy "convective" regions in the evenings can be seen in the Pioneer Venus images from Figure 1.22 and Table 1.4 (rows 13 (morning) and 8 (evening)). However, three pairs of images are not sufficient to draw robust conclusions.

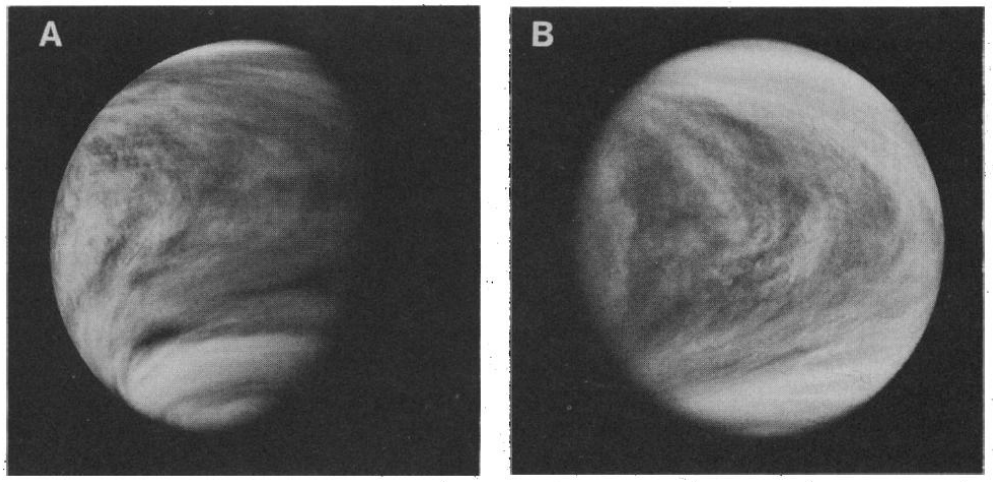

Figure 1.22. From Travis et al. (1979a). Morning (A) and evening (B) regions photographed by the Pioneer Venus cloud polarimeter at 365 nm.

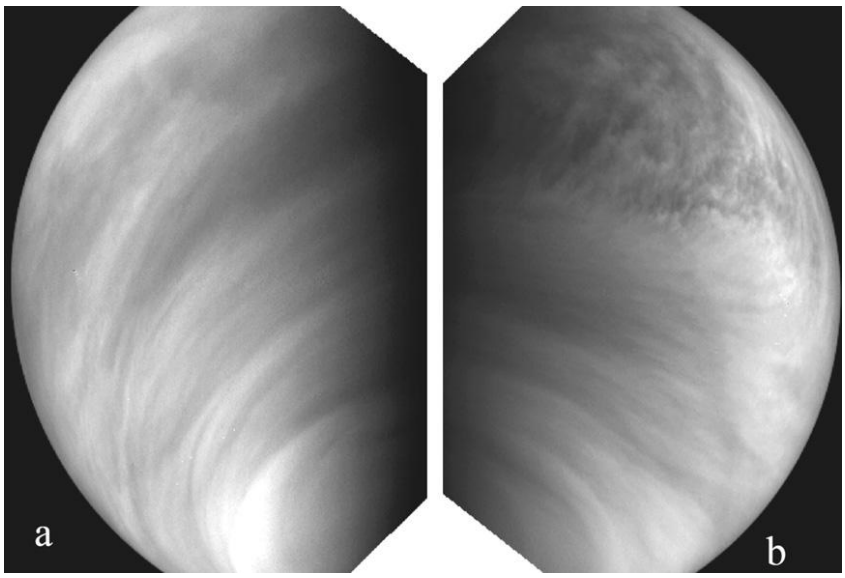

Figure 1.23. From Titov et al. (2012). Images taken by the VMC on Venus Express. The south pole is approximately in the white triangle between the images. The morning (a) and evening (b) terminators. The morning is characterised by streaky clouds, also visible in the southern part the evening terminator. The mottled, patchy patterns around the equatorial region of the evening terminator may indicate greater convection and turbulence.

The absence of darkest blacks from Figure 1.23 is not indicative of lower absorption than seen in the Pioneer Venus images but is instead due to differences in image processing.

1.4.2.4 Conclusions from 2D imaging

The 2D distribution of the unknown UV absorber is governed in large part by the dynamics of the atmosphere. Features are transported by the zonal wind and persist for long periods of time. While observations of the nightside of Venus were not possible, the recurrence of dark regions such as the Y feature, in contrast to brighter regions such as at the poles which showed no such periodicity, suggests a long-lived species responsible for the contrasts, with a lifetime on the order of weeks or months to produce the slow changes in the patterns. It is possible that the absorber could be a more short-lived species if it is readily produced from and destroyed to reform a reservoir species which obeys the long-term periodicity instead.

The trend for brighter poles and darker low latitude regions could have two possible causes: the absorber is not present in the polar regions, or it is present but is obscured by a bright (non-absorbing) hood of, presumably, sulphuric acid particles. The bright polar bands seem to coincide with the cold collars – regions at ± 60° where the cloud top is depressed. This and the dark bow-shaped wave features that occasionally cut through the bright polar features favour the latter interpretation: that the absorber is present below the clouds in the polar regions, but less visible unless brought up to the cloud tops by wave features.

While the 2D patterns do not help identify the absorbing species in the same way that an optical spectrum would, they inform the dynamics that must govern the species and so can play a key

role in strengthening an argument for a species to be considered or discounted based on its suitability or inability to reproduce the observed lifetime and distribution.

1.4.3 Location and properties of the absorber

Pollack et al. (1980), Ragent and Blamont (1980), and Knollenberg and Hunten (1980) proposed, in their studies of the contributions of SO_2 and the "second absorber", that the unknown UV absorber could be in the mode 1 particles. Ekonomov et al. (1984) agreed that a particulate absorber, such as mode 1 particles, would fit the upper cloud absorption best, but they also predicted gaseous absorption in the clouds below. Knollenberg and Hunten (1979a, 1980) proposed that the absorber exists in similar masses in mode 1 and 2 particles (as they believed that mode 1 and 2 grow from the same source in the upper clouds, differing only in that mode 2 particles have overcome the critical size imposed by the Kelvin effect).

Travis et al. (1979b) reported that, were the absorber located above the clouds, the resulting contrasts would be much more prominent than observed. Pollack et al. (1979) reported that the contrast between dark and light regions viewed in UV by the cloud photopolarimeter increased with decreasing phase angle (i.e., greater contrasts were apparent when viewed near 90° than ~120° (Travis et al., 1979b)). They also reported from polarisation measurements that at least 80% of particles at optical depth $\tau = 1$ were consistent with concentrated H_2SO_4. They therefore proposed that:

a. the absorber was not present above the clouds or in the top couple of optical depths of the cloud, and
b. the absorber concentration increased sharply in the top few optical depths of the cloud.

However, the absorber cannot be too deep within the clouds: the absorption can be observed from Earth, but ground-based observations probe only the top 4 – 6 optical depths of the ~10 that make up the upper cloud layer (Knollenberg & Hunten, 1979a). Pollack et al. (1980) therefore imposed a lower bound of ~63 km for the top of the absorber layer, locating it firmly within the upper clouds.

As the upper cloud layer is bimodal, Pollack et al. (1980) modelled two possibilities: the absorber is in mode 1, or the absorber is present as an impurity in both modes 1 and 2, which is also a valid model for a gaseous absorber. They assumed that the unknown absorber was not present in the top layers of their model ($\tau \sim 0.65$) and modelled different distributions of SO_2 and different refractive indices of the unknown absorber.

The models found a best fit to the results for an SO_2 mixing ratio near $\tau = 0.65$ of 1×10^{-7}, and an imaginary refractive index of the absorber of 7.5×10^{-3}. Pollack et al. (1980) used a wavelength-independent refractive index, though they reasoned that including wavelength dependence could further improve the fit. No significant differences between the two cases (absorber in mode 1 only or in both modes) were found. However, they did find that the unknown UV absorber would be

required to absorb at wavelengths longward of 500 nm in the upper clouds to explain the solar flux at 57 – 61 km, but the absorption in the visible should not continue into the middle and lower clouds.

To explain the observed contrasts, Pollack et al. (1980) predicted the contrast expected from the overlying haze detected by the Pioneer Venus polarimeter (Kawabata et al., 1980). They were able to match the observations fairly well with a polar haze (at latitudes poleward of 75°) of optical thickness $\tau = 0.9$ in bright regions, and the absorber sharply increasing in concentration below the cloud tops (Pollack et al., 1979) in the clouds below the haze. They reported that, while not producing perfect agreement, the model would be improved by further fine-tuning of the absorber height, or the use of haze data from a shorter period of time – the results they used were averaged over a year, while the haze may vary over a period of months (Kawabata et al., 1980). Luginin et al. (2016) also found haze variations on the order of months, suggesting that temporal variation did affect Pollack et al. (1980)'s model.

As an alternate method of reducing the absorption to reproduce the bright polar regions, Pollack et al. (1980) modelled the effects of reducing the absorber concentration with depth, but found that it was unable to produce a good fit to the observations. However, at lower latitudes, the contrasts are less pronounced, and Kawabata et al. (1980) found no polarization anomalies, suggesting a uniformly optically thin haze. In these regions, Pollack et al. were able to match the observations reasonably well by increasing the optical depth at the top of the clouds from which the absorber is absent. They emphasised that the choice of exact optical depth the absorber was absent from would depend on the model used, but their values of $\tau = 0.65$ for the darkest regions and $\tau = 1.2$ for the low-latitude brighter regions are qualitatively applicable.

Pollack et al. (1980) proposed that the absorber is somehow destroyed at the top of the upper cloud, in order to explain its absence from the cloud tops. Conversely, Knollenberg and Hunten (1979a) reported that prior studies had interpreted a correlation between UV-dark regions and decreased CO_2 absorption as indicative of rising cloud tops in the darker regions, implying upward motion, and proposed that large, absorbing particles were brought up to higher altitudes on these updrafts. Crisp and Young (1978) explained the correlation between UV dark regions and decreased IR absorption due to CO_2 by reasoning that as the cloud rises, bringing UV-absorbing material up to heights where is it "more visible", the thickness of CO_2 above the cloud decreases, decreasing the IR absorption detected. Knollenberg and Hunten (1980) remarked that small particles (such as mode 1) could be carried as easily up to the cloud tops as larger particles.

Many attempts over the years have been made to locate the absorber within the clouds deck (e.g., Haus et al., 2016; Lee et al., 2021). All come to broadly the same conclusions: the absorber must be in the upper clouds, but not the upper haze. A variety of altitude distributions and modes can all explain the absorber. Models where the absorber is correlated with all cloud modes are

generally assumed to be consistent with models of gaseous absorption, so that also cannot be ruled out.

The identity of the UV absorber remains unknown. It is generally accepted to be particulate and at least part of mode 1 (Ekonomov et al., 1984; Gnedykh et al., 1987, via Titov et al., 2018; Tomasko et al., 1980a), though some gaseous candidates are also popular (Frandsen et al., 2016; Pinto et al., 2021). Proposed candidates for the unknown absorber include ferric chloride, elemental sulphur, and sulphur-containing compounds such as S_2O_2 or polysulphur oxides (S_nO), and microscopic life. Sulphur- and iron-containing candidates are detailed in Sections 1.5 and 1.6 respectively. Some evidence for the absorber's presence in the cloud droplets is detailed in Sections 1.4.3.1 and 1.4.3.2.

1.4.3.1 Cloud condensation nuclei

Knollenberg and Hunten (1980) proposed that part of mode 1 is composed of particles that act as cloud condensation nuclei (CCN) for mode 2 as a way to explain the correlation between the two modes. They theorised that the bimodality is produced by the activation of droplets of above critical size to become mode 2, while bare or only thinly-covered particles remain as mode 1. Both modes grow in size by the condensation of sulphuric acid and water from the gas phase. This is supported by reports that a fraction of mode 1 has a refractive index significantly higher than that of sulphuric acid (Gnedykh et al., 1987, via Titov et al., 2018; Toon et al., 1984).

In recent years, as optical techniques have improved, some measurements of the refractive index at the cloud top have found refractive indices in mode 2 that are too high for pure sulphuric acid, leading to proposals that the absorber is in the mode 2 cloud droplets as well as mode 1. The most straightforward explanation for this (though not the only one) is that the absorber is the component of mode 1 that acts as a CCN (Petrova, 2018; Petrova et al., 2015).

1.4.3.2 Glories

Observations near opposition (when the observer is located between the sun and Venus, resulting in very low phase angles) by Venus Express resulted in the observation of glory patterns in the UV, visible, and IR channels of the VMC (Markiewicz et al., 2014; Petrova et al., 2015). Example images and averaged intensity phase functions for the three wavelengths are shown in Figure 1.24.

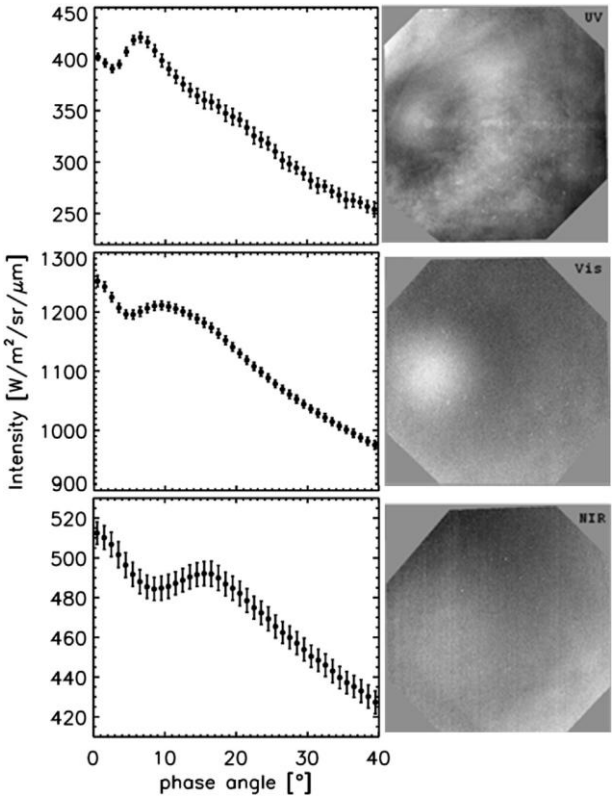

Figure 1.24. From Markiewicz et al. (2014). Left: Intensity phase functions of glory patterns at (top to bottom): 365 nm (UV), 513 nm (visible), and 965 nm (near-IR) and right: glory images at the corresponding wavelengths. The glory is most prominent in the UV image, but superimposed contrasts from the inhomogeneous NUV absorption introduce additional complexity.

Glories are an optical phenomenon in which light undergoes internal reflection in a spherical droplet, producing a series of concentric coloured rings (in white light) or dark and light fringes (at a particular wavelength) (Laven, 2005). Their observation and analysis allow for independent assessment of the size and refractive index of the droplets in the upper cloud layer (Markiewicz et al., 2014; Petrova et al., 2015).

Markiewicz et al. (2014) reported that the observed glory patterns at 965 nm (as absorption in the UV and visible wavelengths made retrieval of the shape of the glory difficult) were consistent with a narrow size distribution of cloud droplets with radius 1.2 μm and horizontal homogeneity of at least 1200 km. However, rather than the expected real refractive index for the cloud droplets of n = 1.44 (for 75 wt% sulphuric acid at cloud top temperatures), the shape of the phase function was consistent with a refractive index of n = 1.48, too high for pure sulphuric acid, even at different temperatures (Figure 1.25). Petrova et al. (2015) predicted spatial homogeneity of ~2000 km, with the radius and real refractive index varying, and found some indication of a dependence on latitude or local time: for example, at midday, poleward of 20°, glories could be fitted well with a real refractive index of 1.44 and a particle radius of 1.05 μm, whereas higher refractive indices were found predominantly (but not exclusively) in the equatorial regions in the

morning. Petrova et al. (2015) noted that, if the size distribution of particles were broad, the phase position of the glory features produced by each droplet size would not align, destroying the feature. While Petrova et al. found regions that could be explained by pure sulphuric acid droplets, they, like Markiewicz et al. (2014), also found glories where the real part of the refractive index n = 1.48 was required.

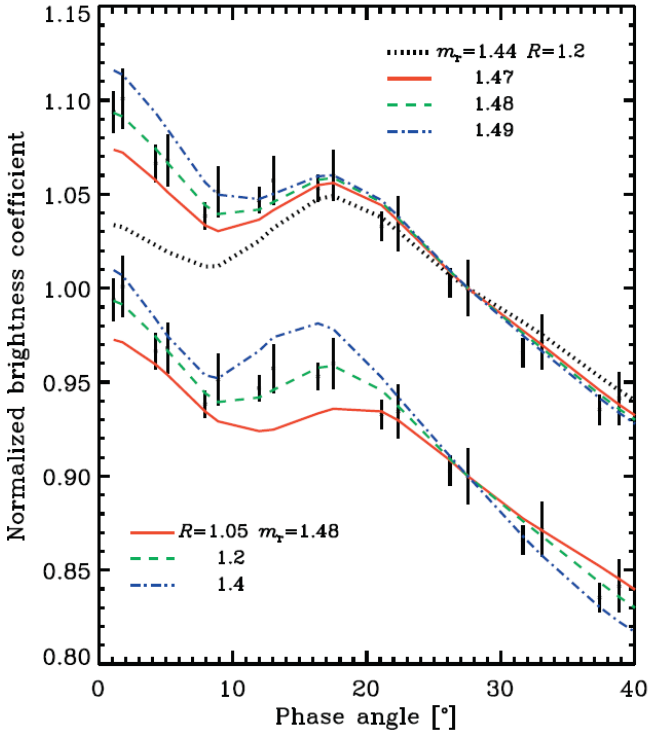

Figure 1.25. From Markiewicz et al. (2014). Intensity phase curve observations at 965 nm with predicted phase functions for (top curve) droplets of radius 1.2 μm with varied real refractive index, and (bottom curve) droplets with best fit refractive index 1.48 and varied radius. The two curves are offset vertically for clarity.

Markiewicz et al. (2014) and Petrova et al. (2015) suggested that an additional component in the droplets was required to increase the refractive index and proposed ferric chloride or sulphur, two particulate candidates for the unknown UV absorber with higher refractive indices than sulphuric acid. Petrova et al. (2015) reported them as >1.60 and 1.95 respectively. The uncertainty in the refractive index of ferric chloride, a birefringent and deliquescent mineral, is indicative of its poorly characterised optical properties.

Petrova (2018) modelled the addition of refractive and absorbing particles of approximately mode 1 size in the cloud droplets using T-matrix modelling (a method of calculating light scattering by non-spherical particles; Waterman, 1971). As can be seen in Figure 1.26, the addition of absorbing particles into a 1.4 μm droplet with n = 1.48 provides a much better match to the observed glory pattern. Petrova took sulphur and ferric chloride as examples, but the findings apply to any absorbing particulate species that behaves in a similar way.

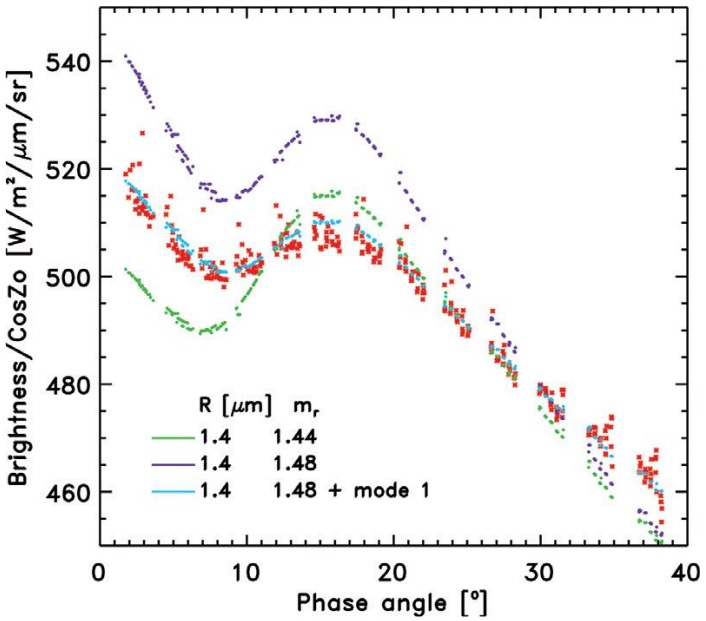

Figure 1.26. From Petrova (2018). For droplet radius 1.4 μm, the fit to observed data (red) is improved when the real refractive index is set to 1.48 and absorbing mode 1-size particles are included in the droplets.

Young (1983) demonstrated that sulphur cannot form a core within a sulphuric acid droplet but will instead stick to the outside of the droplet. This behaviour is so pronounced that almost fully sulphur-coated sulphuric acid droplets cannot become spherical when coalescing, instead forming a dumbbell shape to maintain sufficient surface area for the sulphur. Conversely, ferric chloride can enter into the bulk of a sulphuric acid droplet (Zasova et al., 1981). Petrova (2018) therefore modelled two main cases: mode 1 particles within the droplets, and mode 1 particles stuck to the surface of the droplets. She reported that the inclusions of ferric chloride provided the correct glory shape in intensity, whereas for adhered particles, the glory shape was destroyed if too many particles were adhered to the surface, and the wrong shape if fewer were adhered. This therefore rules out sulphur and any other particulates that cannot be wetted by sulphuric acid from being the cause of the observed glory patterns. Conversely, ferric chloride or other similarly-behaved particulates are capable of producing the observed effect.

However, while the intensity phase functions are well explained by the inclusion of refractive, absorbing particles in the cloud droplets, Petrova (2018) reported that the polarisation phase function was only consistent with homogeneous droplets, and the phase behaviour was destroyed by the inclusion or adhesion of particles to the droplet. Petrova argued that, as polarimetry probes a much thinner layer at the cloud tops than the intensity does, these observations could be explained by having a layer of pure cloud droplets at the top of the cloud and a layer below of cloud droplets with inclusions. Multiple scattering by the cloud layer above that where the intensity phase function is formed would decrease the brightness and smooth the glory somewhat but would not change the shape and ratio of the central (phase angle = 0°) and glory (the local maximum at ~10 – 20° in Figures 1.24 – 1.26) maxima. The overall shape of the glory would still

survive unchanged. This is similar to Pollack et al. (1980)'s requirement that the unknown UV absorber exist within the upper cloud, but be absent from some depth at the cloud top, supporting proposals that the inclusions in the sulphuric acid cloud droplets responsible for the glory shape are the unknown absorber. Alternatively, the requirements for both a higher refractive index and some absorption, and a homogeneous droplet could be achieved by additives to the droplets that dissolve into the droplet, producing a slightly absorbing liquid.

1.4.4 Candidates for the cause of the absorption

In addition to the measured spectral shape, which any unknown absorber candidates should match well, observations of the 2D distribution and variability can inform criteria the candidates need to meet.

The absorber is likely part of mode 1, and potentially within mode 2 as well in the upper clouds. This is explained neatly if the absorber is a suitable CCN that is wetted by sulphuric acid. A gaseous absorber is not ruled out, but an additional particulate species would be required to explain the mode 1 and 2 refractive index anomalies without interfering with the UV absorption in that case. The absorber exists within but not at the very top of the upper clouds, in order to reproduce the observed angular dependence in the strength of absorption.

The absorbing species should have either a long chemical lifetime within the clouds or be formed from and destroyed to reform a reservoir species with generally constant concentration and a long lifetime, in order to produce the observed periodicity of the large 2D dark regions in the cloud tops. The correlation between the unknown absorber and observed absorption at 283 nm (the wavelength of maximum SO_2 absorption) indicates that the absorber should either be correlated to SO_2 concentration or should absorb at 283 nm more strongly than at 365 nm.

Two broad categories exist that most absorber candidates in the literature fall into. Many are sulphur-based, due to the extensive sulphur cycle that exists on Venus (Section 1.5.2) and the high known concentrations of sulphur parent species that absorber candidates, such as polysulphur, polysulphur oxides, and S_2O_2, can form from (e.g., Francés-Monerris et al., 2022; Frandsen et al., 2016; Pinto et al., 2021). Iron-containing compounds were proposed originally because, as a transition metal, it was one of the few metals able to readily produce coloured compounds (Kuiper, 1969). The injection of iron from meteoric ablation (Frankland et al., 2017; Knollenberg & Hunten, 1980) provides a ready source of iron, as could the surface rocks (Krasnopolsky, 2017).

Limaye et al. (2018) proposed the possibility of the UV absorption being caused by microbial life in the clouds of Venus. They argued that the lower cloud could be a suitable location for microbes due to the temperature and pressure being similar to the Earth's surface, and compared the UV absorption to that of various terrestrial microbes, arguing for their suitability as candidates for the absorber. However, the spectra they provided for biomolecules and bacteria bear far less resemblance to the unknown UV absorber spectrum than any of the other candidate, and the

unknown absorber is known to be located in the upper clouds (Pollack et al., 1980), not the lower clouds as Limaye et al. (2018) argue would be suitable. No further consideration will be given to microbes or biological molecules as an absorption candidate.

1.5 Sulphur

1.5.1 Sulphur candidates

1.5.1.1 OSSO

As can be seen in Figure 1.19, a comparison of several absorber candidates to the Venusian absorption spectrum, OSSO has an absorption spectrum that most closely matches that of the unknown UV absorber deduced by Pérez-Hoyos et al. (2018). The "OSSO" spectrum appears to be produced by taking the maximum values at a given wavelength of the predicted absorption spectra of two of molecules: *cis*-OSSO, which has an absorption maximum centred at 316 nm, and *trans*-OSSO, with absorption centred at 364 nm (Frandsen et al., 2016). Formed from two SO monomers in a three body recombination reaction, six isomers of S_2O_2 were reported to be formed, but Frandsen et al. (2016) reported that only three should form in non-negligible quantities: *cis*-OSSO, *trans*-OSSO, and cyclic-S_2O_2, which Frandsen et al. labelled C_1-S_2O_2. Energy level predictions by Hochlaf et al. (2021) agreed with the energies reported by Frandsen et al. (2016). The *cis*-, *trans*-, and cyclic forms were reported to have been observed experimentally by Wu et al. (2018) in a matrix isolation study, and confirmed as the primary products of the recombination. A fourth form, trigonal-S_2O_2, is the lowest energy isomer and so had previously been generally assumed to be the dominant form of S_2O_2 on Venus (Krasnopolsky, 2012). However, it is only formed from cyclic-S_2O_2, which is itself formed from *trans*-OSSO (which is formed either from *cis*-OSSO or directly from two SO monomers). The formation of both cyclic-S_2O_2 and trigonal-S_2O_2 have prohibitively high transition state energies and so the cyclic form is expected to be no more than 1 – 2 % of the Venusian S_2O_2 (Frandsen et al., 2016). *Cis*- and *trans*-OSSO were reported to make up the majority of the S_2O_2 (with an approximately 7:3 ratio of *cis*-OSSO to *trans*-OSSO) (Frandsen et al., 2016).

However, despite its promising agreement with Pérez-Hoyos et al. (2018)'s UV absorber spectrum, OSSO is not proven to be the unknown absorber. The absorption exhibited by OSSO occurs when the molecule photodissociates, producing a very short lifetime (on the order of seconds) of OSSO in sunlight (Frandsen et al., 2016). As the UV contrasts are observed to persist for at least a full rotation of the atmosphere (~4 – 5 days) (Boyer, 1973; Rossow et al., 1980; Travis et al., 1979b), the lifetime of OSSO seems too short to reproduce these effects. 1D photochemical modelling by Pinto et al. (2021) and Krasnopolsky (2018) assumed a 7:3 formation ratio of *cis*- and *trans*-OSSO, rather than a resulting concentration after photolysis as reported by Frandsen et al., but reproduced broadly the same findings, with only differences in the relative concentrations of the different isomers. However, the highest OSSO abundance predicted by photochemical models occurs above the clouds (>75 km) (Krasnopolsky, 2018), whereas the

unknown UV absorber must be located in the upper clouds (Pollack et al., 1980). The predicted abundances of OSSO on Venus are “two orders of magnitude too low” to account for the observed absorption (Pinto et al., 2021), suggesting that, while some contribution to the absorption may be due to OSSO, it cannot be the (or even a) main absorber.

1.5.1.2 S_nO

While the abundance of OSSO may be too low to account for the observed UV absorption, Pinto et al. (2021) proposed that it is instead a key intermediate product in the production of polysulphur oxides, S_nO, where n = 2 – 4 in their photochemical models. They proposed that S_nO could be the unknown absorber. Hapke and Graham (1989) reported that S_2O forms at low temperatures from SO_2. If warmed above (or produced above) 115 K, it partially decomposes and forms polysulphur oxides (S_nO, n>2) and SO_2.

A reported absorption spectrum of S_2O is shown in Figure 1.19. Hapke and Graham (1989) reported reflectance spectra of S_2O and polysulphur oxide and the absorbance spectrum of polysulphur oxide (Figure 1.27), though they found that the thin film deposited for absorption measurements was non-uniform and so no numerical values or units were given. Curiously, there is no indication in the absorbance spectrum of the polysulphur oxide of the plateau seen in the reflectance at 200 – 400 nm.

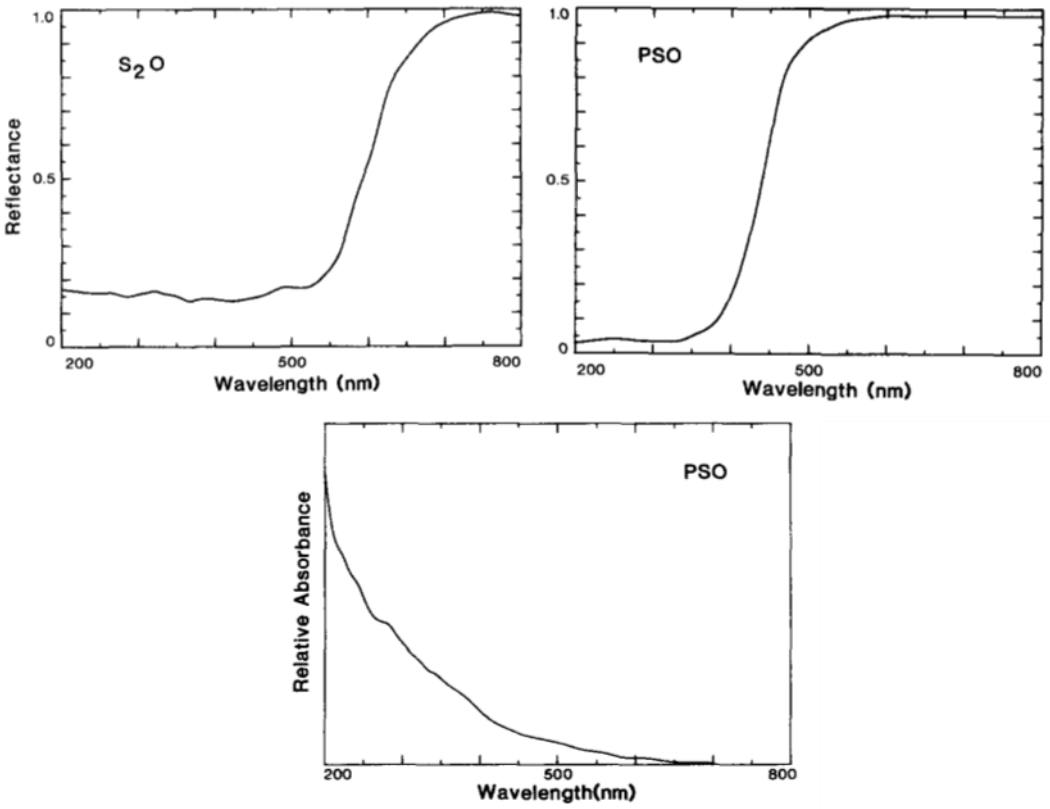

Figure 1.27. From Hapke and Graham (1989). Top left: Reflectance of S_2O at 77 K. Top right: Reflectance of polysulphur oxide (PSO) at 195 K. Reflectance spectra at 400 – 600 nm were also provided at 77 K and 295 K with only minor changes in shape. Bottom: Absorbance of polysulphur oxide thin film at room temperature.

Frandsen et al. (2016) reported that the abundances of S_2O on Venus are too low to provide the required UV absorption. Pinto et al. (2021) appeared to agree, reporting that the gas phase abundances of S_nO are too low to account for all of the observed UV absorption. However, they argued that a combination of condensed and gas-phase elemental polysulphur and S_nO, and potentially an additional absorber such as ferric chloride, could provide the full absorption.

1.5.1.3 S_n

While Pollack et al. (1979) found that elemental sulphur was unable to match the absorption spectrum of the unknown UV absorber at the low temperature in the cloud tops, other works continued to argue for its inclusion among candidates. Steudel et al. (1986) reported that the irradiation of S_8 by UV light caused a colour change from white to yellow that could be responsible for the colouration of Jupiter's moon Io. They speculated that the irradiation produced new absorption bands in the sulphur spectrum. Hapke and Graham (1989) took spectra of these irradiated forms of elemental sulphur formed at 77 K (liquid nitrogen temperature) and found that the absorption peak in the un-irradiated sulphur simply became broader when UV-irradiated, but a small new absorption band did appear when X-ray irradiation occurred. Their reflectance spectra are shown in Figure 1.28. A temperature of 77 K is far lower than the atmospheric temperature in the Venusian clouds, or even the atmosphere more generally (Figure 1.6). Hapke and Graham (1989) reported that when allowed to warm up, the UV-irradiated sample (pale yellow) and the X-ray-irradiated sample (orange-pink) both became white, like the un-irradiated sample, "well below room temperature". They do not give an exact temperature for this change, but Steudel et al. (1986) reported that the yellow colour was lost "near 260 K" when slowly warmed. If the temperatures measured by Steudel et al. and Hapke and Graham are the same, the colour could persist in the upper clouds. However, if the colour loss observed by Hapke and Graham was at a lower temperature, that would preclude the possibility S_8 as a UV absorber on Venus.

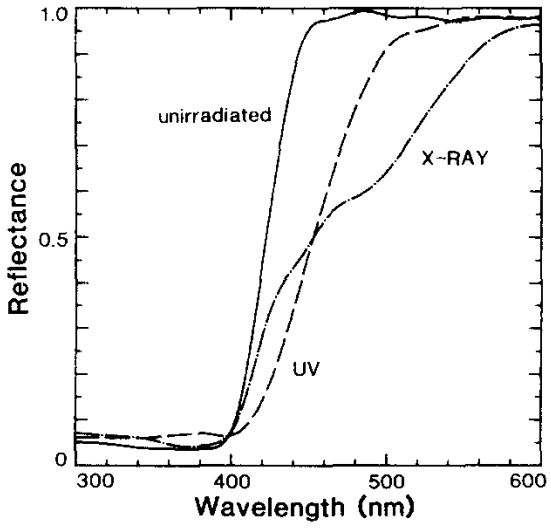

Figure 1.28. From Hapke and Graham (1989). The reflectance spectra of unirradiated, UV-irradiated (by exposure to a Hg-Xe lamp for 30 minutes), and X-ray irradiated (by exposure to a commercial x-ray tube for 2 minutes) flowers of sulphur at 77 K.

Pinto et al. (2021) predicted the formation of elemental sulphur, S_n (n = 1 – 7), in their photochemical model and suggest it, along with polysulphur oxides (and/or ferric chloride) could explain the UV absorption. Francés-Monerris et al. (2022) modelled polysulphur formation (modelling only n = 2 – 4, but taking this as a proxy for total particulate sulphur) from the reaction of S_2O and SO. The absorption spectra of polysulphur (n = 2 – 8) compounds with different molecular structures were investigated by Skog et al. (2024). Two molecules, a bent chain isomer of S_3 and the trigonal isomer of S_4 were reported to have some similarity to the Venusian absorber. Laboratory spectra of these species have not been reported.

1.5.2 Sulphur chemistry

The current understanding of the sulphur chemistry on Venus is summarised in Figure 1.29. Reactions are taken from the Venus PCM, described in Chapter 2. Sulphur chemistry and specifically the formation and loss of S_2O_2 is detailed in Chapter 3.

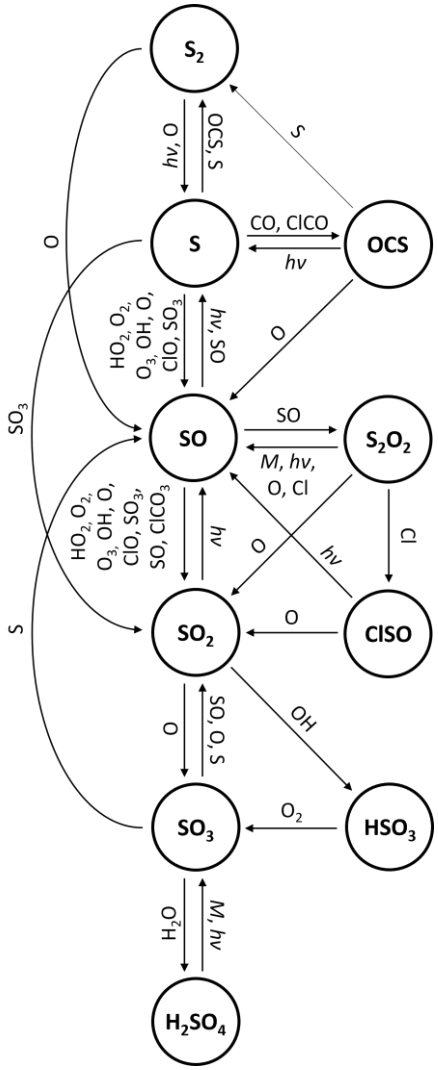

Figure 1.29. An overview of the sulphur chemistry in the Venusian atmosphere. Reactions are from the Venus PCM (Chapters 2 and 3). S_2O_2 is a combination of *cis*- and *trans*-OSSO, and cyclic-S_2O_2. Collision partners are indicated on arrows. *hv* indicates photolysis, *M* indicates thermal decomposition after collision with a third body, usually CO_2.

1.5.3 Open questions

Observations of SO_2 above and below the cloud deck differ by three to four orders of magnitude (Figure 1.30). A sharp decrease is seen at the base of the cloud deck and an increase at the cloud tops (Bertaux et al., 1996; Mahieux et al., 2023a; Sandor et al., 2010). The observed profile currently cannot be explained by known Venusian sulphur chemistry, and it is clear that a significant sulphur reservoir in the cloud layer is missing from photochemical modelling of Venus (Bierson & Zhang, 2020; Rimmer et al., 2021; Vandaele et al., 2017; Yung & DeMore, 1982). Sulphur-containing candidates for the unknown UV absorber are often also candidates for the sulphur reservoir (Frandsen et al., 2016; Zhang et al., 2012).

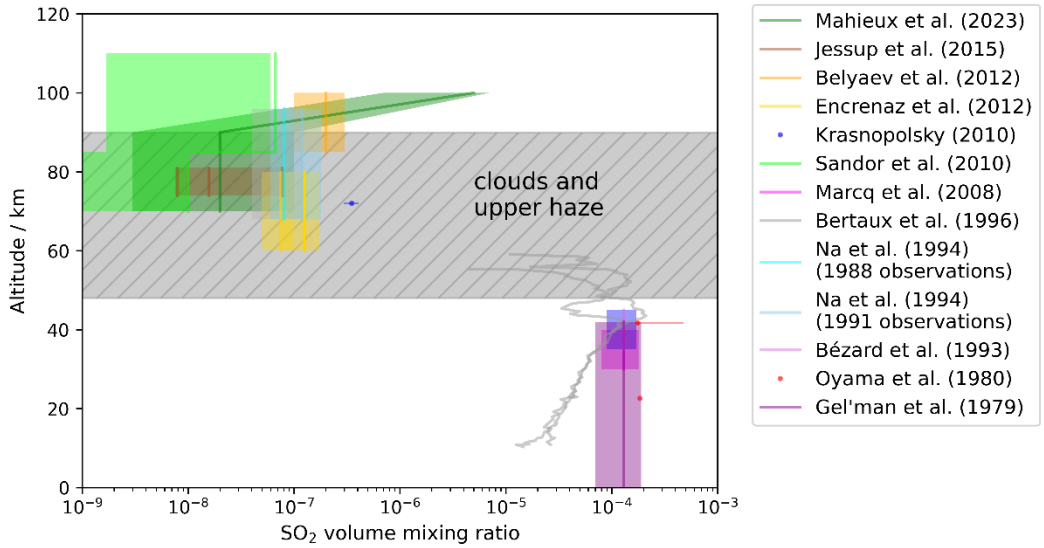

Figure 1.30. SO_2 observations above and below the cloud deck. A decrease of 3 – 4 orders of magnitude is seen between observations above and below the cloud base.

An alternative solution was proposed by Rimmer et al. (2021), who posited that the inclusion of hydroxide salts or hydrocarbons within the sulphuric acid clouds would buffer the acid concentration and increase SO_2 uptake into the droplets. However, they did not identify a source of the buffering materials, and calculated a continuous required flux of 6×10^{10} molecules cm^{-2} s^{-1}, four orders of magnitude higher than meteoric injection could provide, even assuming all injected material could provide the required cloud buffering.

They proposed that, alternatively, the decrease could be explained if the below-cloud observations of SO_2 and/or H_2O are incorrect. By decreasing below-cloud SO_2 below observed levels, or increasing H_2O above observed levels (as H_2O reacts with SO_2 to produce H_2SO_4, but the observed below-cloud ratio is insufficient to remove the observed concentration of SO_2 by this reaction), Rimmer et al. (2021) could reproduce the decrease through the cloud deck in their 1D model, but not the subsequent increase above 80 km reported by Sandor et al. (2010) and Mahieux et al. (2023a).

1.6 Iron

1.6.1 Iron candidates

1.6.1.1 Iron chloride

Before the Venusian cloud structure was measured directly, Kuiper (1969) proposed a list of transition metal compounds that could potentially cause the absorption. At the time, the prevailing model was of a yellow, UV absorbing layer with a patchy, UV-bright layer responsible for the observed UV patterns over the top. Kuiper presented a series of reflectance spectra for the candidates for the "yellow haze layer" and reported best agreement for a bright NH_4Cl haze over yellow "partially hydrated" ferrous chloride clouds.

Once more was known about the Venusian cloud structure and the UV bright clouds known to be sulphuric acid, Zasova et al. (1981) reported that a mixture of 1% ferric chloride in 75% sulphuric acid produced an absorption coefficient consistent with Venus. However, they (and Kuiper, 1969) did not report absorption spectra. Kuiper reported reflectance spectra (Figure 1.31), while Zasova et al. reported only their modelled albedo for the cloud model (Figure 1.32).

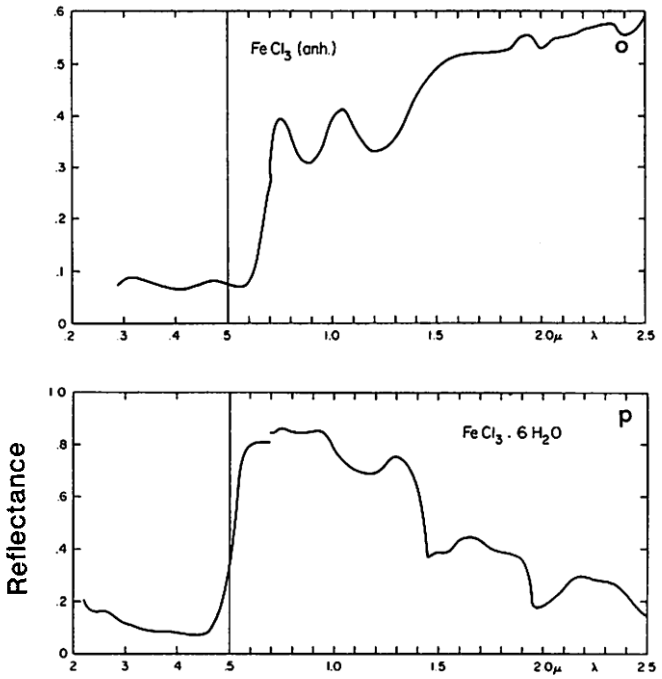

Figure 1.31. From Kuiper (1969). Reflectance spectra of anhydrous (top) and hydrated (bottom) ferric chloride.

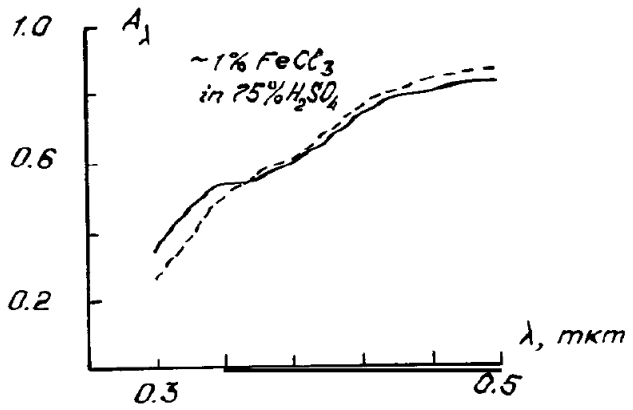

Figure 1.32. From Zasova et al. (1981). Predicted albedo of $FeCl_3$ in sulphuric acid cloud droplets (dashed line) compared to the observed Venusian albedo (solid line). "mkm" in the x-axis label means "μm".

Expanding on Zasova et al. (1981)'s proposal, Krasnopolsky (2017) proposed that a volume mixing ratio (vmr) of 19 ppb of ferric chloride in the Venusian surface rocks would be sufficient to explain the absorption. He proposed that the ferric chloride would evaporate from the rocks due to the high surface temperature and recondense higher in the atmosphere. Their solubility in sulphuric acid would make them suitable CCN, and the inclusion of a ferric chloride particle of 0.2 μm radius in a 1 μm radius sulphuric acid cloud droplet (the approximate radii of modes 1 and 2, respectively, in the upper clouds) would result in a solution of ~1.3 wt%, as predicted by Zasova et al. (1981)

However, as can be seen from Figure 1.19, the absorption spectrum of ferric chloride in use in the literature is too narrow to account for the full Venusian UV absorption (Pérez-Hoyos et al., 2018). While this might be expected to rule out ferric chloride as the absorber (unless mixtures are considered), the optical properties of ferric chloride are poorly understood. It is a "highly deliquescent birefringent crystalline material" (Petrova et al., 2015), and as such its refractive indices are poorly characterised and highly dependent on its environment. The spectrum used by Pérez-Hoyos et al. (2018) was measured in an ethyl acetate solvent (Aoshima et al., 2013) due to the scarcity of available spectra in the literature. Reported spectra of $FeCl_3$ in hypersaline (HCl/LiCl) solutions produce very different spectra (Liu et al., 2006). The choice of solvent is clearly of vital importance when measuring $FeCl_3$ absorbance, so the spectrum measured in ethyl acetate may not be at all representative of $FeCl_3$ absorbance on Venus.

1.6.1.2 Meteoric smoke particles

A compound that is periodically mentioned in the literature as a potential absorber is meteoric material (e.g., Knollenberg & Hunten, 1979a; Pollack et al., 1979). Frankland et al. (2017) proposed that meteoric smoke particles (MSPs), formed by recondensation of the metallic vapours produced by the ablation of cosmic dust above 100 km and likely to have olivine-like composition (i.e., $FeMgSiO_4$), would adsorb into sulphuric acid cloud droplets and catalyse the formation of

CO_2 from CO and O_2. Without such a reaction, the photolysis of CO_2 would result in significantly higher abundances of CO and O_2 than are observed in the lower Venusian atmosphere.

Saunders et al. (2012) measured the dissolution of iron from surrogate MSP particles in sulphuric acid solutions and found that UV absorption occurs, increasing with time as iron sulphate ion complexes form (Figure 1.33). While they identified the spectra as containing contributions from Fe^{3+} and $Fe(SO_4)_2^-$ alone (with no contribution from the undissolved MSP analogues, and insufficient absorption beyond 300 nm to match the unknown absorber), the influx of iron from meteoric sources to produce UV absorption in at least part of the range of the unknown absorber should not be discounted. At the very least, the tail of the sulphate absorption at >300 nm should be accounted for in calculations of the spectrum of the unknown absorber.

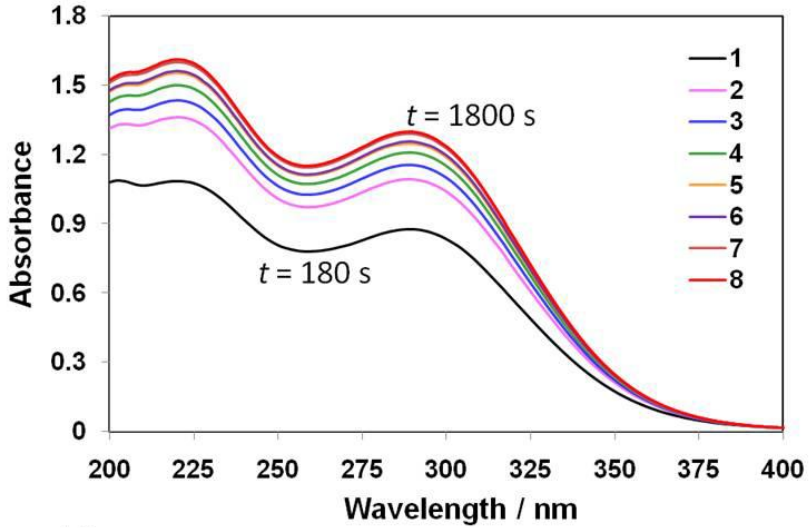

Figure 1.33. From Saunders et al. (2012). UV absorbance spectrum of MSP analogues in sulphuric acid with time after the addition of the particles.

1.6.1.3 Rhomboclase and acid ferric sulphate

Jiang et al. (2024) reported that a combination of two iron-sulphur mineral phases, rhomboclase, $(H_5O_2)Fe(SO_4)_2 \cdot 3H_2O$, and acid ferric sulphate, $(H_3O)Fe(SO_4)_2$, could explain the UV absorption (Figure 1.34). They argued that the clouds may contain regions of more dilute sulphuric acid (<50 wt%) and high water concentration (mixing ratio > 10^{-3}), though these suggestions are not supported by observations. They reported concentrations of 1 – 2 % iron within the clouds in these two phases would be sufficient to explain the absorption.

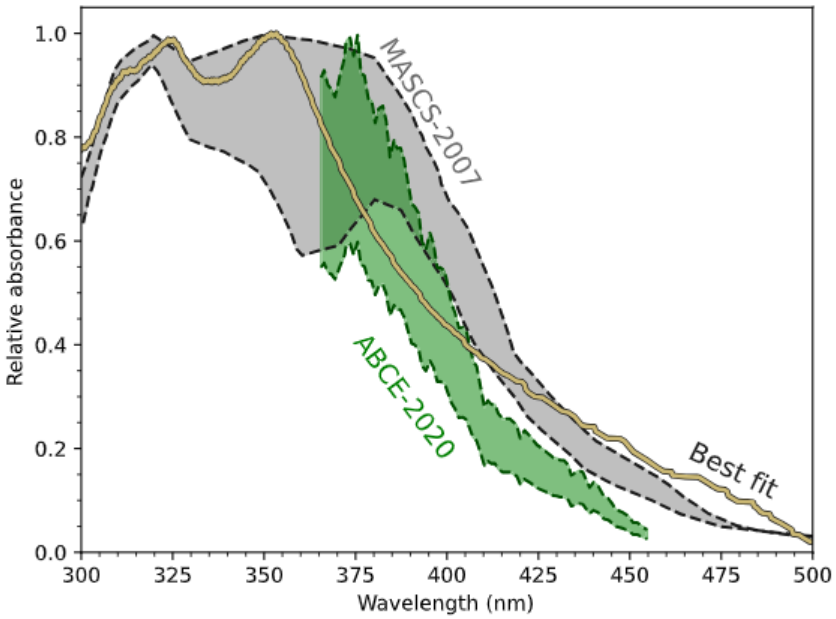

Figure 1.34. From Jiang et al. (2024). The combination of acid ferric sulphate and rhomboclase to produce the best fit (gold) to the measured spectrum of the unknown UV absorber (MASCS-2007: Pérez-Hoyos et al. (2018), ABCE-2020: Lee et al. (2022)).

1.6.2 Observations

Petryanov et al. (1981)[2] reported that Venera 14 detected iron in the atmosphere during its descent. The ratio of iron and chlorine were compared, and best agreement found for ferric chloride. Krasnopolsky (1989) reported that the Vega descenders detected iron mass loading consistent with 1% of the cloud aerosol being ferric chloride. However, only a single average value of iron mass loading was reported from the lower clouds, so this may not be valid for the full cloud layer.

1.6.3 Meteoric injection

The terrestrial planets receive cosmic dust from a variety of sources, including Jupiter Family Comets, the asteroid belt, and Long Period Comets (Carrillo-Sánchez et al., 2020). This material enters the atmosphere at hyperthermal speeds and a significant fraction ablates, producing MSPs. Spherules formed of incompletely ablated meteoric particles are found in polar ice cores on Earth (Brooke et al., 2017). Meteoric ablation introduces fluxes of Mg, Fe, Si, Na, S, Ca, K, and other elements, which form observable atmospheric layers of atoms and ions (Carrillo-Sánchez et al., 2020; Gómez Martín et al., 2017; Plane, 2003). These layers have been observed on Earth (Plane et al., 2015), and Mars (Crismani et al., 2017; Grebowsky et al., 2017; Plane et al., 2018). No direct observations of meteoric metal layers have been reported on Venus, though apparent layers of high electron density have been observed by the VeRa instrument on Venus Express (Pätzold et al., 2009). Similar layers observed on Mars could not be explained by ablation of meteoric metals (which have been directly observed), so these observations are not taken to be reliable measures of meteoric injection at Venus (Crismani et al., 2019). Instead, meteoric input was

[2] Only available in Russian.

estimated with a combined solar system dust model and chemical ablation model, which predicted a total input of 31.0 ± 15.5 t d^{-1} to the Venusian atmosphere (Carrillo-Sánchez et al., 2020). Iron is predicted to ablate above 95 km (maximum at ~115 km) and provide a flux of 4.09 t d^{-1}.

Meteoric sulphur injection is less well measured, but can be calculated by scaling the predicted sodium injection profiles (100 – 130 km, 0.37 t d^{-1}) by a factor of 8.8 to correct for the relative S to Na mass ratio in the source comets and asteroids, with both elements assumed to ablate with similar efficiencies (Carrillo-Sánchez et al., 2020; Gómez Martín et al., 2017).

1.7 Conclusions

Despite its apparent similarity to Earth in size and position within the solar system, Venus is a very different planet, and many assumptions that could be made based on the Earth do not hold. It has a very different atmospheric structure, lacking a stratosphere, and has permanent and total cloud cover across the whole planet. It has a strong greenhouse effect, and little observed diurnal variation in temperature and pressure below the thermosphere despite its slow rotation and long solar days.

Venus's position as Earth's closest and most accessible planetary neighbour led to many early space missions to Venus. However, after an initial golden age of exploration in the 1970s and 80s, only two dedicated Venus missions have been undertaken since (with an additional five spacecraft making observations during gravity assist manoeuvres en-route to their primary bodies of interest). As a result, many of the models of Venus are based on brief sets of observations in the 1980s and have not been updated since. Following JAXA's announcement that they had lost contact with their Akatsuki orbiter in early 2024, there are currently no spacecraft active at Venus.

There are therefore several key parts of Venus that are not well understood, in particular the sulphur chemistry in the lower and middle atmosphere, and the cause of the pronounced inhomogeneous absorption measured in ultraviolet light. The primary aim of this thesis is to contribute to solving the mystery of this absorption.

In this thesis, two candidates for the absorber are considered: OSSO and $FeCl_3$. Both are investigated using a combination of 3D photochemical and dynamical modelling and 1D radiative transfer modelling to investigate the concentrations of the two that can be produced within the atmosphere from predicted chemical processes and the meteoric injection of iron and sulphur. The models used are described in detail in Chapter 2. The results of the sulphur and iron modelling are presented in Chapters 3 and 5 respectively.

As there are no published measurements of the absorption spectrum of $FeCl_3$ in sulphuric acid, laboratory experiments were undertaken to measure the absorption spectrum and estimate its lifetime in the Venusian cloud droplets. These experiments and results are presented in Chapter 4. The results of the lab work were used in the radiative transfer modelling of $FeCl_3$, presented in Chapter 5. The work is summarised and potential future work on the topic outlined in Chapter 6.

2. Overview and validation of models

In this chapter, the three main computer models used in this project are outlined. The IPSL Venus PCM calculates the 3D dynamics, cloud microphysics, and photochemistry. The basics of the model are outlined in Section 2.1 and compared to observations. Radiative transfer modelling is performed using SOCRATES (Suite Of Community Radiative Transfer codes based on Edwards and Slingo), the multiple scattering radiative transfer module developed by the UK Met Office for Earth modelling. An outline of the basic code is provided here, along with details of the alterations made for its application to Venus (Section 2.2). A brief outline is also provided of a 1D coagulation and sedimentation model, which is used to extrapolate model results to longer times than is computationally feasible with the PCM (Section 2.3).

The PCM is used to model the effects of new chemistry detailed in Chapters 3 and Chapter 5. The temperature, pressure, and species mixing ratios from the PCM are used in SOCRATES to predict flux through the atmosphere and estimate the effect of the inclusion of absorber candidates on the TOA reflectance.

2.1 Venus PCM

2.1.1 Version number and grid size

3D modelling is performed using the Venus PCM (e.g., Gilli et al., 2021; Lebonnois et al., 2010; Lebonnois et al., 2016; Martinez et al., 2024; Martinez et al., 2023; Stolzenbach et al., 2023), version r3188. The horizontal grid is divided into 96 latitude and 96 longitude bands (horizontal grid size of 1.875° × 3.75°). The PCM has been described in many previous works (e.g., Garate-Lopez & Lebonnois, 2018; Martinez et al., 2024; Martinez et al., 2023; Stolzenbach et al., 2023). It couples dynamics, photochemistry, and a microphysical cloud model and reproduces the broad features observed on Venus, such as the existence of the cold collar (Section 2.1.2.1), comparable cloud density to observations (Section 2.1.2.2), and atmospheric super-rotation and winds (Section 2.1.2.3).

2.1.2 Released PCM overview and validation

2.1.2.1 Temperature

Figure 2.1 shows a comparison of the zonal mean temperature produced by the PCM (coloured contours) with zonal and temporal mean radio occultation measurements from Venus Express and Akatsuki (grey contours) (Ando et al., 2020). At low latitudes, the model produces slightly warmer temperatures than observations (see, for example, near the equator around 70 km, observations report a temperature of 230 K, while the PCM produces 235 K in this region). The isolines from Ando et al. (2020) have a vertical separation of less than a single PCM gridbox (~ 2 – 3 km), making some discrepancy unavoidable. The discrepancy decreases lower in the atmosphere and the PCM slightly underestimates the temperature at the cloud base and below near the equator.

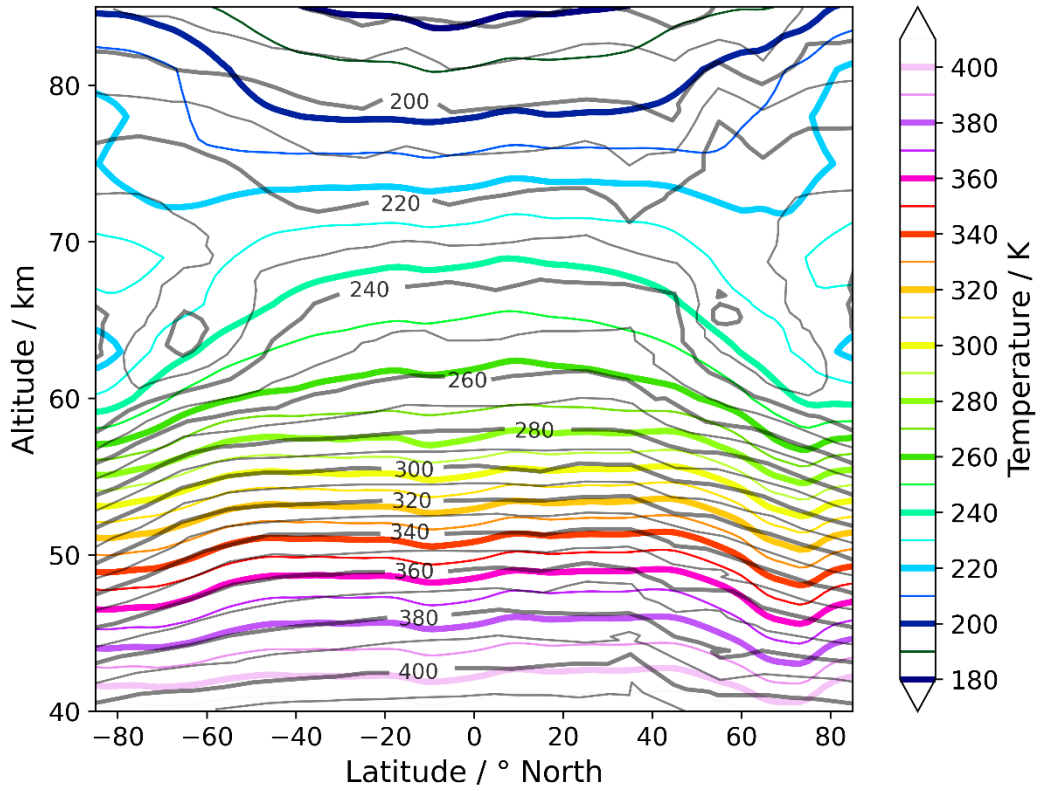

Figure 2.1. Zonal average PCM temperatures (coloured contours) compared to temporal and zonal average of radio occultation measurements from Venus Express and Akatsuki (grey contours) (Ando et al., 2020). Alternating contours are shown with thicker lines to aid comparison between the two datasets.

Stolzenbach et al. (2023) also noted this temperature discrepancy in their validation and highlighted that the lower temperature results in a smaller scale height for the atmosphere. The pressure therefore decreases more rapidly with increasing altitude in the PCM than observed, producing lower number atmospheric number densities at the same altitudes when compared to the Venus International Reference Atmosphere (VIRA).

The most significant difference seen between observations and the model is with regard to latitude: the PCM produces features located approximately 20° higher in latitude in both hemispheres than seen in observations. This is most noticeable in Figure 2.1 for the cold collar – the low temperature region near 65 km at ± 60° in the observations, occurs at ~62 km and ± 80° in the PCM.

Figure 2.2 shows a comparison of the zonal mean PCM temperature in latitude bands (northern and southern hemispheres are combined) compared to instantaneous profiles from the Pioneer Venus descent probes (Seiff et al., 1979), average profiles recorded by the SOIR (Solar Occultation in Infra-Red) instrument on Venus Express (Mahieux et al., 2023b), and average profiles from radio occultation measurements from the Pioneer Venus, Akatsuki, and Magellan orbiters and VIRA and VIRA 2 compilations (Ando et al., 2020).

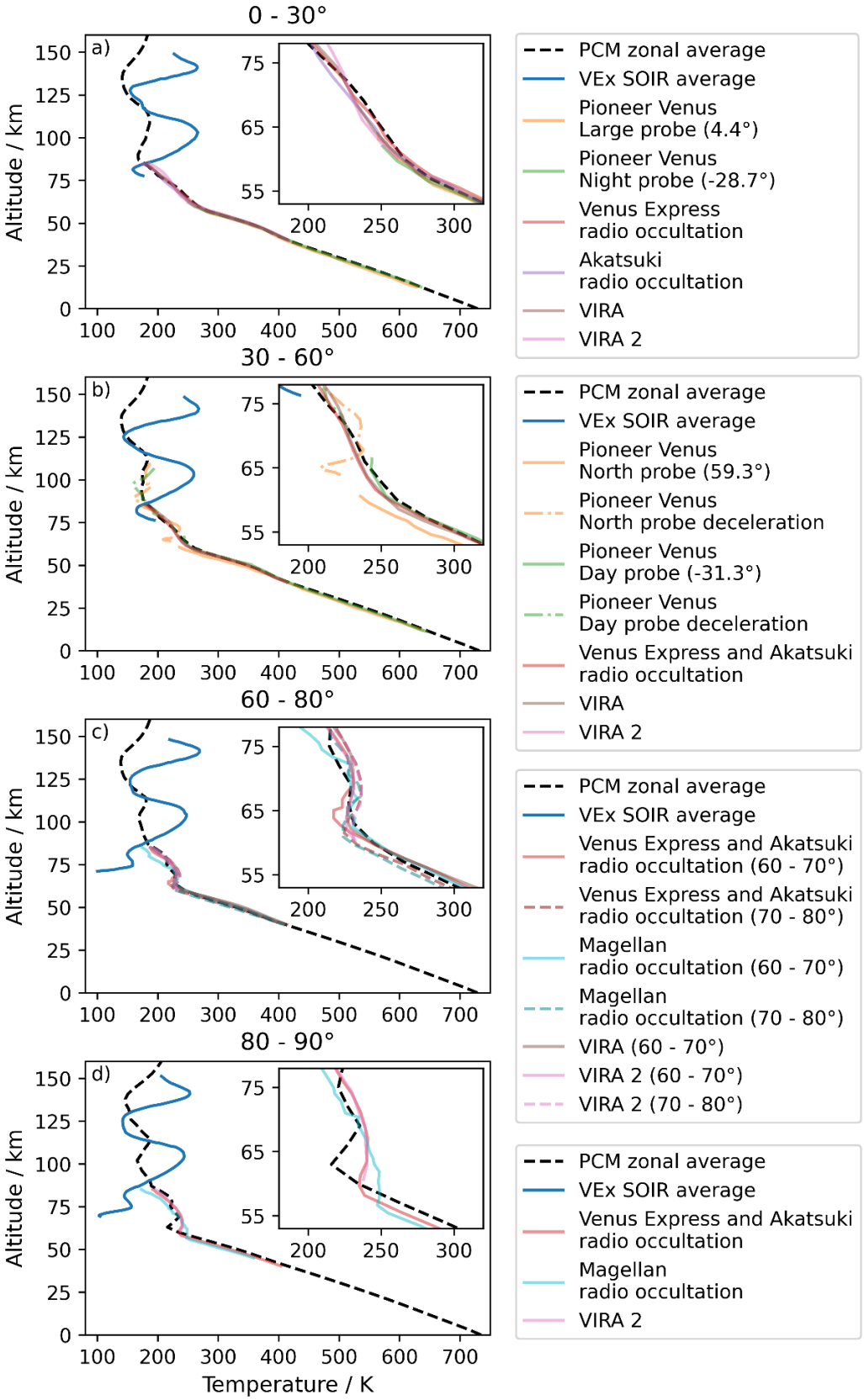

Figure 2.2. Zonal average PCM temperature at a) 0 – 30°, b) 30 – 60°, c) 60 – 80°, and d) 80 – 90° latitude compared to observations and models (Ando et al., 2020; Mahieux et al., 2023b; Seiff et al., 1979). Insets show the cloud region (48 – 78 km) in more detail.

The PCM reproduces the observed shape of all temperature profiles except those measured by SOIR. In the low- to mid-latitude bands, the PCM reproduces the broad trends seen by SOIR, with minima near 90 km and 130 km, but the temperature range produced is much smaller than reported by SOIR, and the minima and maxima occur higher in the atmosphere than recorded by SOIR.

At the narrow ranges of altitudes and latitudes where other observations overlap with SOIR (75 – 110 km in Figure 2.2b; 70 – 85 km in Figure 2.2c; 70 – 85 km in Figure 2.2d), there is broadly good agreement between all observations except SOIR, and of the PCM with the other observations. In particular, in the high latitude and polar regions, SOIR reports very low temperatures, increasing with altitude near 70 km, in direct contradiction of all other observations. It is not currently clear why observations from SOIR are so different from all other observations.

Insets in Figure 2.2 show that while the agreement with observations is generally good, the model tends to be towards the higher end of, or slightly exceed, observations through the clouds deck, as seen in Figure 2.1 and highlighted by Gilli et al. (2021) and Stolzenbach et al. (2023).

2.1.2.2 Cloud microphysics

The microphysical cloud model is described in detail in Stolzenbach (2016) and Stolzenbach et al. (2023), so only a brief overview is provided here. The model assumes thermodynamic equilibrium of the liquid and gas-phase H_2O and H_2SO_4 at all times (i.e., there is no supersaturation or subsaturation allowed in the model). The model adopts three log-normal (Equation 2.1) size modes of cloud particles as measured by the Pioneer Venus LCPS (Knollenberg & Hunten, 1980). Knollenberg & Hunten reported a Gaussian distribution for mode 2, but a log-normal that approximates it is used here instead. The cloud particles consist of pure aqueous sulphuric acid for modes 1 and 2 (100 – 200 nm and 1.0 – 1.4 μm geometric mean radii (r_g) respectively), and mode 3 (r_g = 3.65μm) consisting of 97% basalt by radius, with a coating of sulphuric acid.

The log-normal distribution is given by:

$$\frac{dN}{d\ ln(r)} = \frac{N}{\sigma_g \sqrt{2\pi}} exp\left(- \frac{\left(ln\left(\frac{r}{r_g} \right) \right)^2}{2{\sigma_g}^2} \right) \tag{2.1}$$

where σ_g is the geometric standard deviation and N the total number density of the mode.

The H_2SO_4 and H_2O vapour pressures above the droplets ($p_{H_2SO_4}$, p_{H_2O}) and the H_2SO_4 weight fraction of the condensed phase ($w_{H_2SO_4}$) are found by iteratively solving the Kelvin equation (Equation 2.2) and saturation vapour pressure of the H_2SO_4 (Equation 2.3) while requiring conservation of the species between the gas and liquid phases (Stolzenbach et al., 2023):

$$\ln(p_{H_2O}) - \frac{2M_{H_2O}\theta_S(w_{H_2SO_4})}{RTr\rho_d(w_{H_2SO_4})} - \ln(p_{H_2SO_4}) = 0 \quad (2.2)$$

$$p_{saturation} = p_{H_2SO_4} = \Gamma_{H_2SO_4}(T, w_{H_2SO_4})p_a(T) \quad (2.3)$$

where $\Gamma_{H_2SO_4}(T, w_{H_2SO_4})$ is the chemical activity of the acid, p_a is the saturation vapour pressure over pure H_2SO_4, θ_S is the surface tension of the droplet, ρ_d is the droplet density, M_{H_2O} is the molecular weight of water, R is the ideal gas constant, r is the radius of the droplet, and T is the temperature.

The number densities of the condensed and gas phases of H_2O and H_2SO_4 can then be calculated. The total mass density of the condensed phase is partitioned into the three modes based on mass fractions from the LCPS. The cloud droplets sediment downwards according to the Stokes velocity of the droplets.

Figure 2.3 shows a comparison of the mass loading produced by the PCM compared to the mass loading observed by the LCPS. The PCM follows the broad trend of the observations, but produces a lower cloud base (~42 km) compared to observations (~47 km). Stolzenbach et al. (2023) report that this is due to the temperature difference between the model and observations, which affects the conversion from pressure to altitude, as noted in Section 2.1.2.1.

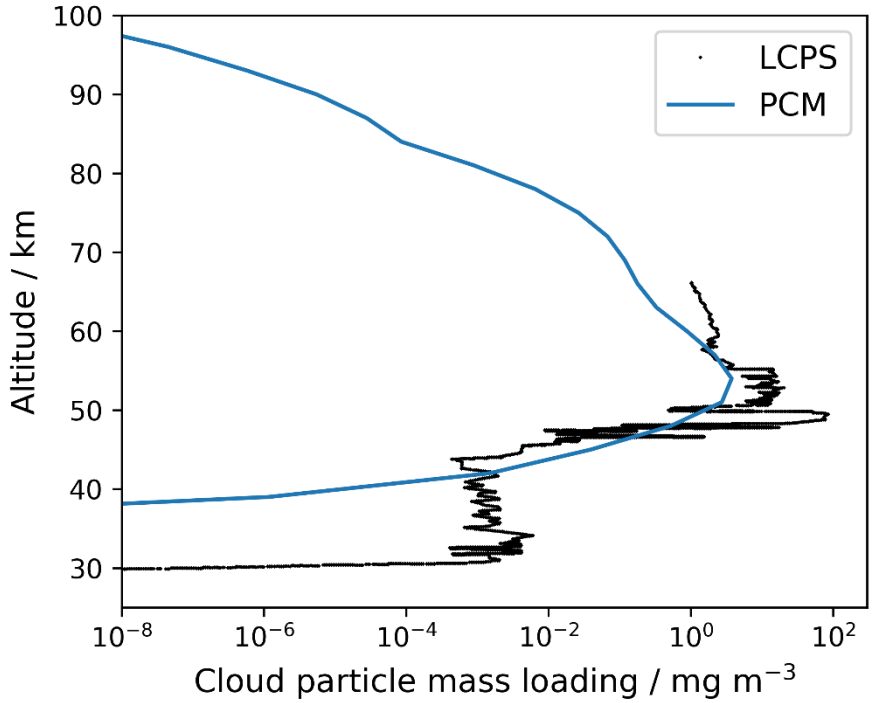

Figure 2.3. PCM global average cloud particle mass loading compared to measurements from the LCPS (Knollenberg & Hunten, 1980).

The lower vertical resolution of the PCM compared to the LCPS data means that the minima between the upper, middle, and lower clouds (at 57 and 50 km) and the lower pre-cloud layers (sharp spike in mass loading at 47 km) cannot be reproduced in the PCM.

The PCM also tends towards the lower end of LCPS observations and does not capture the high mass loading in the lower clouds. This effect is due to the different representations of the cloud deck. The LCPS measured total particle number density across 17 size bins. All particles are included in this, which may not all be sulphuric acid. The conversion to mass loading from the diameter of the cloud particles assumes spherical sulphuric acid and is dominated by the largest size particles due to this conversion. Mode 3 is modelled as thinly coated solid cores rather than pure sulphuric acid droplets in the PCM. The result is therefore the same size distribution of droplets with less than 10% of the sulphuric acid content that was assumed by the LCPS.

The particles detected by the LCPS below the cloud base at 47 km are generally referred to as the "lower haze". Due to the high temperatures below the cloud deck, it is generally accepted that the lower haze is not composed of sulphuric acid (Titov et al., 2018), and as such is not reproduced by the PCM.

2.1.2.3 Winds

The PCM dynamics reproduce the overall trends seen in observations: mean zonal wind is westward, following the retrograde rotation of the planet, with strong super-rotation produced at the cloud tops (60 – 70 km), reaching speeds of 100 – 120 m s^{-1} (Lebonnois et al., 2010). Winds through the clouds deck and lower atmosphere have been measured sporadically over the past 40 years by a variety of methods. Observations are summarised in Table 2.1, and winds produced by the PCM compared to observations in Figures 2.4 – 2.7.

Table 2.1. List of observations and models included in Figures 2.4 – 2.7.

Reference	Wind	Method	Altitude range / km	Latitude range	Local time	Comments
Counselman et al. (1980)	u, v (instantaneous)	Radio tracking of probes	0 – 60 km	4.4° 59.3° -31.3° -28.7°	07:58 03:35 06:46 00:07	Large North Day Night
Kerzhanovich and Limaye (1985)	u	Model	70, 60, 50, 40 km	All	All	VIRA
	u	Radio tracking of Venera probes	0 – 60 km	-10° 32° 16° -7° -7.5° -13.4°	06:24 13:12 13:42 11:16 09:27 09:54	Venera 8 Venera 9 Venera 10 Venera 12 Venera 13 Venera 14
	u	Mariner 10 UV cloud tops	Upper clouds	60 – 0°	Day	Data from Travis (1978)
Khatuntsev et al. (2017)	u_{avg}, v_{avg}	VEx: VMC cloud tracking (965 nm)	49 – 57 km	-75 – -5°	Day	

Limaye (1985)	*u*	Pioneer Venus OCPP Polarimetry 270 nm 365 nm 550 nm 935 nm	Upper clouds Middle clouds Lower clouds	-55 – 43° -35 – 25° -48 – 37° -40 – -8°	Day	
Limaye et al. (1982)	*u*, *v*	Pioneer Venus OCPP Images	Upper clouds	-60 – 50°	Day	
Limaye and Suomi (1981)	*u* *v*	Mariner 10 UV cloud tops	Upper clouds	-56 – 51° -52 – 40°	Day	
Machado et al. (2022)	*u*	VEx: VIRTIS-M cloud tracking (380 nm)	66 – 72 km	-80 – -5°	10:00 – 17:00 12:00 – 15:00	
	u_{avg}, v_{avg}	TNG/NICS (2.28 μm)	~48 km	-80 – 80°	Night	
Newman et al. (1984)	*u*	Model	63, 65, 67 km	5 – 80°	All	Model assumes cyclostrophic balance and is based on Pioneer Venus Probe radio occultation

Peralta et al. (2007)	u_{avg}, v_{fit}	Gallileo SSI (418 nm)	65 – 70 km	-70 – 70°	Day	Reanalysis of data from Belton et al. (1991)
	u_{avg}	986 nm	57 – 62 km	-14 – 62°	Day	8 km lower than 418 nm
Peralta et al. (2017)	u, v	MESSENGER MDIS (996 nm)	60 km	-40 – 40°	Day	
	u, v	VEx: VIRTIS-M (1.74 μm)	50 km	-35 – 0°	Night	
Peralta et al. (2018)	u_{avg}, v_{avg}	Akatsuki IR2 (2.26 μm)	50 – 60 km	-65 – 65°	Night	
Peralta et al. (2019)	u_{avg}, v_{avg}	Akatsuki IR1 (900 nm)	50 – 60 km 50 – 55 km	-70 – 70°	Day	
Rossow et al. (1980)	u, v	Pioneer Venus OCPP Images	Upper clouds	-60 – 50°	Day	
Rossow et al. (1990)	u_{avg}, v_{avg}	365 nm	Upper clouds	-66 – 66°	Day	
Sánchez-Lavega et al. (2008)	u_{avg}, v_{avg}	VEx: VIRTIS (380 nm)	62 – 70 km 66 km	-85 – -4°	Day	
	u_{avg}, v_{avg}	VEx: VIRTIS (980 nm)	58 – 64 km 61 km	-85 – -6°	Day	
	u_{avg}, v_{avg}	VEx: VIRTIS (1.74 μm)	44 – 48 km 47 km	-85 – 3°	Night	

Figure 2.4 shows a comparison of the PCM-modelled and observed zonal winds at a range of heights through the atmosphere.

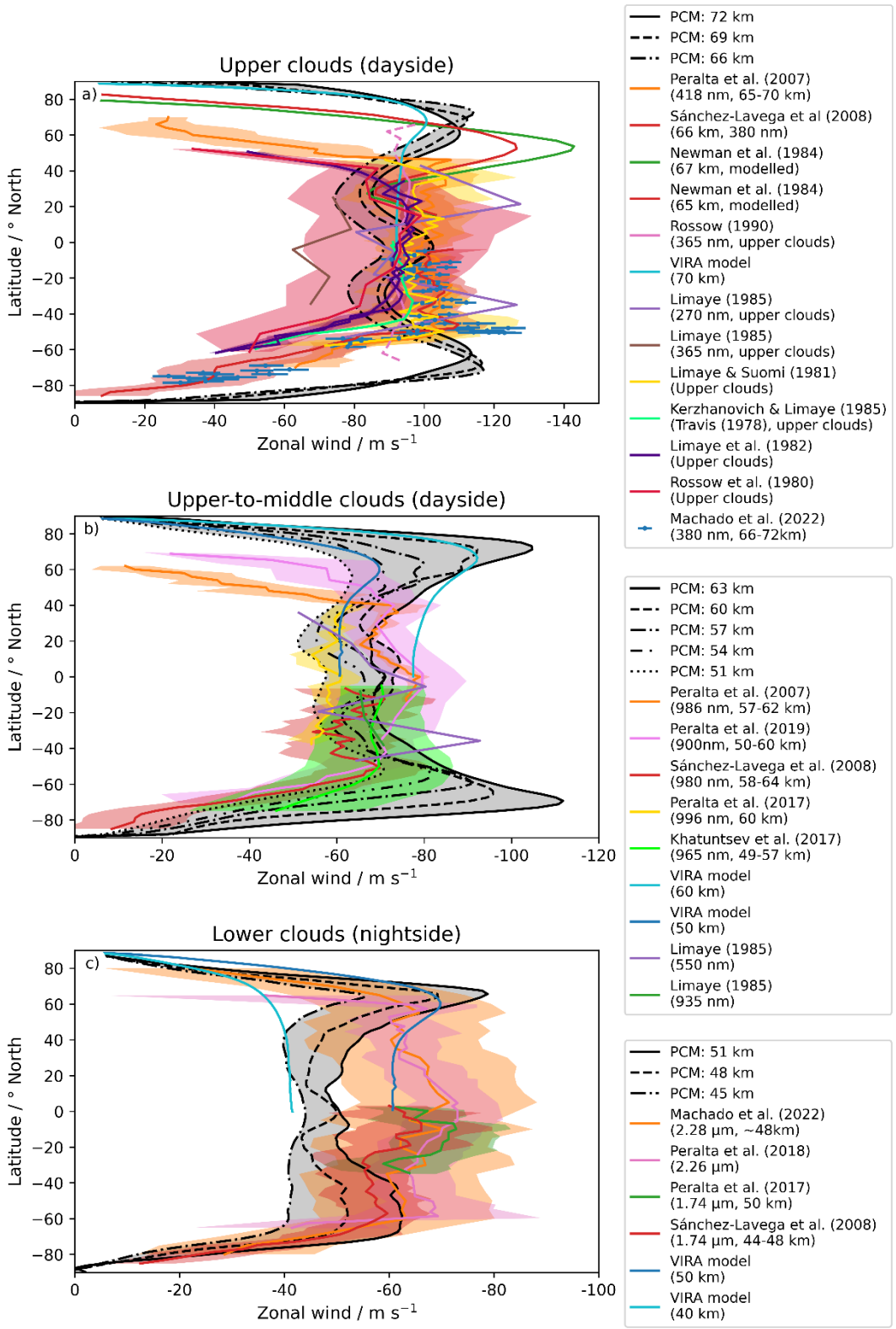

Figure 2.4. Comparison of observations of zonal wind in the a) upper clouds, b) upper-to-middle clouds and c) lower clouds with zonally averaged PCM modelled winds. As the observation heights are often somewhat imprecise, a range of model heights is included on each plot.

It is important to note that many observations were recorded from Venus Express. Due to its elliptical orbit, with its pericentre above the northern hemisphere (Svedhem et al., 2007), there are many more observations for the southern hemisphere, where the spacecraft was sufficiently far from the planet to image significant proportions of the illuminated disc. The model outputs from Kerzhanovich and Limaye (1985) and Newman et al. (1984), when plotted, are symmetric about the equator, but are only plotted for the northern hemisphere to aid readability.

Comparison of the zonal wind observations and the VIRA model with the PCM results shows that while the general features are reproduced, their specific locations differ between the PCM and observations. Super-rotating jets are produced in the upper and middle clouds. The PCM predicts that the fastest zonal winds occur at ± 70°, in contrast to the observations, which find the strongest winds between 20 and 50°. The PCM shares marked similarities with the profiles from the VIRA model (Kerzhanovich & Limaye, 1985), and Newman et al. (1984). Both models assume simple cyclostrophic balance and show the same shortcomings with reproducing the observations: overestimating the magnitude of the wind speeds, and locating the maxima too far poleward to match observations. Observations suggest that the jets are localised to the upper cloud region, with observed middle cloud wind speeds of approximately 70 m s^{-1}, and mid-latitude winds typically the same strength as or lower than those in the low latitude regions (Figure 2.4b). Conversely, the PCM produces higher winds at mid- to high-latitudes in both hemispheres throughout the upper and middle clouds.

The magnitude of the zonal wind is reproduced fairly well in the upper and middle clouds, but in the lower clouds, the PCM underestimates the low- to mid-latitude winds by ~20 m s^{-1}. The PCM produces a marked asymmetry in the profile of the winds between the northern and southern jets in the low-to-middle clouds. With comparatively few observations of the winds, it is difficult to say if this is expected.

Specific comparison of the PCM meridional winds with observations (Figure 2.5) is difficult due to the large uncertainties in observations (due both to variability in measured winds, and large measurement uncertainties, especially in the lower clouds) but general trends and magnitudes of the meridional winds are reproduced well equatorward of ± 60°. Meridional wind changes rapidly with height in the PCM, so specific profiles at particular heights may differ from observations due to differences (and uncertainties) in the altitude at which they were measured.

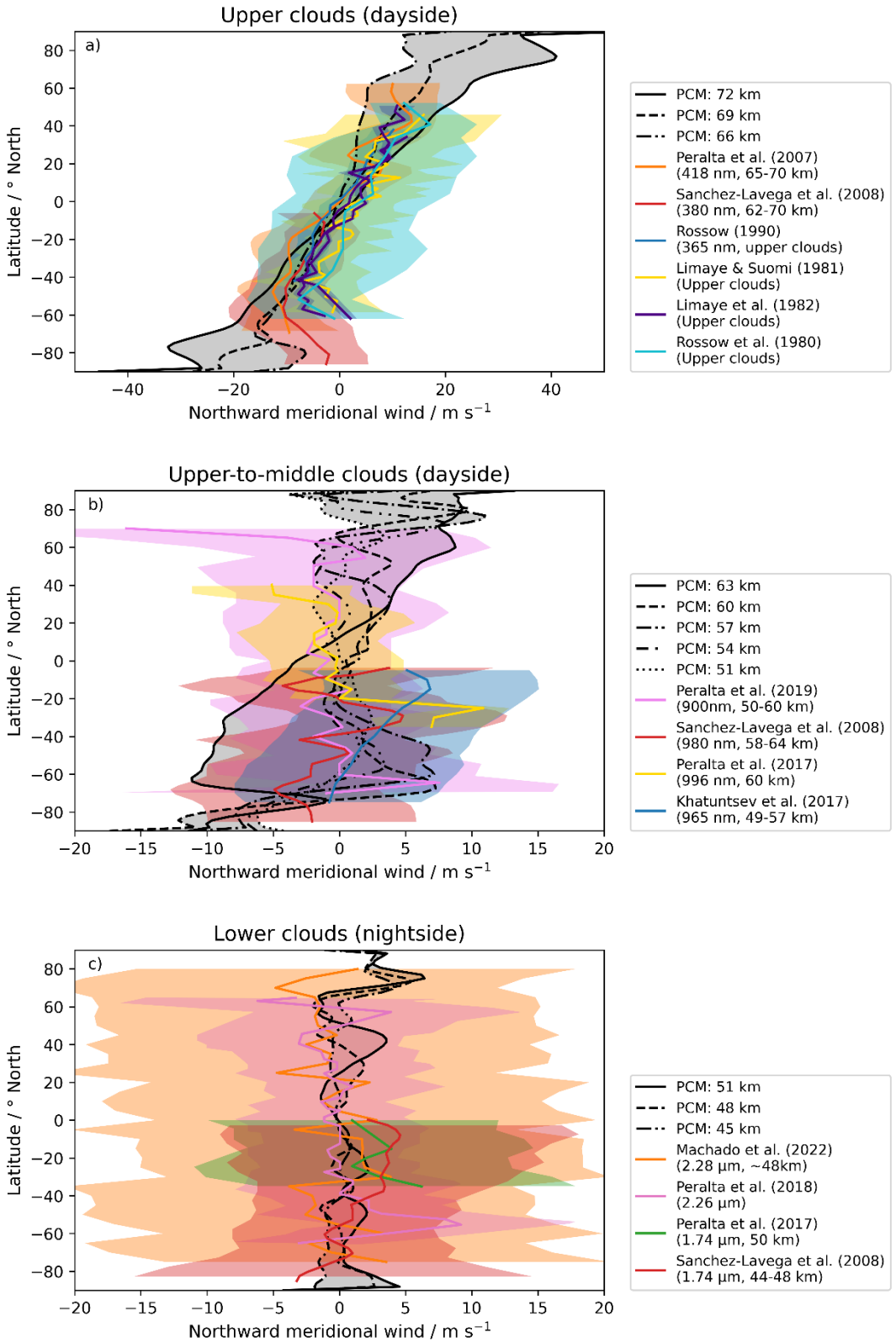

Figure 2.5. Comparison of observations of meridional wind in the a) upper clouds, b) upper-to-middle clouds and c) lower clouds with zonally averaged PCM modelled winds. Wind direction is set such that northward (southerly) winds are positive in both hemispheres, i.e., poleward flow in the southern hemisphere is negative.

Though there are few observations in the polar and high latitude regions, the PCM is clearly incorrect in these regions. The few observations that there are (Khatuntsev et al., 2017; Peralta et al., 2007; Sánchez-Lavega et al., 2008) show a decrease in magnitude polewards of 60 – 70°, while PCM models produce an increase, resulting in the highest meridional wind speeds at and near the poles. Figure 2.6 shows a 2D slice of the meridional winds modelled at 60 km. Some observations (Peralta et al., 2019; Sánchez-Lavega et al., 2008) that reach mid- to high-latitudes show a peak in meridional wind near 60°. The strong winds reaching all the way to the poles will likely transport too much material to the poles from the low latitudes, limiting the ability of the PCM to model the latitudinal distribution of the near-UV absorber reliably.

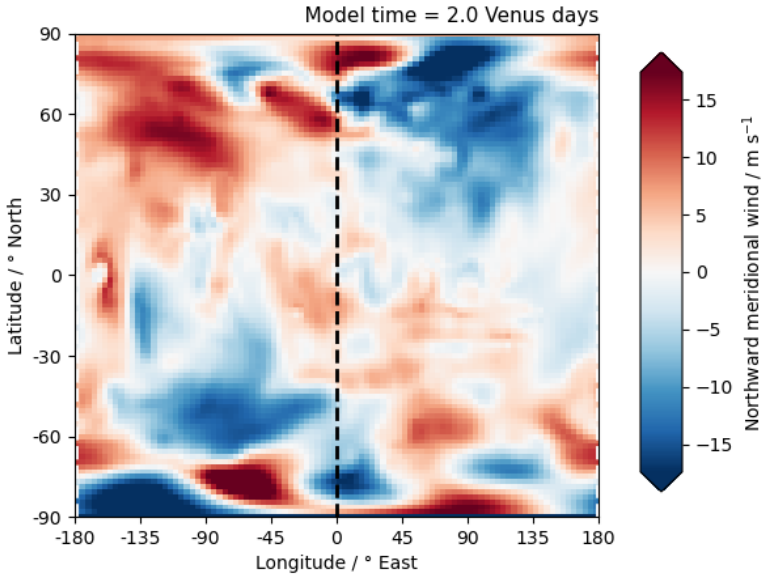

Figure 2.6. Instantaneous PCM-modelled meridional winds at 60 km altitude. The black dashed line (0°) indicates midnight, the white dashed lines (± 180°, just visible at the edges of the plot) is midday.

In the instantaneous winds (Figure 2.6), there is a general trend for poleward flow in the mornings (-180° – 0°) and equatorward flow in the evenings (0° – 180°), but flow is chaotic, with many small regions showing opposite flow to the general trends. There are several regions of very strong winds in the high latitude regions which do not seem to be supported by observations.

The poles show a clear anomaly (also visible as a spike in Figure 2.5 at the poles) which is presumed to be related to the model grid at the poles.

Figures 2.7 and 2.8 show a comparison of the PCM to altitude wind profiles measured by Pioneer Venus and Venera descent probes (Figure 2.7 only) and the VIRA model (Kerzhanovich & Limaye, 1985). The PCM is generally in good agreement with the VIRA model, showing the same general trend and approximate values. There is generally less agreement between the PCM profiles and probe profiles. All PCM zonal wind profiles below the clouds coincide with each

other and agree well with the North Probe, which produces significantly lower zonal winds (by ~20 m s^{-1}) than the average of the probes. However, the meridional component at the North probe location shows an opposite trend to observations. It is apparent that the PCM is not reproducing the variation in zonal winds with location that were observed by the Pioneer and Venera probes. The best meridional wind agreement occurs of for the night probe location, though this is likely coincidental.

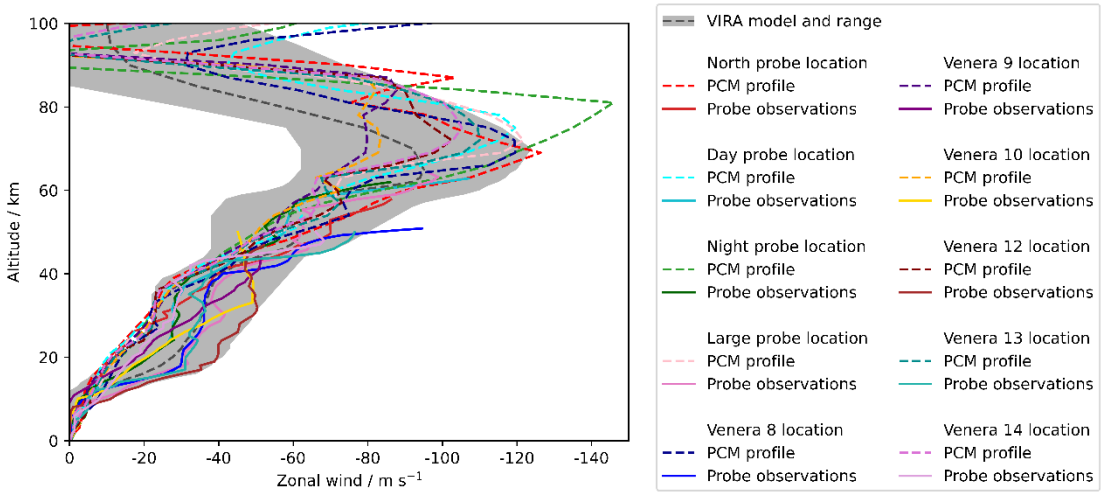

Figure 2.7. Instantaneous zonal wind measurements from the four Pioneer Venus probes (Counselman et al., 1980) and Venera 8 – 10 and 12 – 14 during descent (Kerzhanovich & Limaye, 1985), along with the PCM profiles at each of their latitudes and local times, and the VIRA model.

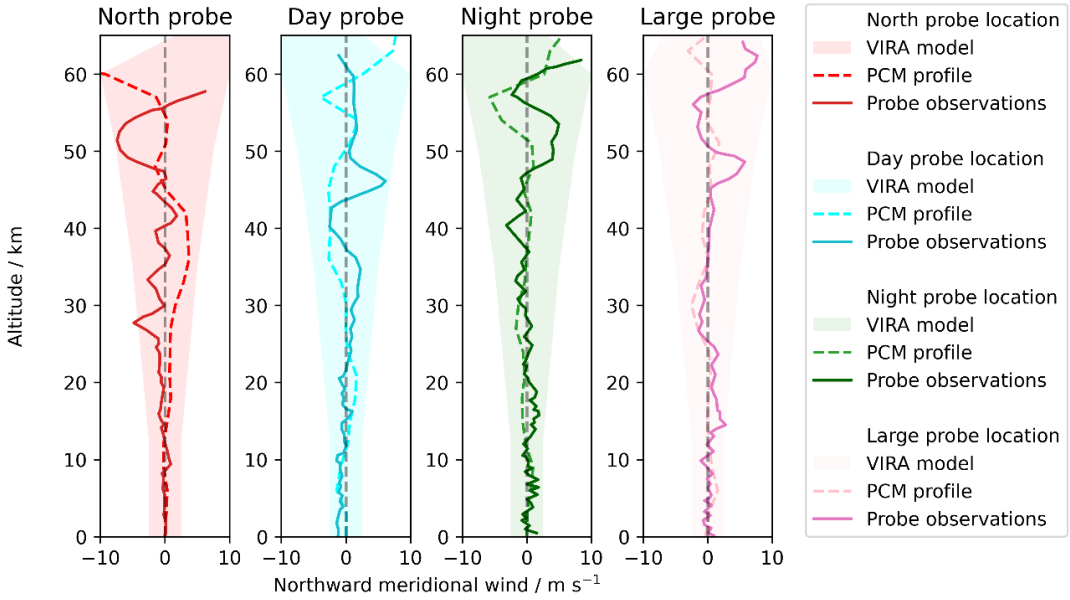

Figure 2.8. Comparison of instantaneous Pioneer Venus probe-measured meridional winds with the VIRA model and PCM profiles at the same latitudes and local times (Counselman et al., 1980; Kerzhanovich & Limaye, 1985).

2.1.3 Model development

To optimise the model running times, two separate branches of model development took place, one to introduce additional sulphur chemistry into the model, and one to introduce iron chemistry into the model. This kept the number of tracers in the model to a minimum in both cases, minimising the time required to run the models.

2.1.3.1 Sulphur model

The model is run with 78 pressure levels from the surface (9.3×10^6 Pa) to ~172 km (3.3×10^{-6} Pa) with neutral chemistry as described in Lebonnois et al. (2010; 2016) and no ion chemistry. The model was run for 9.0 Venus solar days (Vd) to reach photochemical steady state.

Three versions of the model are compared: the released version, r3188, henceforth labelled the "out-of-the-box" run; a version with more detailed and new sulphur chemistry ("new chemistry"); and a version with the new chemistry and injection of sulphur from meteoric ablation ("SO MIF"). All three versions of the model are started from the same initial conditions (mixing ratios of key species are shown in Figure 2.9). Species that do not appear in the start file (including all new sulphur species, such as S_2O_2 and ClSO) are initialised with a vmr of 10^{-30}.

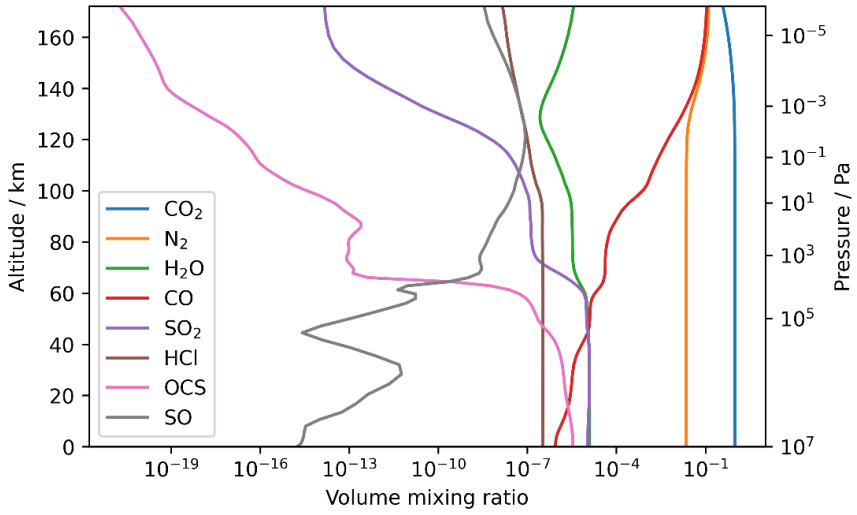

Figure 2.9. Initial molar (volume) mixing ratios of key species in the 78-level model.

2.1.3.2 Fe model

To study iron chemistry, the model is run with 90 levels (extending the top to 8×10^{-9} Pa, ~250 km) with neutral and ion chemistry as described by Gilli et al. (2021), Martinez et al. (2023), and Martinez et al. (2024). The model runs on a non-uniform altitude grid, with higher vertical resolution near the surface. The model output has been interpolated to grid boxes of uniform altitude for comparison with observations.

The model was run for 3.0 Vd (the inclusion of the ionosphere made the model run significantly more computationally intensive) with full ionosphere chemistry to capture the reactions of the injected metal atoms and ions. The behaviour of most species shows the same general trends as for the sulphur model. In the absence of a sink for iron (e.g., by settling) the total $FeCl_3$

concentration in the model increases gradually with time, but most other iron species, being part of chemical cycles (discussed further in Section 5.2), reach steady state rapidly. The initial concentrations of certain species in the model (Figure 2.10) are slightly different than for the sulphur model, where the SO_2 has been deliberately increased (see Chapter 3 and Section 2.1.4). Species that do not appear in the start file (including all iron species) are initialised to a vmr of 10^{-30}.

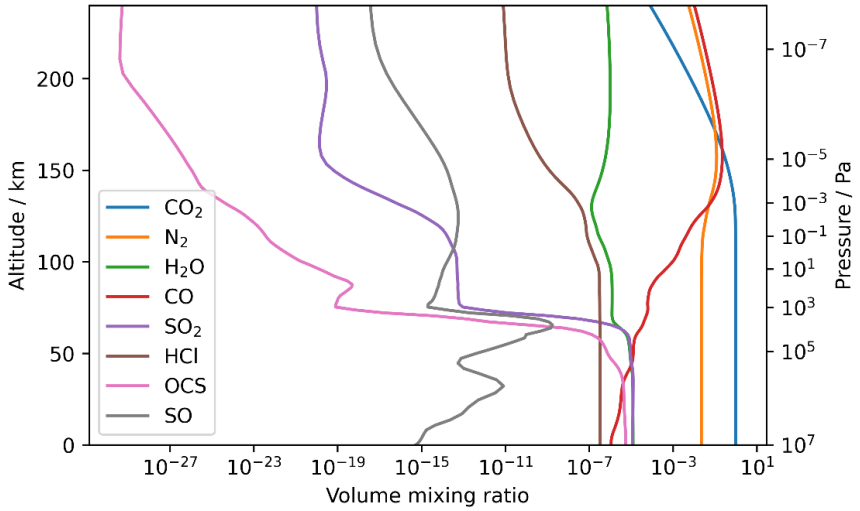

Figure 2.10. Initial molar (volume) mixing ratios of key species in the 90-level model.

2.1.4 Important chemical species

Figure 2.11 shows the initial and final values of various key species in both the sulphur (SO MIF version, final values after 9.0 Vd) and iron (final values after 3.0 Vd) models compared to observations. A summary of observations is provided in Table 2.2. Acronyms used for instruments are defined below the table. Observations are generally the best fit across an altitude range, rather than a profile, though some profiles are included.

Table 2.2. Observations of key species plotted in Figures 2.11 and 2.16 – 2.25. The wavelength region of observations is given with the instrument name if it is not already included therein.

Reference	**Species**	**Instrument**	**Type**	**Notes**
Belyaev et al. (2012)	SO_2	VEx: SPICAV-UV and SPICAV-SOIR	Orbiter	UV: 85 – 105 km, SOIR: 65 – 80 km.
de Bergh et al. (1991)	HDO	Canada-France-Hawaii Telescope (IR)	Ground-based	HDO/H_2O ratio only.

Bertaux et al. (2007)	H_2O HCl HF HDO	VEx: SPICAV-SOIR	Orbiter	HCl profiles from two orbits are plotted. H_2O is a best fit to several orbits. HF results are for one orbit. No uncertainties are reported for HDO/H_2O ratio.
Bertaux et al. (1996)	SO_2	Vega 1&2: ISAV UV Spectrometer	Descent probe	Individual profiles from Vega-1 and -2 are plotted. No uncertainties given.
Bézard et al. (1993)	H_2O SO_2 HF OCS	Canada-France-Hawaii Telescope (IR)	Ground-based	No uncertainties given.
Bézard et al. (1990)	CO_2 CO H_2O HCl HF OCS	Canada-France-Hawaii Telescope (IR)	Ground-based	CO_2 mixing ratio assumed to be constant throughout the atmosphere. No uncertainties given.
Bjoraker et al. (1992)	HF HDO	Kuiper Airborne Observatory (IR)	Earth atmosphere	HDO/H_2O ratio only.
Connes et al. (1968)	CO HCl HF	Observatoire de Saint Michel: Michelson interferometer infrared spectroscopy	Ground-based	Data was later reanalysed by Young (1972).
Cottini et al. (2012)	H_2O	VEx: VIRTIS-H	Orbiter	
Crisp et al. (1991)	H_2O	FIGS at Anglo-Australian Telescope (IR)	Ground-based	
Donahue et al. (1982)	HDO	Pioneer Venus Large Probe Gas Chromatograph	Descent probe	HDO/H_2O ratio only.
Drossart et al. (1993)	H_2O	Galileo: NIMS	Flyby	

Encrenaz et al. (2012)	H_2O SO_2	TEXES at NASA IRTF	Ground-based	H_2O inferred from HDO absorption line observations. SO_2 minimum and maximum profiles shown.
Fedorova et al. (2008)	H_2O HDO	VEx: SPICAV-SOIR	Orbiter	
Gel'man et al. (1979)	CO N_2 SO_2	Venera-12 Gas Chromatograph	Descent probe	
Hartle and Taylor (1983)	HDO	Pioneer Venus Orbiter Ion Mass Spectrometer	Orbiter	HDO/H_2O ratio only.
Irwin et al. (2008)	CO	VEx: VIRTIS-M	Orbiter	
Jessup et al. (2015)	SO_2	HST/STIS	Space telescope	Uncertainties are plotted but not visible beyond the width of the line. Shaded area reflects the variation between three observation periods.
Keating et al. (1985)	CO_2 N_2	-	Compilation of descent probes	VIRA, a compilation of observations from the Venera and Pioneer Venus probes. No uncertainties given.
Krasnopolsky (2010a)	CO	CSHELL at NASA IRTF	Ground-based	Morning and afternoon values plotted.
Krasnopolsky (2010b)	SO_2 OCS HDO	CSHELL at NASA IRTF	Ground-based	
Krasnopolsky (2008)	H_2S HCl HF	CSHELL at NASA IRTF	Ground-based	H_2S upper limit only
Mahieux et al. (2023a)	SO_2 OCS	VEx: SPICAV-SOIR	Orbiter	Best fit profile overview.

Mahieux et al. (2023b)	CO H_2O HCl HF HDO	VEx: SPICAV-SOIR	Orbiter	Only data from the equatorial region is plotted. $H^{35}Cl$ and $H^{37}Cl$ measured separately, plotted value is their sum.
Marcq et al. (2008)	CO H_2O SO_2 OCS	VEx: VIRTIS-H	Orbiter	
Na et al. (1994)	SO_2	UV-sounding rocket observations	Rocket	Results of two observations, taken in 1988 and 1991.
Oyama et al. (1980)	CO_2 CO N_2 H_2O H_2S OCS	Pioneer Venus Large Probe Gas Chromatograph	Descent probe	H_2S and OCS are upper limits only.
Sandor et al. (2010)	SO_2	JCMT (sub-mm)	Ground-based	No SO_2 detected below a base altitude (~86 km). The SO_2 upper limit below 86 km is the instrumental limit of detection.
Vandaele et al. (2008)	CO HCl HF	VEx:SPICAV-SOIR	Orbiter	
Young (1972)	CO HCl			Reanalysis of data from Connes et al. (1968)
von Zahn and Moroz (1985)	CO_2 N_2	-	Compilation of descent probes	VIRA, a compilation of *in situ* probe observations. Reported uncertainties are less than the line width.

VEx: Venus Express; SPICAV: Spectroscopy for Investigation of Characteristics of the Atmosphere of Venus; SPICAV-UV: SPICAV Ultraviolet channel; SPICAV-SOIR: SPICAV Solar Occultation in the InfraRed channel; VIRTIS: Visible and InfraRed Thermal Imaging Spectrometer; VIRTIS-H: VIRTIS High-resolution IR channel; FIGS: Fabry-Perot Interferometer Grating Spectrometer; NIMS: Near-Infrared Mapping Spectrometer; TEXES: Texas Echelon-cross-Echelle Spectrograph (IR); IRTF: InfraRed Telescope Facility; VIRTIS-M: VIRTIS Mapper channel in UV-IR; HST/STIS: Hubble Space Telescope Imaging Spectrograph; VIRA: Venus International Reference Atmosphere; CSHELL: Cryogenic Echelle Spectrograph (IR); JCMT: James Clerk Maxwell Telescope.

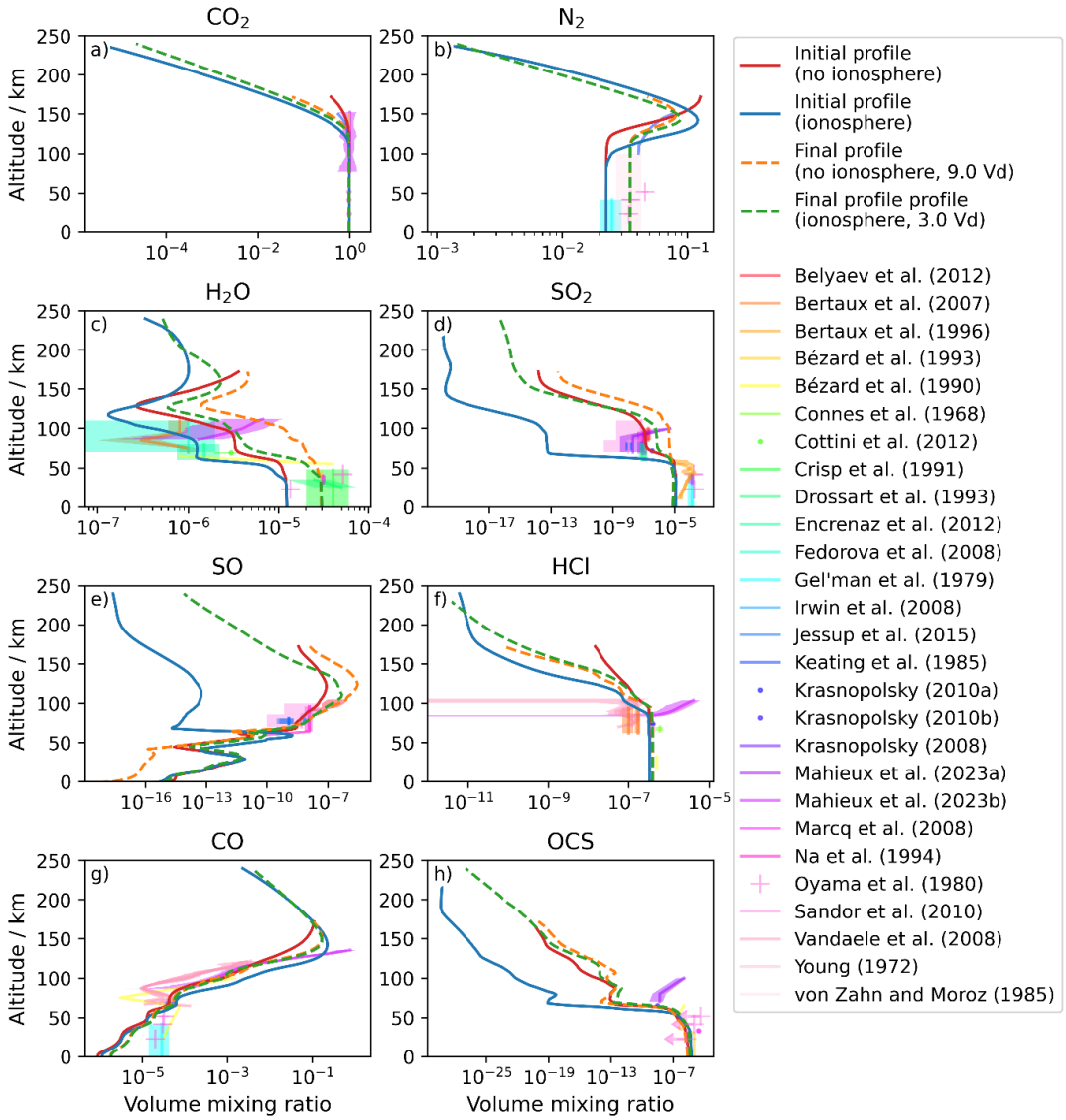

Figure 2.11. Initial and final mixing vmr of key species compared to observations.

The model shows good agreement for CO_2 (Figure 2.11a), N_2 (Figure 2.11b), SO (Figure 2.11e), and CO (Figure 2.11g). The decrease in CO_2 vmr above 120 km is moderately steeper in the model than the observations, but this occurs above the altitude region of interest. Near the surface, the N_2 observations reported by Gel'man et al. (1979) differ from those reported by Oyama et al. (1980) and selected by the VIRA compilation (von Zahn & Moroz, 1985). The initial N_2 concentration profiles are consistent with Gel'man et al. (1979), but the N_2 concentration increases when the model is run, in line with the other observations (Keating et al., 1985; Oyama et al., 1980; von Zahn & Moroz, 1985).

The model SO results are consistent with the upper limit of observations. The initial profiles are very different between the model runs with and without the ionosphere. Both models retain a minimum near 60 km, but both are significantly higher than their initial profiles above this minimum.

The CO model profiles show little change from their initial conditions. The concentration near the surface is an order of magnitude too low, but increases to coincide with observations by the bottom of the cloud deck. Observations show a rapid decrease to a minimum at the cloud top, followed by an increase above, while the models produce a constant profile through the clouds, followed by an increase above. Overall agreement of the shape is good, despite the failure to capture the minimum in the clouds.

HCl (Figure 2.11f) and OCS (Figure 2.11h) both show model concentrations significantly lower than observations above the clouds. HCl observations show lower values at the cloud tops, with an increase with altitude up to 100 km (the maximum height of observations), while the model results show a decreasing trend with altitude. OCS shows good agreement with the few existent observations below the clouds, but the model profiles then decrease sharply by 8 orders of magnitude near 60 km, compared to the two orders of magnitude decrease in observations. Mahieux et al. (2023a) reported an increase in concentration with altitude above the clouds. A similar shape in the modelled profile is produced, but it is far too low to approach observations.

H_2O (Figure 2.11c) and SO_2 (Figure 2.11d) differ significantly from observations. The H_2O profile has good agreement with the observations below the clouds and follows the same general shape as observations: a decrease to a minimum, followed by an increase, but it occurs 40 km higher in the model than observed. In the model with no ionosphere, sulphur chemistry has been added and the result appears to be an increase in the H_2O. This is assumed to be due to a decrease in the uptake of H_2O into the clouds. The SO_2 profile does not reproduce the decrease seen in the observations through the clouds: the decrease apparent in the ionosphere model profile (green) through the clouds is due to the very low concentration in the initial profile (blue). The SO_2 increases until a constant vmr is achieved, as can be seen in the non-ionosphere model result (orange). As a result, the below cloud SO_2 is deliberately set an order of magnitude lower than observations to limit the total SO_2 in the model. The version of the model with the ionosphere was significantly more computationally intensive, and so the iron model was run for only 3.0 Vd, compared to 9.0 Vd without the ionosphere. The non-ionosphere model has therefore reached steady state with respect to SO_2, while the ionosphere version has not. Sandor et al. (2010) and Mahieux et al. (2023a) both reported increasing SO_2 with altitude above 90 km, which the model does not reproduce.

2.1.2.5 Summary of the PCM

Overall, the PCM satisfactorily reproduces the general trends and chemistry of Venus, with some limitations: the temperature is slightly higher than observed towards the cloud tops and lower than observed at the cloud base, producing chemical and physical features higher or lower than observed, respectively. This is most apparent with the cloud base (Figure 2.5), which is 5 km lower than observed.

The temperature and wind profiles both show a displacement of identifiable features – such as the cold collar and super-rotational jets – poleward in both hemispheres by approximately 20°. This appears to be a common feature of many Venusian models and suggests a missing driving force in atmosphere. This will affect the latitudinal distribution of long-lived species in the atmosphere most significantly as they will be transported further towards the poles than observations suggest is realistic.

Several species related to the sulphur chemistry of Venus (SO_2, OCS, H_2O) show significant deviation from observations. Sulphur chemistry in the Venusian atmosphere is a significant unsolved problem in the field, with no explanation for the deep minimum in SO_2 in the clouds readily apparent (Vandaele et al., 2017).

2.2 SOCRATES

2.2.1 Basic model

SOCRATES uses a two-stream approximation to resolve the upward and downward direct and diffuse fluxes and heating rates through the atmosphere (Edwards & Slingo, 1996). Before the two-stream equations can be formed and solved, the gas absorption coefficients are determined, and a spectral file produced. The correlated-k method (Goody et al., 1989) is used to treat the absorption. An overview of the model is provided in this section and specifics of the modified model to run for Venus are described in Section 2.2.2.

The spectral file specifies the spectral region being modelled and divides it up into bands. It lists the major and minor gaseous absorbers in each spectral band and whether overlapping absorption should be treated with full random overlap of spectral lines or a simplified model, in which the absorption from all minor gases is represented by a single “equivalent absorption” which then randomly overlaps the major absorbing gas within each band (Manners et al., 2022a). The Rayleigh scattering coefficients and continuum absorption coefficients in each band, and the parametrisation of the aerosol and cloud (water droplets and ice crystals) properties are also specified. As SOCRATES is primarily used integrated with a 3D global climate model (GCM), the spectral file is pre-generated for the intended use and optimised for the approximate composition of the atmosphere. The SOCRATES code is then run with the actual gas, temperature, and aerosol profiles, (which would normally be provided directly from the coupled GCM at each grid cell and time step of the model) to calculate the fluxes. The workflow for making the spectral file and running the model are outlined below. Steps 1, 2, 3, 4, and 6 are explained in more detail in Sections 2.2.1.1 – 6.

1. The skeleton file is made, in which the spectral bands are defined, and the lists of gases, continua, and aerosols that will be included in the model are provided.
2. Gas absorption coefficients ("correlated-k terms") are calculated. The gas absorption cross-sections at given reference temperatures and pressures can be calculated directly from absorption line database files (a computationally intensive step) or provided as cross-section files (particularly in the UV or for continuum absorption). These are parametrised into correlated-k terms for each band in the skeleton file given a solar spectrum and nominal gas column abundance to use for weighting.
3. The monochromatic aerosol data is generated (or must be provided) at a given range of wavelengths. The complex refractive index across the wavelength range and aerosol size distribution must be provided. The average aerosol profiles in each band are then calculated from the monochromatic profiles, skeleton file and solar spectrum.
4. The gas and continuum k files, a list of gases for which Rayleigh scattering should be considered, and the average aerosol properties are combined with the skeleton file to produce a spectral file. The file contains all of the species that contribute to each band and their k coefficients in each band. The spectral file is "tidied" – very weakly absorbing gases are removed from bands – to optimise the running of the model, and the final spectral file is produced.
5. The pressure and temperature at the levels and layers of the model and the gas and aerosol mass mixing ratio (mmr) files are produced. This can be done manually or by providing a single file containing the pressure, temperature, and mixing ratios to the programme *raw_input*, which will process them automatically. The solar zenith angle, surface reflectance, and solar irradiance must also be provided and are stored as netcdf files.
6. Finally, the SOCRATES two-stream solver is run, using the mmr files and the spectral file to calculate the radiative fluxes.

2.2.1.1 The skeleton file

The skeleton for the spectral file specifies the number and wavelength (or wavenumber) limits of the spectral bands, the number of aerosol species, absorbing gases, and continua, and the ID numbers of each species. This skeleton is then used to define the band limits in future steps of the preprocessing and forms the template for the final spectral file when the data for the gases, continua, and aerosols are added.

2.2.1.2 Gas pre-preprocessing

Gas absorption data are generally available as either absorption line, collision induced absorption, or absorption cross-section data. Most absorption data is from HITRAN2020 (Gordon et al., 2022), but it can be provided from other sources provided it uses HITRAN file formats. Absorption cross-sections for the S_2O_2 isomers studied in Chapter 3 were calculated using *ab initio* quantum theory (Section 3.3.3) as these are not available in HITRAN. The data is scaled to the temperature and pressure of the atmosphere. This can be done by either providing a reference

temperature and pressure and specifying the scaling (e.g., quadratic temperature scaling and exponential pressure scaling) or by providing a pressure-temperature lookup table.

The absorption data is processed into correlated k coefficients which are added into the spectral file as gas absorption coefficients and continuum absorption coefficients for the spectral bands. This processing is generally done by the program *Ccorr_k*, an overview of which is available in Manners et al. (2022b).

2.2.1.3 Aerosol treatment

The scattering properties of an aerosol distribution are calculated from the refractive indices of the material and the size distribution of the aerosol, assuming spherical particles. This can be done by two preprocessing programs included with SOCRATES, or the scattering and absorption of the aerosol population can be supplied directly.

If a full calculation is performed, the program *Cscatter* is used. The total number density of the aerosol and either a log-normal or modified gamma distribution is specified for the particle sizes. The parameters of each mode (for instance, a weight, geometric mean radius and geometric standard deviation for a log-normal distribution) are defined independently.

Alternatively, the particle number density in a range of size bins can be specified in an input file. The real and imaginary refractive index of the aerosol at specified wavelengths that span the spectrum must be provided. The program can then perform a Mie theory calculation (or anomalous diffraction theory for a modified gamma distribution) to calculate the monochromatic single scattering properties (absorption, scattering, and the first *n* moments of the phase function, where *n* can be specified) at specified wavelengths.

The output of *Cscatter* (or predetermined scattering properties of the aerosol) can then be averaged to calculate the scattering, absorption, and asymmetry (the first moment of the phase function) of the aerosol across each of the spectral bands by the program C*scatter_average*. These band-averaged scattering properties are included in the spectral file. An overview of *Cscatter* and *Cscatter_average* is available in Manners et al. (2022b).

2.2.1.4 The spectral file

The spectral file is set up following the outline in the skeleton file. The gases for which Rayleigh scattering will be considered are added to the file. Then, for each gas and continuum, absorption data is added to each of the bands that the gas or continuum absorbs in. The average aerosol scattering files are also added to the spectral file.

The spectral file is then tidied: the overlap treatment (full random treatment or equivalent extinction method as described above) for the generalised continua is set; gases and continua are removed from bands where their absorption is weak (defined to be a transmission greater than a given value); and the major gas in each band is set.

2.2.1.5 Radiation code

SOCRATES is called using *Cl_run_cdf*, with various options for the cloud treatment, aerosol treatment, and continua provided. The different computational options available in SOCRATES are described in detail in Manners et al. (2022a, 2022b). As it was developed for use with a full GCM, SOCRATES has no time evolution or spatial grid. The conditions, including solar zenith angle (local time) and the instantaneous atmospheric profiles of temperature and gas or aerosol mmrs are provided (either by the GCM when run as part of the full model, or by the user for purely radiative transfer runs, as in this case) and the instantaneous fluxes are generated.

SOCRATES uses a two-stream approximation to calculate the direct and diffuse radiative fluxes and therefore heating rates in the atmosphere (Edwards & Slingo, 1996). A full explanation of the calculations is provided in Manners et al. (2022a), but a summary is provided here.

The atmosphere is split into N homogeneous layers, numbered from 1 (at the TOA) to N (the layer just above the surface). Each layer is referred to by its central pressure. The boundaries of the layers are called the levels, numbered from 0 (TOA) to N (surface), as illustrated in Figure 2.12.

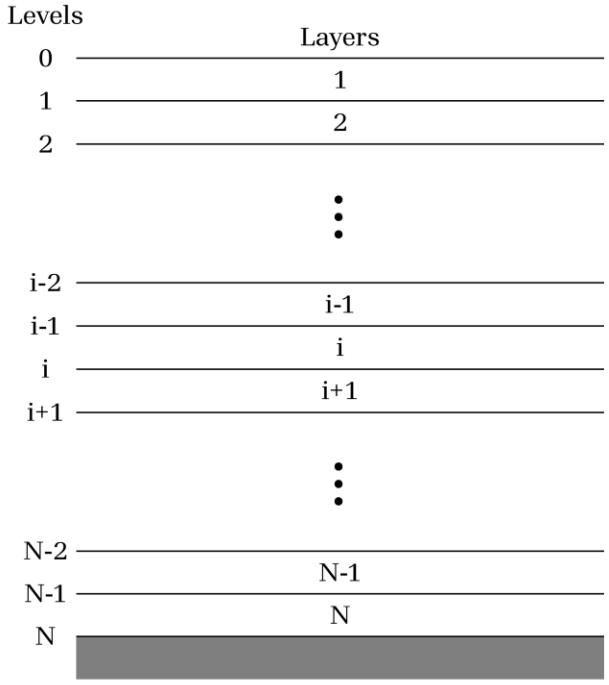

Figure 2.12. Diagram of the levels and layers in SOCRATES. Adapted from Manners et al. (2022a).

The region of the spectrum being modelled is divided into spectral bands. Within a band, all properties except the gaseous mass absorption coefficient are taken to be independent of wavelength. Each band is split into "quasi-monochromatic regions", where a single k-term applies for each of the gases. A quasi-monochromatic flux is calculated for each region. The flux $F_j^{(b)}$ in the band j is given by the weighted sum of the i quasi-monochromatic fluxes $F_i^{(qm)}$ in the band:

$$F_j^{(b)} = \sum_i w_i F_i^{(qm)} \tag{2.5}$$

and the total flux is the sum of the fluxes in each band:

$$F = \sum_j F_j^{(b)} \tag{2.6}$$

The weighting of the quasi-monochromatic fluxes is determined by the k-term weights in the spectral file representing the fraction of the band over which a given absorption coefficient applies. Each quasi-monochromatic flux (henceforth "flux" for simplicity) is calculated using the two-stream approximation.

In the two-stream approximation, the fluxes at each level are related to the fluxes at the levels above and below and the optical properties of the layers. The absorption and scattering coefficients of each species are used to calculate the optical properties (optical depth, single scattering albedo, and asymmetry) of each layer. The method of calculating the k-terms and optical properties for absorbing gases, continua, Rayleigh scattering, aerosols, and clouds are detailed in Manners et al. (2022a).

The flux is considered in three components: the upward flux, U, the total downward flux, V, and the direct solar flux, Z. V can be written as the sum of the diffuse downward flux, D, and the direct solar flux Z. In each layer, the flux is transmitted, scattered, and reflected. The net (downward) flux is given by $V-U$.

At a particular level i, some of the direct flux will be transmitted, and some will be scattered. The direct flux Z_i, is given by

$$Z_i = T_{0i} Z_{i-1} \tag{2.7}$$

where T_{0i} is the direct transmission coefficient in layer i. Some of the direct flux is scattered into diffuse flux in either the upward (+) or downward (-) directions. These fluxes are given by

$$S_i^+ = c_{1i} Z_{i-1} \tag{2.8}$$

$$S_i^- = c_{2i} Z_{i-1} \tag{2.9}$$

where c_{1i} and c_{2i} are coefficients that depend on the optical properties of the layer and the choice of two stream approximation parametrisation. The different choices are detailed in Manners et al. (2022a).

The upward and downward fluxes at each level are therefore given by the sum of the transmitted and reflected fluxes from adjacent layers and any of the direct beam that is scattered into the diffuse beam in those layers:

$$U_{i-1} = T_i U_i + R_i V_{i-1} + S_i^+ \tag{2.10}$$

$$V_i = T_i V_{i-1} + R_i U_i + S_i^- \tag{2.11}$$

where T_i and R_i are the diffuse transmission and reflection in layer i, which also depend on the optical properties of the layer and the choice of the two-stream approximation parametrisation. The contributions to each flux are shown in Figure 2.13.

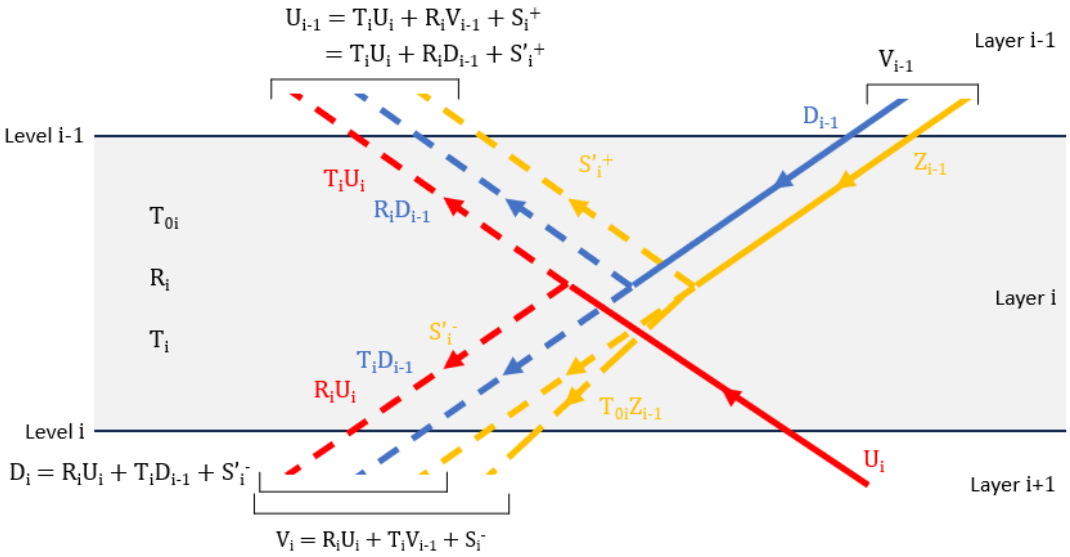

Figure 2.13. The contributions of each of the fluxes to the upward and downward flux at each level. For clarity, fluxes are shown on an angle to allow for separation of incident and reflected fluxes. The fluxes are calculated on levels while T_i, T_{0i}, and R_i are properties of the layer.

The downward flux is explicitly divided into D and Z in the figure. S'^+_i and S'^-_i, the scattered direct fluxes are different functions of Z_{i-1} than S_i^+ and S_i^-, arising from the conversion between the total downward flux, V, and diffuse downward flux, D:

$$\begin{aligned} U_{i-1} &= T_iU_i + R_iD_{i-1} + S'^+_i \\ &= T_iU_i + R_i(V_{i-1} - Z_{i-1}) + S'^+_i \\ &= T_iU_i + R_iV_{i-1} - R_iZ_{i-1} + S'^+_i \end{aligned} \tag{2.12}$$

and

$$D_i = T_iD_{i-1} + R_iU_i + S'^-_i \tag{2.13}$$

$$\begin{aligned} V_i &= Z_i + T_i(V_{i-1} - Z_{i-1}) + R_iU_i + S'^-_i \\ &= T_{0i}Z_{i-1} + T_iV_{i-1} - T_iZ_{i-1} + R_iU_i + S'^-_i \end{aligned} \tag{2.14}$$

so by comparison of Equations 2.12 with 2.10 and Equations 2.14 with 2.11,

$$S'^+_i = S_i^+ + R_iZ_{i-1} \tag{2.15}$$

and

$$S'^-_i = S_i^- + (T_i - T_{0i})Z_{i-1} \tag{2.16}$$

This conversion from S'^+_i and S'^-_i to S_i^+ and S_i^-accounts for different optical properties of the layers with regard to diffuse and direct fluxes. The equations can therefore be simply expressed in terms of the total upward and downward fluxes.

Boundary conditions are defined at the surface and TOA. At the TOA, there is no incident diffuse flux, so

$$V_0 = Z_0 = \phi_0 \, cos\theta_z \tag{2.17}$$

where ϕ_0 is the solar irradiance in the spectral band and θ_z is the solar zenith angle. At the surface, the only upward flux is that reflected from the surface, calculated by

$$U_N = \alpha_s \times direct\ downward\ flux + \alpha_d \times diffuse\ downward\ flux$$
$$U_N = \alpha_s Z_N + \alpha_d (V_N - Z_N) \tag{2.18}$$

where α_s is the surface albedo for direct radiation and α_d is the surface albedo for diffuse radiation. As V_N is the total (diffuse + direct) downward radiation at the surface, taking the difference of V_N and Z_N leaves only the diffuse component.

A set of linear simultaneous equations is formed and solved (Edwards & Slingo, 1996). SOCRATES includes eight different solvers which can be selected when the model is run. Each is optimised and recommended for different atmospheric configurations, in particular for the choice of cloud treatment. A list of solvers is available in Manners et al. (2022b) and the method is outlined in Manners et al. (2022a).

2.2.2 SOCRATES-Venus

2.2.2.1 The spectral bands

SOCRATES-Venus has 280 spectral bands of varying widths, summarised in Table 2.3. As the motivation for the development of this model is to investigate the UV absorption, the visible and near-UV region of the spectrum is covered at 5 nm resolution. The resolution of the bands decreases as wavelength increases, up to 500 nm resolution in the final bands in the infrared (IR). The IR bands are included for completeness should further model development be undertaken, and will only be considered briefly.

Table 2.3. Wavelength limits and widths of the 280 SOCRATES-Venus spectral bands

Band numbers	Lower bound / μm	Upper bound / μm	Band width / μm
0 – 104	0.175	0.700	0.005
105 – 154	0.70	1.20	0.01
155 – 214	1.20	2.40	0.02
215 – 232	2.40	3.30	0.05
233 – 249	3.3	5.0	0.1
250 – 279	5.0	20.0	0.5

2.2.2.2 Altitude bins and temperature

For simplicity, the central pressures of the layers in SOCRATES-Venus are set as the 78 pressure levels of the PCM (non-ionosphere version), as this is the primary source of gas mixing ratios for the model. Gas and aerosol mixing ratios are provided for each layer. Temperatures are set for

each level and layer, and a range of temperatures either side of the average temperature are also provided for each layer to account for the variation in temperature that could occur. These pressures and temperatures are used to scale the gas absorption lines.

The PCM temperatures are model-time and longitudinal averages at a given latitude across 6 timesteps (~60 Earth days) of an out-of-the-box run of the PCM (Figure 2.14a). For each latitude, the longitude-averaged temperature profile from PCM Venus at each timestep is taken and the average calculated (Figure 2.14b). There is minimal difference (~1 K) seen between longitude-averaged profiles at a given latitude. The average, minimum and maximum of the profiles are calculated (Figure 2.14c). The maximum divergence of a temperature profile from the average was found to be 23.2 K, so the temperature profiles used for SOCRATES-Venus were the average ± 0, 17, 34, and 50 K to ensure the instantaneous profile is never outside the range of temperatures the lines can be scaled to.

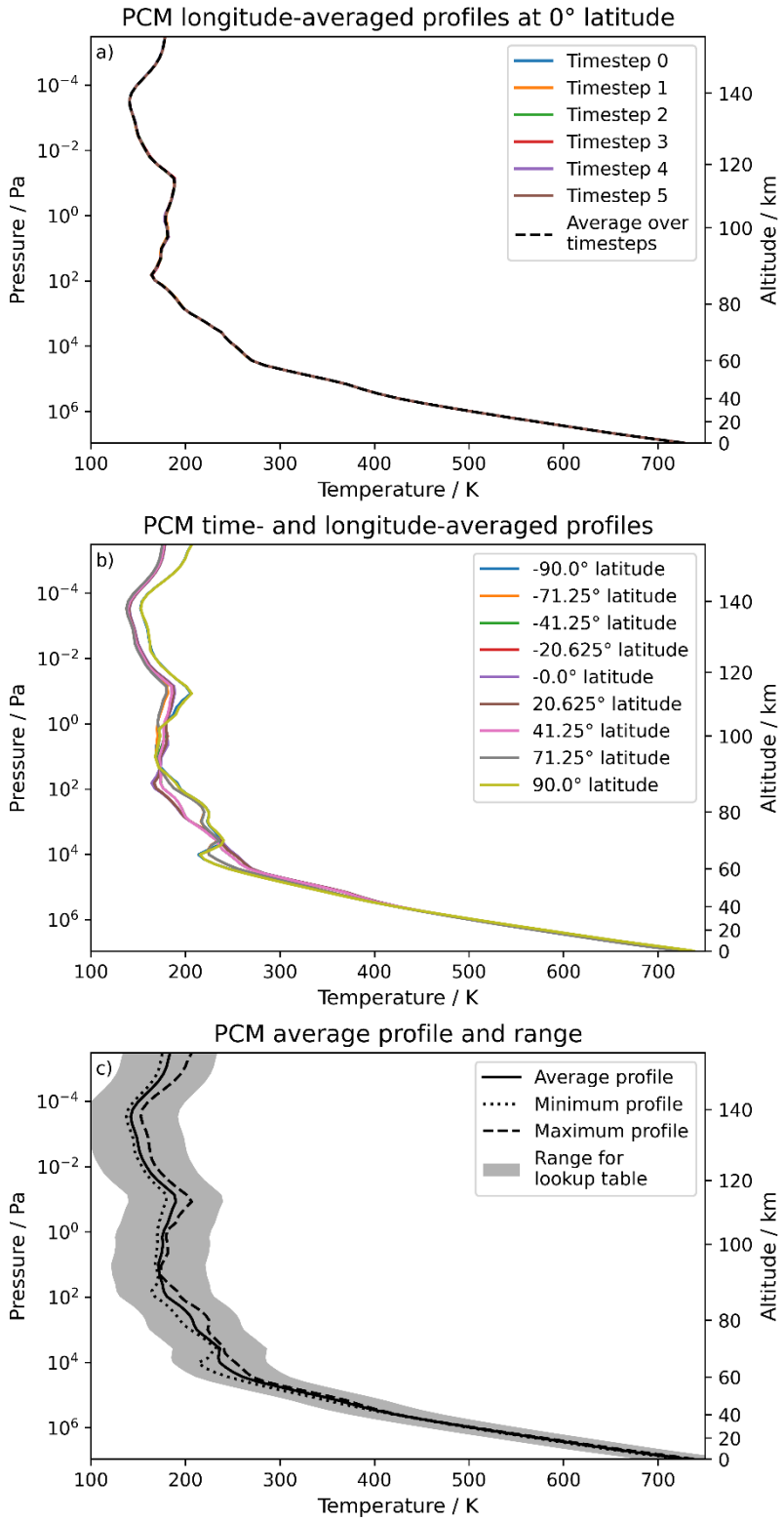

Figure 2.14. a) An example of the longitude-averaged temperature profiles at a given latitude (0°) and their average. The variation between timesteps is less than the width of the lines. b) Some example average temperature profiles at different latitudes. c) The average, minimum, and maximum temperature for all latitudes and range of temperatures provided in the SOCRATES lookup table to account for all possible conditions.

2.2.2.3 Location and local time

The solar zenith angle and surface reflectivity are set for each SOCRATES run. The tables are optimised for a full array of latitudes and local times. However, for comparison to the MASCS spectrum 151 (Pérez-Hoyos et al., 2018), the PCM data is from the equatorial region near local noon and all SOCRATES plots use a zenith angle of 52°. A surface albedo of 0.1 (Ekonomov et al., 1980) was used for both diffuse and direct fluxes.

2.2.2.4 Aerosol vs. cloud treatment

SOCRATES has a complex cloud treatment. It models clouds made of liquid water and ice crystals and can do so separately – ice clouds and water clouds – or homogeneously mixed together – ice and water clouds – within each atmospheric layer. It can also model stratiform and convective clouds (for either separate ice and water clouds, or mixed clouds) separately or together. There is then a parametrisation for the fraction of cloud cover in each layer and the treatment of overlapping clouds in different layers.

While ice clouds have been theorised to form on Venus above 100 km, they are predicted to be short-lived phenomena and have not yet been observed (Murray et al., 2023), so no ice clouds are included in SOCRATES-Venus. In addition, the Venusian cloud cover is consistent and total. The SOCRATES cloud treatment, while ideal for Earth-like planets with discrete and changeable cloud structures, is not applicable for Venus, which has persistent cloud cover across the whole planet (Titov et al., 2018). Therefore, rather than adapt the complex cloud treatment to include sulphuric acid cloud droplets, SOCRATES-Venus uses the aerosol treatment for Venus's clouds.

Aerosols in SOCRATES use the same scattering treatment as the clouds do, but their size distribution cannot vary over time and aerosols are taken to cover a full model gridbox, while clouds can cover only a fraction of a gridbox. As SOCRATES is used without spatial or temporal variation (one gridbox and one time instance) in this case, and the Venusian cloud cover is total, the aerosol scheme is sufficient to model the needed behaviour. It is a much simpler job to adapt existing aerosol species in SOCRATES to become the different cloud modes of Venus than to adapt the cloud scheme. In addition, while the modes on Venus are typically called clouds for their obvious visual similarity to terrestrial stratus clouds, in terms of number density and modal droplet size, the larger modes of the Venusian clouds are much less dense than terrestrial clouds, with somewhat smaller droplet sizes, aligning much more with terrestrial aerosol or haze definitions. For example, a terrestrial cloud might be expected to consist of droplets of 5 – 50 μm and a number density of a few hundred per cubic centimetre (e.g., Miles et al., 2000), whereas mode 2, the main component of the sulphuric acid clouds, has a modal diameter of just 2 μm, with little spread above or below this size, and a number density of just 50 cm^{-3} (Titov et al., 2018). These densities are much more consistent with those of terrestrial stratospheric aerosol (e.g., Zalach et al., 2020). Given the similarity between terrestrial aerosol distributions and Venusian clouds, the use of the aerosol rather than cloud treatment is not expected to present issues.

2.2.2.5 Gases

SOCRATES-Venus models 10 gases (13 when S_2O_2 is included, see Chapter 3). Venusian isotope ratios are (with the exception of the D:H ratio) generally poorly studied, but the few measurements that exist indicate comparable values to terrestrial ratios for most species (Hoffman et al., 1979). Isotope ratios of gases are therefore assumed to be equal to terrestrial values, with the exception of HDO, which is treated separately to all other isotopologues of H_2O. Any errors introduced by this assumptions are expected to be much smaller than the uncertainties in the concentrations of the gases themselves. With the exception of N_2, which is included for Rayleigh scattering alone, these gases have non-zero expected absorption on Venus in the spectral region being considered. Altitude mixing ratio profiles are taken from PCM model runs where available, and Eymet et al. (2009) otherwise. SOCRATES uses mass mixing ratios for gas and aerosol concentrations, while the PCM uses molar (volume) mixing ratios. All gases included in the PCM, as well as condensed sulphuric acid and water, and SOCRATES-Venus species not included in the PCM (H_2S and HF)[3] were included in the conversion from molar to mass mixing ratio.

For each pressure layer *j* in the model, and species *i,* the mass mixing ratio $C_{i,j}^{mass}$ is given by

$$C_{i,j}^{mass} = \frac{C_{i,j}^{mol} \times M_i}{\sum_k C_{k,j}^{mol} \times M_k} \tag{2.19}$$

where $C_{i,j}^{mol}$ is the molar mixing ratio of species *i* in pressure layer *j*, and M_i is the molar mass (in g mole^{-1}) of species *i*.

The column mass of each species *i* is then calculated by

$$Column\ mass_i = \sum_j \frac{\Delta p_j \times C_{i,j}^{mass}}{g} \tag{2.20}$$

where Δp_j is the change in pressure across layer *j*, and g is the acceleration due to gravity (8.87 m s^{-2}), which is assumed to be constant throughout the atmosphere.

Gases are neglected from spectral bands they would otherwise contribute to where their transmission is greater than 0.999990. The modelling process is shown in Figure 2.15.

[3] Full list of species used for the calculation:
CO_2, H_2O (g), SO_2, CO, OCS, HCl, *cis*-OSSO, *trans*-OSSO, cyclic-S_2O_2, H_2S, HF, HDO, Cl, Cl_2, ClCO, $ClCO_3$ ClO, $ClSO_2$, H, H_2, H_2O_2, H_2SO_4 (g), He, HO_2, HOCl, HSO_3, N_2, O, O(^{1}D), O_2, O_2($a^1\Delta_g$), O_3, OH, ClSO, S, S_2, SO, SO_3, H_2O (l), and H_2SO_4 (l).

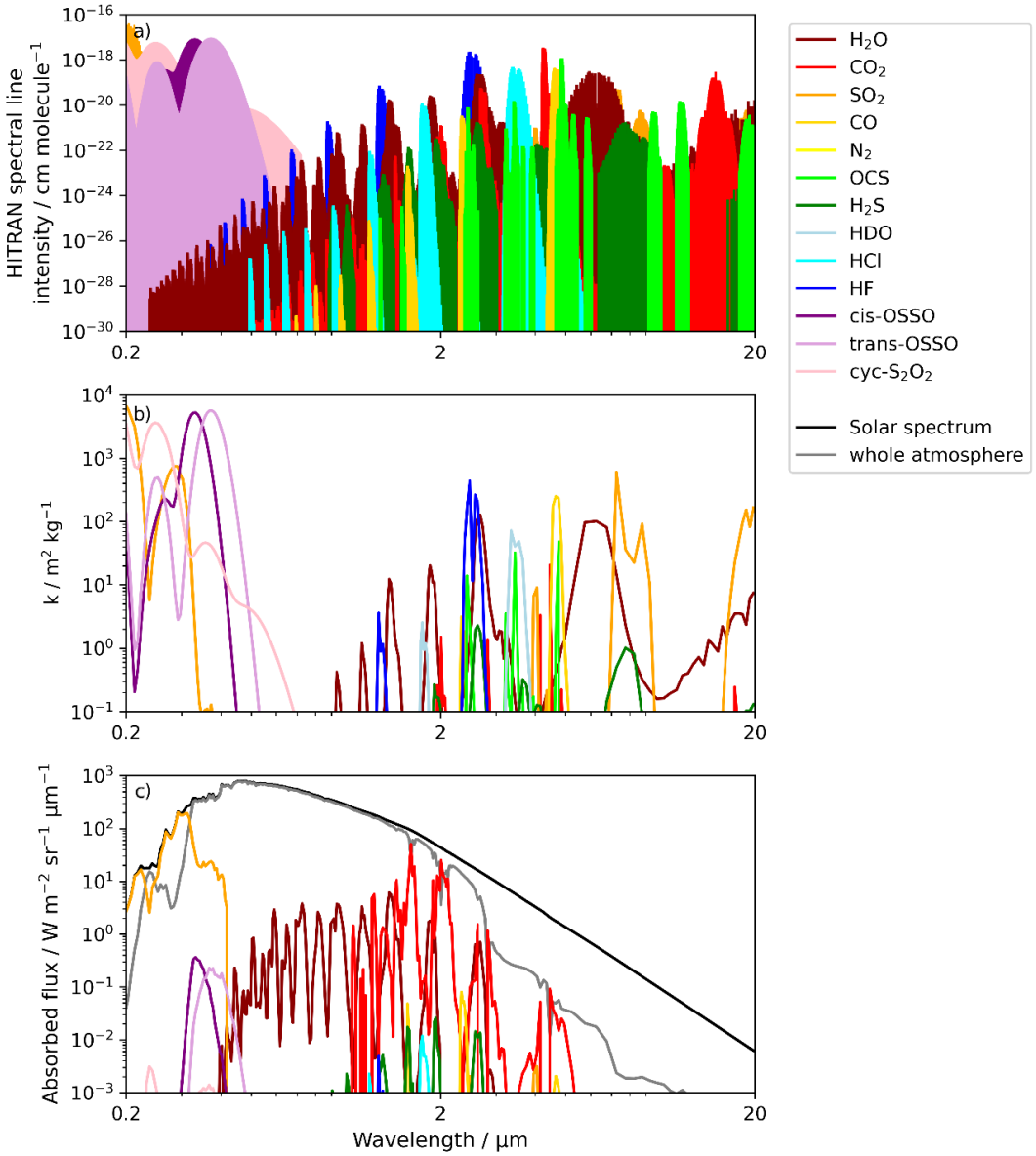

Figure 2.15. a) Spectral line intensities and UV cross-sections from HITRAN, and calculated for *cis*-OSSO, *trans*-OSSO, and cyclic-S_2O_2, b) k coefficients per band for the gases in the spectral file generated by SOCRATES, c) modelled flux absorbed by each individual gas in the model. Note: $FeCl_3$ is not included in this model run.

The gas absorption lines and cross-sections available from HITRAN (or predicted, if spectra are not available in HITRAN) are presented in Figure 2.15a. The gas absorption coefficients (k) for each gas are binned into spectral bands (Figure 2.15b), then any weakly absorbing species are removed from bands. Finally, the model is run and the contribution of each species to the final absorption is shown in Figure 2.15c. The black line in Figure 2.15c shows the total solar flux incident on the atmosphere, while the grey line is the TOA reflected flux for the full atmosphere. The "tidying" of the spectral file uses the estimated column densities of each gas, provided before the model runs, to predict which gases will be dominant in each band. The column densities of minor gases such as HF, *cis*-OSSO, *trans*-OSSO, and cyclic-S_2O_2 are deliberately over-estimated

in this step to prevent their removal from bands and the tidying therefore produces no change to the spectra shown in Figure 2.15b at the current scale.

The PCM vmr profile, observations, and SOCRATES-Venus modelled absorption for each gas (excluding S_2O_2) are shown in Figures 2.16 – 2.25. The impacts of the three S_2O_2 isomers are discussed in Section 3.7. Details of the observations are listed in Table 2.2 in Section 2.1.4. The PCM mixing ratio is plotted as a volume mixing ratio (despite SOCRATES using mass mixing ratio) to make comparison with literature easier, as most observations are provided as volume mixing ratios. Observations are generally shown as profiles or points, uncertainties (where reported) are shaded areas or horizontal lines. Exceptions will be explained in the specific sections. Many of the CO_2 and N_2 observations were taken during the Pioneer Venus and Venera missions. The results were compiled into the Venus International Reference Atmosphere (VIRA) (von Zahn & Moroz, 1985) and the later update VIRA-2 (Keating et al., 1985), which are plotted instead, along with two examples of measurements from the missions.

For each gas, its individual impact on the atmospheric model is calculated by running the model with the full atmosphere, and then with all components except the one under consideration. The difference of the two spectra can then be taken to assess the impact of the species (Figures 2.16b – 2.24b and 2.25c). A positive value for the difference indicates absorption by the gas in question, while a negative difference indicates scattering. As the gas contributions are plotted on a log scale, negative values cannot be shown. For scattering components of gas contributions, the difference is multiplied by -1 and differences are plotted as positive values in yellow.

CO_2

The CO_2 vmr profile is taken from the PCM output. CO_2 is the most abundant gas in most of the atmosphere, dropping slightly below CO above ~150 km where photolysis of CO_2 to CO and O occurs. Absorption line data with self-broadening and continuum absorption comes from HITRAN2020 (Gordon et al., 2022). Rayleigh scattering is calculated for CO_2. The vmr profile, observations, and contribution to the total flux are shown in Figure 2.16. Below ~1 μm in wavelength, CO_2 Rayleigh scattering has a net reflective impact on the spectrum (Figure 2.16b, yellow) while the gas absorption lines (Figure 2.16a, blue) become apparent at longer wavelengths. CO_2-CO_2 continuum lines also contribute but are much smaller in magnitude than the CO_2 lines.

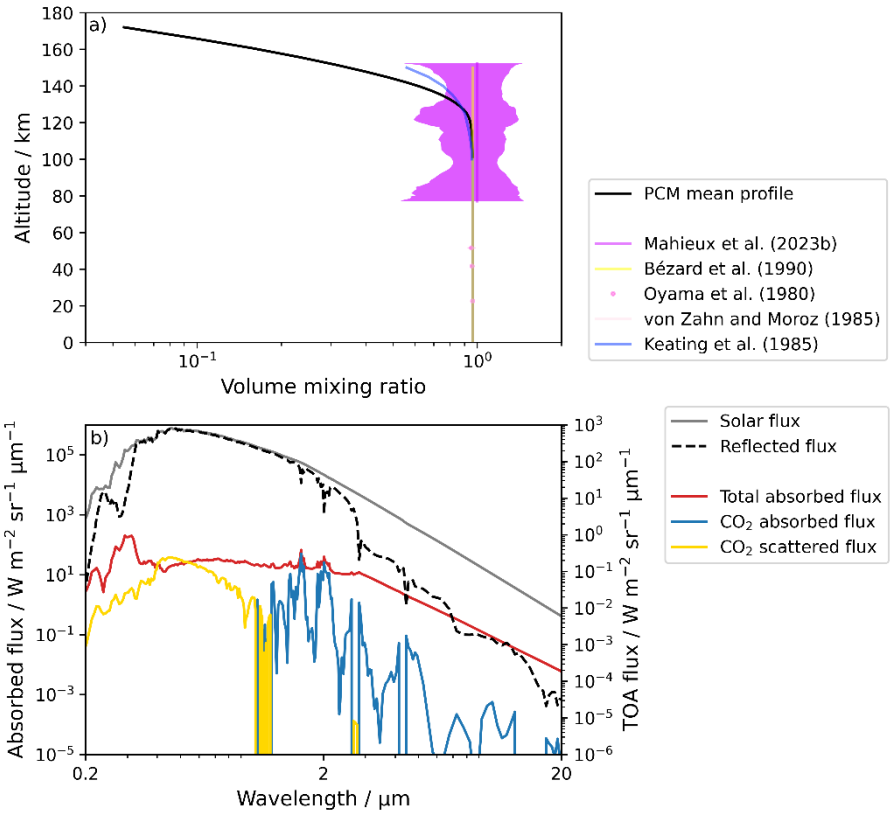

Figure 2.16. a) Modelled vmr profile of CO_2 and observations, b) the absorbed and scattered flux due to CO_2 compared to total absorbed flux and TOA incident solar and outgoing fluxes.

CO

The CO vmr profile is taken from the PCM output. Absorption line data with CO_2 broadening is taken from HITRAN2020 (Gordon et al., 2022). The vmr profile, observations, and contribution to the total flux are shown in Figure 2.17. Plotted observations from Vandaele et al. (2008) show three individual profiles (lines) and the combined area of their uncertainties (shaded area). As discussed in Section 2.1.4, the model profile follows the same trends as observations, but profiles measured by Bézard et al. (1990) and Vandaele et al. (2008) show a sharp minimum above the clouds (80 – 90 km) that is not reproduced by the PCM profile.

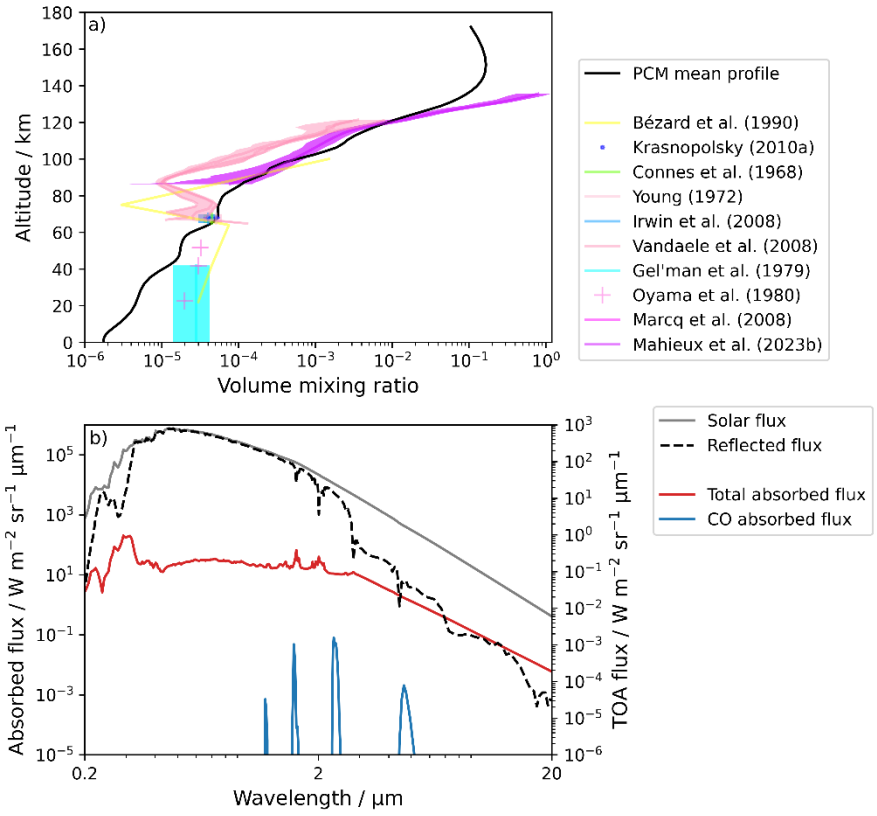

Figure 2.17. a) Modelled vmr profile of CO and observations, b) the absorbed flux due to CO compared to total absorbed flux and TOA incident solar and outgoing fluxes.

N_2

The N_2 vmr profile is taken from the PCM output. The profile, observations, and contribution to the total flux are shown in Figure 2.18. No N_2 absorption lines are included in the model, so its contribution is purely due to Rayleigh scattering.

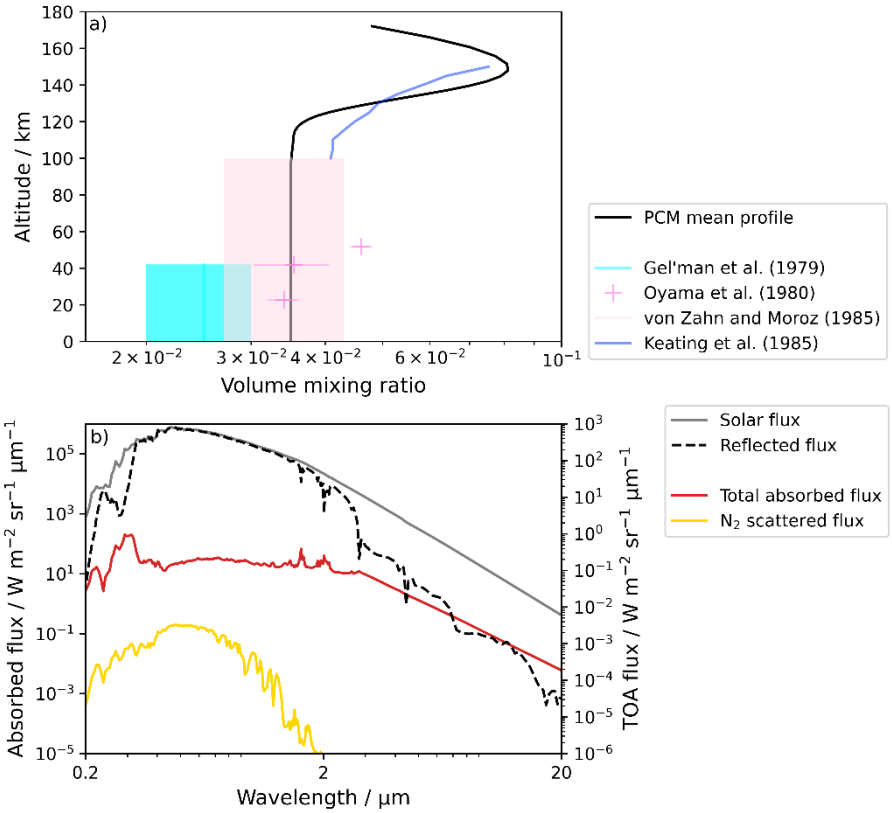

Figure 2.18. a) Modelled vmr profile of N_2 and observations, b) the scattered flux due to N_2 compared to total absorbed flux and TOA incident solar and outgoing fluxes.

H_2O

The H_2O gas vmr profile is taken from the PCM output. Absorption line data with air broadening and self-broadened continuum absorption is taken from HITRAN2020 (Gordon et al., 2022). CO_2 broadening data for H_2O was not available in HITRAN at the time the model was produced. CO_2-broadened H_2O absorption could be included in future modelling, but is not anticipated to make a significant difference to the resulting spectrum. The PCM contains a full microphysical cloud model, and H_2O and H_2SO_4 condense to form the clouds (Section 2.1.2.2). The model currently matches the cloud mass loading fairly well (Figure 2.5), at the expense of the H_2O and SO_2 (Figures 2.19 and 2.20) vmrs. Both H_2O absorption and H_2O-H_2O continuum absorption are included in the contribution of H_2O to the total flux. The modelled profile agrees well with observations below the clouds, but overestimates the vmr through the cloud and haze layers (~60 – 100 km) by at least an order of magnitude. The increase above the cloud and haze deck observed by Mahieux et al. (2023b) and the minimum at near 85 km observed by Bertaux et al. (2007) occur approximately 40 km higher in the PCM model than in the observations.

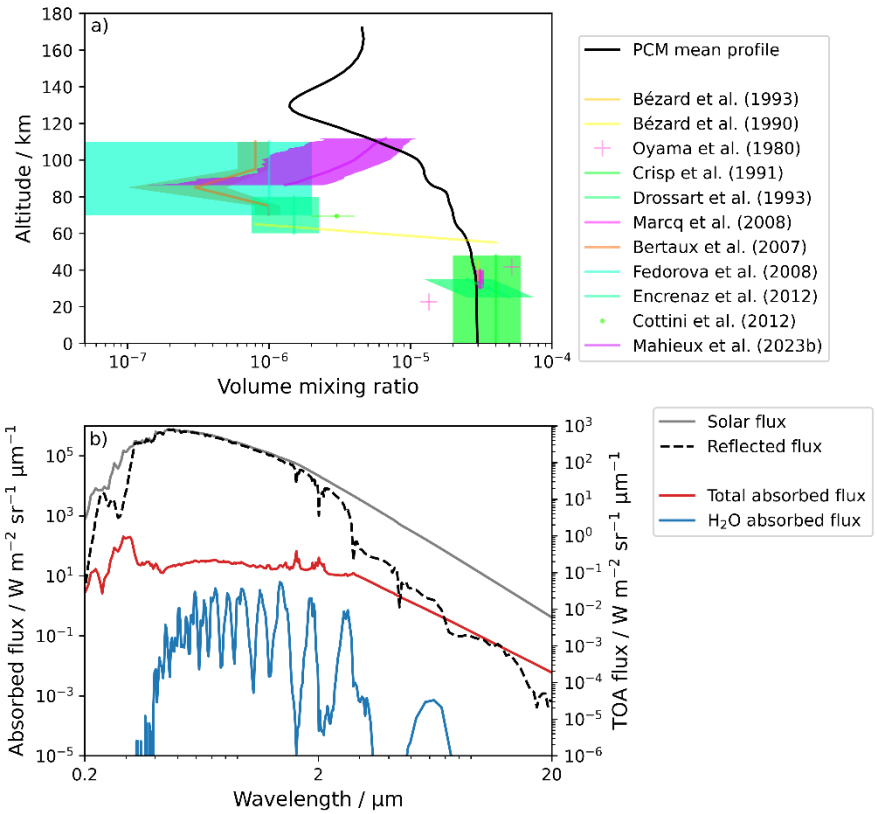

Figure 2.19. a) Modelled vmr profile of H_2O and observations, b) the absorbed flux due to H_2O compared to total absorbed flux and TOA incident solar and outgoing fluxes.

SO_2

The SO_2 profile is taken from the PCM output. Absorption line data with CO_2 broadening and UV cross-section data is taken from HITRAN2020 (Gordon et al., 2022). The profile, observations, and contribution to the total flux are shown in Figure 2.20.

The SO_2 profile produced by the PCM over estimates SO_2 absorption as the PCM concentration above the clouds is two orders of magnitude higher than observations. A large decrease in SO_2 concentration through the cloud deck is seen in all observations from below-cloud concentrations of ~150 ppm (1.5×10^{-4}) to 10 – 100 ppb ($1 \times 10^{-8} – 1 \times 10^{-7}$) above the clouds. The PCM does not reproduce this decrease, and the atmosphere fills with SO_2 if the model is allowed to run to steady state. The model is therefore initialised with a below-cloud concentration an order of magnitude lower than observations to limit the above cloud concentration. In addition, Sandor et al. (2010) and Mahieux et al. (2023a) both observed an increase in vmr somewhere above 85 km, but no corresponding increase is produced by the Venus PCM. It is evident that significant sulphur chemistry is still missing from our understanding of the Venusian atmosphere (Vandaele et al., 2017). SO_2 is the dominant known absorber in the UV, but it cannot match the shape or width of the NUV absorption (Zasova et al., 1981).

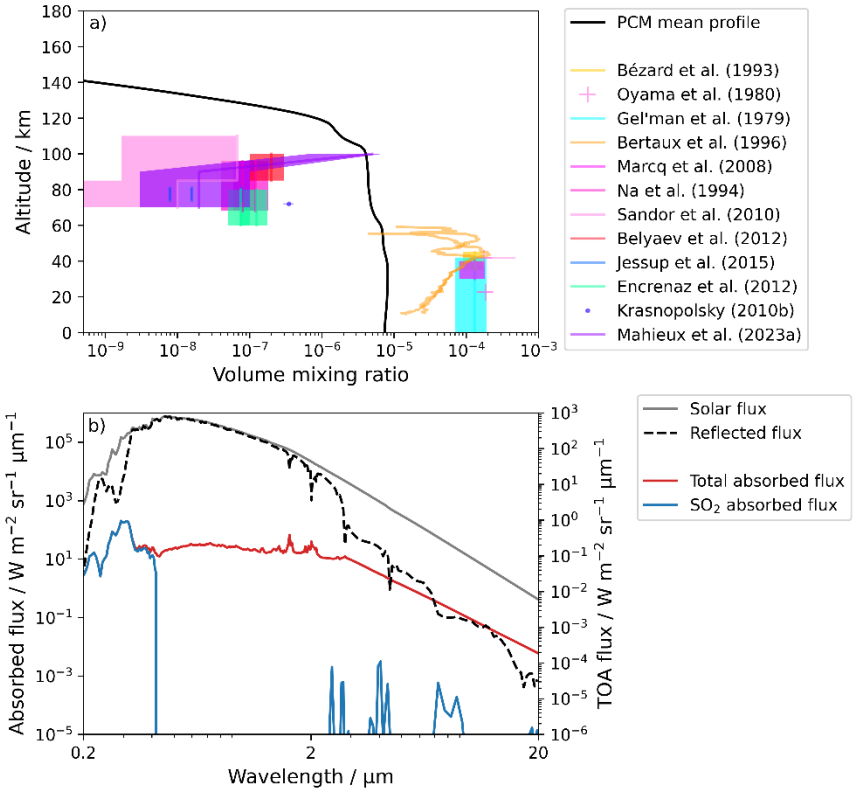

Figure 2.20. a) Modelled vmr profile of SO_2 and observations, b) the absorbed flux due to SO_2 compared to total absorbed flux and TOA incident solar and outgoing fluxes.

H_2S

The H_2S profile is taken from Eymet et al. (2009) as it is not modelled in the PCM. Absorption line data with air broadening (CO_2 broadening was not available) is taken from HITRAN2020 (Gordon et al., 2022). The assumed vmr profile, observations, and contribution to the total flux are shown in Figure 2.21. Very few attempted H_2S observations have been reported, and all have only returned an upper limit for the H_2S concentration. The impact of H_2S on the modelled spectrum is small and has no effect on the visible and ultraviolet region of the spectrum that is of most interest to this study, so the uncertainty in the concentration (or indeed presence) of H_2S should not impact the results.

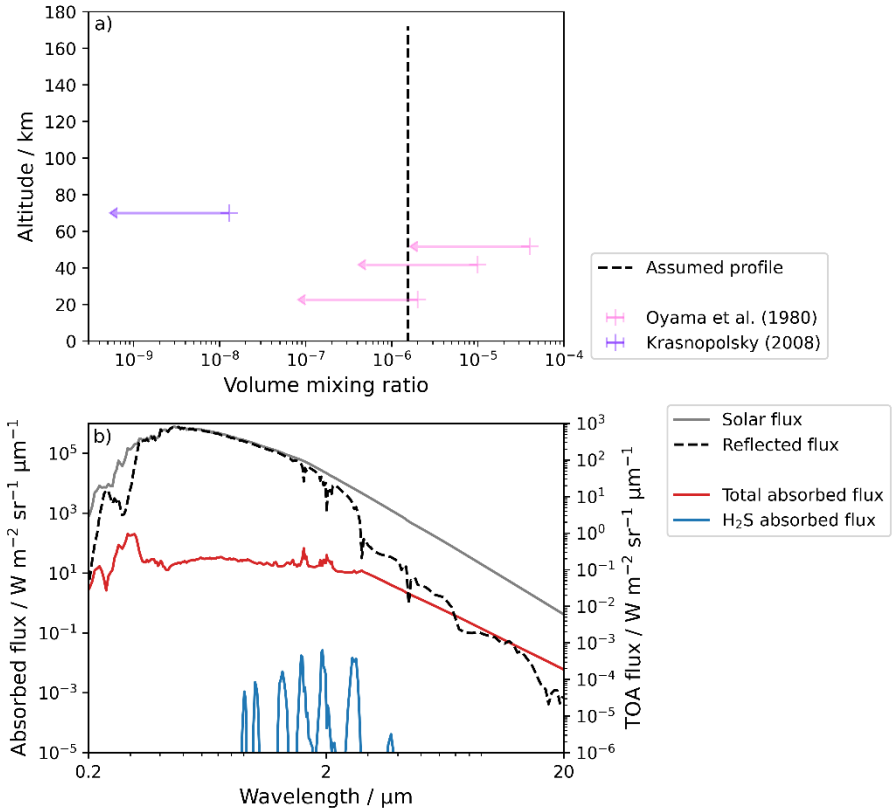

Figure 2.21. a) Assumed vmr profile of H_2S from Eymet et al. (2009), and observations, b) the absorbed flux due to H_2S compared to total absorbed flux and TOA incident solar and outgoing fluxes.

HCl

The HCl profile is taken from the PCM output. Absorption line data with CO_2 broadening is taken from HITRAN2020 (Gordon et al., 2022). The SOCRATES-Venus vmr profile, observations, and contribution to the total flux are shown in Figure 2.22. The model is broadly consistent with observations below and through the clouds, though the observations differ by an order of magnitude near 100 km. Above the clouds, the observations show the profile is either approximately constant (Bertaux et al., 2007; Vandaele et al., 2008) or increasing (Mahieux et al., 2023b), while the PCM predicts a rapid decrease above 100 km.

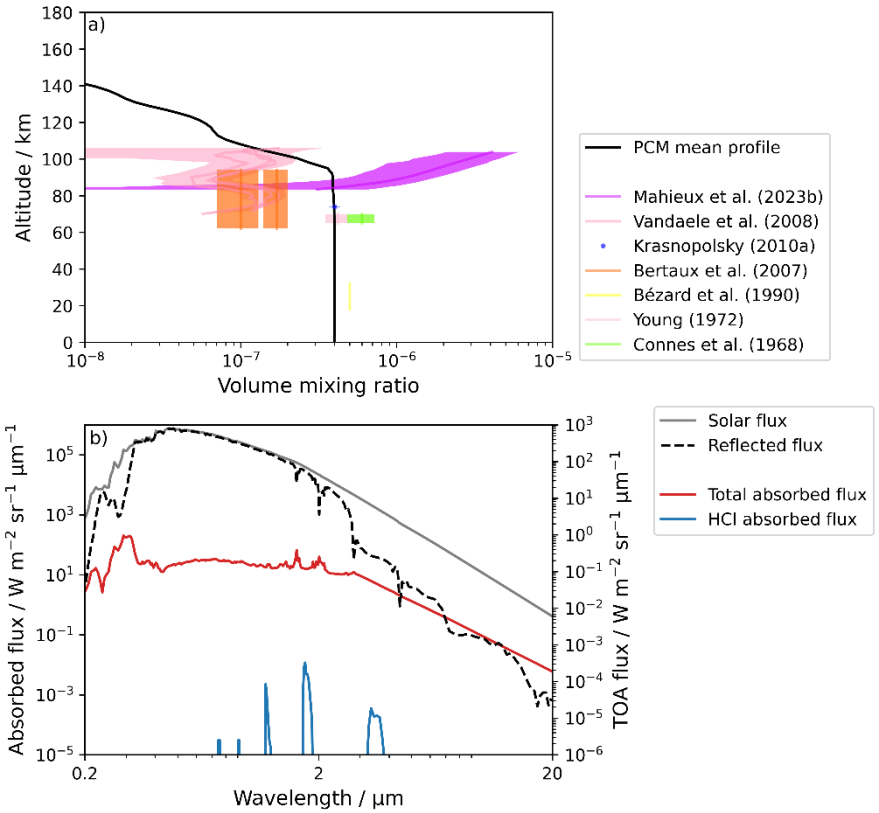

Figure 2.22. a) Modelled vmr profile of HCl and observations, b) the absorbed flux due to HCl compared to total absorbed flux and TOA incident solar and outgoing fluxes.

HF

The HF profile is taken from Eymet et al. (2009). Absorption line data with CO_2 broadening is taken from HITRAN2020 (Gordon et al., 2022). The vmr profile, observations, and contribution to the net flux are shown in Figure 2.23. The impact of HF on the spectrum is small due in large part to its low atmospheric concentration. However, an increase from ~1 ppb to ~10 ppb, to bring the profile in line with observations, is still unlikely to cause a significant impact on the spectrum. As the HF absorption occurs in the IR, it will not impact the UV absorption under consideration.

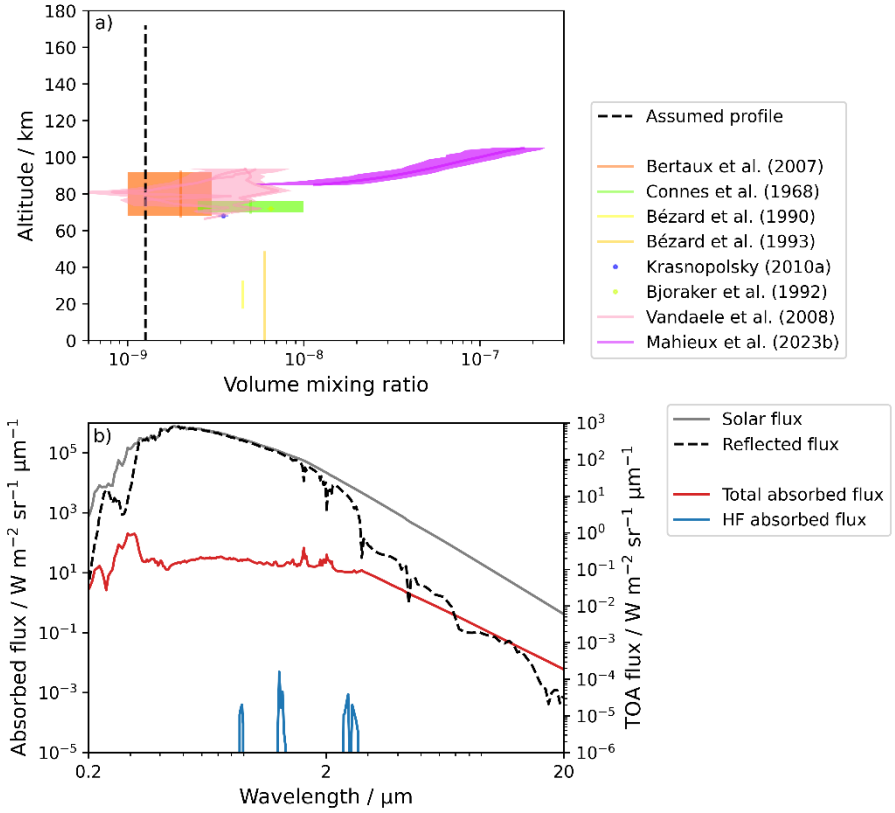

Figure 2.23. a) Assumed vmr profile of HF from Eymet et al. (2009) and observations, b) the absorbed flux due to HF compared to total absorbed flux and TOA incident solar and outgoing fluxes.

OCS

The OCS profile is taken from the PCM Venus output. Absorption line data with CO_2 broadening is taken from HITRAN2020 (Gordon et al., 2022). The vmr profile, observations, and contribution to the net flux are shown in Figure 2.24. The rapid decrease in OCS vmr at 60 – 80 km in the PCM and observations occurs at the same height as the decrease in observed SO_2 (Figure 2.20, though it is more apparent before the model reaches steady state, see Chapter 3), indicating missing sulphur chemistry. While a decrease of ~3 orders of magnitude is seen in the OCS observations in this region, the 8 orders of magnitude decrease modelled is clearly far too large. This decrease through the cloud layer leads to very low concentrations of OCS above the cloud layer, where they could have the most impact on the observed spectrum. The low predicted absorbed flux is likely due to this abnormally low OCS concentration above the clouds. However, as the absorption takes place in the IR, it should not affect the UV absorption under consideration.

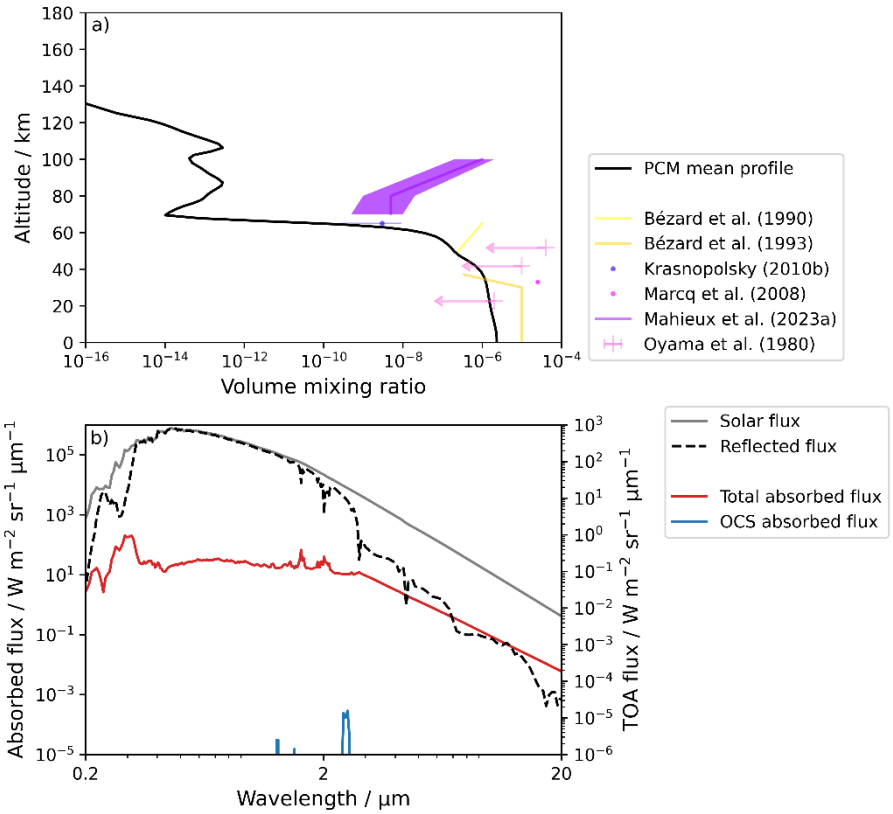

Figure 2.24. a) Modelled vmr profile of OCS and observations, b) the absorbed flux due to OCS compared to total absorbed flux and TOA incident solar and outgoing fluxes. Observations from Oyama et al. (1980) are an upper limit, not detections.

HDO

Many HDO measurements report only the Venusian H_2O/HDO (or D/H) ratio, not the HDO concentration directly. The ratio of HDO to H_2O reported in Eymet et al. (2009) is used with the PCM H_2O profile to construct the SOCRATES HDO profile. The HDO profile will therefore share the limitations of the H_2O profile (Figure 2.19) as well as any from disagreement between the modelled and observed HDO. The effects of this can be seen in Figure 2.25a, where observations show a minimum near 80 km, while the modelled profile based on the H_2O PCM profile locates the minimum near 130 km. Figure 2.25b shows the HDO/H_2O ratio compared to observations. For clarity, these ratios are shown on a linear axis.

Absorption line data with air broadening is taken from HITRAN2020 (Gordon et al., 2022). The contribution of HDO absorption to the net flux is shown in Figure 2.25c. HDO has the smallest impact of any of the standard 10 modelled species.

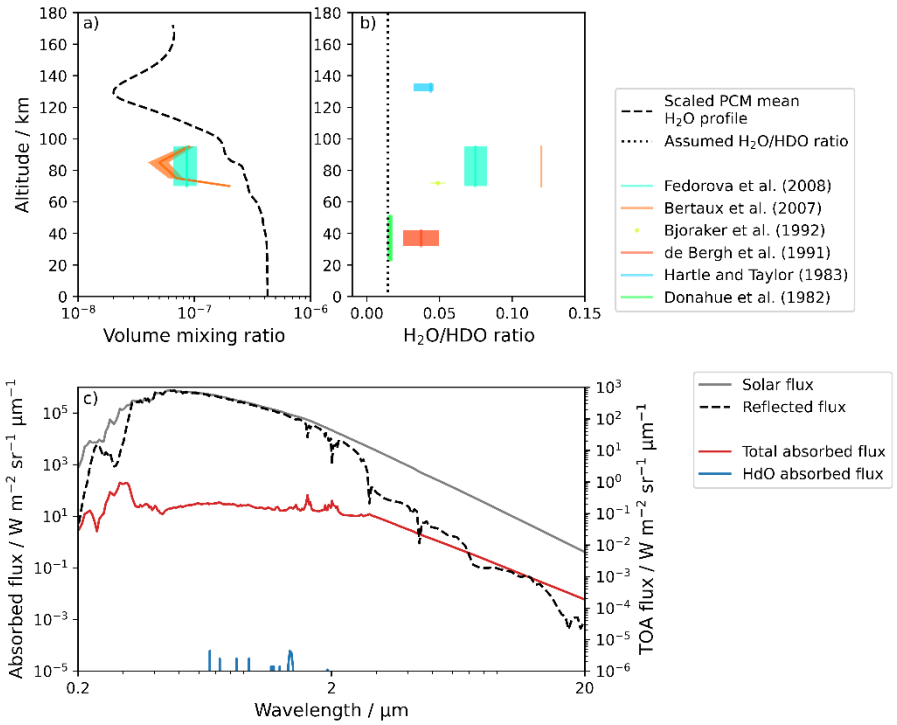

Figure 2.25. a) Predicted HDO vmr, calculated by modelled H_2O vmr profile scaled by a factor of 0.0144 (Eymet et al., 2009) and observations, b) H_2O/HDO ratio compared to observations, c) the absorbed flux due to HDO compared to total absorbed flux and TOA incident solar and outgoing fluxes.

Absence of SO

Despite its absorption in the 190 – 235 nm region, SO is not included in the model. As the model is being compared to observations with a lower limit of ~300 nm (Pérez-Hoyos et al., 2018), SO would not absorb in the wavelength range under comparison, and so would have no impact of the results. In future, if other observations are being used for comparison, SO should be included in the model.

2.2.2.6 Other gas properties

Rayleigh scattering

Rayleigh scattering is included for CO_2 and N_2, the two most abundant gases (Figure 2.26). Comparison with the individual gas contributions for CO_2 (Figure 2.16) and N_2 (Figure 2.18) shows that the majority of the scattering due to CO_2 (peak value of ~ 40 W m^{-2} sr^{-1} μm^{-1}), with only a small N_2 contribution (~ 0.2 W m^{-2} sr^{-1} μm^{-1}), as expected from the low abundance of N_2 compared to CO_2.

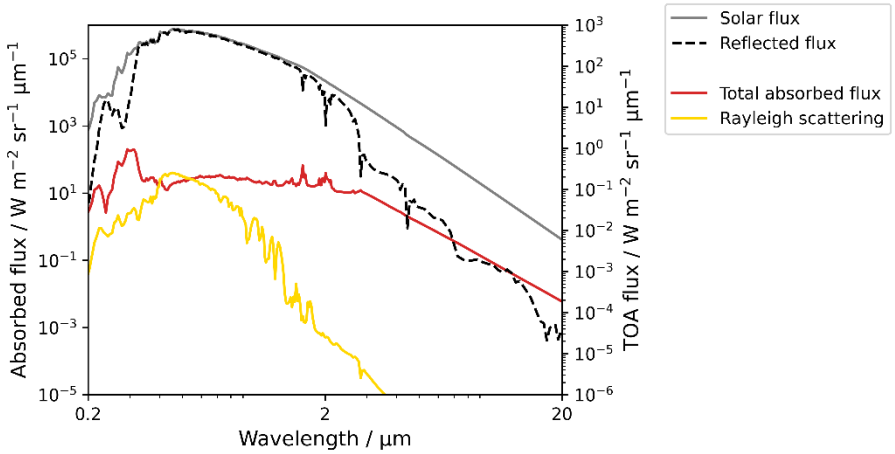

Figure 2.26. The total impact of N_2 and CO_2 Rayleigh scattering on the TOA spectrum.

Continuum absorption

Two sources of continuum absorption are included: CO_2-CO_2 collision induced broadening data and standard H_2O-H_2O continuum data from HITRAN2020 (Gordon et al., 2022). The continuum is taken to be perfectly correlated with H_2O, while the CO_2 continuum uses the overlapping gaseous absorption treatment. The contribution of continuum absorption to the absorbed flux is shown in Figure 2.27. CO_2 continuum absorption is very weak compared to H_2O continuum absorption, and the low H_2O concentrations limit the strength of the H_2O contribution, resulting in low continuum absorption contributions.

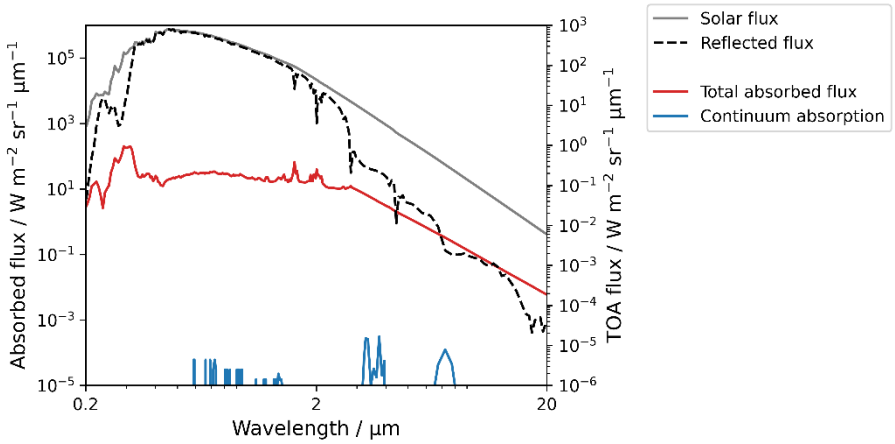

Figure 2.27. Total flux absorbed due to H_2O-H_2O and CO_2-CO_2 continuum absorption compared to the TOA solar and reflected flux spectrum.

2.2.2.7 Aerosol treatment

Cloud modes and locations

Five cloud modes are currently set up for use in SOCRATES-Venus, though only four are currently in use, and any number can be added comparatively easily. The main four are different modes of the clouds – modes 1, 2, 2', and 3 – each of which are initially assumed to have the optical properties of aqueous sulphuric acid. The refractive index for each mode can be modified to include different concentrations of $FeCl_3$ in the different modes (Section 5.3.2.2).

The fifth mode can be used to model an absorbing aerosol species separate to the sulphuric acid clouds, for example replacing some of mode 1 to account for the findings of the Vega descenders reported by Gnedykh et al. (1987) as reported by Titov et al. (2018): around 20% of mode 1 was found to have a refractive index significantly too high to be sulphuric acid. This could be interpreted as mode 1 being a combination of CCN and droplets that have grown on some of the nuclei as proposed by Knollenberg and Hunten (1980). However, without reliable refractive index data for pure $FeCl_3$ or other CCN candidates to model this case, this mode is not generally used.

The vmr of liquid phase water and sulphuric acid is taken from the PCM output. Venusian measurements provide estimates of the number density of the different modes through the atmosphere (e.g., Kawabata et al., 1980; Knollenberg & Hunten, 1980; Luginin et al., 2016; Satoh et al., 2015). Stolzenbach (2016) calculated the mass loading of each mode as a fraction of the total required to reproduce the number densities reported by Knollenberg and Hunten (1980). The size modes and calculated weightings used by Stolzenbach and SOCRATES-Venus are listed in Table 2.4. Stolzenbach's mass loading fractions are used to calculate the vmr of cloud particles in each of the four cloud modes (Figure 2.28). SOCRATES does not have the utility to alter the size distribution of an aerosol mode with height, so the sizes and number densities are an average over the cloud system to give the best fit overall. Mode 2 and 2' are sometimes considered to be one mode which grows in average size as it descends through the cloud layer (Titov et al., 2018). SOCRATES-Venus models the two as separate cloud modes to be able to account for the different average sizes.

Table 2.4. Mass weighting of the cloud modes. r is the geometric mean radius of the log-normal distribution, σ_g the geometric standard deviation and k_{mass} the fraction of the total cloud in that region that is in that mode. Heights refer to the centres of the layers. Layers are approximately 2 km thick, clouds do not have gaps between the layers.

	Values from Stolzenbach (2016)						Values used in SOCRATES-Venus				
	Height / km	**Modes**	***r* / μm**	**σ_g**	**k_{mass}**		**Height / km**	**Modes**	***r* / μm**	**σ_g**	**k_{mass}**
Upper haze	72 – 100	1	0.2	2.16	1.0	Upper haze	72 – 156	1	0.3	1.56	1.0
Upper cloud	60 – 70	1 2	0.2 1.0	2.16 1.29	0.72 0.28	Upper cloud	59 – 70	1 2	0.3 1.0	1.56 1.29	0.72 0.28
Middle cloud	50 – 58	1 2 3	0.15 1.4 3.65	1.9 1.23 1.28	0.0084 0.21 0.7816	Middle cloud	50 – 57	1 2’ 3	0.3 1.4 3.65	1.56 1.23 1.28	0.0084 0.21 0.7816
Lower cloud	48	1 2 3	0.2 1.0 3.65	1.8 1.29 1.28	0.014 0.02 0.966	Lower cloud	48	1 2 3	0.3 1.0 3.65	1.56 1.29 1.28	0.014 0.02 0.966
Pre-cloud	46	1 2	0.15 1.0	1.8 1.29	0.04 0.96	Pre-cloud	45	1 2	0.3 1.0	1.56 1.29	0.04 0.96
Lower haze	30 – 44	1	0.1	1.57	1.0	Lower haze	0 – 42	1	0.3	1.56	1.0

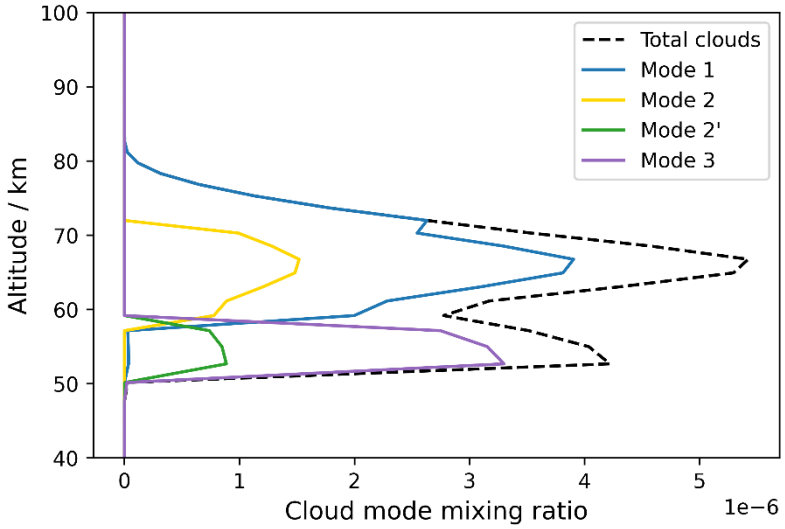

Figure 2.28. Volume mixing ratios of the four cloud modes with altitude. Mixing ratio here refers to the total mole fraction of liquid H_2SO_4 and H_2O.

One limitation of pressure-based vertical layers is that the height of each layers varies through the atmosphere. One of the places where this becomes most unfavourable is in the lower cloud and precloud layers, each of which is one layer thick. The precloud layer is, by chance, closer to 3 km thick than the average of ~2 km for the whole model, which may slightly overestimate the mode 2 and 3 cloud particle concentrations. Fortunately, as the lower clouds and below have only a minor impact on the observed spectrum, the effect of this overestimation is minor. The thin vertical extent of the lower cloud and precloud layers and the large size of the mode 3 particles (causing their dominance in the middle and lower cloud despite their low measured number density) obscures the properties of the lower cloud and precloud layers in Figure 2.28, but mode 1 and 2 particles are present in the relevant layers.

All four cloud modes are described with log-normal size distributions as specified in Table 2.5. These size distributions are used to calculate the monochromatic scattering properties for each mode, which are then averaged over the spectral bands and added into the spectral file.

Table 2.5. Number density and size distribution values used to calculate the single scattering aerosol properties. Number densities are calculated to approximate the mass weightings in Table 2.4, averaged across the atmosphere.

Mode	Particle number density / m^{-3}	Geometric mean radius / µm	Geometric standard deviation
1	3.98×10^8	0.3	1.56
2	7.49×10^7	1.0	1.29
3	6.14×10^7	1.4	1.23
4	1.34×10^7	3.65	1.28

Mode 3 is poorly understood, with some suggestions that it could either be a non-sulphuric acid species (possibly crystalline) or may not exist, its apparent detection instead being due to instrumental error in LCPS that provided most of the cloud number size and density measurements (Knollenberg & Hunten, 1980; Ragent & Blamont, 1980; Toon et al., 1984; see Section 1.3.3.3). In the absence of any certainty about the composition of mode 3, it is modelled as sulphuric acid (though with a basalt core, as described in Section 2.1.2.2), but it must be acknowledged that this may be incorrect. The refractive index of mode 3 is taken to be that of sulphuric acid.

Figure 2.29 shows the impact of each of the cloud modes on the TOA spectrum. As for the gases, this is done by calculating the difference between the TOA spectrum of the whole atmosphere and for the atmosphere with the single cloud mode neglected. All cloud modes have a net scattering effect (negative flux difference). The absolute value is therefore plotted for compatibility with the log scale.

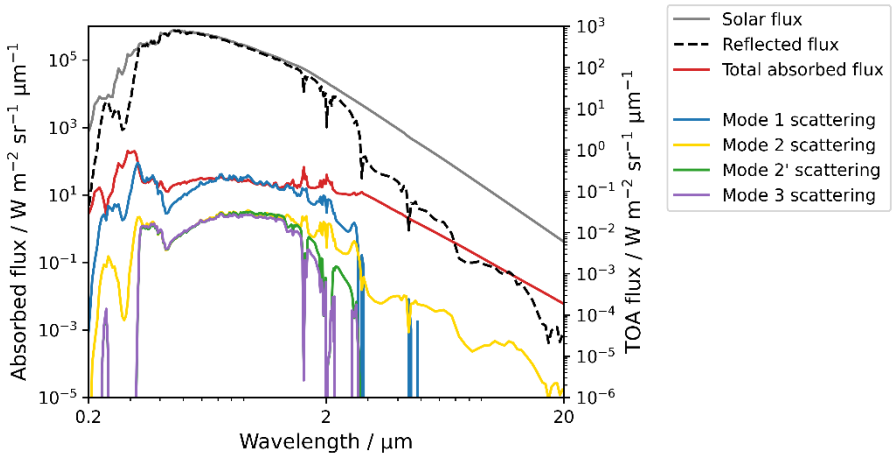

Figure 2.29. Modelled effect of aqueous sulphuric acid modes 1, 2, 2' and 3 cloud particles on the TOA spectrum. All modes have a scattering effect on the spectrum.

Due to its dominance in the upper clouds and haze, mode 1 has the largest effect on the TOA spectrum of all the cloud modes. The refractive index of sulphuric acid contains both scattering and absorbing components (Figure 2.30), but the absorbed light in the visible and UV region is negligible, accounting for the purely scattering effect of the particles. The lower masses of modes 2, 2' and 3 in the upper parts of the cloud deck mean they have a less significant effect than mode 1. Modes 2' and 3 in particular have a much lower effect than might be expected for their size and dominance in the middle and lower clouds due to their depth below the cloud top.

Refractive indices

The sulphuric acid refractive index data is the standard sulphuric acid model used in SOCRATES, adapted from Palmer and Williams (1975) and shown in Figure 2.30.

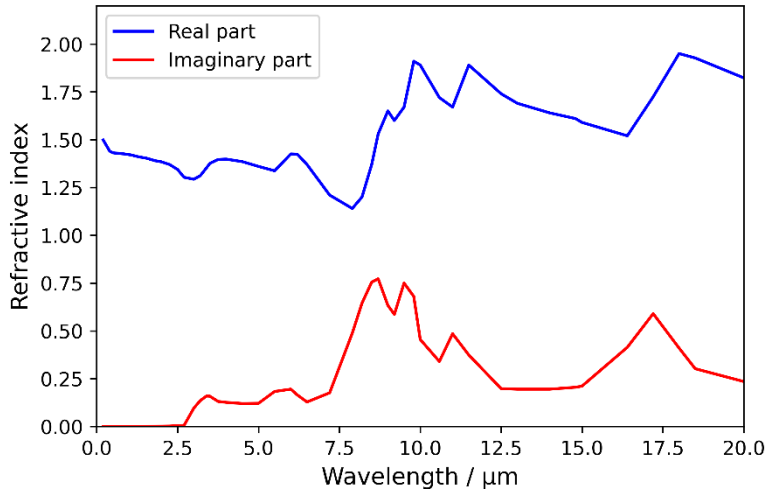

Figure 2.30. Real and imaginary components of the refractive index of 75 wt% sulphuric acid.

2.3. 1D coagulation and sedimentation modelling

Initial analysis of PCM runs with meteoric iron injection showed (as expected) slowly increasing gas-phase $FeCl_3$ concentrations. Prior work suggested that $FeCl_3$ should condense to form solid particles in the upper atmosphere and clouds (Krasnopolsky, 2017), which cannot currently be modelled in the PCM. Instead, the 1D model initially developed to study the transport of MSPs between 100 km and the surface by Frankland et al. (2017) was used. Vertical profiles of the eddy diffusion coefficient (K_{zz}) and pressure are based on 1D models by Krasnopolsky (2007, 2012), and the temperature profile is an equatorial zonal average from the PCM. The profiles of T and K_{zz} are illustrated in Figure 2.31.

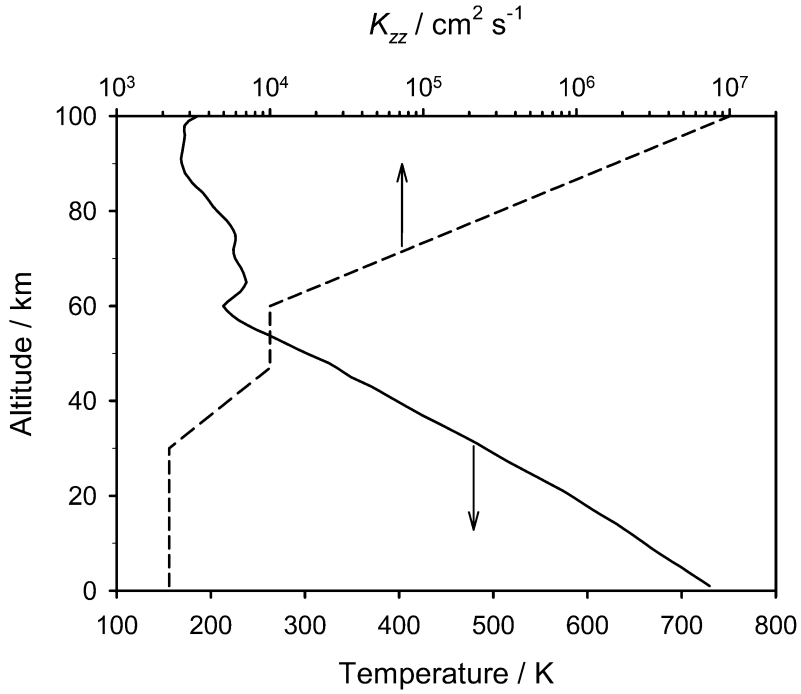

Figure 2.31. Vertical profiles of temperature (solid line, PCM model daytime average at the equator) and eddy diffusion coefficient (K_{zz}, dashed line) from Krasnopolsky (2007, 2012).

Due to high concentrations of HCl around 100 km (~4×10^7 cm^{-3}), all the meteoric elements were assumed to form metal chlorides at this altitude through acid-base reactions, by analogy with the example of $FeCl_3$ (Chapter 5). Using the ablation profiles from Carrillo-Sánchez et al. (2020), the global mass injection rate at the upper model boundary was predicted to be (in descending order of mass input): $FeCl_3$ (11.9 t d^{-1}); OSi(OH)Cl (6.57 t d^{-1}); $MgCl_2$ (6.28 t d^{-1}); NaCl (0.94 t d^{-1}); $NiCl_3$ (0.73 t d^{-1}); $AlCl_3$ (0.45 t d^{-1}); and $CaCl_2$ (0.31 t d^{-1}). The weighted average molar mass of a metal chloride molecule is then 116 amu. These chloride molecules were assigned a density of 2350 kg m^{-3}, so that the monomer chloride molecules (treated as spheres) have a radius of 0.27 nm. Assuming that the injection from above 100 km is globally homogenous, this represents a monomer particle flux of 3.4×10^5 cm^{-2} s^{-1}, 31% of which are iron chlorides. Particles are removed at the surface with a deposition velocity of 1 cm s^{-1}.

The model has the option to allow the monomers to coagulate into MSPs. In reality, this should occur to some extent above the haze layer (i.e., above 80 km), but the metal chloride molecules are likely incorporated into droplets below that. Coagulation is treated in the model using a semi-implicit, volume-conserving sectional code (Saunders & Plane, 2006), where particle growth occurs through 65 discrete size bins. These start with the first bin size (r = 0.27 nm) corresponding to the monomer, and the volume of each successive bin then increases by a factor of 1.5 up to the largest size of 1.54 μm. Particle growth is assumed to be dominated by Brownian diffusion; collisions between particles result in coalescence where the spherical morphology and particle density are maintained. The collision rate coefficients of the particles are calculated using the expression for the free molecular regime (Knudsen number >> 1), interpolated into the transition regime for larger particles (Fuchs, 1964). A collision efficiency of 1%, decreasing the collision rate coefficients by a factor of 100, is applied to allow for collisions which do not result in coalescence.

The vertical sedimentation velocity of particles is determined in the model from the form of Stokes' law describing a spherical particle falling through a stationary fluid (Jacobson, 2005), which includes the Cunningham slip correction factor to take account of the non-continuum effects of drag on small particles. The continuity equation for the particles in each size bin was then solved using a time-implicit integration scheme (Shimazaki, 1985). Full details and description are available in Frankland et al. (2017). Results of the modelling are presented in Chapter 5.

3. Photochemical and radiative transfer modelling of OSSO

Much of the work presented in this chapter is also in a co-authored publication:

> Egan, J. V., Feng, W., James, A. D., et al. (2025). Is OSSO a significant contributor to the unknown UV absorber in Venus' atmosphere? *Geophysical Research Letters*, 52, e2024GL113090. https://doi.org/10.1029/2024GL113090

3.1 Introduction

In this chapter, the reaction kinetics of the production of S_2O_2 from SO + SO third body recombination (Frandsen et al., 2016) are revisited, and the reaction of the S_2O_2 isomers with atomic O, which has been detected above the clouds (Hübers et al., 2023), and Cl are investigated. Photolysis cross-sections and the resulting photolysis rates of the S_2O_2 isomers are predicted. The Venus PCM (described in Section 2.1) was modified to include the new S_2O_2 isomers and their reactions, from which their concentrations could be predicted. The sensitivity of the isomers to the O and Cl reactions was investigated and the S_2O_2 concentration predicted with and without those reactions. The modelled concentrations were then used with SOCRATES (described in Section 2.2) to model the resulting TOA reflectance resulting from absorption by S_2O_2.

3.1.1 Terminology

Despite being a relatively young field of study, the nomenclature in use for isomeric geometries of S_2O_2 is already evolving. The terminology used to refer to the first four isomers of S_2O_2 (Figure 3.1) is listed in Table 3.1. Additional terminology exists for other isomers (Frandsen et al., 2016; Hochlaf et al., 2021), but they are only used in a limited number of papers and are broadly consistent, so will not be included here.

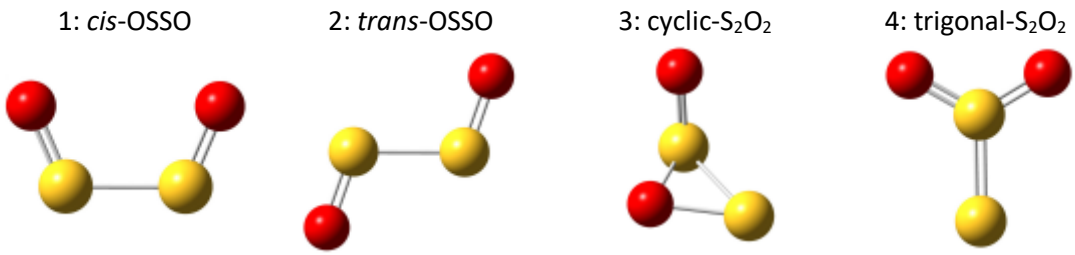

Figure 3.1. Adapted from Frandsen et al. (2016). Diagrams of the four relevant S_2O_2 isomers considered in this thesis. Oxygen atoms are shown in red, sulphur atoms in yellow. Isomer numbers are indicated in labels. Table 3.1 details the nomenclature in use for these isomers in the literature.

Table 3.1. Summary of the nomenclature used to refer to the first four isomers of S_2O_2 in the current literature.

Paper	**Name given in paper**				
Isomer number	**Collective**	**1**	**2**	**3**	**4**
Frandsen et al. (2016)	S_2O_2	*cis*-OSSO	*trans*-OSSO	c_1-S_2O_2 C_1-S_2O_2	trigonal-S_2O_2
Krasnopolsky (2018)	S_2O_2	*cis*-OSSO	*trans*-OSSO	–	S=SO_2
Wu et al. (2018)	S_2O_2	*syn*-OSSO	*anti*-OSSO	*cyclic* OS(=O)S	S=SO_2
Pinto et al. (2021)	$(SO)_2$	*cis*-OSSO cis-OSSO	*trans*-OSSO trans-OSSO	C1-S_2O_2 cyclic OS(=O)S	trigonal S=SO_2 trigonal-S_2O_2
Hochlaf et al. (2021)	S_2O_2	*cis*-OSSO	*trans*-OSSO	*cyc*-OSSO	*trigonal*-OSSO
This thesis	S_2O_2	*cis*-OSSO	*trans*-OSSO	cyclic-S_2O_2 *cyc*-S_2O_2	trigonal-S_2O_2 *trig*-S_2O_2

Throughout this thesis, the following conventions are adopted: individually, the four forms are *cis*-OSSO, *trans*-OSSO, cyclic-S_2O_2, and trigonal-S_2O_2. If space is short, such as in figures, cyclic-S_2O_2 is shortened to *cyc*-S_2O_2, and trigonal-S_2O_2 to *trig*-S_2O_2. Collectively, the isomers are referred to as S_2O_2. The updated atmospheric models do not include trigonal-S_2O_2, so any references to S_2O_2 with regard to the updated PCM runs should be taken to refer solely to *cis*-OSSO, *trans*-OSSO, and cyclic-S_2O_2. Where *cis*- and *trans*-OSSO isomers are required to be referred to separately to cyclic- and trigonal-S_2O_2, they are collectively referred to as "OSSO".

3.1.2 Prior work

3.1.2.1 Concentrations

The combination of two isomers of S_2O_2 – *cis*- and *trans*-OSSO – was proposed to be a significant contributor to the unknown UV absorption due to their theoretically-predicted ready formation from the recombination of gas-phase SO, and good spectral agreement with the shape of the unknown UV absorber (Frandsen et al., 2020; Frandsen et al., 2016). The absorption is due to cleavage of the S-S bond of the OSSO isomers to reform SO molecules, resulting in a short lifetime for the species, with predicted photolysis rate coefficients of 0.16 s^{-1} and 0.39 s^{-1} for *cis*- and *trans*-OSSO, respectively. Frandsen et al. (2016) predicted the formation of three isomers of S_2O_2 under Venusian conditions. Assuming equal production of *cis*- and *trans*-OSSO, and modelling a photochemical steady state between formation from SO and destruction by photolysis, *cis*-OSSO would account for 69% of total S_2O_2, *trans*-OSSO 29%, and the remaining

2% would be cyclic-S_2O_2. This was supported by laboratory measurements by Wu et al. (2018) of these species as the products of SO + SO combination in a matrix isolation study. Frandsen et al. (2016) reported a single layer of S_2O_2 at an altitude around 62 km, with a peak concentration of ~6×10^{10} cm^{-3}.

However, 1D photochemical modelling of the sulphur cycle in the Venusian atmosphere found that OSSO concentrations were two orders of magnitude too low to explain the observed UV absorption (Krasnopolsky, 2018; Pinto et al., 2021). Pinto et al. (2021) reported modelled profiles for *cis*-OSSO, *trans*-OSSO and the fourth isomer, trigonal-S_2O_2, with a peak vmr at 65 km of 2.5×10^{-10} and a concentration ratio *cis*-OSSO:*trans*-OSSO:trigonal-S_2O_2 of 64:16:20%, while Krasnopolsky (2018) reported two layers, with peaks of 2.9×10^7 cm^{-3} at 59 km and 4.7×10^8 cm^{-3} at 67 km, and a concentration ratio of *cis*-OSSO:*trans*-OSSO after photolysis of 82:18%, with no mention made of a third isomeric form present.

It should however be noted that Pinto et al. (2021) and Krasnopolsky (2018) both assumed 70:30% production of the *cis*- and *trans*- isomers, and Pinto et al.'s inclusion of trigonal-S_2O_2 seems to be a misinterpretation of Frandsen et al. (2016). They reported: "[Frandsen et al. (2016)] concluded that SO recombination yields ~49% as cis-OSSO, ~49% as trans-OSSO isomers and no more than 2% as the trigonal isomer ($S=SO_2$) which is the lowest energy isomer." Frandsen et al. in fact reported equal production of *cis*-OSSO and *trans*-OSSO from SO, and the yields after photolysis and transformation between isomers of *cis*-OSSO, *trans*-OSSO, and cyclic-S_2O_2 (which they term C_1-S_2O_2) to be 69.3%, 28.9% and 1.8% respectively (Table S18 of Frandsen et al. (2016)). Frandsen et al. reported the formation of trigonal-S_2O_2 from cyclic-S_2O_2 via a 152 kJ mol^{-1} barrier was "not important" and did not model or estimate trigonal-S_2O_2 concentrations. Pinto et al.'s inclusion of trigonal-S_2O_2 instead of cyclic-S_2O_2 is taken to be an error, not an indication of missing chemistry.

Photolysis was the only loss process of S_2O_2 considered by Frandsen et al. (2016) and Krasnopolsky (2018), with Frandsen et al. arguing that collision with SO – the only sufficiently abundant reactive species at the altitudes considered to collide with OSSO in its short lifetime – would result in destruction of OSSO that would be 2 orders of magnitude slower than photolysis, and could therefore be neglected. Pinto et al. (2021) included additional reactions of the S_2O_2 isomers with O, H, SO, S, S_2, and NO, with rate constants taken or inferred from Zhang et al. (2012). Zhang et al.'s reactions, dating from before Frandsen et al.'s emphasis of the need to treat the correct isomers of S_2O_2 in models, assumed all S_2O_2 is trigonal-S_2O_2, so all of their reported rates should be treated with caution.

3.1.2.2 Absorption cross-sections

Frandsen et al. (2016) initially reported only the wavelength maxima of the *cis*- and *trans*-OSSO cross-sections (316 and 364 nm, respectively), and assumed a Lorentzian lineshape for the two

species. Pérez-Hoyos et al. (2018) reported a combined and normalised spectrum of both OSSO isomers, citing Frandsen et al. (2016), though the spectrum they report does not match that provided by Frandsen et al. (2016). Frandsen et al. (2020) presented fully computed spectra rather than the lineshapes assumed previously.

Wu et al. (2018) reported experimentally measured UV-Vis spectra of the products of high-vacuum flash pyrolysis of ethylene episulphoxide (C_2H_4SO), which they condensed to a solid at 15 K and irradiated at different wavelengths. By comparison of IR and UV-vis spectra and modelled spectra, they identified the formation and loss of different isomers following irradiation with different wavelengths of light. The spectra they reported are not pure samples of any one of the isomers, but probably contain contributions from several isomers and other species, such as SO_2. They did not measure the strength of the absorption and no concentrations of the individual isomers were reported.

Figure 3.2 shows a comparison of the *cis*- and *trans*-OSSO spectra calculated, reported, or measured by Frandsen et al. (2020); Frandsen et al. (2016); Pérez-Hoyos et al. (2018); and Wu et al. (2018), along with the spectra calculated in this work (Section 3.3.3). Spectra from Frandsen et al. (2016) and Frandsen et al. (2020) and this work report cross-sections (primary y axis). Spectra from Wu et al. (2018) and Pérez-Hoyos et al. (2018) are plotted as unitless absorbance (secondary axis) as Pérez-Hoyos et al. reported normalised absorbance for the sum of both *cis*- and *trans*-OSSO, while Wu et al. reported measured spectra of the unirradiated products of their reaction, followed by several subsequent irradiations. They observed a decrease in absorption at 390 and 517 nm following irradiation with 579 nm light, which they attributed to the loss of *trans*-OSSO. Subsequent irradiation at 365 nm depleted the absorption band at 375 nm, which they attributed to loss of *cis*-OSSO, and increases absorption at 517 nm, which they then attributed to "*syn*-OSOS" (which Frandsen et al. (2016) called "*cis*-SOSO" and is not included in this study) rather than *trans*-OSSO due to its response to later irradiations. The spectra presented in Figure 3.2 are calculated by taking the differences of the spectra reported by Wu et al. before and after depletion of the OSSO isomers (*cis*-OSSO is the 597 nm-irradiated spectrum minus the 365 nm-irradiated spectrum, while *trans*-OSSO is the unirradiated spectrum minus the 597 nm-irradiated spectrum). The relative heights of spectra from Pérez-Hoyos et al. and Wu et al. should not be compared to each other or to the other spectra.

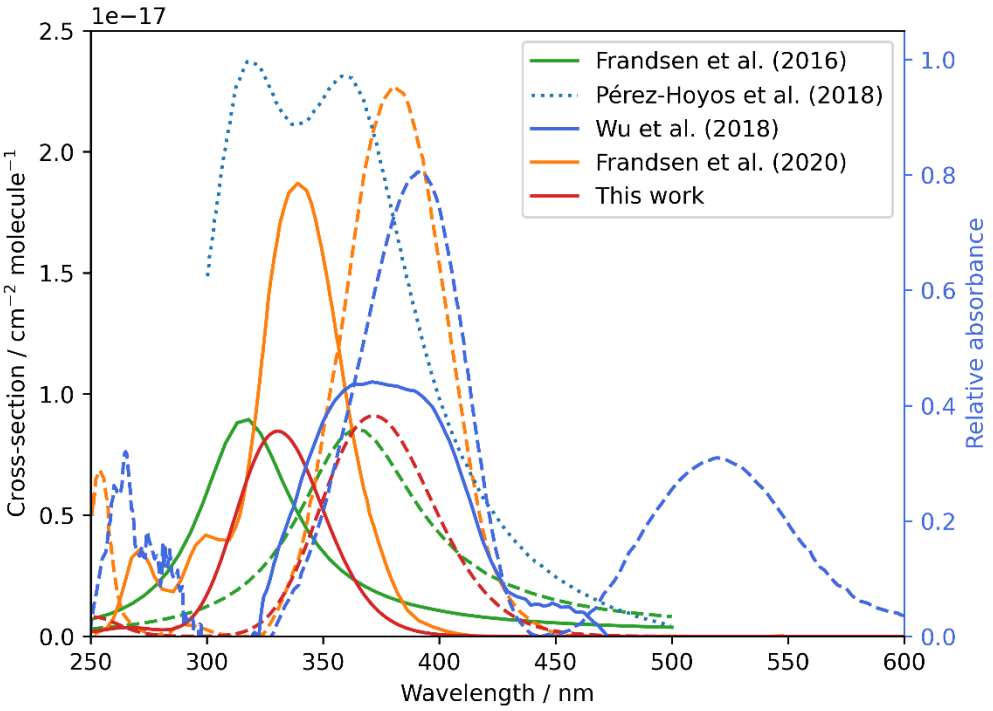

Figure 3.2. Comparison of the literature OSSO spectra with those of this work. Solid lines are *cis*-OSSO spectra, dashed lines are *trans*-OSSO. Spectra from Frandsen et al. (2016) and Frandsen et al. (2020) and this work are plotted on the primary axis and compare cross-section values. Spectra from Wu et al. (2018) and Pérez-Hoyos et al. (2018) are plotted on the secondary axis (blue) as the authors did not report cross-sections, only absorbance. In the case of the spectrum from Pérez-Hoyos et al. (dotted line), this absorbance is normalised to maximum of 1.0 and is a combination of both *cis*- and *trans*- isomers.

The cross-sections predicted by Frandsen et al. (2020) are more than twice the strength of those from their earlier work (Frandsen et al., 2016) and those predicted in this work. There are also small shifts in the central wavelengths of the absorbance spectra. The spectrum from Pérez-Hoyos et al. (2018) references Frandsen et al. (2016), and is plotted on the secondary axis with a maximum of 1, so should not be interpreted as an additional source supporting the strength of absorption reported in Frandsen et al. (2020). Frandsen et al. (2020) report the difference from the spectrum reported in their earlier work is due to the different method used to calculate the spectra.

The spectra reported by Wu et al. (2018) differ significantly from the predicted spectra. The absorption band that Wu et al. identified as *cis*-OSSO is shifted to significantly longer wavelengths than is predicted and would not be suitable for reproducing the NUV absorption. They also found additional absorption at 517 nm which they attributed to *trans*-OSSO. If this absorption band is present in gas phase species, it would preclude OSSO as the unknown UV absorber as it is not consistent with observations. Some differences are to be expected as the predicted spectra are for gas-phase species, but expected spectral shifts from matrix isolation are significantly smaller than the differences seen and not sufficient to explain the difference in the

spectra. It is likely that the species measured are therefore not *cis*-OSSO and *trans*-OSSO as Wu et al. claim.

3.2 Existing PCM chemistry

3.2.1 Sulphur chemistry

3D photochemical modelling is carried out using the Venus PCM. Validation of the model and comparison to observations is available in Chapter 2. Table 3.2 lists the sulphur chemistry included in the "out-of-the-box" run.

For recombination reactions, marked with [a], the rate coefficient, k, is given by

$$\mathrm{k} = \frac{\mathrm{k_0[n]}}{1 + \frac{\mathrm{k_0[n]}}{\mathrm{k_\infty}}} \times F_c^{\,xpo} \tag{3.1}$$

where

$$\mathrm{xpo} = \frac{1}{1 + \log_{10}\left(\left(\frac{\mathrm{k_0[n]}}{\mathrm{k_\infty}}\right)^2\right)}$$

and [n] is the total number concentration of the atmosphere.

Table 3.2. Sulphur chemistry in r3188 of the Venus PCM.

ID	Reaction	Rate[b]
	SO_2 + hv → SO + O	Computed online, see Stolzenbach et al. (2023)
	SO + hv → S + O	
	S_2 + hv → 2 S	
	OCS + hv → CO + S	
	H_2SO4 + hv → SO_3 + H_2O	
†	trigonal-S_2O_2 + hv → 2 SO	
g001	S + O_2 → SO + O	$k = 1.6 \times 10^{-12} exp\left(\frac{100}{T}\right)$
g002	S + O_3 → SO + O_2	$k = 1.2 \times 10^{-11}$
g003	SO + O_2 → SO_2 + O	$k = 1.6 \times 10^{-13} exp\left(\frac{-2280}{T}\right)$
g004	SO + O_3 → SO_2 + O_2	$k = 3.4 \times 10^{-12} exp\left(\frac{-1100}{T}\right)$
g005	SO + OH → SO_2 + H	$k = 2.6 \times 10^{-11} exp\left(\frac{330}{T}\right)$
g006	S + OH → SO + H	$k = 6.60 \times 10^{-11}$
g007†[a]	SO + O (+ CO_2) → SO_2	$k_0 = 4.2 \times 10^{-30}$ $k_\infty = 5.3 \times 10^{-11}$ $F_c = 0.6$
g008	SO + HO_2 → SO_2 + OH	$k = 2.8 \times 10^{-11}$

g009 [a]	$SO_2 + O\ (+ CO_2) \rightarrow SO_3$	$k_0 = 5\ \times 9.5 \times 10^{-23}\ T^{-3}\ exp\left(\frac{-2400}{T}\right)$ $k_\infty = 6.12 \times 10^{-13} exp\left(\frac{-850}{T}\right)$ $F_c = 0.558 \times exp\left(\frac{T}{316}\right) + 0.442 \times exp\left(\frac{-T}{7442}\right)$
g010†[a]	$S + O\ (+ CO_2) \rightarrow SO$	$k_0 = 1.5 \times 10^{-34}\ [n]\ exp\left(\frac{900}{T}\right)$
g011	$SO_3 + H_2O\ (+ H_2O) \rightarrow H_2SO_4$	$k = \begin{cases} k_T & if\ T \geq 100\ K \\ 5.71\ \times 10^{-13} & otherwise \end{cases}$ where $k_T = 2.26 \times 10^{-43}\ T \times exp\left(\frac{6540}{T}\right)$
g012	$SO + ClO \rightarrow SO_2 + Cl$	$k\ = 2.8 \times 10^{-11}$
g013	$SO + SO_3 \rightarrow 2\ SO_2$	$k\ = 2.0 \times 10^{-15}$
g014	$SO_3 + O \rightarrow SO_2 + O_2$	$k = 2.32 \times 10^{-16} exp\left(\frac{-487}{T}\right)$
g015†	$2\ SO\ (+ CO_2) \rightarrow$ trigonal-S_2O_2	$k_0 = 1.1 \times 10^{-29}$ $k_\infty = 1.0^{-11}$ $F_c = 0.6$
g016†	trigonal-$S_2O_2\ (+ CO_2) \rightarrow 2\ SO$	$k = \frac{k_{g016}}{2.5 \times 10^{-28} \times exp\left(\frac{6000}{T}\right)}$
g017	$ClCO_3 + SO \rightarrow Cl + SO_2 + CO_2$	$k\ = 1.0 \times 10^{-11}$
g018	$S + CO\ (+ CO_2) \rightarrow OCS$	$k = 2.5\ \times 4.0 \times 10^{-33} exp\left(\frac{-1940}{T}\right)$
g019	$ClCO + S \rightarrow OCS + Cl$	$k\ = 3.0 \times 10^{-12}$
g020 [a]	$SO_2 + OH\ (+ CO_2) \rightarrow HSO_3$	$k_0 = 2.5 \times 3.3 \times 10^{-31} \left(\frac{300}{T}\right)^{4.3}$ $k_\infty = 1.6 \times 10^{-12}$ $F_c = 0.6$
g021	$HSO_3 + O_2 \rightarrow HO_2 + SO_3$	$k = 1.3 \times 10^{-12} exp\left(\frac{-330}{T}\right)$
g022 [a]	$2\ S\ (+ CO_2) \rightarrow S_2$	$k_0 = 1.19 \times 10^{-29}$ $k_\infty = 1.0 \times 10^{-10}$ $F_c = 0.6$
g023	$S_2 + O \rightarrow SO + S$	$k = 2.2 \times 10^{-11} exp\left(\frac{-84}{T}\right)$
g024	$S + OCS \rightarrow S_2 + CO$	$k = 6.63 \times 10^{-20}\ T^{2.57}\ exp\left(\frac{-1180}{T}\right)$

g025	$OCS + O \rightarrow SO + CO$	$k = 1.6 \times 10^{-11} exp\left(\frac{-2150}{T}\right)$
g026	$S + SO_3 \rightarrow SO_2 + SO$	$k = 1.0 \times 10^{-16}$
g027	$S + HO_2 \rightarrow SO + OH$	$k = 3.0 \times 10^{-11} exp\left(\frac{200}{T}\right)$
g028	$S + ClO \rightarrow SO + Cl$	$k = 4.0 \times 10^{-11}$
g029	$H_2SO_4 (+ H_2O) \rightarrow SO_3 + H_2O$	$k = 7.0 \times 10^{-14} exp\left(\frac{-5170}{T}\right)$
g030†	$SO_3 + OCS \rightarrow$ *trigonal*-$S_2O_2 + CO_2$	$k = 1.0 \times 10^{-11}\ exp\left(\frac{-10\ 000}{T}\right)$
g031†	*trigonal*-$S_2O_2 + OCS \rightarrow SO_2 + CO + S_2$	$k = 1.0 \times 10^{-20}$
g032	$2\ SO \rightarrow SO_2 + S$	$k = 1.0 \times 10^{-12} exp\left(\frac{-1700}{T}\right)$

† Indicates reactions that were changed in later model development.

[a] Recombination reactions, see Equation 3.1.

[b] Units: photolysis reactions, s^{-1}; bimolecular reactions, cm^3 $molecule^{-1}$ s^{-1}; termolecular, cm^6 $molecule^{-2}$ s^{-1}.

The variation in observable sulphur-containing species and H_2O in the out-of-the-box model run over 9.0 Venus days are shown in Figure 3.3. The accumulation of SO_2 to a near-constant vmr throughout the atmosphere indicates that there is insufficient SO_2 removal chemistry in the cloud layer. Observations of SO_2 through the Venusian clouds show a decrease of three to four orders of magnitude through the cloud deck (Figure 1.30), which is not reproduced by models, including the PCM (Bierson & Zhang, 2020; Rimmer et al., 2021; Vandaele et al., 2017; Yung & DeMore, 1982). The SO_2 is destroyed in the PCM by photolysis to form SO, which occurs towards the cloud tops, and oxidation to form HSO_3 or SO_3, from which H_2SO_4 is formed and condenses to produce the clouds. At the cloud base, H_2SO_4 dissociates to reform SO_2 and H_2O.

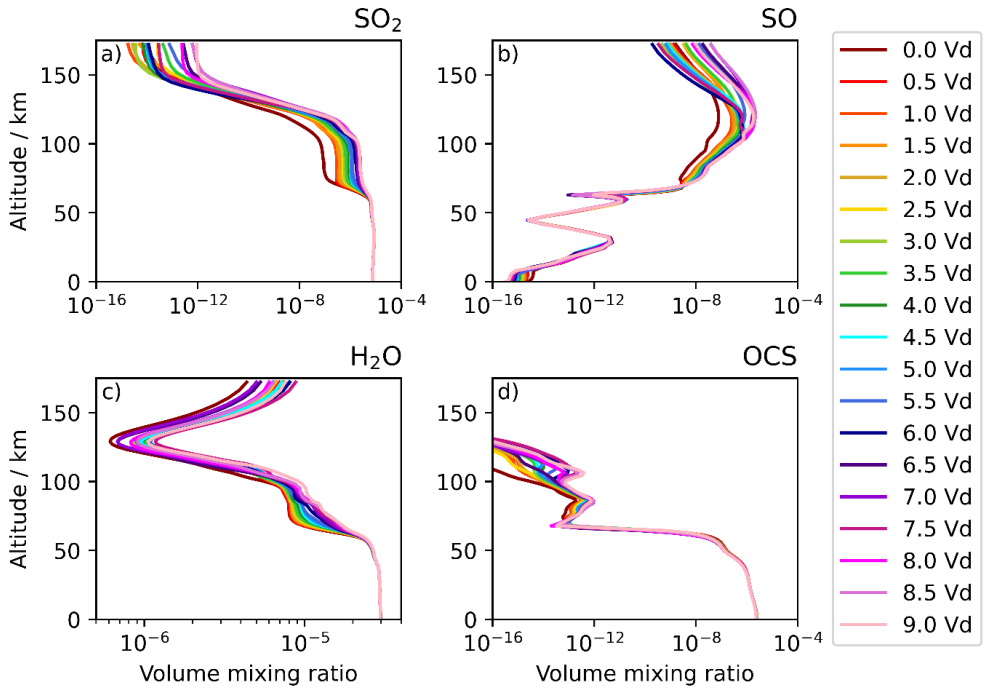

Figure 3.3. Variation of global mean a) SO_2, b) SO, c) H_2O, and d) OCS over 9.0 Vd in the out-of-the-box PCM run.

Rimmer et al. (2021) reasoned that as the formation of H_2SO_4 requires the destruction of at least one H_2O and one SO_2 molecule (or two SO_2 molecules if the SO_2 is oxidised to SO_3 with oxygen from a second SO_2 molecule), H_2O and SO_2 concentrations would be expected to be within a factor of two of one another. The actual ratio of SO_2 to H_2O is observed to be 5:1. The maximum SO_2 decrease through the cloud deck attributable to reaction with H_2O is therefore approximately one fifth, significantly lower than the three to four orders of magnitude observed. An additional sink of H_2O is expected from condensation into cloud droplets, as the observed concentration of 80 wt% suggests an approximately 1:1 ratio of H_2O to H_2SO_4 molecules in the condensed phase, requiring an extra H_2O molecule for SO_2 removal to H_2SO_4, further decreasing the amount of SO_2 that can be removed by this method.

Increased SO_2 loss to a reservoir species that could then reform SO_2 at the cloud tops (where Mahieux et al. (2023a) and Sandor et al. (2010) report an increase in SO_2 concentration with increasing altitude) has been suggested to explain the observations (Frandsen et al., 2016; Zhang et al., 2012). The feasibility of OSSO to provide this sink is considered in this study.

With the exception of OCS, which remains broadly constant throughout the run, the plotted species increase in concentration in and above the upper clouds to around 125 km, above which there is variation in all species, but no clear trend with time across the model run. There is very little change below the clouds due to slow vertical mixing in the lower atmosphere (Cohen et al., 2024). After 8.0 Vd, steady state is reached with an almost constant SO_2 profile through the lower and middle atmosphere.

3.2.2 S_2O_2 chemistry

The out-of-the-box PCM run includes S_2O_2 chemistry, but, like other previous models (e.g., Krasnopolsky, 2016; Zhang et al., 2012), it treats all S_2O_2 present as the most stable isomer, trigonal-S_2O_2. The S_2O_2 concentration across a 9.0 Venus day model run is shown in Figure 3.4. Consideration of the potential energy surface of the SO + SO reaction (Section 3.3.3) found, in agreement with Frandsen et al. (2016), that trigonal-S_2O_2 would not be a significant form of the molecule in the Venusian atmosphere. All trigonal-S_2O_2 chemistry was therefore removed from the model for subsequent runs, and replaced with chemistry for the three dominant isomers, *cis*-OSSO, *trans*-OSSO, and cyclic-S_2O_2.

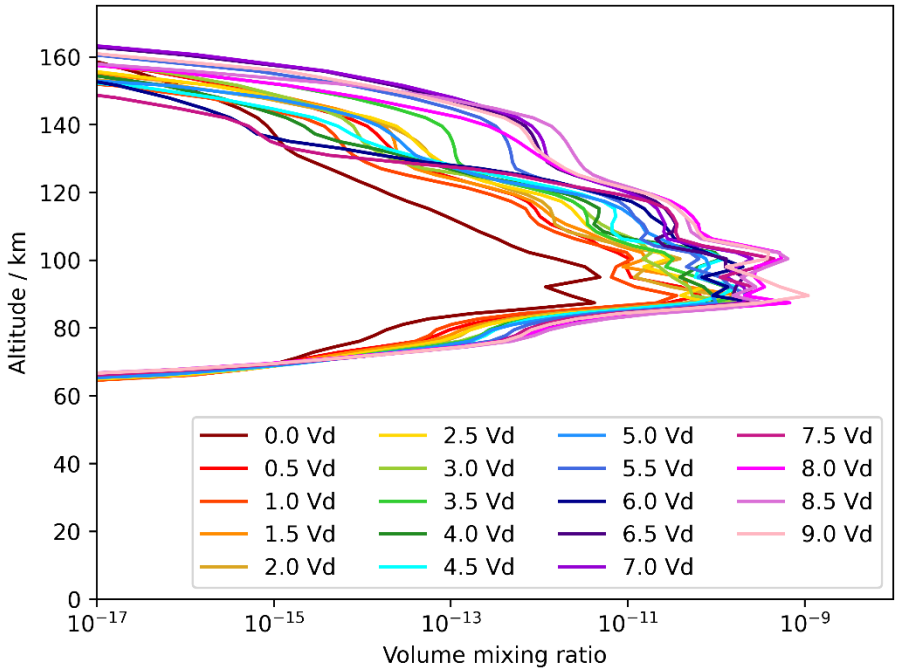

Figure 3.4. Variation of global mean trigonal-S_2O_2 in the out-of-the-box PCM run.

The trigonal-S_2O_2 concentration increases over time for the first ~6.5 Vd, then remains approximately constant, with some variation. Steady state has been reached, with a maximum concentration of ~1 ppb (vmr of 1×10^{-9}). This is approximately an order of magnitude lower than the concentrations of S_2O_2 predicted by Frandsen et al. (2016). It would therefore not be sufficient to simply reallocate the trigonal-S_2O_2 concentration to other isomers; the new chemistry must increase the total S_2O_2 by an order of magnitude as well to reproduce Frandsen et al.'s findings.

3.3 Quantum chemistry calculations

3.3.1 Relevant isomers

Rate coefficients for the reactions of SO and S_2O_2 were estimated by J. M. C. Plane by combining electronic structure (*ab initio* quantum) calculations with Rice-Ramsperger-Kassel-Markus (RRKM) statistical rate theory. These calculations were performed with the Gaussian 16 suite of programs (Frisch et al., 2016), using the w1bd (Brueckner Doubles Variations of W1 Theory) compound method (Barnes et al., 2009). The molecular geometries of the stationary points on the

potential energy surfaces (PESs) for the recombination reaction SO + SO were optimized and vibrational frequencies calculated. The geometries, rotational constants, vibrational frequencies and heats of formation (at 0 K) of these stationary points are listed in Table 3.3. The PESs are shown in Figures 3.5 and 3.6, which also illustrate the molecular geometries of the stationary points. The w1bd method was developed to determine high accuracy bond energies: for example, the bond energy of SO_2 (i.e., $SO_2 \rightarrow SO + O$) is calculated to be 546.16 kJ mol^{-1} at 0 K, which is in excellent agreement with a value of 546.17 kJ mol^{-1} calculated from the literature heats of formation of O, SO and SO_2 (Chase et al., 1985).

Table 3.3. Molecular properties and heats of formation (at 0 K) for the stationary points on the singlet and triplet potential energy surfaces for the dimerization reaction SO + SO (the singlet surface is illustrated in Figure 3.5), and for the SSO, SO_2 and ClSO products formed in the reactions of *cis*-OSSO with CO, O and Cl atoms (Section 3.3.2 and Figure 3.7 – 3.9).

Molecule (electronic state)	**Geometry (Cartesian coordinates in Å)** [a]	**Rotational constants (GHz)** [a]	**Vibrational frequencies (cm^{-1})** [a]	**$\Delta_f H^o$(0 K) (kJ mol^{-1})** [a,b]
SO ($^3\Sigma_g$)	S, 0., 0., 0.0044 O, 0., 0., 1.4935	21.37645	1158	5.0
Singlet surface (Figure 3.5)				
cis-OSSO ($^1A_1$)	S, 0., 1.0062, -0.4410 O, 0., 1.6353, 0.8886 S, 0., -1.0062, -0.4410 O, 0., -1.6353, 0.8886	13.4056 3.36254 2.68824	128, 284, 478, 492, 1143, 1193	-132.1
TS1 from *cis*-OSSO to *trans*-OSSO (^1A)	S, 1.0577, -0.3555, -0.3557 O, 1.7906, 0.6904, 0.4156 S, -1.0577, -0.3552, 0.3561 O, -1.7907, 0.6898, -0.4163	13.6786 2.69174 2.55986	131*i*, 188, 268, 352, 1058, 1100	-50.1
trans-OSSO (^1A_g)	S, 0.4903, 0.9133, 0.0000 O, -0.5103, 2.005, -0.0000 S, -0.4903, -0.9133, 0.0000 O, 0.5103, -2.0050, -0.0000	21.4126 2.77608 2.45747	165, 173, 307, 432, 1119, 1134	-117.5
TS2 from *trans*-OSSO to cyclic-S_2O_2 (^1A)	S, 0.8208, 0.003, 0.3541 O, 1.8354, -0.6707, -0.4402 S, -1.1410, -0.2909, -0.0710 O, -0.8618, 1.2857, -0.2261	13.5928 3.51409 3.06128	641*i*, 239, 303, 517, 827, 1224	-10.1

cyclic-S_2O_2 (^1A)	S, 0.5205, 0.9863, -0.2533 O, 0.0137, 2.0494, 0.5737 S, -0.3281, -0.9336, 0.0665 O, 1.2024, -0.2233, 0.6088	13.3817 3.88044 3.45908	264, 416, 443, 565, 811, 1283	-99.3
TS3 from cyclic-S_2O_2 to trigonal-S_2O_2 (^1A)	S, -0.3872, 0.1600, -0.5482 O, 0.1550, 1.3092, -1.2244 S, 0.1200, -0.2664, 1.4486 O, 0.1120, -1.2028, -0.7971	10.3162 4.00820 3.06470	619*i*, 255, 376, 464, 1031, 1299	33.8
trigonal-S_2O_2 ($^1A_1$)	S, 0., 0., 0.3878 O, 0., -1.2371, 1.1114 S, 0., 0., -1.4956 O, 0., 1.2371, 1.1114	10.3219 4.36243 3.06644	346, 405, 470, 666, 1185, 1381	-173.5
Triplet Surface (Figure 3.6)				
OSSO (^3A)	S, -1.0430, -0.3433, -0.3742 O, -1.8103, 0.6551, 0.4278 S, 1.0432, -0.3433, 0.3742 O, 1.8103, 0.6551, -0.4278	14.0109 2.67067 2.58269	81, 197, 254, 361, 1052, 1095	-51.7
TS4 from OSSO to trigonal-S_2O_2 (^3A)	S, -0.7453, 0.0690, -0.0732 O, -1.0301, 1.1992, 0.7926 S, 1.4342, -0.2954, -0.7081 O, 0.3417, -0.9728, 0.6664	13.1965 3.39511 3.08776	1247*i*, 141, 361, 386, 713, 1235	122.2
trigonal-S_2O_2 (^3A”)	S, 0.2603, 0., -0.5455 O, -0.2247, 1.2650, -1.0578 S, -0.0820, 0., 1.5716 O, -0.2247, -1.2650, -1.0578	9.16138 3.94042 2.87989	141, 244, 420, 481, 1094, 1291	-22.5

[a] Calculated at the w1bd level of theory

[b] Using $\Delta_f H^o$(SO) = 5.0 kJ mol^{-1}, $\Delta_f H^o$(SO_2) = -294.3 kJ mol^{-1}, $\Delta_f H^o$(CO) = -113.8 kJ mol^{-1}, $\Delta_f H^o$(O) = 246.8 kJ mol^{-1}, $\Delta_f H^o$(S) = 274.7 kJ mol^{-1}, $\Delta_f H^o$(Cl) = 119.6 kJ mol^{-1} (Chase et al., 1985).

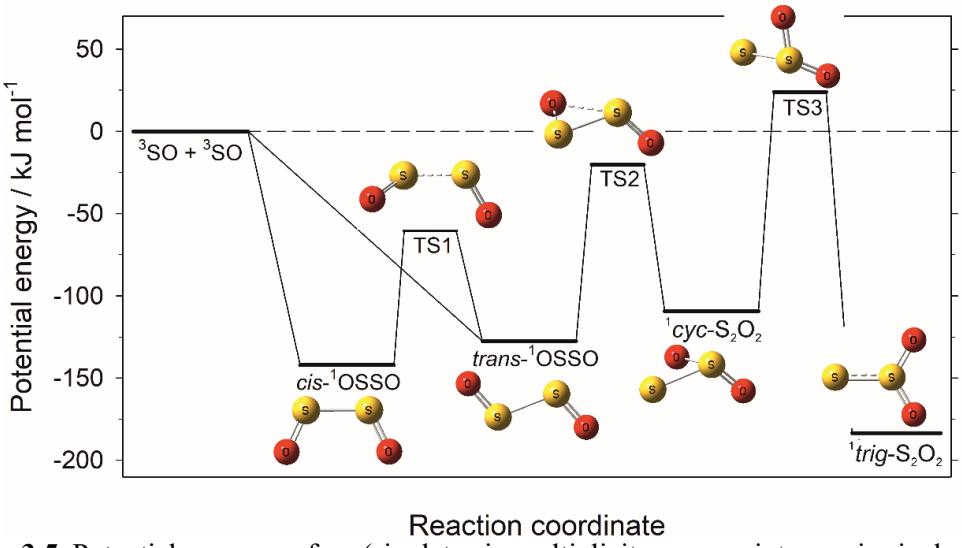

Figure 3.5. Potential energy surface (singlet spin multiplicity, zero-point energies included) for the reaction SO + SO (the triplet surface is not shown here to maintain clarity – see Figure 3.6). Calculations are at the w1bd level of theory (Barnes et al., 2009) .

Inspection of Figure 3.5 indicates that singlet *cis*-OSSO, *trans*-OSSO and cyclic-S_2O_2 will be produced at temperatures below 350 K (i.e., pertinent to the upper clouds of Venus), with *cis*-OSSO being the major product as it is the most stable of these isomers and they are connected by submerged barriers TS1 and TS2. The most stable isomer, trigonal-S_2O_2, is not accessible at low temperatures because of the 23.3 kJ mol^{-1} barrier above the entrance channel (TS3).

The SO + SO reaction can also occur on a triplet surface. However, the initial triplet OSSO is weakly bound and there is a large barrier to forming triplet trigonal-S_2O_2 (Figure 3.6), so reaction on the triplet surface should not be an important source of OSSO.

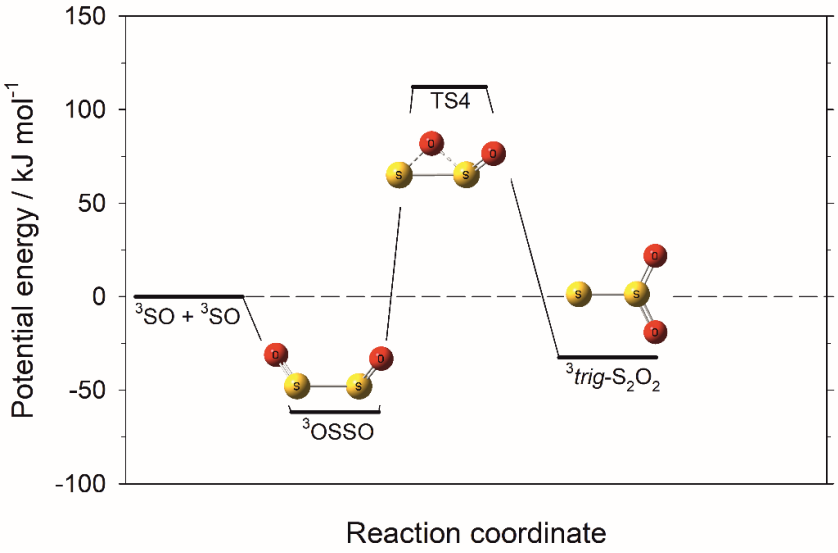

Figure 3.6. Potential energy surface of triplet spin multiplicity for the reaction SO + SO. Calculated at the w1bd level of theory (Barnes et al., 2009).

3.3.2 Rate constants

RRKM calculations of the rate coefficients for formation of S_2O_2 isomers by the termolecular recombination reaction SO + SO + M were preformed by J. M. C. Plane using the Master Equation Solver for Multi-Energy well Reactions (MESMER) program (Glowacki et al., 2012). MESMER assumes that the reaction initially forms an excited adduct, which can either dissociate back to the reactants or be stabilized by collision with N_2, the third body, into any minimum on the PES (Figure 3.5). The internal energy of the adduct was divided into a contiguous set of "grains" (width 70 cm^{-1}). Each grain, which contains a bundle of rovibrational states, was then assigned a set of microcanonical rate coefficients for dissociation back to the reactants. These microcanonical rate coefficients were linked by inverse Laplace transformation to the high-pressure limiting recombination coefficients. These were estimated from the total capture rate, determined using long-range transition state theory to be $6.6 \times 10^{-10} (T/298)^{0.167}$ cm^3 $molecule^{-1}$ s^{-1} (Georgievskii & Klippenstein, 2005). Since reactions of two triplet SO molecules can occur on either singlet, triplet or quintet surfaces, statistically 1/3 of the collisions will be on the singlet surfaces, which will form either *cis*- or *trans*-OSSO, as shown in Figure 3.5 (additional potential isomers SOOS and OSOS are not stable enough to require further consideration). Assuming that the SO molecules have equal probability of approach at the range of angles to form *cis*- and *trans*-OSSO, then their high-pressure limiting recombination coefficients are $1.1 \times 10^{-10} (T/298)^{0.167}$ cm^3 $molecule^{-1}$ s^{-1}.

The exponential-down model (Gilbert & Smith, 1990) was used to estimate the probability of collisional transfer between grains. The average energy for downward transitions $\langle \Delta E \rangle_{down}$ was set to 300 cm^{-1} for N_2 at 300 K, and a small $T^{0.25}$ temperature dependence. The resulting temperature-dependent rate coefficients for formation of *cis*-OSSO, *trans*-OSSO and cyclic-S_2O_2 were then multiplied by a factor of 2.5 to account for the increased efficiency of CO_2 (the major component of the Venusian atmosphere), compared with N_2 (Gilbert & Smith, 1990). The rate coefficient for the thermal dissociation of each S_2O_2 isomer was then determined by detailed balance.

Several possible reactions for the loss of OSSO were considered. Besides thermal dissociation and photolysis, the isomers could also react with SO, CO, O, and Cl, which are all relatively abundant above 70 km. Reaction with SO, which was considered and subsequently rejected by Frandsen et al. (2016), can only occur on the triplet surface. It has a large barrier to formation and is therefore discounted. The molecular geometries of the stationary points on PESs for the reactions of OSSO with CO, O and Cl were optimized and vibrational frequencies calculated. The geometries, rotational constants, vibrational frequencies and heats of formation (at 0 K) of these stationary points are listed in Table 3.4. The PESs for reactions of *cis*-OSSO with CO, O, and Cl reactions are shown in Figures 3.7 – 3.9. PESs for reactions with *trans*-OSSO are similar, so figures are not repeated for both isomers.

Table 3.4. Molecular properties and heats of formation (at 0 K) for SSO, SO_2, and ClSO products and stationary points on the PESs for the reactions of *cis*-OSSO with CO, O and Cl (Figures 3.7 – 3.9).

Molecule (electronic state)	**Geometry (Cartesian coordinates in Å)** [a]	**Rotational constants (GHz)** [a]	**Vibrational frequencies (cm^{-1})** [a]	**$\Delta_f H^o$(0 K) (kJ mol^{-1})** [a,b]
TS5 from *cis*-OSSO + CO to SSO + CO_2 (^1A)	S, 0.8822, 0.5305, 0.6703 O, 0.9630, 1.5685, -0.3576 S, 0.1213, -1.2437, 0.0945 O, -1.1176, -0.8959, -0.8846 C, -2.1918, 0.1164, -0.2873 O, -1.8219, 0.8358, 0.5545	3.59672 2.41254 1.72147	641*i*, 123, 150, 200, 276, 380, 435, 500, 632, 761, 1184, 1860	-91.2
TS6 from *cis*-OSSO + O to SSO + O_2 (^3A)	S, 1.4488, -0.0905, -0.2779 O, 1.4140, 1.2016, 0.4389 S, -0.4373, -1.0473, -0.0022 O, -1.3265, 0.0312, 0.6382 O, -2.1082, 1.0737, -0.5190	5.41951 2.28865 1.79628	600*i*, 68, 128, 183, 287, 367, 427, 901, 1134	182.8
SSO ($^1A'$)	S, 0., 0.9588, -0.4270 O, 0., 1.6397, 0.8634 S, 0., -0.9376, -0.4363	41.8098 5.01200 4.47549	384, 686, 1205	-53.6
OS-SO_2 (^3A)	S, -2.2277, -0.2357, -0.0005 O, -2.2566, 1.1996, 0.0006 S, 2.1274, -0.0447, 0.0001 O, 3.5613, 0.3621, -0.0005 O, -0.9559, -0.9087, 0.0004	12.6023 0.83908 0.78670	12, 30, 50, 57, 70, 523, 1153, 1182, 1382	-295.4
SO_2 ($^1A_1$)	S, 0.0015, 0., 0.0008 O, 0.0019, 0., 1.4375 O, 1.2549, 0., -0.7011	59.8652 10.2846 8.77681	522, 1183, 1386	-294.3
OS(Cl)SO (^2A)	S, 0.2846, 1.1334, -0.7170 O, 0.5523, 1.7811, 0.2776 S, -0.3147, -1.0708, -0.7725 O, 0.0963, -1.6208, 0.5466 Cl, -0.5455, 1.3325, -2.6695	4.24621 1.76190 1.32199	51, 112, 179, 269, 295, 397, 463, 1099, 1229	-164.0
ClSO ($^2A''$)	S, -0.0003, 0.8130, 0. O, 1.4655, 0.8462, 0. Cl, -0.6841, -1.1592, 0.	32.7101 4.40075 3.87889	295, 472, 1181	-105.2

[a] Calculated at the w1bd level of theory

[b] Using $\Delta_f H^o$(SO) = 5.0 kJ mol^{-1}, $\Delta_f H^o$(SO_2) = -294.3 kJ mol^{-1}, $\Delta_f H^o$(CO) = -113.8 kJ mol^{-1}, $\Delta_f H^o$(O) = 246.8 kJ mol^{-1}, $\Delta_f H^o$(S) = 274.7 kJ mol^{-1}, $\Delta_f H^o$(Cl) = 119.6 kJ mol^{-1} (Chase et al., 1985).

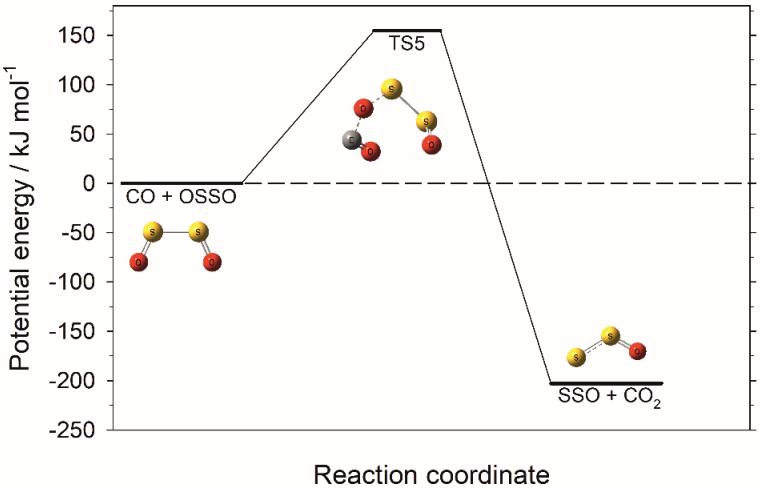

Figure 3.7. Potential energy surface for the reaction *cis*-OSSO + CO (singlet spin multiplicity), calculated at the w1bd level of theory (Barnes et al., 2009).

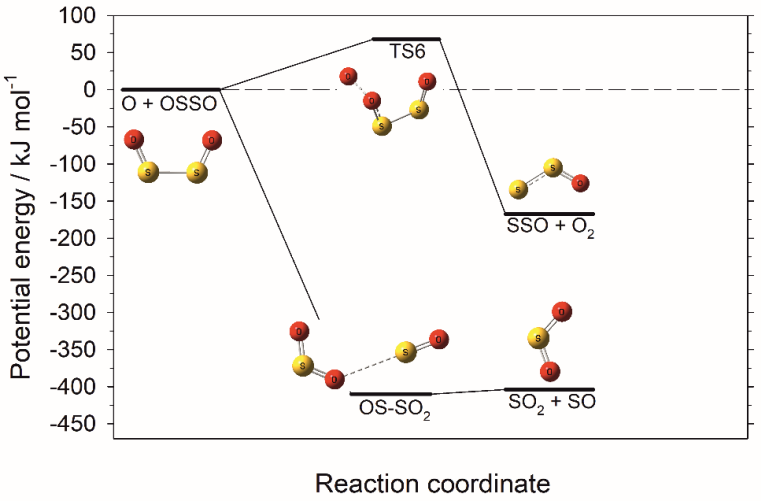

Figure 3.8. Potential energy surface for the reaction *cis*-OSSO + O (triplet spin multiplicity), calculated at the w1bd level of theory (Barnes et al., 2009).

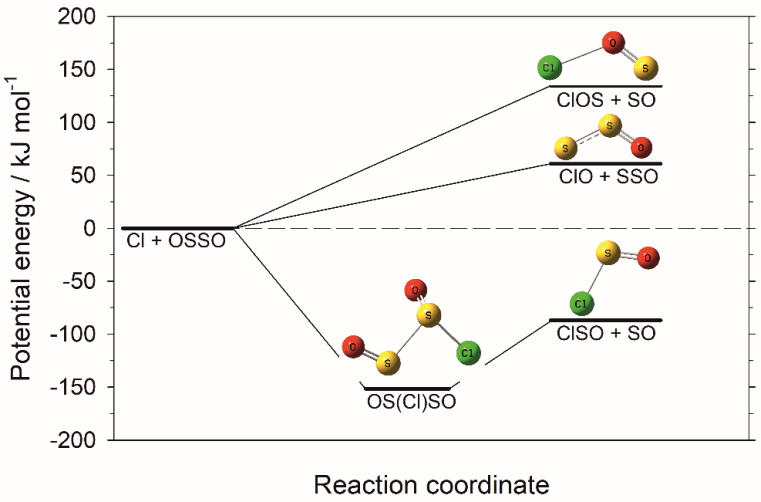

Figure 3.9. Potential energy surface for the reaction *cis*-OSSO + Cl (doublet spin multiplicity), calculated at the w1bd level of theory (Barnes et al., 2009).

Although the reaction of OSSO with CO is quite exothermic (ΔH_r^o (0 K) = -203 kJ mol^{-1}), the reaction is prevented by a pronounced barrier of 155 kJ mol^{-1} (Figure 3.7). Reaction of OSSO with O can either produce SSO + O_2, or SO_2 + SO. The first of these channels was explored in a recent paper by Francés-Monerris et al. (2022) as a route to making polysulphur. However, there is a substantial barrier of 68 kJ mol^{-1} which will shut down this channel at low temperatures (Figure 3.8), and the products SO_2 + SO would form through a highly exothermic channel (ΔH_r^o (0 K) = -404 kJ mol^{-1}). Atomic Cl will react rapidly with OSSO to form ClSO + SO with no barrier (ΔH_r^o (0 K) = -88 kJ mol^{-1}) (Figure 3.9).

The rate constants of formation and loss of ClSO, *cis*-OSSO, *trans*-OSSO, and cyclic-S_2O_2, are listed in Table 3.5. Reactions of S_2O_2 with O and Cl were assigned a value close to the collision capture rate, with a small T dependence due to their barrierless formation pathways.

Table 3.5. Reactions and rate coefficients describing S_2O_2 chemistry that has been added to the Venus PCM. Recombination reactions, marked with [a], have rates defined by Equation 3.1.

No.	Number in code	Reaction	Rate coefficient[b]
1	g033	SO + SO (+CO_2) → *cis*-OSSO[a]	$k_0 = 3.85 \times 10^{-31}$ (T/298)$^{-3.36}$ $k_\infty = 1.1 \times 10^{-10}$ (T/298)$^{0.167}$ $F_C = 0.42$
-1	g034	*cis*-OSSO (+CO_2) → SO + SO	k_1 / (1.02 × 10^{-27} exp(17231/T))
2	g035	SO + SO (+CO_2) → *trans*-OSSO[a]	$k_0 = 2.82 \times 10^{-31}$ (T/298)$^{-3.38}$ $k_\infty = 1.1 \times 10^{-10}$ (T/298)$^{0.167}$ $F_C = 0.42$
-2	g036	*trans*-OSSO (+CO_2) → SO + SO	k_2 / (1.73 × 10^{-27} exp(15395/T))
3	g037	SO + SO (+CO_2) → cyclic-S_2O_2[a]	$k_0 = 4.24 \times 10^{-32}$ (T/298)$^{-3.38}$ $k_\infty = 1.1 \times 10^{-10}$ (T/298)$^{0.167}$ $F_C = 0.42$
-3	g038	cyclic-S_2O_2 (+CO_2) → SO + SO	k_3 / (6.75 × 10^{-28} exp(13392/T))
4	g040 g042 g044	*cis*-OSSO, *trans*-OSSO, and cyclic-S_2O_2+ O → SO_2 + SO	1.1 × 10^{-10} (T/298)$^{0.167}$
5	g039 g041 g043	*cis*-OSSO, *trans*-OSSO and cyclic-S_2O_2 + Cl → ClSO + SO	1.1 × 10^{-10} (T/298)$^{0.167}$
6	g045	ClSO + O → Cl + SO_2	1.1 × 10^{-10} (T/298)$^{0.167}$

[a] Recombination reactions, see Equation 3.1.

[b] Units: bimolecular reactions, cm^3 molecule^{-1} s^{-1}; termolecular, cm^6 molecule^{-2} s^{-1}.

3.3.3 Cross-sections and photolysis

The optical absorption cross-sections of the relevant S_2O_2 isomers and ClSO were calculated by J. M. C. Plane using EOM-CCSD theory (Goings et al., 2014) with the aug-cc-pVQZ basis set (Frisch et al., 2016), for the first 30 excited electronic states for each molecule. The resulting spectra are illustrated in Figure 3.10. Each cross-section was then convolved up to its dissociation threshold with the solar actinic flux from the SOLAR2000 empirical solar irradiance model (Tobiska et al., 2000), scaled to Venus's orbit. The resulting photodissociation reactions are listed in Table 3.6. These TOA rates were fixed at all levels in the Venus PCM; this is a reasonable approximation above 60 km where OSSO is abundant, since most of the photolysis occurs in spectral bands at wavelengths greater than 200 nm where attenuation of incoming solar radiation by CO_2 absorption is not significant.

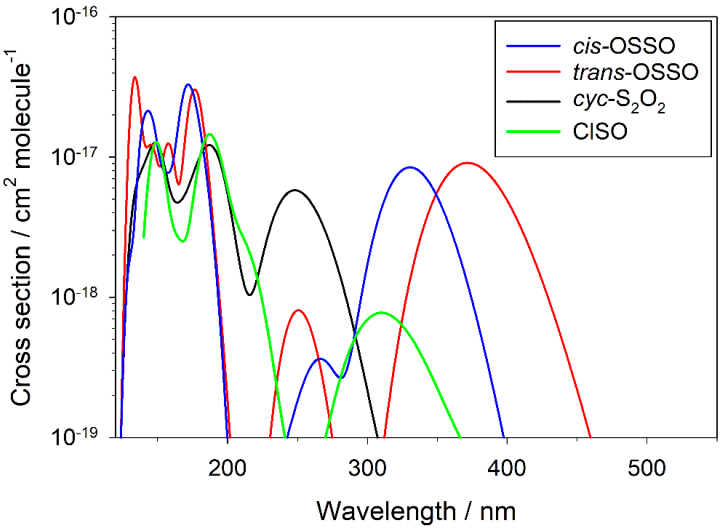

Figure 3.10. Absorption cross-sections versus wavelength: *cis*-OSSO and *trans*-OSSO calculated using EOM-CCSD theory (Goings et al., 2014) with the aug-cc-pVQZ basis set; cyclic-S_2O_2 and ClSO calculated with TD-B3LYP theory and the 6-311+g(2d,p) level of theory (Frisch et al., 2016).

Table 3.6. Photolysis rates of S_2O_2 isomers and ClSO that have been added to the Venus PCM.

Photolysis	**Rate / s^{-1}**
cis-OSSO	0.11
trans-OSSO	0.23
cyclic-S_2O_2	9.5×10^{-3}
ClSO	0.11

3.3.4 Summary of additional changes to the published PCM

In addition to the new photolysis and chemistry detailed in Sections 3.3.2 and 3.3.3 (Tables 3.5 and 3.6), changes were made to the chemistry in the released PCM (Table 3.1), which are summarised and explained in Table 3.7. Recombination reactions, marked with [a], have rates defined by Equation 3.1.

Table 3.7. Changes to the chemistry scheme from the released PCM version 3188.

Reaction ID	Reaction	Previous rate[b]	New rate[b]	Explanation
e001	CO + OH → CO_2 + H	$k_0 = 2.5 \times 6.9 \times 10^{-33} \left(\frac{398}{T}\right)^{2.1}$	$k_0 = 2.5 \times 6.9 \times 10^{-33} \left(\frac{298}{T}\right)^{2.1}$	Typo in expression for k_0 in released code when compared to its reference (Burkholder et al., 2019). All other expressions unchanged.
g007	SO + O (+ CO_2) → SO_2[a]	$k_0 = 4.2 \times 10^{-30}$ $k_\infty = 5.3 \times 10^{-11}$ $F_c = 0.6$	$k_0 = 5.21 \times 10^{-30} \left(\frac{298}{T}\right)^{2.01}$ $k_\infty = 5.4 \times 10^{-11} \left(\frac{298}{T}\right)^{-0.167}$ $F_c = 0.64$	Explicit temperature dependence added in
g010	S + O (+ CO_2) → SO[a]	$k = 1.5 \times 10^{-34}\ [n]\ exp\left(\frac{900}{T}\right)$	$k_0 = 8.72 \times 10^{-32} \left(\frac{298}{T}\right)^{1.40}$ $k_\infty = 5.4 \times 10^{-11} \left(\frac{298}{T}\right)^{-0.167}$ $F_c = 0.93$	Pressure dependence added in

g015	2 SO (+ CO_2) → trigonal-S_2O_2[a]	$k_0 = 2.5 \times 4.4 \times 10^{-31}$ $k_\infty = 1.0 \times 10^{-11}$ $F_c = 0.6$	0	All reactions involving trigonal-S_2O_2 are removed and replaced with reactions with *cis*-OSSO, *trans*-OSSO, and cyclic-S_2O_2
g016	trigonal-S_2O_2 (+ CO_2) → 2 SO	$k = \frac{k_{g015}}{deq}$ $deq = 2.5 \times 1.0 \times 10^{-28}\left(\frac{6000}{T}\right)$	0	
g030	SO_3 + OCS → trigonal-S_2O_2 + CO_2	$k = 1.0 \times 10^{-11} exp\left(\frac{-10\,000}{T}\right)$	0	
g031	trigonal-S_2O_2 + OCS → SO_2 + CO + S_2	$k = 1.0 \times 10^{-20}$	0	

[a] Recombination reactions, see Equation 3.1.

[b] Units: bimolecular reactions, cm^3 $molecule^{-1}$ s^{-1}; termolecular, cm^6 $molecule^{-2}$ s^{-1}.

3.4 Meteoric injection

3.4.1 Background

The ablation of sulphur-containing cosmic dust injects atomic sulphur into the atmosphere above 100 km (Carrillo-Sánchez et al., 2020). The meteoric sulphur flux is poorly studied, even on Earth, so it is calculated by scaling the modelled Na to account for the relative abundances of the two in meteoric material (Gómez Martín et al., 2017). This sulphur enters the atmosphere at hyperthermal speeds, striping O from CO_2 to produce SO (Gómez Martín et al., 2017). For efficiency when running the model, the required S flux is injected as SO directly.

3.4.2 Implementation in the code

Using a meteoric input function (MIF) from Carrillo-Sánchez et al. (2020), sodium (and other metals as required, see Chapter 5) was explicitly added into the model at each height (*zlocal*) in the subroutine *physiq* in module *physique_mod* by Wuhu Feng. The input is in mmr and a value from the MIF is applied for each range of altitudes from 75 to 250 km in steps of 1 km (95 – 100 km), 5 km (75 – 95 km and 100 – 130 km) or 10 km (130 – 250 km). The sulphur input is calculated by scaling the sodium by a factor of 8.8 (Gómez Martín et al., 2017) and converted to mmr by

$$S\ input\ s^{-1} = \frac{8.8\ \times\ Na\ input\ cm^{-3}s^{-1}}{total\ density\ cm^{-3}} \times \frac{M_S}{M_{mean}} \tag{3.2}$$

where M_{mean} is the average molar mass of the atmosphere and M_S the molar mass of sulphur, and the total density is calculated from the ideal gas law.

As all sulphur is injected directly as SO, the SO mixing ratio is then increased by the amount of sulphur injected in each timestep (t_{step}):

$$total\ SO\ mmr = previous\ SO\ mmr + \left(SO\ input \times\ t_{step}\right) \tag{3.3}$$

If the resulting total mixing ratio is less than 1×10^{-30}, it is instead set to 1×10^{-30}, the lowest concentration the model produces.

Development and analysis of the chemistry for meteoric sodium (and magnesium and silicon) is not part of this project but is planned as future work. Meteoric iron is discussed in Chapter 5. Meteoric layers of atomic Na should be observable from terrestrial telescopes, and Na, Mg and Mg^+ from orbiting NUV spectrometers. While meteoric sulphur and iron cannot be observed, future validation of the MIF by comparison of observations to Mg and Na models should be feasible.

3.5 New chemistry results

The PCM was run for 9.0 Venus days (1050.75 Earth days) to reach steady state. Figures 3.11 and 3.12 show the evolution over time of relevant observable species in the new chemistry run

(Figure 3.11) and the SO MIF run (Figure 3.12). The different cases are compared to one another in Figure 3.13.

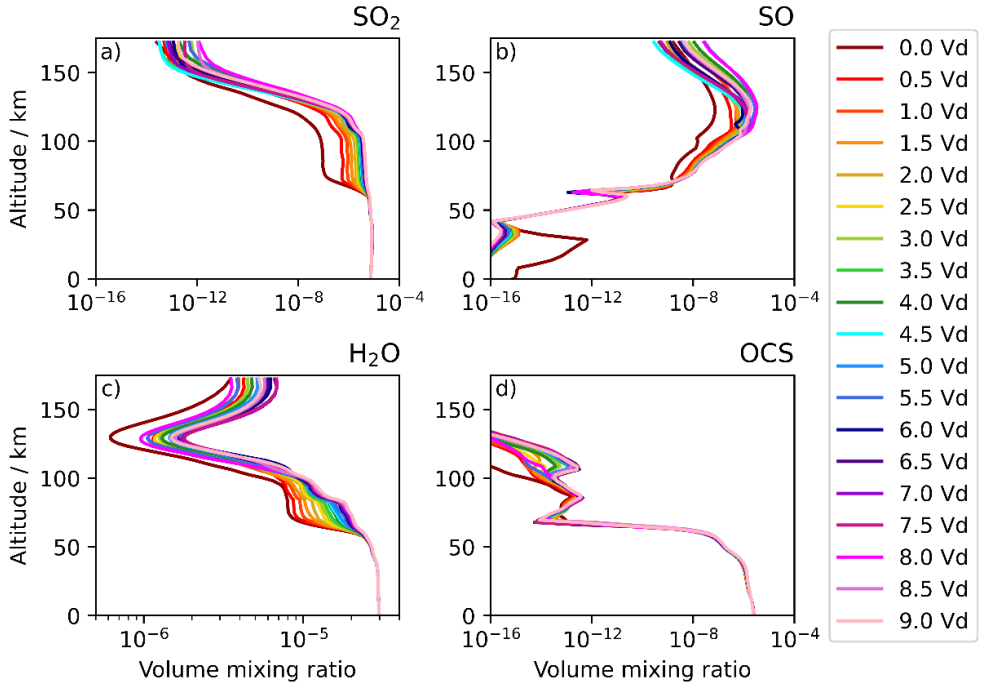

Figure 3.11. Variation in global mean a) SO_2, b) SO, c) H_2O, and d) OCS concentration for the new chemistry PCM run.

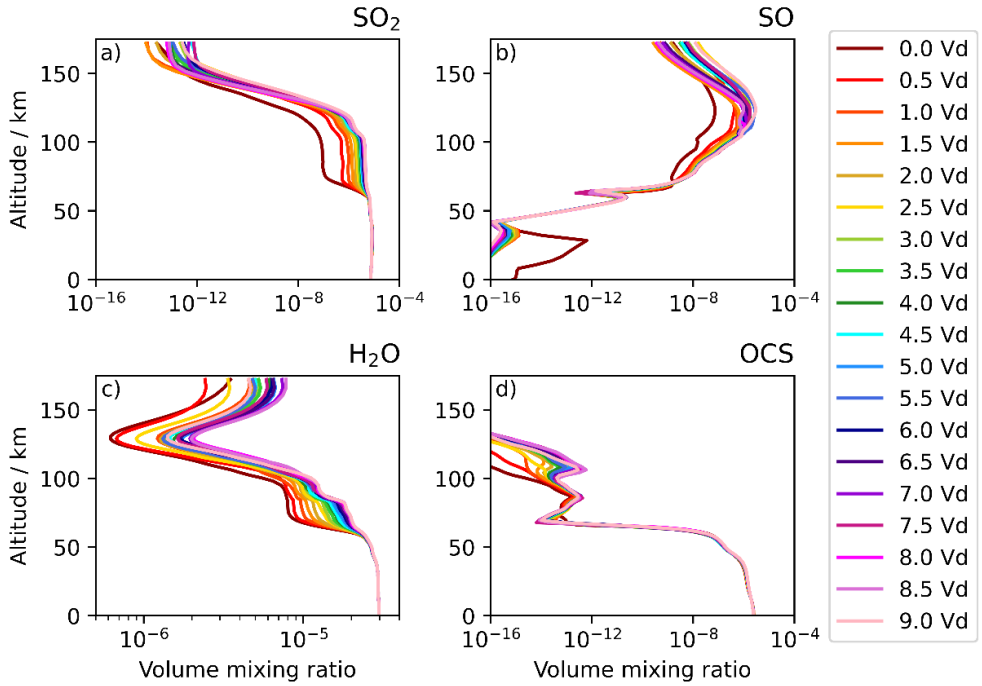

Figure 3.12. Variation in global mean a) SO_2, b) SO, c) H_2O, and d) OCS concentration for the SO MIF PCM run.

As was the case for the out-of-the-box run, the new chemistry and SO MIF runs result in an almost constant SO_2 vmr from the surface to 100 km. There is minimal change in the vmrs in the lower atmosphere, and a steady increase with time is seen for SO and H_2O below 100 km as before.

While the H_2O profile takes approximately 8.0 Vd to reach steady state, as before, the sulphur species reach steady state sooner in both the new chemistry and SO MIF runs, after approximately 6.0 Vd. The effects of the introduction of the SO MIF are subtle and occur mainly above 100 km; these can be seen more clearly in Figure 3.13 (Section 3.6.1).

3.6 Photochemical modelling results

Unless specified otherwise, all results and Figures in this section are taken from the SO MIF version of the model after 9.0 Venus days.

3.6.1 Relevant observable species

Figure 3.13 shows model profiles of SO_2, SO, H_2O, and OCS after 9.0 Vd for the SO MIF run (red and blue solid lines and black dashed lines), new chemistry (labelled "no MIF") run (pale red and blue solid lines) and out-of-the-box run (very pale red and blue dashed lines). There is little change to the OCS profiles, which remain significantly lower than observations for all versions. The introduction of the new chemistry causes a small decrease in SO concentration from 60 – 100 km, and the introduction of the SO MIF causes an increase in SO_2 and SO concentration above 100 – 120 km. The new chemistry causes a small increase in H_2O concentration above 60 km. The introduction of the SO MIF causes a small decrease in nightside H_2O above 100 km, consistent with reaction of the H_2O with sulphur species in this region. Observations are detailed in Table 2.2.

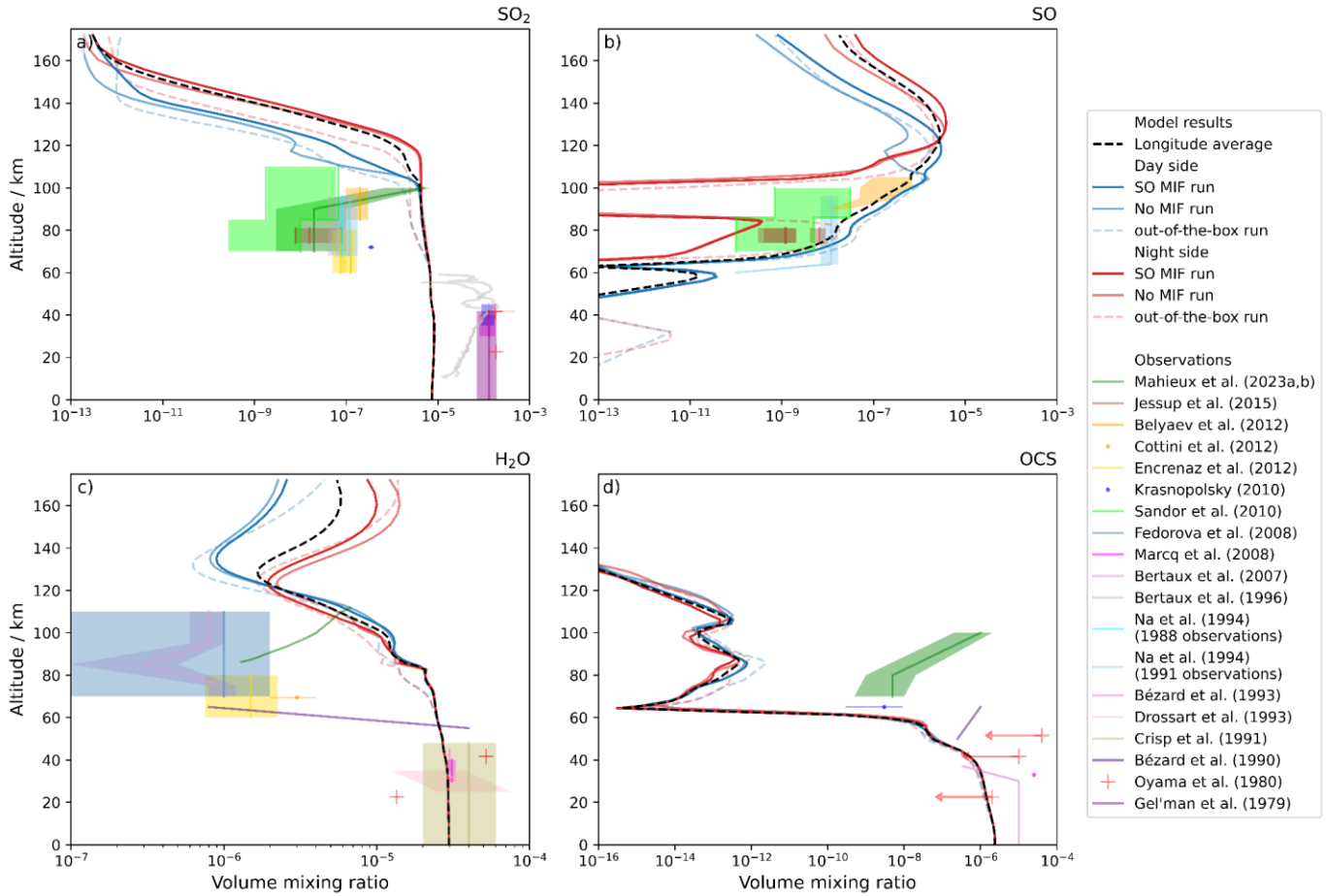

Figure 3.13 Comparison of PCM modelled vmr to observations for a) SO_2, b) SO, c) H_2O, and d) OCS. Model results are averaged from -30° – 30° latitude. Dayside (nightside) is defined as the 140° longitude centred on the subsolar (antisolar) point to prevent capturing terminators. Observations of OCS by Oyama et al. (1980) constitute an upper limit on OCS concentration due to the limit of detection of the instrument. Dayside (blue) and nightside (red) results are plotted after 9.0 Venus days for the three runs, the longitude-averaged profiles are for the SO MIF run only.

SO_2 is initialised to 10 ppm near the surface, and maintains a near-constant mixing ratio from the surface to the upper cloud layer (>60 km). This is more than an order of magnitude lower than observations of the below-cloud region, which consistently report 150 ppm SO_2 near the surface (Bertaux et al., 1996; Bézard et al., 1993; Gel'man et al., 1979; Marcq et al., 2008; Oyama et al., 1980). It is clear that a significant sulphur reservoir in the cloud layer is missing from photochemical modelling of Venus (Vandaele et al., 2017, and references therein), resulting in a negligible decrease in modelled SO_2 through the clouds. Recognising this as a significant unsolved problem for Venusian research, a value was selected, on the advice of the PCM development group, that under-estimates below-cloud observations but still over-estimates above-cloud observations. This results in an above-cloud vmr that is sufficiently high to test the feasibility of S_2O_2 to provide part of the required sulphur reservoir, while not completely overwhelming later S_2O_2 absorbance calculations with 150 ppm SO_2 above the clouds. S_2O_2 cannot provide a sulphur reservoir to decrease the above-cloud SO_2. No further attempts were made to constrain the SO_2 concentration to observed levels, and instead it was allowed to exceed observed levels to maximise the possible OSSO concentration.

The SO_2 is clearly not reacting with sufficient water in the cloud deck. H_2O profiles show a 20-fold decrease with height above 60 km, in line with observations, though this decrease occurs ~40 km too high in the model. The decrease would be expected to occur throughout the cloud deck, where H_2O reacts with SO_2 to form the sulphuric acid clouds. The problems with the H_2O and SO_2 profiles and chemistry are beyond the scope of this project, but further research is clearly required.

On the dayside of the planet, SO is primarily produced by photolysis of SO_2 into SO and O, and is broadly consistent with observed concentrations. On both sides of the planet, injection of SO by the ablation of cosmic dust contributes a modelled flux of 3.2 t d^{-1}, with a maximum at 115 km (Carrillo-Sánchez et al., 2020; Gómez Martín et al., 2017). In Figure 3.13, the lack of photolytically produced SO on the nightside is apparent as a sharp decrease in concentration at 90 – 110 km, while the SO peak above 110 km is maintained by meteoric input and transport. The effect of photolysis below 100 km is not apparent in the SO_2 profile due to the log scale.

OCS concentrations decrease sharply by 9 orders of magnitude above 60 km in the model, contrary to the one order of magnitude seen in observations. OCS is produced by the reaction of S with CO or ClCO, and the dominant loss mechanism is reaction with atomic O to form CO and SO. An additional source of OCS is clearly required, providing further indication of the incomplete understanding of the sulphur chemistry on Venus.

3.6.2 OSSO results

3.6.2.1 Spatial variation

S_2O_2 is most abundant in a thin layer (note 12 orders of magnitude across the log scale) near 70 km (Figure 3.14), at the boundary of the upper cloud and haze. Higher concentrations of S_2O_2 occur on the nightside of the planet by an order of magnitude near the peak of the abundance, with a slight decrease in peak concentration from low to high latitudes. The decrease in nightside S_2O_2 concentration near 100 km reflects a decrease in production because of reduced SO, rather than an increase in the S_2O_2 loss rate. A 2D colourmap of S_2O_2 column abundance above 59 km is shown in Figure 3.15, which highlights the high concentrations on the nightside. The dominant form of S_2O_2 is *cis*-OSSO at all altitudes above ~70 km, followed by *trans*-OSSO and then cyclic-S_2O_2, in the ratio 57:34:9% at the dayside peak. In the 50 – 60 km region where photolysis dominates the loss of S_2O_2, the cyclic form becomes the dominant isomer due to its longer lifetime against photolysis (Table 3.6).

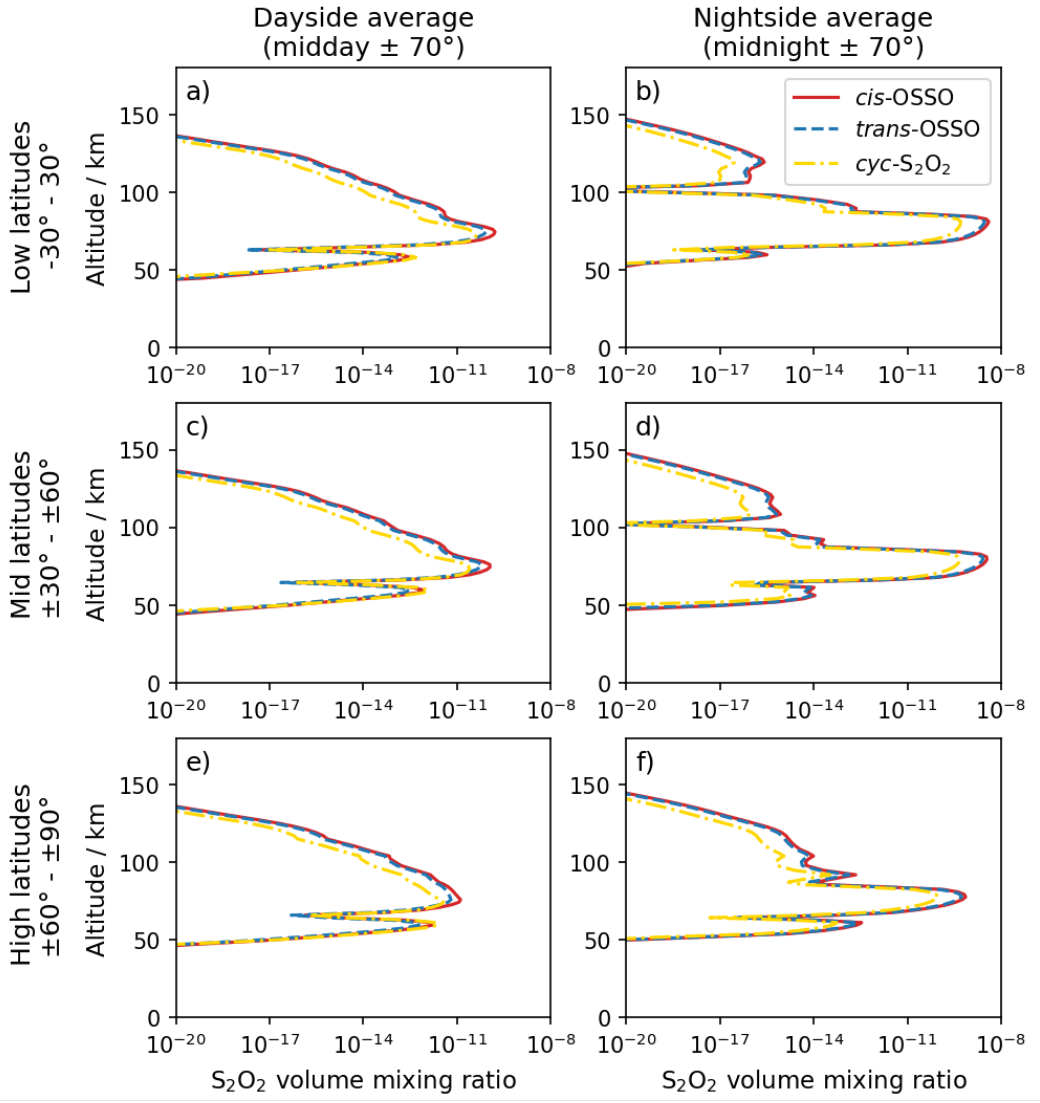

Figure 3.14. Vmr profiles of the three S_2O_2 isomers in different latitude bands and local times. An average is taken across 140° centred on the subsolar or antisolar points to avoid capturing the terminators in dayside and nightside averages, respectively.

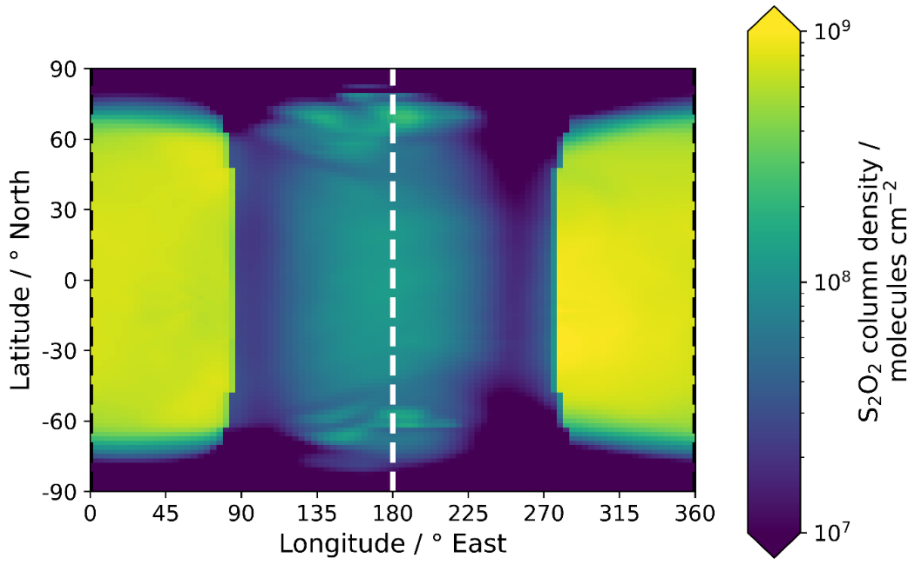

Figure 3.15. Column abundance of S_2O_2 from 59 km to TOA. The black dashed line indicates local midnight (which is at the break of the plot), midday is the white dashed line. Morning and evening terminators are clear at 270 and 90°, with an abrupt change in concentration due to photolysis. The column density on the nightside is approximately an order of magnitude higher than the dayside.

In Figure 3.15, the higher concentrations on the nightside are clearly visible, along with lower concentrations in the high latitude and polar regions (see also Figure 3.14). This correlates with the observed 2D distribution of the unknown absorber (Section 1.4.2), with dark (absorbing) low latitude regions and brighter (non-absorbing) poles.

3.6.2.2 Production and loss processes

Dayside production and loss, and the dominance of the different loss processes with altitude are shown in Figure 3.16. The higher peak S_2O_2 concentration at 60 – 80 km at night (Figure 3.14) is attributed to the lack of photolysis on the nightside, as it is the dominant loss mechanism in much of this region on the dayside. The primary loss mechanism above 70 km on the dayside and above 60 km on the nightside is reaction with atomic O to produce SO_2 and SO. Below 40 km, thermal decomposition of S_2O_2 following collision with a third body (assumed to be CO_2) dominates the loss. Loss of S_2O_2 by reaction with atomic chlorine is never dominant on the dayside as the Cl concentration is much lower than O in and above the cloud layer. Reaction with Cl becomes faster than O below the clouds, but S_2O_2 destruction in this region is dominated by thermal decomposition. O and Cl destruction are comparable in the photolytically dominated region on the dayside and both contribute on the nightside.

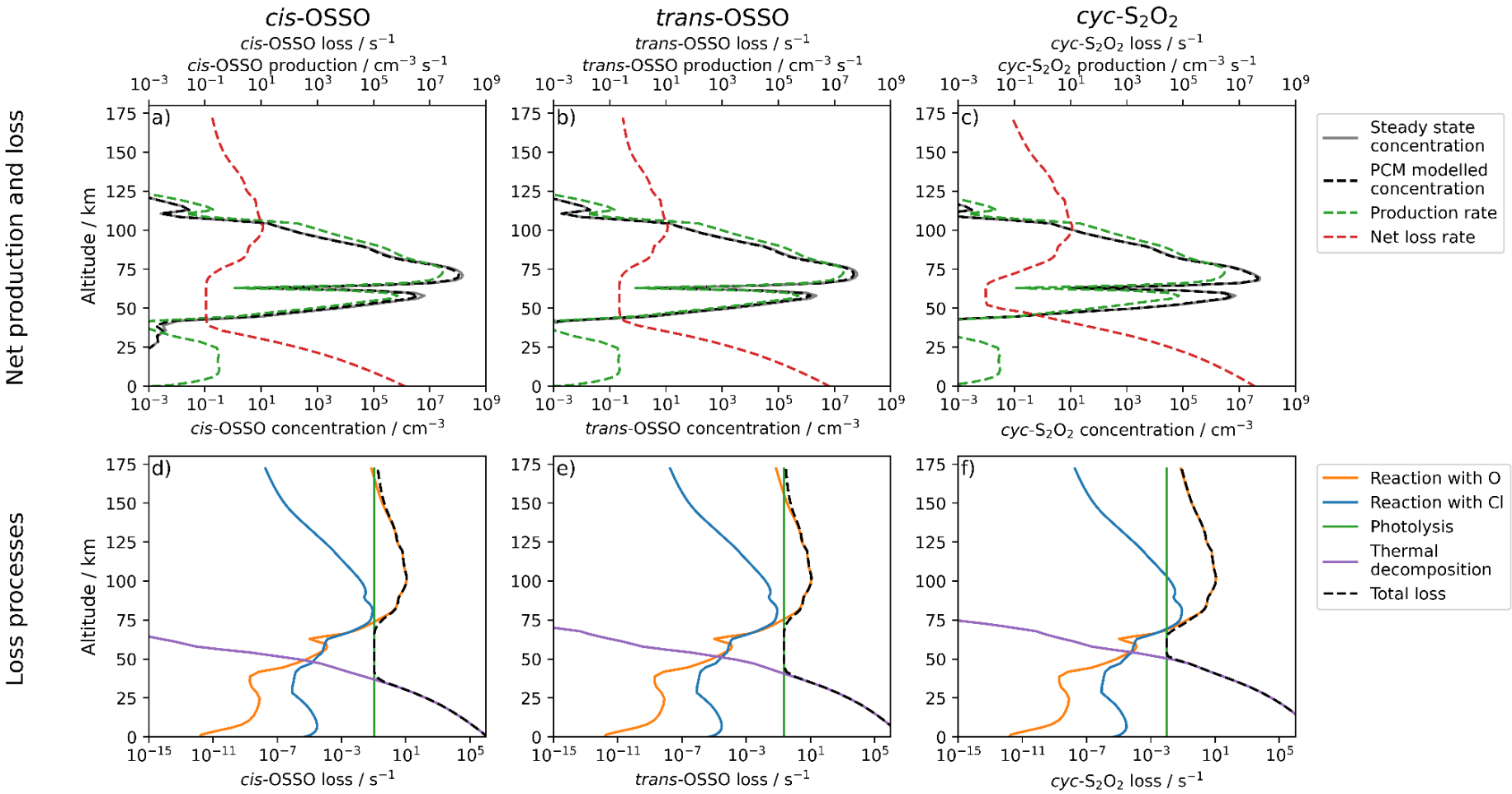

Figure 3.16. Net production and loss of a) *cis*-OSSO, b) *trans*-OSSO, and c) cyclic-S_2O_2 compared to modelled and steady-state concentrations, and d) – f) contribution of each loss mechanism to the total loss of each isomer with altitude. Photolysis is taken to be constant through the atmosphere. The excellent agreement between black (PCM modelled concentration) and grey (steady state) lines shows the model has reached steady state.

The photolysis rate is taken to be constant throughout the atmosphere as it is only the dominant loss process in a thin region through the clouds. There is negligible absorption in the relevant regions higher in the atmosphere, and S_2O_2 is optically thin (Section 3.7) because of its low concentration, and so the expected effect on photolysis rate by depletion of the relevant wavelengths of light through the atmosphere is negligible, thereby validating this choice of photolysis treatment.

3.6.2.4 Sensitivity studies

For direct comparison to previous work which did not include reaction of the relevant S_2O_2 isomers with O and Cl (Frandsen et al., 2016; Krasnopolsky, 2018; Pinto et al., 2021), the sensitivity of the OSSO concentrations to these reactions was investigated. Although examination of the PESs of the reactions of O and Cl with OSSO indicates no energy barriers with respect to the reaction entrance channels, and hence the reactions were assigned nominal capture rate coefficients (Table 3.7), a sensitivity analysis was performed by considering two test cases: 1) decreasing the rate coefficients by a factor of 100 ("Sensitivity Test 1"), and 2) removing the O and Cl reactions as loss processes for S_2O_2 ("Sensitivity Test 2"). In each case, the model was run for 9.0 Venus days from the same initial conditions as the SO MIF run. All other rate coefficients were the same. For Test 1, the peak OSSO concentrations increase by factors of 3.97 and 2.87 for *cis*- and *trans*-OSSO, respectively. For Test 2, *cis*- and *trans*-OSSO increase by factors of 4.07 and 2.90 (Figure 3.17). The majority of the changes in OSSO concentrations occur above 80 km where reaction with O is the dominant loss mechanism.

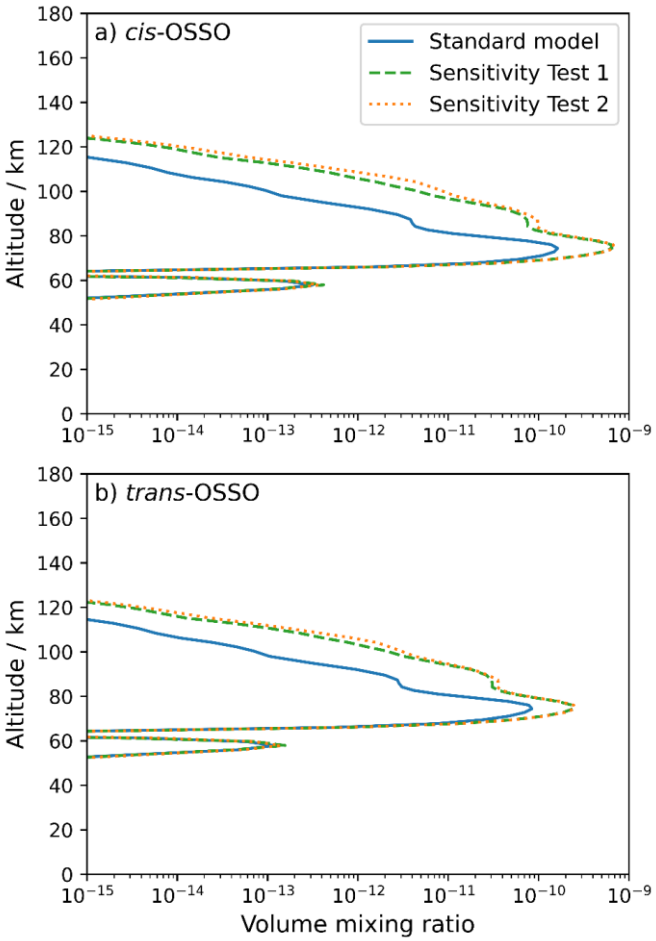

Figure 3.17. Low-latitude (30°S – 30°N latitude) dayside (subsolar point ± 70° longitude) a) *cis*-OSSO and b) *trans*-OSSO concentrations for the standard chemistry scheme, Sensitivity Test 1 and Sensitivity Test 2 (see text for details).

The most significant change in OSSO concentration is on the nightside above 90 km. In this region, lack of photolytic production decreases the SO concentration, and therefore the S_2O_2 concentration, so any S_2O_2 lost is replaced much more slowly. Decreasing the dominant loss mechanism in this region therefore has a significant impact on the OSSO concentration.

3.7 SOCRATES results

The ability of the modelled S_2O_2 concentrations to explain the observed UV absorption is evaluated by comparison to the observations by MESSENGER/MASCS during its 2007 gravity assist manoeuvre at Venus reported by Pérez-Hoyos et al. (2018). Concentrations of SO_2 and S_2O_2 produced by the PCM after 9.0 Venus days (standard SO MIF run, or Sensitivity Test 1 or 2, where relevant) were sampled near local noon at low latitudes, the region observed by MASCS. The concentrations were then used in SOCRATES to predict the TOA reflectance in the presence of S_2O_2.

3.7.1 PCM-modelled S_2O_2 concentrations

The TOA reflectances computed using SOCRATES are presented in Figure 3.18. The purple dashed line is the reflectance calculated for the SO MIF PCM run. The deep absorption shortwards

of 320 nm is due to SO_2, which is significantly overestimated by the PCM, as addressed in Section 3.6.1. Higher absorption in the 320 – 400 nm range for the case with no absorber and a constructed SO_2 profile in line with observations (light blue, solid line) compared to the PCM concentrations is attributed to the higher SO_2 concentrations below the clouds in observations. The PCM-modelled S_2O_2 concentrations are clearly insufficient to reproduce the strength of the NUV absorption observed by MESSENGER (grey crosses, Pérez-Hoyos et al. (2018)).

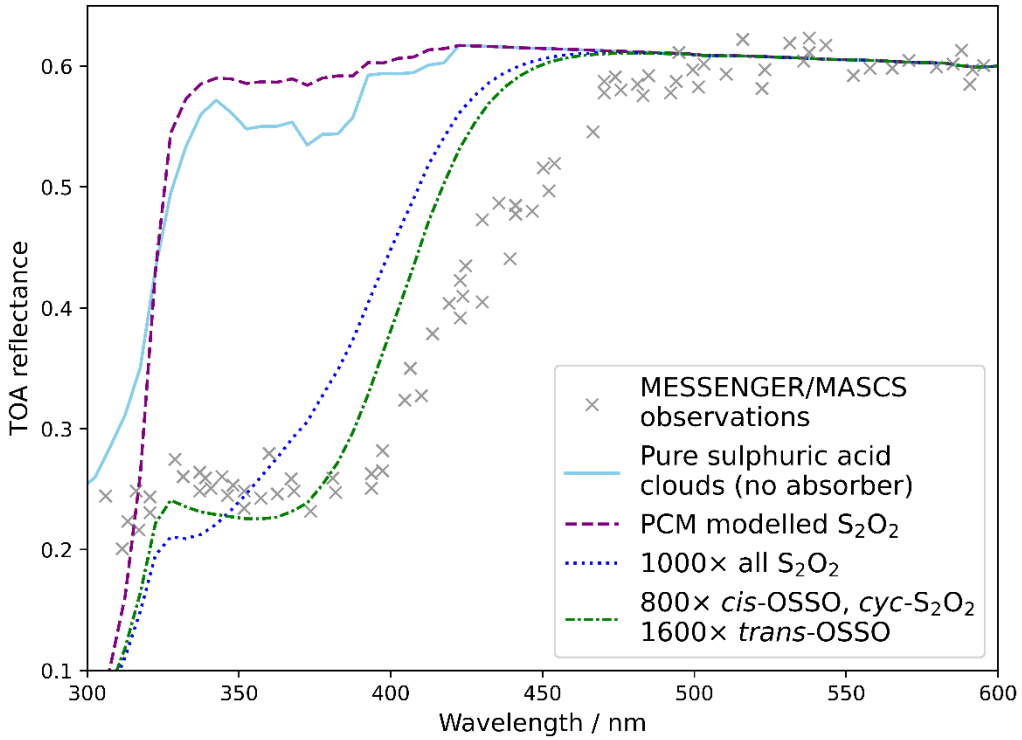

Figure 3.18. SOCRATES modelled TOA reflectance for PCM concentrations of OSSO and various scalings. See the text for interpretation of these scalings.

The approximate scale of the deficit in S_2O_2 was estimated by increasing the modelled concentration profiles by different factors. An increase by three orders of magnitude (dark blue, dotted line) in OSSO concentration is required to reach reflectance of 0.2 – 0.3 in the NUV. However, there is poor agreement between the shape of the absorption spectrum and observations, with the model producing a significantly narrower absorption region than observed. The shape can be improved slightly by increasing the ratio of *trans*-OSSO to *cis*-OSSO by a factor of 2 (green, dash-dotted line). This produces a broader absorption feature, though it is not sufficiently broadened to reproduce observations well, particularly from 400 – 500 nm. The cyclic-S_2O_2 is, in all cases, scaled by the same factor as the *cis*-OSSO, and contributes negligibly to the observed absorption (Figure 3.19).

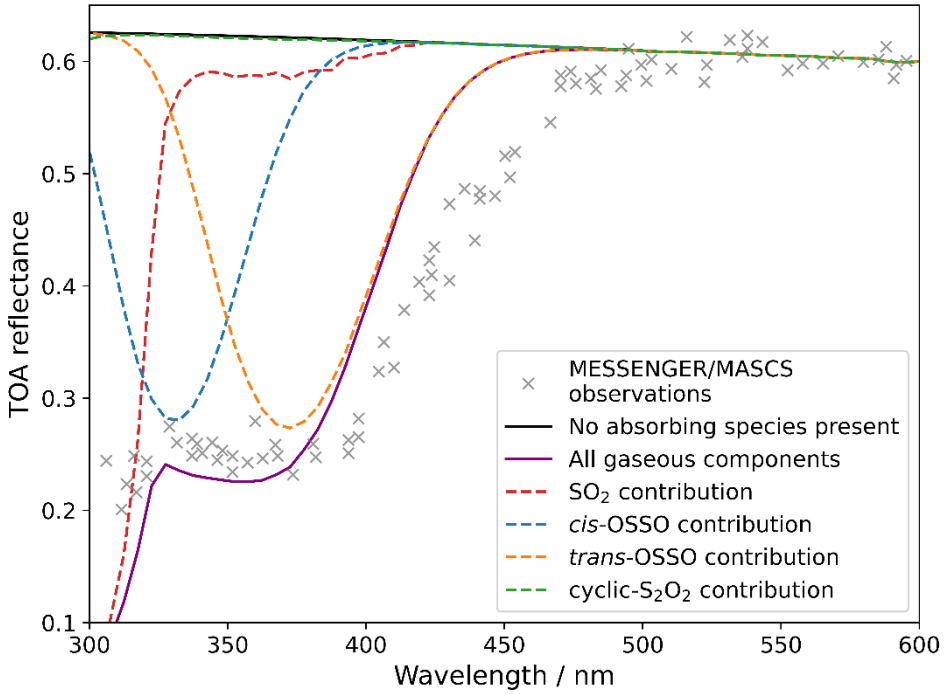

Figure 3.19. Contributions of each of the four absorbing species below 600 nm to the modelled TOA absorption. To ensure contributions are visible, the scaled version which best reproduces the absorption near 350 nm (*cis*-OSSO and cyclic-S_2O_2 are scaled by a factor of 800, *trans*-OSSO by a factor of 1600) is used.

The three forms of S_2O_2 are produced in the ratio 54:40:6% *cis*-OSSO:*trans*-OSSO:cyclic-S_2O_2, which becomes 57:34:9% after loss processes. The factor of two increase of *trans*-OSSO relative to the other forms would bring the fractions to 43:51:6%. It must be emphasised that there is no chemical justification for this increase in *trans*-OSSO over *cis*-OSSO, and the required increase would make *trans*-OSSO the dominant form of S_2O_2, which all previous works are agreed is not the case.

3.7.2 Sensitivity study results

When the rate coefficients for the reaction of the S_2O_2 isomers with O and Cl are decreased or set to zero, there is an overall increase in the concentration of S_2O_2. This increase is still insufficient to explain the observed absorption, and concentrations are two orders of magnitude too low to provide sufficient absorption, in agreement with Krasnopolsky (2018) and Pinto et al. (2021). Specifically, for Tests 1 and 2, a 200-fold increase in *cis*-OSSO (and cyclic-S_2O_2) and a 600-fold increase in *trans*-OSSO are required (Figure 3.20).

The standard model required an additional factor of two increase of *trans*-OSSO compared to *cis*-OSSO (requiring 1600-fold and 800-fold increases, respectively). An additional factor of three increase of *trans*-OSSO to *cis*-OSSO (600-fold compared to 200-fold) is required to produce the required *cis*-OSSO to *trans*-OSSO ratio for the best fit to the shape of the absorber for the sensitivity tests. When removal of S_2O_2 by O and Cl is decreased or removed, the dominant loss mechanism above the cloud becomes photolysis. *Trans*-OSSO is the most readily photolysed of

the three isomers (Table 3.7), while cyclic-S_2O_2 is the most photochemically stable. The fraction of *trans*-OSSO therefore decreases and cyclic-S_2O_2 increases, producing a poor fit to the observed spectral shape of the absorber unless the *trans*-OSSO concentration is increased artificially. Inspection of Figure 3.20 shows that even in this best-case scenario (which is chemically unsupported) the shape of the absorption spectrum exhibits poor agreement in the 400 – 500 nm region.

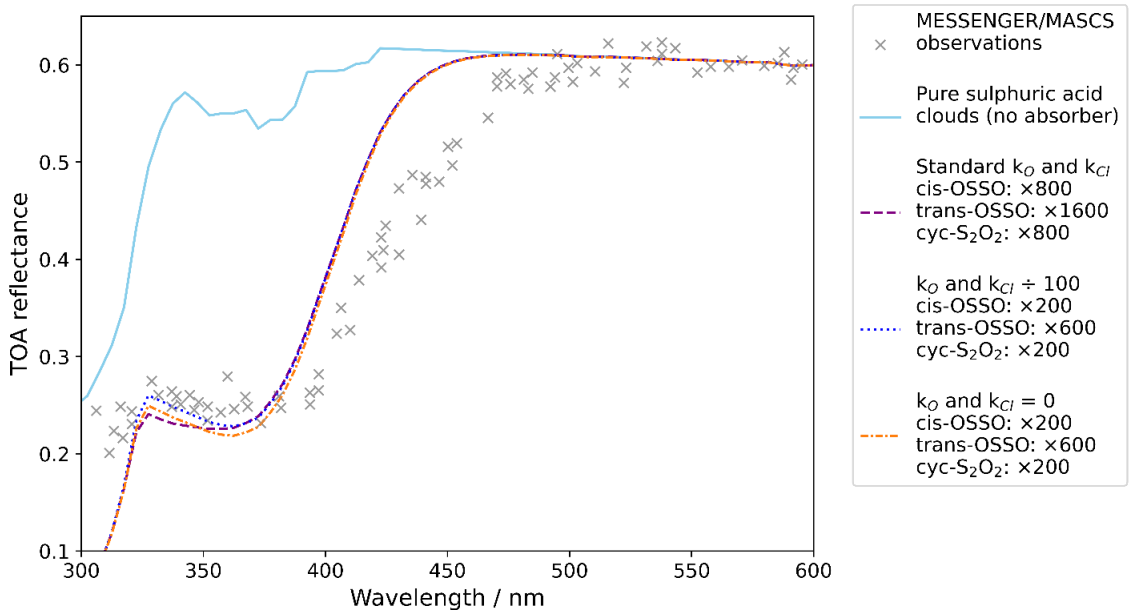

Figure 3.20. Required PCM S_2O_2 scalings in each case of the sensitivity study to approximately reproduce the TOA reflectance.

3.8 Conclusions

This chapter presents an updated sulphur chemistry treatment for the Venus PCM to create and destroy three forms of S_2O_2: *cis*-OSSO, *trans*-OSSO, and cyclic-S_2O_2. The meteoric injection of sulphur, which collides hyperthermally with the atmosphere to produce SO above 100 km, was included in the model. The model was then allowed to run to steady-state, increasing the cloud-level SO_2 significantly above observed levels, which in turn produced the highest SO and therefore OSSO concentrations achievable. S_2O_2 cannot provide the missing sulphur reservoir in the cloud deck required to explain SO_2 observations.

The concentrations of S_2O_2 produced by the model result in a 57:34:9% ratio of *cis*-OSSO:*trans*-OSSO:cyclic-S_2O_2 and have no observable effect on the TOA reflectance as modelled by SOCRATES, a 1D multiple scattering radiative transfer programme. The dominant loss mechanism of S_2O_2 is found to be reaction with O above ~70 km, thermal decomposition below 40 km, and photolysis (on the dayside) or reaction with O and Cl (on the nightside) from 40 – 70 km. Using this chemistry scheme, the OSSO concentrations are approximately 3 orders of magnitude too low to explain the observed absorbance, and the spectral shape of the absorption shows poor agreement with that of the unknown absorber. To improve the agreement of the

spectral shape, a further factor of two increase in *trans*-OSSO concentration is required. If loss of OSSO with O and Cl is discounted, the OSSO concentration increases, but is still two orders of magnitude lower than required to explain the observed level of absorption, and provides poor agreement with the observed spectral shape.

In light of these deficiencies, it is concluded that OSSO does not make a significant contribution to the Venusian UV absorption.

4. Laboratory studies of ferric chloride ($FeCl_3$)

In this chapter, laboratory experiments to measure the absorption spectrum of ferric chloride are presented, along with the experiments performed to support the calculation of the spectrum and the fitting programme developed to analyse the data.

4.1 Overview and justification

4.1.1 Introduction

The strongest evidence for $FeCl_3$ as the unknown UV absorber comes from Zasova et al. (1981), who reported that 1% $FeCl_3$ in mode 2 cloud droplets provided a good match to the observed spectrum of Venus. However, they did not publish a spectrum of $FeCl_3$, only the predicted Bond albedo (Figure 1.32). In the absence of an absorption spectrum of $FeCl_3$ in sulphuric acid, recent research has used a spectrum measured in ethyl acetate for comparison with the Venusian absorber (Aoshima et al., 2013; Pérez-Hoyos et al., 2018). The $FeCl_3$ spectrum in ethyl acetate bears little similarity to the reported Venusian absorption spectrum (Figure 4.1). Given that $FeCl_3$ can react with ethyl acetate (Szafert et al., 1994), and the spectrum of ions is dependent on the solvent, the validity of using this spectrum to model $FeCl_3$ in the Venusian atmosphere is in doubt.

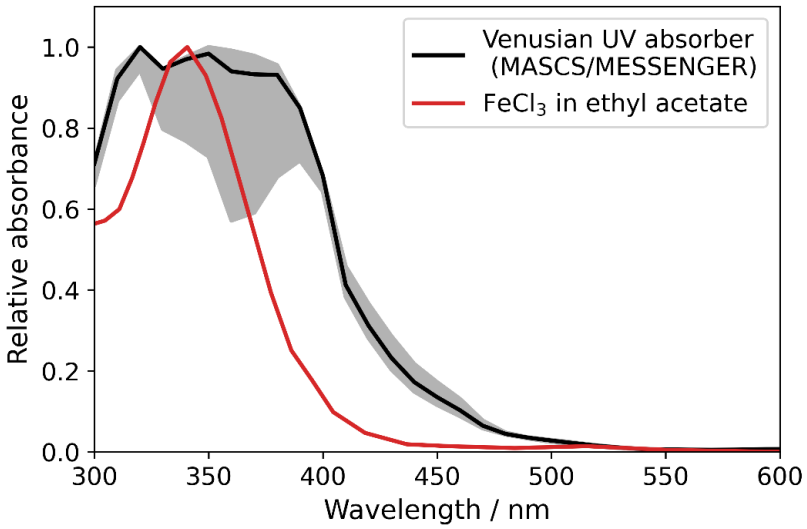

Figure 4.1. Normalised absorption spectrum measured by the MASCS instrument on MESSENGER during its 2007 gravity assist manoeuvre (Pérez-Hoyos et al., 2018) and the absorption spectrum of $FeCl_3$ in ethyl acetate (Aoshima et al., 2013).

In this chapter, the reaction of $FeCl_3$ with sulphuric acid,

$$x\ FeCl_3 + y\ H_2SO_4 \rightleftharpoons \mathrm{m\ HCl} + n_i \begin{cases} Fe_2(SO_4)_3 \\ FeSO_4^+ \text{ or } Fe(SO_4)_2^- \\ (H_5O_2)Fe(SO_4)_2.3H_2O \text{ or } (H_3O)Fe(SO_4)_2 \end{cases} \quad \text{(R4.1)}$$

will be explored. Potential products shown in the brace include neutral species, ions, and minerals, which are considered throughout this chapter (Sections 4.4 and 4.5) (note that H_2O is not shown, and the reactions are not balanced). The $FeCl_3$ absorption spectrum and refractive indices in solution were measured and its molar absorptivity calculated for use in atmospheric modelling

(Chapter 5). Initial experiments were carried out (Section 4.2) reproducing the concentrations reported by Zasova et al. (1981), but the samples were too highly absorbing for standard UV-Vis spectroscopy. Different methods for measuring the absorbance at lower concentrations were tested and HCl added to low concentration solutions to measure the absorbance of the $FeCl_3$ by driving the equilibrium R4.1 to the left-hand side.

The measured absorbance spectra were found to change shape over time (Section 4.3). The product of the reaction was identified as ferric sulphate and no further reaction was observed (Sections 4.4 and 4.5). The absorptivities of ferric chloride and ferric sulphate were measured (Section 4.6) and then used to determine the change in concentration and therefore the rate of the reaction of $FeCl_3$ with sulphuric acid (Section 4.7). The reaction was repeated at a range of temperatures down to those relevant to the Venusian clouds and the change in rate measured (Section 4.8). The measured rate had poor reproducibility. The spectra and concentrations measured were then used in Chapter 5 to model $FeCl_3$ as the unknown UV absorber.

4.1.2 UV-Visible spectroscopy

UV-Visible spectroscopy was performed to measure the absorbance of $FeCl_3$. Spectra were measured across the 200 – 600 nm range from longer wavelengths to shorter wavelengths using an Agilent Cary 100 UV-Visible spectrophotometer. Samples were made up and stored in volumetric flasks, then approximately 3.5 ml of the sample was pipetted into a 10 mm optical pathlength quartz cuvette for spectroscopy. Sample spectra were measured relative to a deionised water baseline.

4.1.3. Refractometry

The real components of the refractive indices of the solutions were measured using a Bellingham and Stanley analogue refractometer. The spectrometer uses a white light source with a compensator to measure the refractive index of the solution at 589 nm (sodium D-lines). The solution was pressed between two prism faces and the refractive index measured.

4.2 Initial experiments

4.2.1 Reproducing literature $FeCl_3$ concentrations

Attempting to replicate the findings of Zasova et al. (1981), a sample of 1 wt% $FeCl_3$ in 75 wt% sulphuric acid was prepared for UV-Vis spectroscopy. The resulting solution was bright yellow, opaque, and rapidly saturated the detector when UV-Vis spectroscopy was attempted. Instead, the real refractive index of the solution was measured over five weeks. Photographs of the solution were taken to monitor the change in the colour of the solution over time. Figure 4.2 shows the measured real refractive index (Figure 4.2a) and photographs of the solutions (Figures 4.2b – e and f – i) over time. UV-Vis spectroscopy of the supernatant was attempted after 16 and 65 days. The detector became saturated at ~430 nm and ~370 nm respectively, and no peaks could be identified in the spectra.

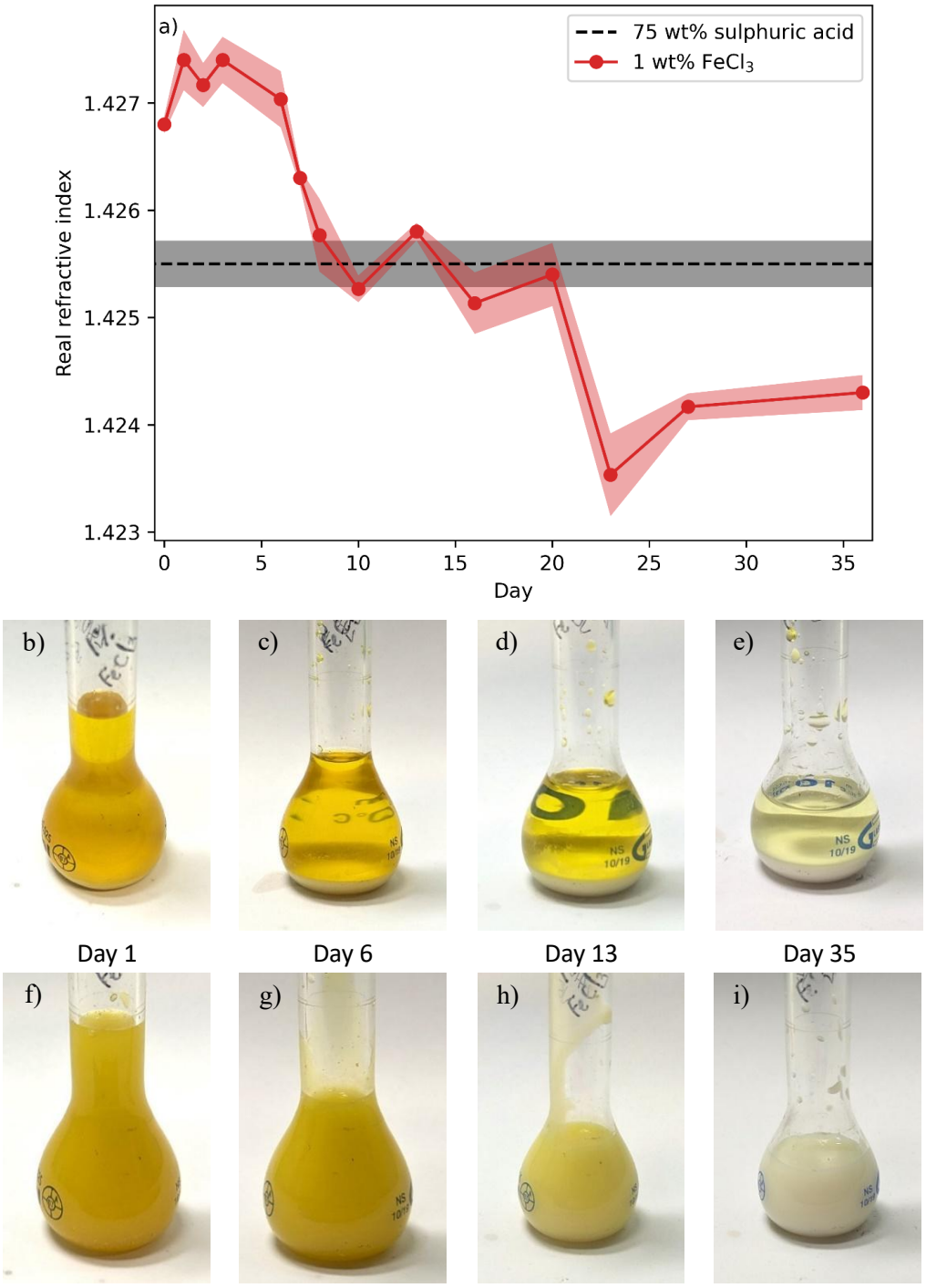

Figure 4.2. a) Measured real refractive index of 1 wt% $FeCl_3$ in 75wt% sulphuric acid. Photographs of the solution over time b – e) before mixing, or f – i) after inverting to mix. The solution becomes a paler yellow over time, but the supernatant remains yellow even after its refractive index becomes consistent with H_2SO_4 on day 10. The volume of the sample decreases as small portions are taken for spectroscopy over time. The volume of the precipitate increases over time.

Krasnopolsky (2017) reported that the lifetime of $FeCl_3$ in sulphuric acid was estimated by Zasova et al. (1981) to be around a week at room temperature, before it formed "colourless" ferric sulphate. This estimate of lifetime does not in fact appear in the paper from Zasova et al. (1981),

but as Prof. Krasnopolsky is a co-author on the paper, the lifetime may have been measured but not published. The yellow colour observed in this experiment persists for significantly longer than a week, with the supernatant remaining visibly yellow for over 5 weeks. The e-folding lifetime may be on the order of a week, but without a reliable measure of the rate of the reaction, this cannot be accurately established.

Immediately after 1% anhydrous $FeCl_3$ was added to the sulphuric acid, the mixture initially contained both light and dark particles (Figure 4.3). By comparison to anhydrous and hydrated ferric chloride powders (Figure 4.4), the dark particles are tentatively identified as unreacted anhydrous $FeCl_3$, and the yellow particles as hydrated $FeCl_3$. In many cases (though not all) the dark particles are larger than the lighter particles, which may indicate that only the surface of particles has reacted with the aqueous sulphuric acid, becoming hydrated.

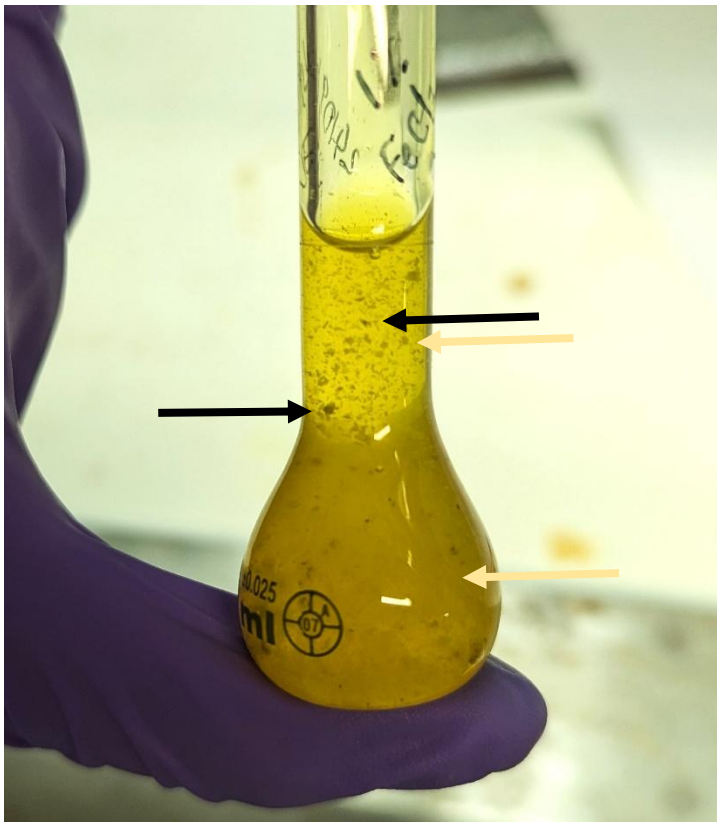

Figure 4.3. 1% $FeCl_3$ in 75 wt% sulphuric acid shortly after the solution was made up. Black and pale yellow arrows indicate some dark and light particles.

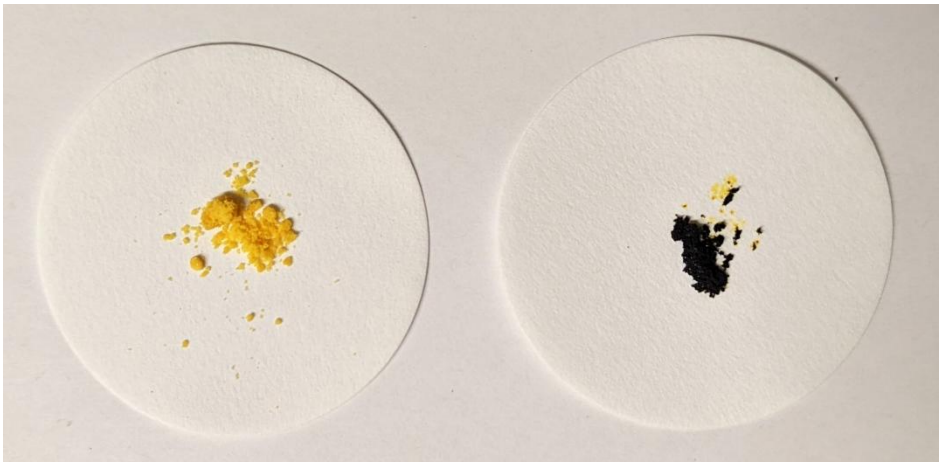

Figure 4.4. $FeCl_3.6H_2O$ (yellow, left) and anhydrous $FeCl_3$ (black, right). The anhydrous form is highly hygroscopic and absorbs ambient water from the air. This is apparent as the yellow staining on the filter paper to the top right of the anhydrous sample.

Within a day, the particles settled to the bottom of the flask, and appeared to be pale yellow or white (Figure 4.5). The presence of particles limits the robustness of conclusions that can be drawn. The flask was inverted and the particles resuspended to produce an opaque sample (Figure 4.2f). The presence of particles makes concentration calculations unreliable, as the quantity of particles in any sample taken cannot be assessed, and the concentration of the liquid will not be the same as the whole solution. The precise composition of the particles is also unknown.

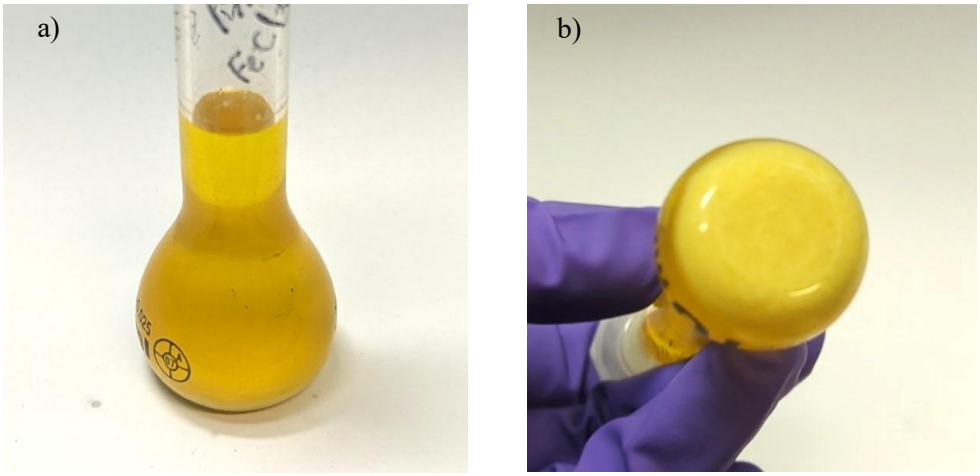

Figure 4.5. 1% $FeCl_3$ in 75 wt% sulphuric acid one day after mixing. a) The particles have settled to the bottom of the flask, leaving a translucent liquid. b) Particles are pale, either yellow or white.

The high absorption which saturated the detector when UV-Vis measurements were attempted means that lower iron concentrations must be used to draw quantitative conclusions about the absorption spectrum. The real refractive index cannot be used to estimate the rate of the reaction as the measured refractive index becomes consistent with pure sulphuric acid when the solution still contains visible absorption from $FeCl_3$ (Figure 4.2). In addition, the presence and increasing volume of the precipitate meant that the concentration of iron in the solution could not be reliably measured or controlled when the refractive index was measured. The absorption spectrum of the

supernatant was measured on days 16 and 65, but the sample saturated the detector as at the beginning of the experiment. The rate of reaction was therefore estimated from the absorbance measurements at lower concentrations of $FeCl_3$ (Section 4.7).

When $FeCl_3$ concentrations were lowered sufficiently that the detector was not saturated, measured spectra showed negligible absorption in the visible region, and were more consistent with literature spectra of ferric sulphate (Saunders et al., 2012). The rapid reaction was assumed to be caused, at least in part, by two factors: the higher temperature in the laboratory than in the upper haze and clouds on Venus (170 – 260 K), and an excess of sulphate to chloride in the samples. For all reported experiments, anhydrous $FeCl_3$ was used. The anhydrous and hydrated forms have very different appearances (Figure 4.4) and therefore optical properties outside a solution. Investigating the hydration behaviour is outside the scope of this study.

As iron can form complexes with either the chloride or the sulphate ions present in the solution, the equilibrium between the iron chloride and iron sulphate will depend on the ratio of sulphate to chloride available in the solution. When the concentration of $FeCl_3$ is decreased by three orders of magnitude (to make UV-Vis spectroscopy feasible) but the H_2SO_4 concentration is kept the same, the equilibrium position will shift dramatically towards the sulphate, resulting in the rapid formation of the iron sulphate as was seen at the lower concentrations.

Three possibilities were investigated to decrease the rate of the reaction: decreasing the temperature, decreasing the sulphate concentration, and increasing the chloride concentration.

4.2.2 Decreasing the temperature

10 ml of a solution of 80 wt% sulphuric acid was made up and left to stand in an ice bath to cool. 0.0073g of anhydrous $FeCl_3$ was added to the solution at a temperature of 12.5 °C. The solution was inverted repeatedly to mix, and removed from the ice bath. The $FeCl_3$ did not dissolve in the cold sulphuric acid and pipetting it into cuvettes was slow and difficult due to the viscosity of the sulphuric acid at low temperatures. As the $FeCl_3$ did not dissolve, the concentration of $FeCl_3$ in the sample was not known, and the presence of particulates in a UV-Vis cuvette can introduce scattering in the sample, which will introduce errors. It is interesting to note that while the particles did not dissolve, they did change colour from black to a yellow consistent with hydrated $FeCl_3$ (Figure 4.4), as seen at higher concentrations.

4.2.3 Decreasing the sulphate concentration

A 1 wt% solution of $FeCl_3$ in 75 wt% H_2SO_4 has a chloride to sulphate ratio, $[Cl^-]/[SO_4^{2-}]$, of 0.024. To maintain the same chloride to sulphate ratio when the $FeCl_3$ concentration is decreased, the sulphate concentration must be decreased proportionally. Figure 4.6 shows the measured spectrum of $1.44 \pm 0.12 \times 10^{-4}$ M $FeCl_3$ in $1.70 \pm 0.14 \times 10^{-2}$ M sulphuric acid ($2.3 \pm 0.2 \times 10^{-3}$ wt% $FeCl_3$ and 0.167 ± 0.014 wt% H_2SO_4), with $[Cl^-]/[SO_4^{2-}]$ of 0.025(3). The remainder of the solution is deionised water. Throughout this work, reported errors refer to the

precision of instrumentation or variation between repeated measurements alone. Other sources of errors are likely, such as from the purity of reagents, but cannot be reliably quantified.

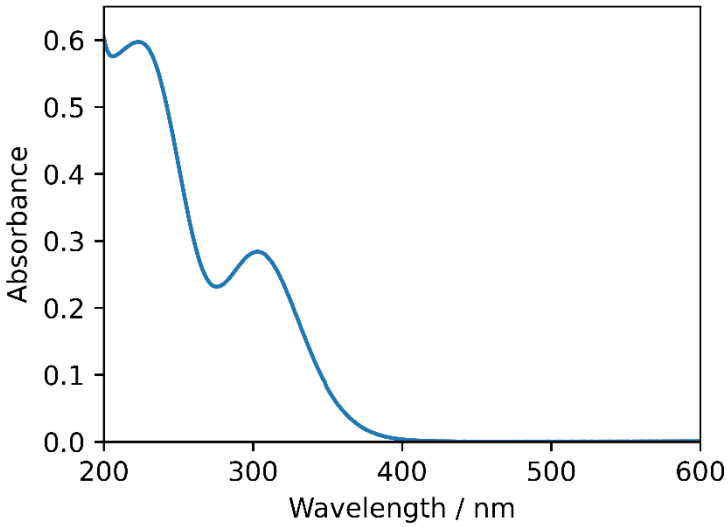

Figure 4.6. The average of four measured absorption spectra of $1.44 \pm 0.12 \times 10^{-4}$ M $FeCl_3$ in $1.70 \pm 0.14 \times 10^{-2}$ M sulphuric acid. Variation between repeats is within the thickness of the line.

The resulting spectrum has a different shape than the spectra obtained at higher sulphuric acid concentrations (data not shown), with the peak near 300 nm much lower than the peak near 220 nm. The spectrum is consistent with either $Fe(SO_4)^+$ or $Fe(OH)^{2+}$ (Saunders et al., 2012; Whiteker & Davidson, 1953). The difference in shape due to the lower sulphate concentration means this is not a suitable method for comparison to Venus.

4.2.3 Increasing the chloride concentration

As the sulphate concentration cannot be decreased, the alternative way to maintain the chloride to sulphate ratio at lower $FeCl_3$ concentrations is to increase the chloride concentration. This effectively moves the equilibrium shown in Reaction R1 towards $FeCl_3$.

Williams and Golden (1993) reported the predicted uptake of HCl into stratospheric sulphate aerosol in the Earth's Junge layer. By analogy, HCl uptake onto sulphuric acid cloud droplets would be expected on Venus. Using the Henry's law constant for HCl in H_2SO_4 reported by Williams & Golden, HCl uptake into Venusian cloud droplets is estimated to produce 1×10^{-6} to 3×10^{-4} M HCl in the droplets for pure aqueous sulphuric acid (Figure 4.7). The inclusion of $FeCl_3$ in the droplets would be expected to change this value. The HCl gas phase concentration profile is taken from the longitude-averaged out-of-the-box Venus PCM results (Figure 2.11) at low latitudes.

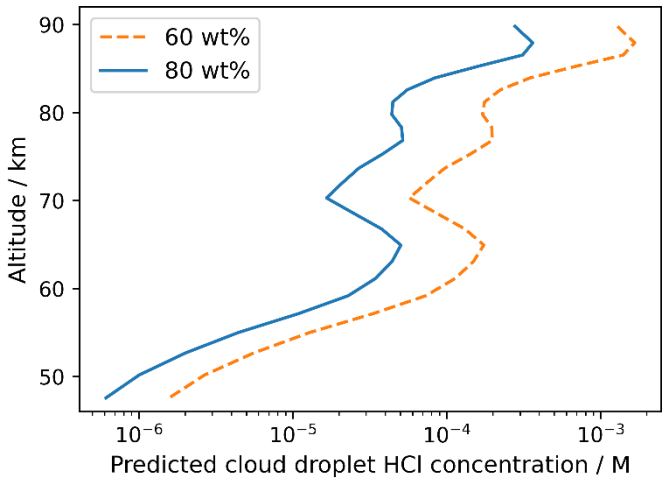

Figure 4.7. Cloud droplet predicted HCl concentration using a PCM HCl mixing ratio profile and Henry's law coefficients reported by Williams and Golden (1993) at 60 wt% sulphuric acid (orange) and extrapolated to 80 wt% (blue).

When the $FeCl_3$ concentration is decreased from 1 wt% to 2×10^{-3} wt% in 75 wt% sulphuric acid, the remaining chloride to retain a Cl:SO_4 ratio of $[Cl^-]/[SO_4^{2-}] = 0.024$ can be provided by the addition of approximately 0.7 wt% HCl. Figure 4.8 shows the absorption spectrum of $2.3 \pm 0.2 \times 10^{-4}$ M $FeCl_3$ in a solution of 12.45 ± 0.02 M H_2SO_4 and an initial concentration 0.2847 ± 0.0007 M HCl ($2.3 \pm 0.2 \times 10^{-3}$ wt% $FeCl_3$, 74.71 ± 0.02 wt% H_2SO_4 and 0.6356 ± 0.0013 wt% HCl, with $[Cl^-]/[SO_4^{2-}] = 0.023(5)$). HCl nucleated out of the solution during preparation, so the true HCl concentration is unknown, but is lower than the amount added.

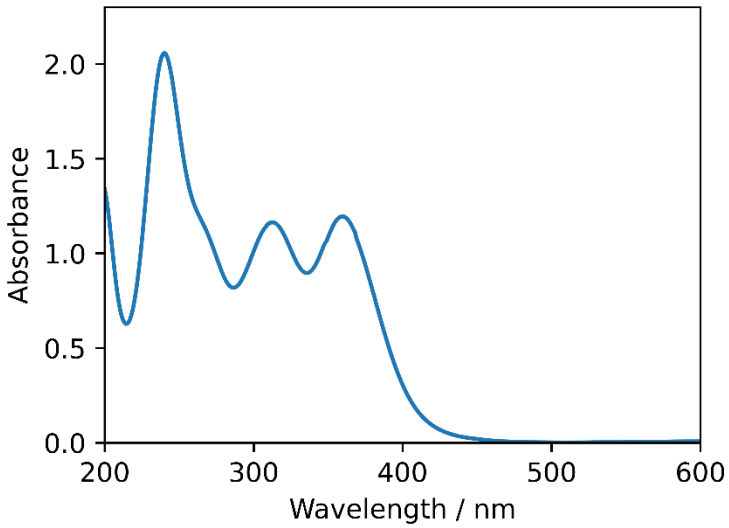

Figure 4.8. The average of four measured absorption spectra of $2.3 \pm 0.2 \times 10^{-4}$ M $FeCl_3$ in a solution of <0.2847 ± 0.0007 M HCl and 12.45 ± 0.02 M H_2SO_4. Variation was within the thickness of the line.

The resulting spectrum bears strong similarity to those reported by Liu et al. (2006) for $FeCl_3$ in a solution of HCl and LiCl, and the solution had a yellow colour by eye. The high concentration of HCl used led to HCl evaporating out of solution after it was prepared, so the exact

concentrations of HCl will need to be considered to both prevent the evaporation and to reproduce the expected Venusian HCl droplet concentration (Figure 4.7) most accurately. The inclusion of HCl to increase the chloride concentration in the solutions is the best available method – both for performing the lab work, and in similarity to Venusian conditions – to measure the absorption spectrum of ferric chloride in Venusian concentrations of sulphuric acid.

4.2.4. Proposed explanation for [Cl^-] dependence

In the absence of any added HCl, all Cl^- in the solution must have been produced by the dissociation of $FeCl_3$. When high concentrations of $FeCl_3$ (such as proposed in Venusian cloud droplets) are added, only a very small fraction would need to partially dissociate, forming $FeCl_2^+$, before the solution is saturated with respect to Cl^-. The partial dissociation of some $FeCl_3$ "protects" most of it from rapid dissociation as the solution becomes saturated with respect to Cl^-.

When lower concentrations of $FeCl_3$ are added to the solution, the $FeCl_3$ must dissociate more fully to produce Cl^- concentrations to saturate the solution and protect the undissociated or partially undissociated iron chloride molecules or ions. When HCl is added to the solution, the Cl^- from the HCl saturates the solution, preventing rapid dissociation of the $FeCl_3$.

4.2.5 Summary of experiments

Six stages of experiments were carried out, which are detailed in Sections 4.3 – 4.8. The change in absorption with time was measured for mixtures of sulphuric acid and varying concentrations of HCl and $FeCl_3$ (Section 4.3); the absorption spectra of $Fe_2(SO_4)_3$ and $FeCl_3$ in H_2SO_4 were measured and compared to identify the product of the reaction as ferric sulphate (Section 4.4); the spectral dependence of the same concentration of $Fe_2(SO_4)_3$ in different concentrations of H_2SO_4 was measured over time to investigate if further reactions could occur (Section 4.5); the molar absorptivity of $FeCl_3$ in HCl and $Fe_2(SO_4)_3$ in H_2SO_4 were measured (Section 4.6) for use in a fitting program to estimate the sulphate and chloride partitioning in the mixtures and the rate of the reaction (Section 4.7); and finally, the effect of temperature on the rate of the reaction for a single concentration of $FeCl_3$, HCl and H_2SO_4 was measured (Section 4.8).

4.3 Change of absorption over time for $FeCl_3$ in an HCl/H_2SO_4 mixture

4.3.1 Sample preparation

Two sets of samples were prepared and measured, the first starting in November 2023 (N23), the second in August 2024 (A24). Each set contained 18 samples at three HCl concentrations and six $FeCl_3$ concentrations (five concentrations up to 5×10^{-4} M to avoid saturating the detector with either initial ferric chloride or the final expected ferric sulphate concentration, and one sample with no $FeCl_3$ in it). In the N23 set, samples were added by volume, but the pipette used was later found to be unreliable. The masses of the samples were also recorded to check concentrations, so calculations use the recorded masses, not the measured volumes. For the A24 set, the expected masses of solutions were calculated beforehand and addition of the required quantities of different solutions performed by mass. The concentrations of each of the samples are listed in Table 4.1.

Table 4.1. Concentrations of H_2SO_4, HCl, and $FeCl_3$ in each sample.

Set	Sample	H_2SO_4 concentration / M	H_2SO_4 concentration / wt%	HCl / M	$FeCl_3$ / $\times 10^{-4}$ M
N23	0A	12.81(8)	76.5(5)	$10.309(14) \times 10^{-2}$	-
	0B	12.85(8)	76.5(5)	$9.452(9) \times 10^{-2}$	0.863(14)
	0C	12.84(8)	76.5(5)	$9.334(9) \times 10^{-2}$	1.72(3)
	0D	12.87(8)	76.6(5)	$9.158(9) \times 10^{-2}$	2.49(4)
	0E	12.76(8)	76.5(5)	$7.99(8) \times 10^{-2}$	2.85(5)
	0F	12.90(8)	76.6(5)	$9.177(13) \times 10^{-2}$	4.18(7)
	1A	12.92(8)	76.6(5)	$10.297(16) \times 10^{-3}$	-
	1B	12.91(8)	76.7(5)	$10.250(11) \times 10^{-3}$	1.43(2)
	1C	12.88(9)	76.7(5)	$9.2(3) \times 10^{-3}$	1.77(7)
	1D	12.91(8)	76.7(5)	$10.065(11) \times 10^{-3}$	2.97(5)
	1E	12.80(8)	76.9(5)	$7.922(10) \times 10^{-3}$	2.79(5)
	1F	12.87(8)	76.6(5)	$10.351(16) \times 10^{-3}$	4.63(8)
	2A	12.93(12)	77.0(9)	$9.49(16) \times 10^{-4}$	-
	2B	13.02(8)	76.7(5)	$9.96(12) \times 10^{-4}$	1.33(2)
	2C	13.07(8)	76.5(5)	$10.26(12) \times 10^{-4}$	2.12(3)
	2D	12.94(8)	76.6(5)	$10.94(13) \times 10^{-4}$	3.28(5)
	2E	12.99(8)	76.8(5)	$8.60(11) \times 10^{-4}$	3.10(5)
	2F	13.10(8)	77.1(5)	$9.67(16) \times 10^{-4}$	4.31(7)
A24	0A	13.37(2)	78.138(17)	$9.56(13) \times 10^{-2}$	-
	0B	13.26(2)	78.12(2)	$9.43(11) \times 10^{-2}$	0.918(10)
	0C	13.36(2)	78.17(2)	$9.52(9) \times 10^{-2}$	1.92(2)
	0D	13.40(2)	78.12(2)	$9.62(10) \times 10^{-2}$	2.88(3)
	0E	13.34(2)	78.161(19)	$9.28(11) \times 10^{-2}$	3.71(3)
	0F	13.48(2)	78.176(18)	$9.37(13) \times 10^{-2}$	4.65(5)
	1A	13.25(2)	78.11(2)	$9.52(13) \times 10^{-3}$	-
	1B	13.42(2)	78.218(19)	$9.57(11) \times 10^{-3}$	0.945(10)
	1C	13.27(2)	78.049(18)	$9.62(10) \times 10^{-3}$	1.86(2)
	1D	13.36(2)	78.184(15)	$9.37(9) \times 10^{-3}$	2.73(3)
	1E	13.36(2)	78.145(18)	$9.68(11) \times 10^{-3}$	3.78(4)
	1F	13.31(2)	77.976(16)	$10.31(14) \times 10^{-3}$	5.02(5)
	2A	13.26(2)	78.080(19)	$9.59(13) \times 10^{-4}$	-
	2B	13.31(2)	78.163(18)	$9.58(11) \times 10^{-4}$	0.955(11)
	2C	13.24(2)	77.939(19)	$9.83(10) \times 10^{-4}$	1.90(2)
	2D	13.31(2)	78.080(18)	$9.62(10) \times 10^{-4}$	2.82(3)
	2E	13.42(2)	78.16(2)	$10.22(12) \times 10^{-4}$	4.06(4)
	2F	13.17(2)	78.07(2)	$9.81(13) \times 10^{-4}$	4.79(5)

4.3.2 Change in spectral shape over time

A clear change in shape can be seen in high HCl concentration (batch 0) spectra: the initial spectrum is similar to Figure 4.8, with three distinct peaks at 241, 313 and 361 nm. Over time, the shape changes to become more consistent with literature spectra of ferric sulphate. Figure 4.9 shows samples 0C from the N23 and A24 sets with all spectra.

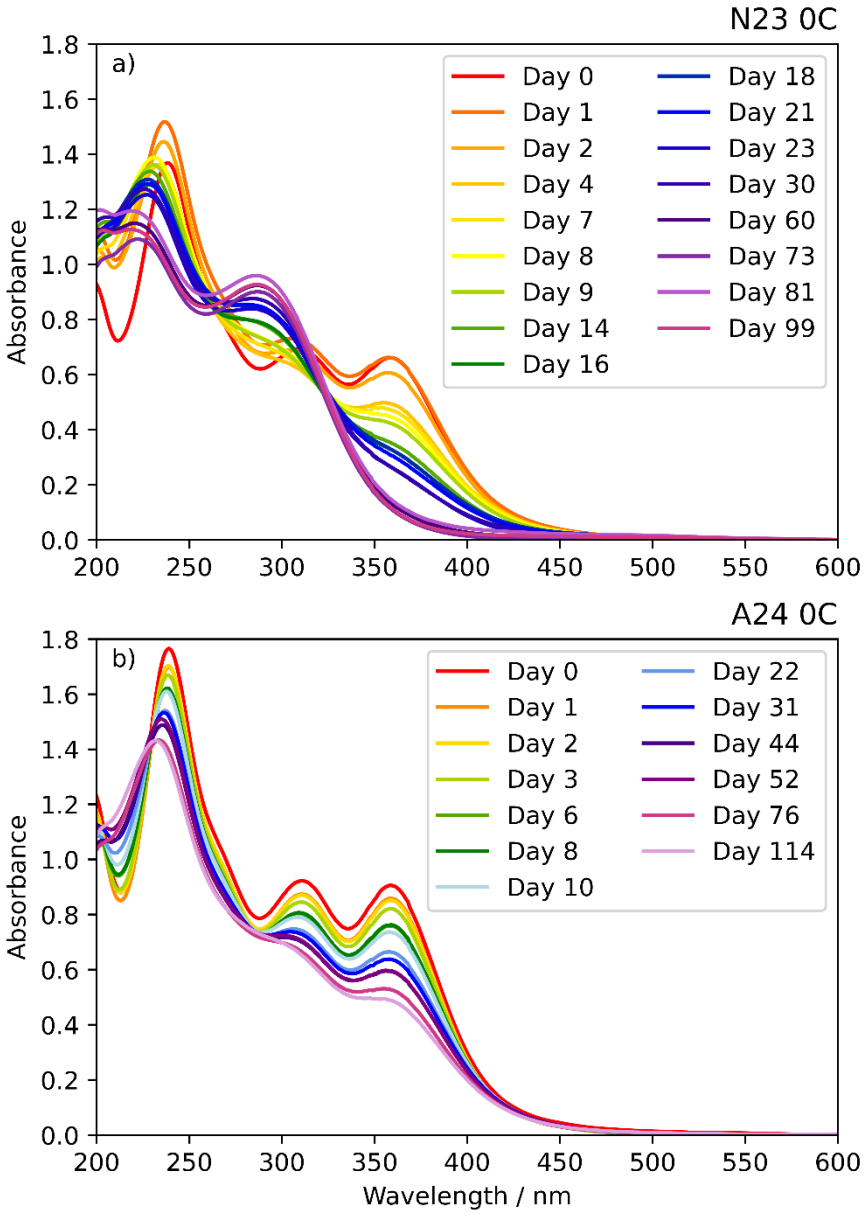

Figure 4.9. Change in the measured absorbance spectrum of sample 0C from both sets of samples with time. The reader is referred to Table 4.1 (page 164) for concentrations.

The change in shape of all samples over time are shown in Figures 4.10 (set N23) and 4.11 (A24). In some cases, subsequent spectra exhibited only small changes. Representative spectra over time are therefore shown for clarity. Spectra at low concentrations of HCl are broadly consistent with ferric sulphate for the whole experiment.

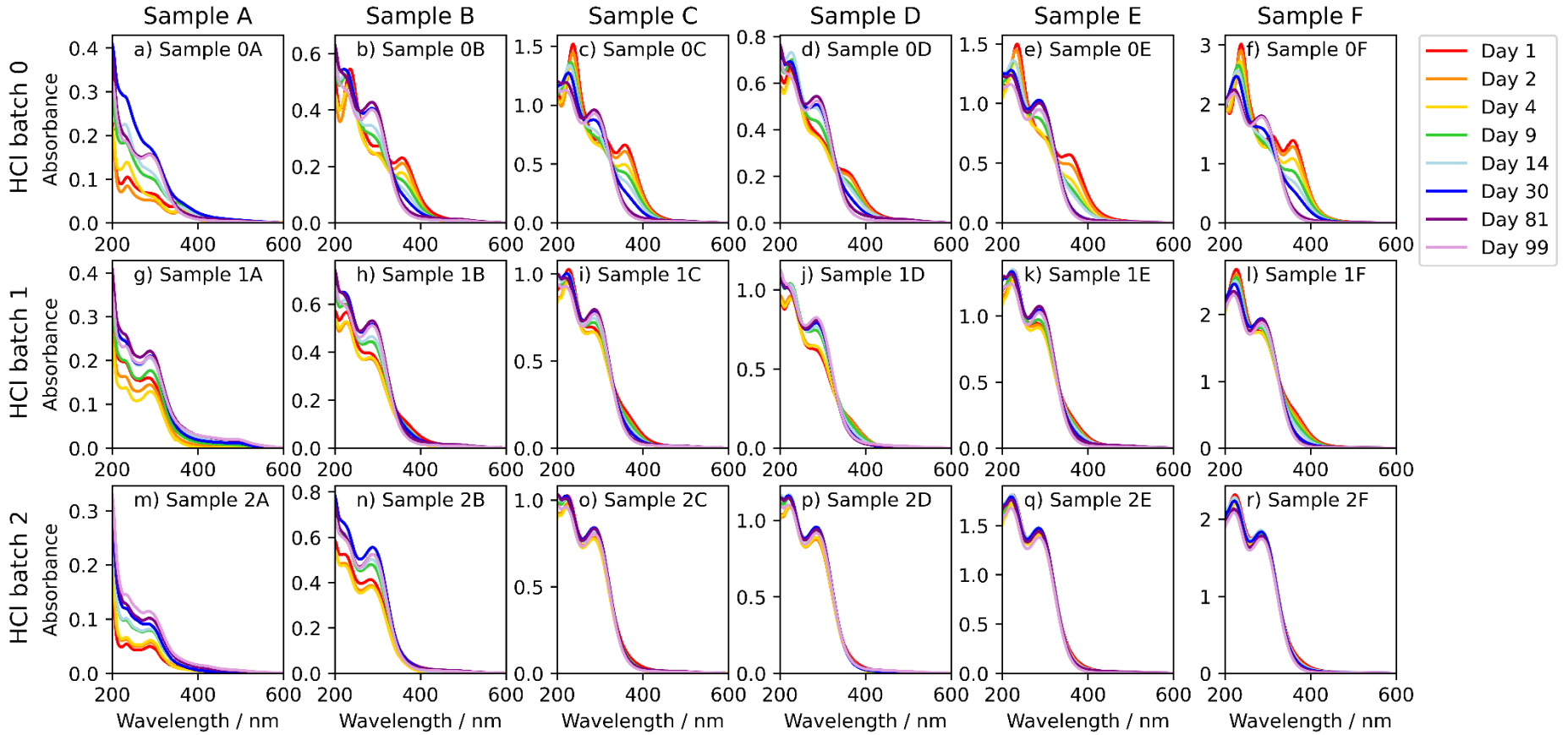

Figure 4.10. Spectra over time for all samples in set N23. HCl concentration decreases from top to bottom, initial $FeCl_3$ concentration roughly increases from left to right. The reader is referred to Table 4.1 (page 164) for interpretation of concentrations.

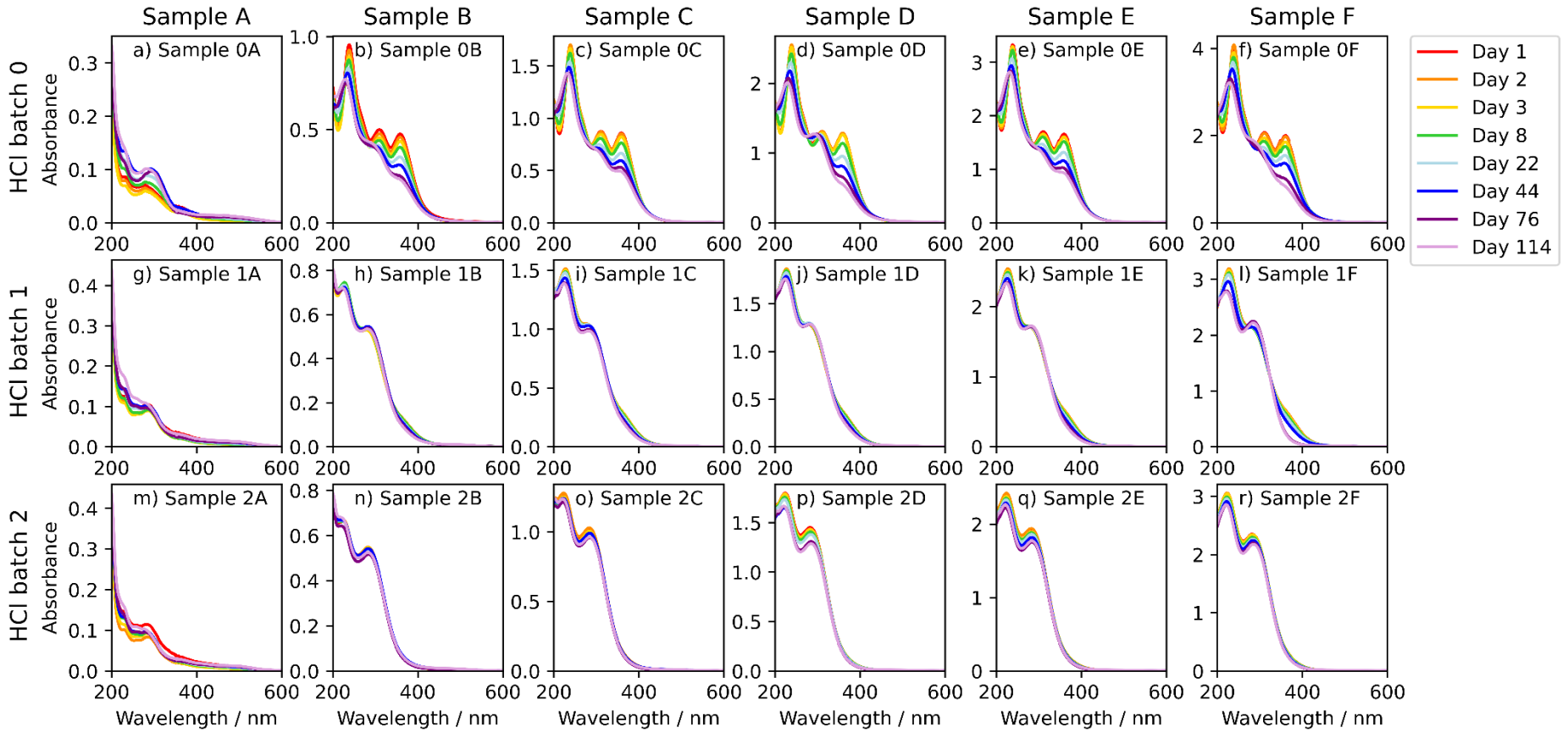

Figure 4.11. Spectra over time for all samples in set A24. HCl concentration decreases from top to bottom, initial $FeCl_3$ concentration increases from left to right.

The reader is referred to Table 4.1 (page 164) for interpretation of concentrations.

There is a clear difference in reaction rate between the N23 and A24 sets, which is unexpected due to the similarity in concentrations and conditions. The rates in each case are calculated in Section 4.7. The N23 sample set was prepared and measured on the same day. The absorbance measured immediately after preparation (Day 0) was significantly lower than on subsequent days (Figure 4.9a), which may indicate that the $FeCl_3$ had not fully dissolved when the first spectra were measured. The samples for the A24 sample set were therefore prepared the night before the first spectra (Day 0) were measured, and do not exhibit the same low initial absorbance.

As the reaction happens rapidly at low concentrations of HCl, it is likely that the initial spectra at high concentrations contain some small amount of ferric sulphate as well. To confirm the hypothesis that the change in shape of over time is due to the reaction of the ferric chloride to form ferric sulphate, additional investigations were carried out to identify the species present (Sections 4.4 and 4.5). Spectra of ferric chloride in HCl and ferric sulphate in sulphuric acid (Section 4.6) were measured and a fitting programme developed (Section 4.7) to estimate the concentrations of ferric chloride and ferric sulphate in the solutions at all times.

4.4. Identification of the reaction product as ferric sulphate

Samples of iron salts and sulphuric acid were made up, one with Fe(III) chloride ($FeCl_3$) and one with Fe(III) sulphate ($Fe_2(SO_4)_3.5H_2O$). Shapes of spectra were compared to confirm the end product seen in Section 4.3 is ferric sulphate.

4.4.1 Method

For each of $FeCl_3$ and $Fe_2(SO_4)_3$, six 25.00 ± 0.04 ml stock solutions of sulphuric acid were prepared at a range of concentrations from 10 – 89 wt% as listed in Tables 4.2 and 4.3 respectively. To produce the samples, $FeCl_3$ was initially added to concentrated (98 wt%) sulphuric acid to produce a stock iron solution, but it did not dissolve and a lower concentration of sulphuric acid was therefore used instead. Samples were produced by adding a small amount of iron stock solution to 10.00 ± 0.05 ml volumetric flasks, made up with the stock acids. For each of the sulphate and chloride samples, a spectrum of the stock sulphuric acid was measured for baseline removal, then the undiluted sample was measured. Approximately 3.5 ml of sample was removed from the volumetric flask (the exact mass removed was measured) and the volumetric flask made back up to 10.00 ± 0.05 ml with the corresponding stock sulphuric acid resulting in a decrease of the iron concentration while maintaining the sulphuric acid concentration. The concentrations of $FeCl_3$ solutions after each dilution are listed in Table 4.2, concentrations of $Fe_2(SO_4)_3$ are listed in Table 4.3.

Table 4.2. Resulting concentrations of $FeCl_3$ in different concentrations of sulphuric acid.

Sample	H_2SO_4 concentration		$FeCl_3$ / × 10^{-4} M* (Dilution number)				
	/ M	/ wt%	0	1	2	3	4
A	18.02(9)	88.917(11)	7.1(5)	5.8(4)	4.7(3)	3.9(3)	3.1(2)
B	15.81(8)	79.796(10)	6.9(5)	5.5(4)	4.5(3)	3.6(2)	2.9(2)
C	12.88(6)	67.431(9)	7.2(5)	5.9(4)	4.8(3)	3.9(3)	3.2(2)
D	9.36(5)	51.084(8)	7.7(5)	6.5(4)	5.4(4)	4.5(3)	3.7(2)
E	5.73(3)	31.676(7)	7.2(5)	6.1(4)	5.1(3)	4.3(3)	3.6(2)
F	3.36(2)	15.610(5)	7.3(5)	6.2(4)	5.3(3)	4.5(3)	3.8(2)

*Undiluted samples (dilution number 0) saturated the detector and are not used.

Table 4.3. Resulting concentrations of $Fe_2(SO_4)_3$ in different concentrations of sulphuric acid.

Sample	H_2SO_4 concentration		Fe / × 10^{-4} M * (Dilution number)				
	/ M	/ wt%	0	1	2	3	4
A	18.25(9)	89.505(11)	4.8(5)	3.9(4)	3.1(3)	2.6(3)	2.1(2)
B	15.83(8)	79.695(10)	4.8(5)	4.0(4)	3.2(3)	2.6(3)	2.1(2)
C	12.90(7)	67.532(9)	5.0(5)	4.1(4)	3.4(3)	2.8(3)	2.3(2)
D	9.43(5)	52.071(8)	5.0(5)	4.1(4)	3.4(3)	2.9(3)	2.4(2)
E	5.63(3)	31.874(7)	4.8(5)	4.0(4)	3.4(3)	2.9(3)	2.4(2)
F	3.50(2)	17.026(6)	4.8(5)	4.1(4)	3.5(3)	3.0(3)	2.5(2)

*One mole of $Fe_2(SO_4)_3$ contains two moles of Fe. Fe concentration is calculated for direct comparison with $FeCl_3$.

4.4.2 Molar absorptivity comparison

For each sample, the spectrum of the corresponding stock acid was subtracted from all of the iron spectra. The Beer-Lambert law relates the concentration, c, of an absorbing species to its measured absorption, A:

$$A = \varepsilon c l \tag{4.1}$$

where the beam path, l = 1 cm and ε is the molar absorptivity of the absorbing species. The molar absorptivity is a measure of the strength of absorption of a species in solution. It has units of L mol^{-1} cm^{-1} (or M^{-1} cm^{-1}) and is related to the cross-section (σ, in cm^2 $molecule^{-1}$) of the molecule (the traditional gas phase measure of absorption strength) by $\sigma = 3.82 \times 10^{-21}\ \varepsilon$ (Lakowicz, 2006).

The linearity of the absorption with iron concentration was checked at several wavelengths and spectra discounted if they did not obey linearity. All undiluted $FeCl_3$ spectra were neglected for this reason. Figure 4.12 shows the measured spectra relative to the stock acid and linearity at certain wavelengths for sample C (12.9 M, 67 wt% H_2SO_4) for both $FeCl_3$ (left) and $Fe_2(SO_4)_3$ (right) samples.

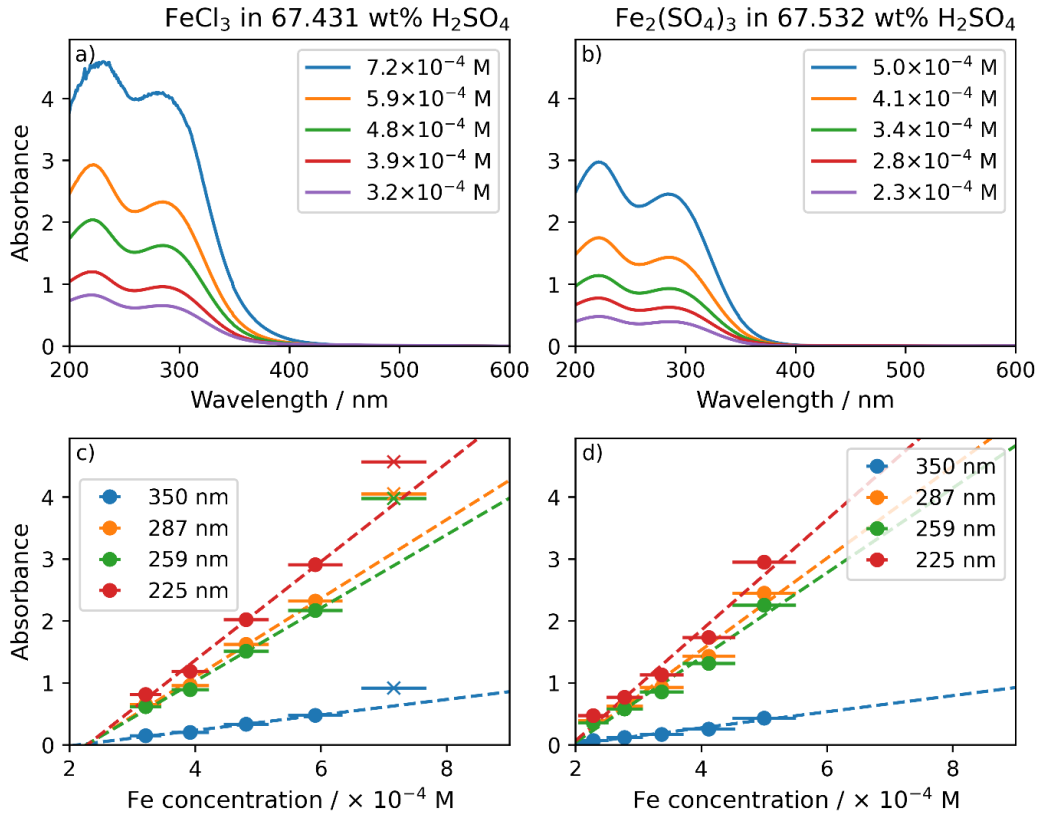

Figure 4.12. Measured spectra relative to stock acids for a) $FeCl_3$ and b) $Fe_2(SO_4)_3$. The Fe concentration in the samples is plotted against absorbance at several wavelengths (c, d) and any concentrations that do not obey a linear relationship are shown as crosses and excluded from the calculation of absorptivity. Linear regression lines are fitted through the solid points.

All undiluted $FeCl_3$ samples (~7×10^{-4} M) show noise in the measured spectra (Figure 4.12a), indicative of saturated absorption, and the datapoints at that 7.2×10^{-4} M at all wavelengths clearly deviate from linearity (Figure 4.12c). Spectra of the undiluted $FeCl_3$ samples (shown as crosses, rather than points) are not included in the linear best fit. Samples at all other concentrations obey linearity to within the uncertainty of the concentration. The $FeCl_3$ sample lines of best fit do not pass through the origin, which may indicate the presence of a second species, likely a small amount of unreacted $FeCl_3$.

Orthogonal distance regression using the built-in scientific python (SciPy) module (scipy.odr) was used to fit the data to the Beer-Lambert law (Equation 4.1) and calculate the molar absorptivity of iron for each sample. Figure 4.13 shows the calculated molar absorptivity for all 12 sets of samples.

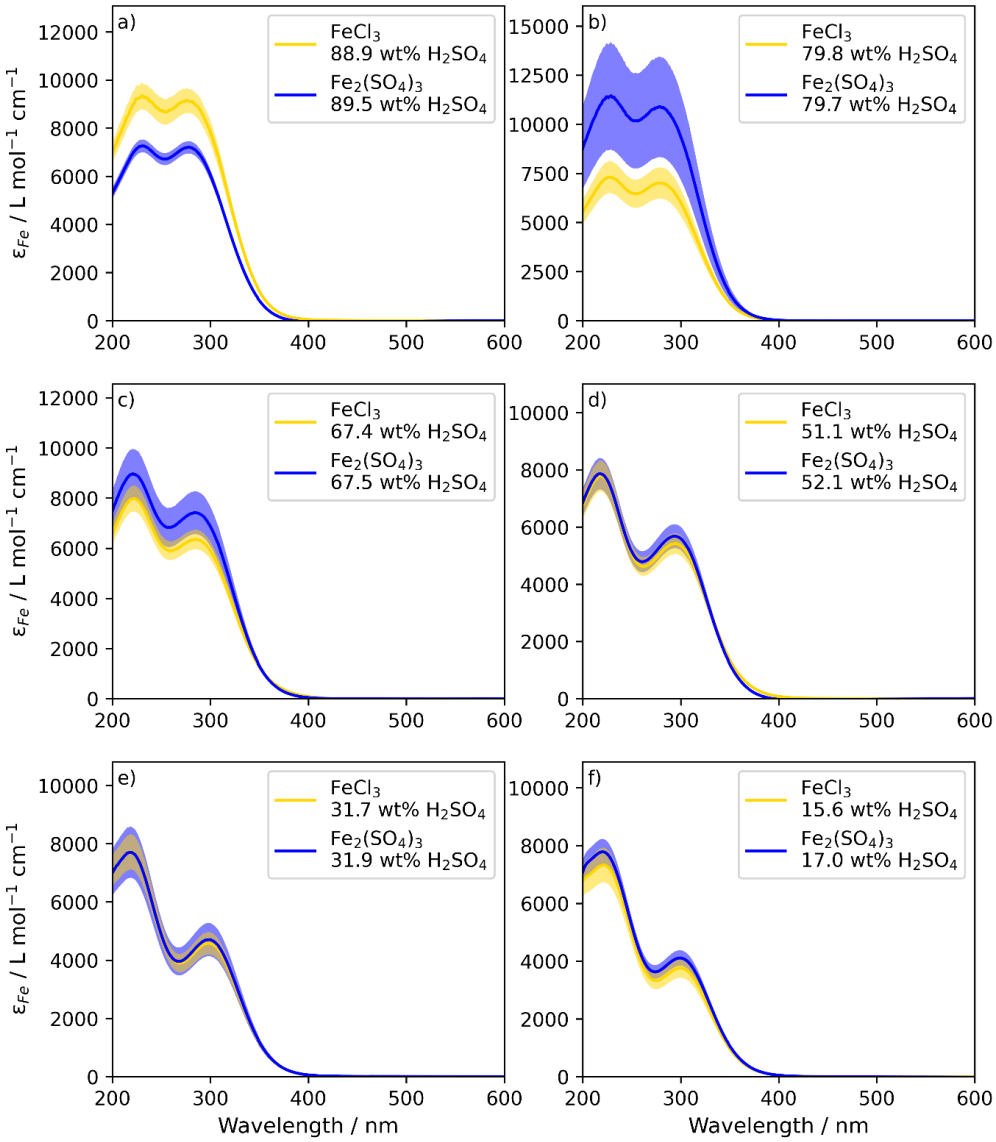

Figure 4.13. Calculated molar absorptivity of Fe for $FeCl_3$ (yellow) and $Fe_2(SO_4)_3$ (blue). Samples at similar sulphuric acid concentrations are plotted together for comparison.

At low H_2SO_4 concentrations, the spectra show good agreement. The spectra are mostly within uncertainty of each other, and only small differences are present. For example, in Figures 4.13d and e, there is lower absorptivity for $FeCl_3$ in the peak near 300 nm, but similar absorptivity in the peak near 225 nm. This may indicate the continued presence of small amounts of unreacted $FeCl_3$. The higher absorption in the tail near 400 nm appears to support this, as this is the region assumed to be dominated by $FeCl_3$ by comparison with Figures 4.9 – 4.11. The differences between the spectra are much greater at high H_2SO_4 concentration. The $FeCl_3$ and $Fe_2(SO_4)_3$ spectra have very similar shapes to each other, but the actual absorptivity values vary between the two (Figures 4.13a and b), suggesting that the same species are present, but there is a systematic error in the concentrations. It is possible that the dissolution of the iron salts at higher concentrations was much slower due to the lower concentration of water in the solutions, and the reported uncertainties in the concentrations shown are a significant underestimate due to lower concentrations of iron than the bulk value in some samples.

There is a change in shape of the sulphate spectra with H_2SO_4 concentration as well, with the ratio between the two peaks changing and the location in wavelength of the second peak shifting from 300 nm to 290 nm with increasing H_2SO_4 concentration (see Figure 4.15). This highlights the importance of using spectra measured at the correct sulphuric acid concentration for comparison between spectra, especially when using spectra to identify species.

4.5 Investigation of further reaction of ferric sulphate

Jiang et al. (2024) reported the formation of rhomboclase, $(H_5O_2)Fe(SO_4)_2.3H_2O$, and acid ferric sulphate, $(H_3O)Fe(SO_4)_2$ from iron in sulphuric acid. 21 samples of ~2.2×10^{-4} M $Fe_2(SO_4)_3$ in varying concentrations of H_2SO_4 were tested over four months to see if any further reaction should be considered, or if ferric sulphate was the final product in the samples measured in Section 4.3.

4.5.1 Sample preparation

~0.05g of $Fe_2(SO_4)_3$ was made up to 25.00 ± 0.04 ml in a volumetric flask with 90 wt% H_2SO_4 to produce a sulphate stock solution. For H_2SO_4 concentrations of 72 – 98 wt% (10 – 60 wt%), ~2.1g (~0.84g) of sulphate stock solution was added to 25.00 ± 0.04 ml (10.00 ± 0.05 ml) volumetric flasks and made up with deionised water and sulphuric acid to the required concentrations. Samples were allowed to stand overnight to equilibrate to room temperature, and made up with additional sulphuric acid if required. The concentrations of the samples are listed in Table 4.4.

Table 4.4. Concentrations of $Fe_2(SO_4)_3$ and H_2SO_4 in each sample.

Sample name	H_2SO_4 concentration		$Fe_2(SO_4)_3$ / $\times 10^{-4}$ M	Fe / $\times 10^{-4}$ M
	/ wt%	/ M		
15 %	14.66(2)	1.653(9)	2.22(6)	4.44(11)
24 %	23.78(2)	2.809(14)	2.16(5)	4.33(11)
35 %	35.321(19)	4.54(2)	2.24(6)	4.48(11)
45 %	44.745(18)	6.10(3)	2.27(6)	4.53(11)
54 %	54.113(17)	7.85(4)	2.24(6)	4.47(11)
63 %	63.289(16)	9.80(5)	2.22(6)	4.43(11)
72 %	72.033(6)	11.844(19)	2.22(5)	4.44(11)
74 %	74.181(6)	12.36(2)	2.24(5)	4.48(11)
76 %	76.073(6)	12.90(2)	2.25(5)	4.50(11)
78 %	77.882(6)	13.35(2)	2.19(5)	4.39(11)
80 %	79.474(6)	13.68(2)	2.29(6)	4.58(11)
81 %	81.285(6)	14.16(2)	2.25(6)	4.50(11)
83 %	83.228(6)	14.79(2)	2.26(6)	4.52(11)
85 %	84.997(6)	15.26(2)	2.24(5)	4.47(11)
87 %	86.804(6)	15.73(3)	2.25(5)	4.49(11)
89 %	88.612(6)	16.21(3)	2.27(6)	4.53(11)
90 %	90.433(6)	16.71(3)	2.25(6)	4.51(11)
92 %	92.305(6)	17.18(3)	2.22(5)	4.44(11)
94 %	94.189(6)	17.61(3)	2.24(5)	4.48(11)
96 %	96.060(6)	18.03(3)	2.27(6)	4.53(11)
98 %	97.633(6)	18.29(3)	2.22(5)	4.44(11)

4.5.2 Change in spectral shape over time

Spectra were measured periodically for 118 days after the solutions were produced. A selection of spectra over time at various H_2SO_4 concentrations are shown in Figure 4.14.

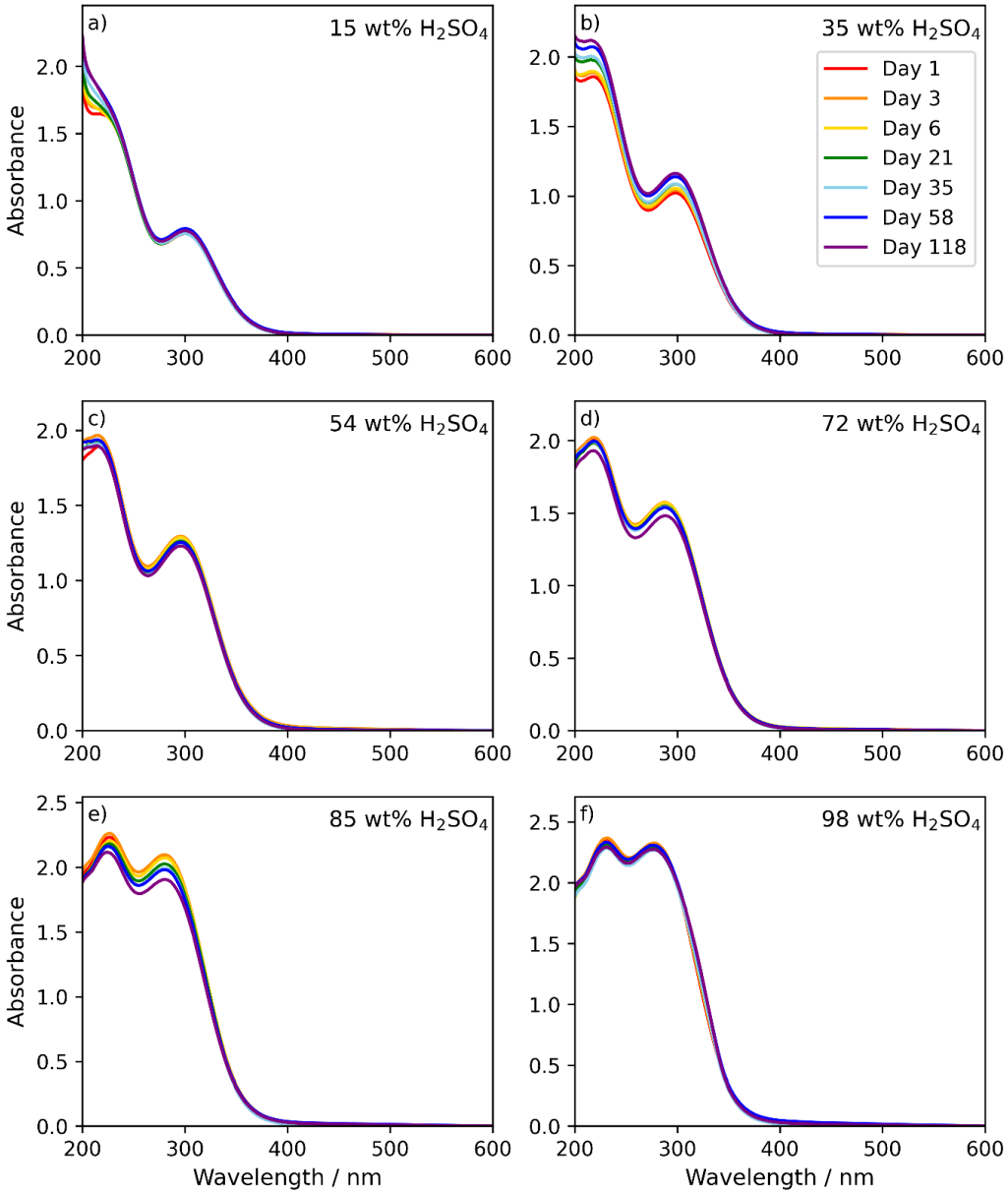

Figure 4.14. Measured absorption spectra at different H_2SO_4 concentrations over time. The reader is referred to Table 4.4 (page 172) for precise concentrations.

Subtle changes in the spectra can be seen over time. At low concentrations, there is a slight increase in absorbance with time near 220 nm (Figure 4.14a, b). Higher concentrations show a slight decrease in peak absorbance at long times (Figure 44d, e), which may indicate the sulphate salt has come out of solution and the inversion of the samples was unable to re-dissolve it. There is no indication of the formation of other phases reported by Jiang et al. (2024), who found absorption by acid ferric sulphate and rhomboclase in the 300 – 500 nm wavelength region. There is some increase in absorption at 400 – 500 nm at high concentrations, but it is less than the variation seen at the peaks of the absorption over the same time period, so may be due to variation

in samples, not the formation of a new species. If it is absorption due to the formation of other species, it is broadly negligible compared to the strong absorption exhibited by the ferric sulphate ions.

4.5.3 Dependence of spectral shape on sulphate concentration

Figure 4.15 shows the average spectrum of each sample over time. A broad trend can be seen for increasing absorption near 300 nm with increasing H_2SO_4 concentration, and a gradual shift in the wavelength of this second absorption peak from 300 nm to 290 nm. Two exceptions to this trend exist: the lowest concentrations exhibit a sharp increase towards 200 nm, and from 45 – 63 wt%, the height of the second peak decreases slightly and exhibits a larger shift towards shorter wavelengths. The height of the first peak remains more consistent throughout and appears to correlate to the concentration of iron, not of sulphuric acid.

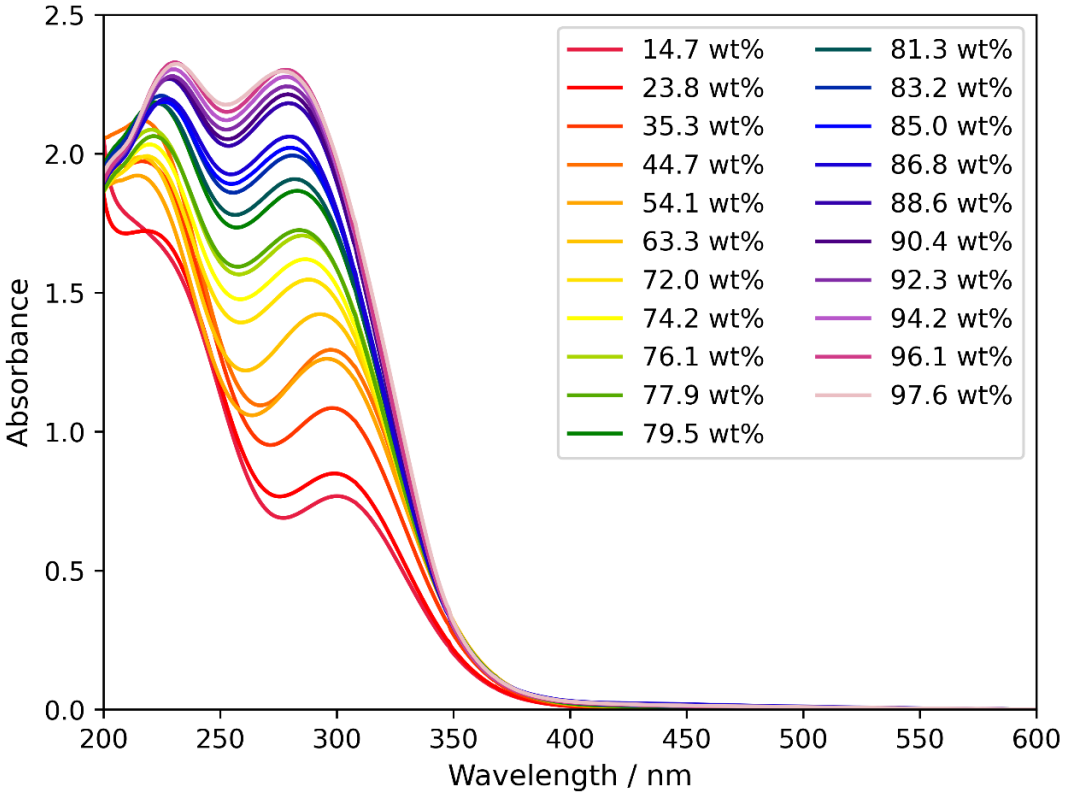

Figure 4.15. Average absorbance spectrum over time for each sample.

While the general term "ferric sulphate" is used, there are four potential ion complexes to consider, listed by Saunders et al. (2012) for a similar system: Fe^{3+}, $Fe(OH)^{2+}$, $FeSO_4^{+}$, and $Fe(SO_4)_2^{-}$. At high sulphuric acid concentrations, they identified the two peaks at 220 nm and 290 nm as Fe^{3+} and $Fe(SO_4)_2^{-}$, respectively. Another iron ion complex, potentially $Fe(OH)^{2+}$, which Saunders et al. reported dominating at low acidity, is assumed to be the cause of the high absorption at 200 nm at 15 and 24 wt% H_2SO_4. As it disappears well before representative Venusian concentrations, no further attempt is made to identify this species.

The second peak, which moves from ~300 nm at low sulphuric acid concentration to ~290 nm at high concentrations, is therefore assumed to be a superposition of $FeSO_4^+$ (which has an absorptivity maximum of ~2200 L mol^{-1} cm^{-1} at 300 nm) at low concentrations and $Fe(SO_4)_2^-$ (maximum of ~3000 L mol^{-1} cm^{-1} at 289 nm) at higher concentrations (Saunders et al., 2012; Whiteker & Davidson, 1953). The conversion of the iron from the $FeSO_4^+$ to $Fe(SO_4)_2^-$ complex ions fits the pattern of increasing absorption strength and the shift of the wavelength maximum of the second peak. However, the change in height of the second peak is not linearly correlated with sulphuric acid concentration, nor does the ratio of the peaks correspond to any simple relationship with sulphuric acid concentration.

Using a simplified model of two Gaussian curves to model the absorption peaks of $FeSO_4^+$ and $Fe(SO_4)_2^-$ (each is arbitrarily assigned a full width at half maximum of 70 nm) and assuming the concentration of $FeSO_4^+$ is proportional to the sulphuric acid concentration and $Fe(SO_4)_2^-$ has a squared relationship, the increase, decrease, and increase again in absorption seen from 35 – 63 wt% sulphuric acid can be reproduced qualitatively, as shown in Figure 4.16. The concentrations used in Figure 4.16 are not representative of the true concentrations, they are merely illustrative. The sum of the two sulphate ions is not constant, any excess is assumed to be Fe^{3+}, which is not modelled.

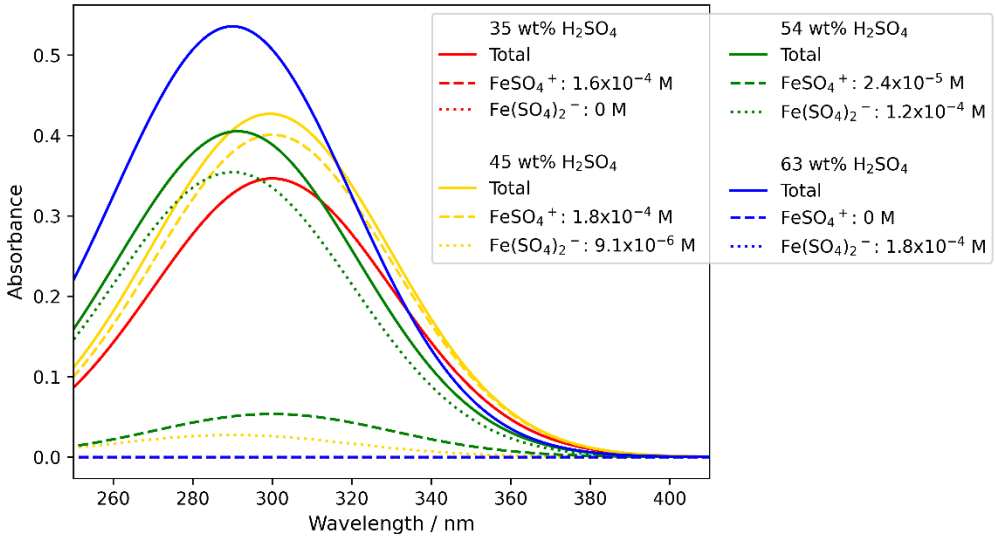

Figure 4.16. A model to show qualitatively how the observed change in shape of the spectrum in Figure 4.15 can be produced with two absorbing species. Dashed lines are the absorption due to the $FeSO_4^+$ analogue, dotted lines are due to the $Fe(SO_4)_2^-$ analogue, solid lines are the sum.

This investigation again demonstrates the importance of using sulphuric acid concentrations as close to Venusian conditions as possible to produce applicable models of the produced spectra. Note that there is no indication in any of the measured spectra of the formation of mineral species that were reported previously (Jiang et al., 2024).

4.6 Molar absorptivity measurements of iron chlorides and sulphates

To estimate the concentration of ferric sulphate and ferric chloride ions in the $FeCl_3/HCl/H_2SO_4$ samples detailed in Section 4.3, spectra of pure ferric sulphate and pure ferric chloride were measured at different concentrations to calculate the molar absorptivity of each species.

4.6.1 Sample preparation

Five concentrations of hydrochloric and sulphuric acid were mixed with ~1×10^{-4} M $FeCl_3$ and ~6×10^{-4} M $Fe_2(SO_4)_3$, respectively. The samples were measured and diluted repeatedly with acid of the same concentration, as described in Section 4.4, to produce a variety of spectra, and the molar absorptivity of the ions calculated using the Beer-Lambert law (Equation 4.1). Only sulphuric acid concentrations near the concentrations used in Section 4.3 are considered, with a small step size to match the shape of the spectrum when fitting is performed (Section 4.7) most accurately. The concentrations of the chloride samples are presented in Table 4.5, and the sulphate sample concentrations in Table 4.6.

Table 4.5. Resulting concentrations of $FeCl_3$ in different concentrations of hydrochloric acid.

Sample	HCl concentration / M	$FeCl_3$ / x 10^{-5} M (Dilution number)				
		0	1	2	3	4
A	12.20(6)	10.7(1.0)	7.0(6)	4.6(4)	3.0(3)	1.9(2)
B	10.44(5)	10.7(1.0)	7.1(6)	4.7(4)	3.1(3)	2.04(18)
C	8.96(4)	12.8(1.1)	8.5(8)	5.5(5)	3.7(3)	2.4(2)
D	6.09(3)	14.3(1.3)	9.6(9)	6.4(6)	4.2(4)	2.7(2)
E	4.15(2)	11.6(1.0)	7.8(7)	5.2(5)	3.4(3)	2.2(2)
F	1.543(8)	13.0(1.2)	9.0(8)	6.1(5)	4.1(4)	2.8(3)

Table 4.6. Resulting concentrations of $Fe_2(SO_4)_3$ in different concentrations of sulphuric acid.

Sample	H_2SO_4 concentration		Fe / x 10^{-4} M * (Dilution number)					
	/ M	/ wt%	0	1	2	3	4	5
73	12.14(6)	73.095(12)	3.4(3)	2.25(18)	1.57(13)	1.10(9)	0.76(6)	0.55(4)
75	12.54(6)	75.005(15)	3.4(3)	2.38(19)	1.67(14)	1.19(10)	0.81(7)	0.56(5)
77	13.11(7)	76.824(12)	3.4(3)	2.31(19)	1.67(14)	1.17(10)	0.80(7)	0.55(5)
79	13.51(7)	78.625(13)	3.3(3)	2.37(19)	1.71(14)	1.23(10)	0.86(7)	0.58(5)
80	14.07(7)	80.327(12)	3.4(3)	2.28(18)	1.56(13)	1.08(9)	0.75(6)	0.54(4)

4.6.2 Ferric chloride spectra

4.6.2.1 Measured spectra

All measured chloride spectra are presented in Figure 4.17. There is a clear change in shape with HCl concentration, from three peaks with a similar shape to that in Figure 4.8 at high concentrations, to spectra with a single peak at ~350 nm and high absorption towards 200 nm seen at lower HCl concentrations. The high absorption at 200 nm in all cases is due to the HCl,

which became background-noise limited at all concentrations. Absorption peaks in stock acids B and C at 265 nm are due to the presence of acetone, which was used to dry the stock acid volumetric flasks and then left to evaporate. In these two cases, small amounts have not fully evaporated. As the contamination was in the stock acids, and therefore in all of the samples, it was removed by the subtraction of the stock acid spectrum from the samples (Figure 4.18).

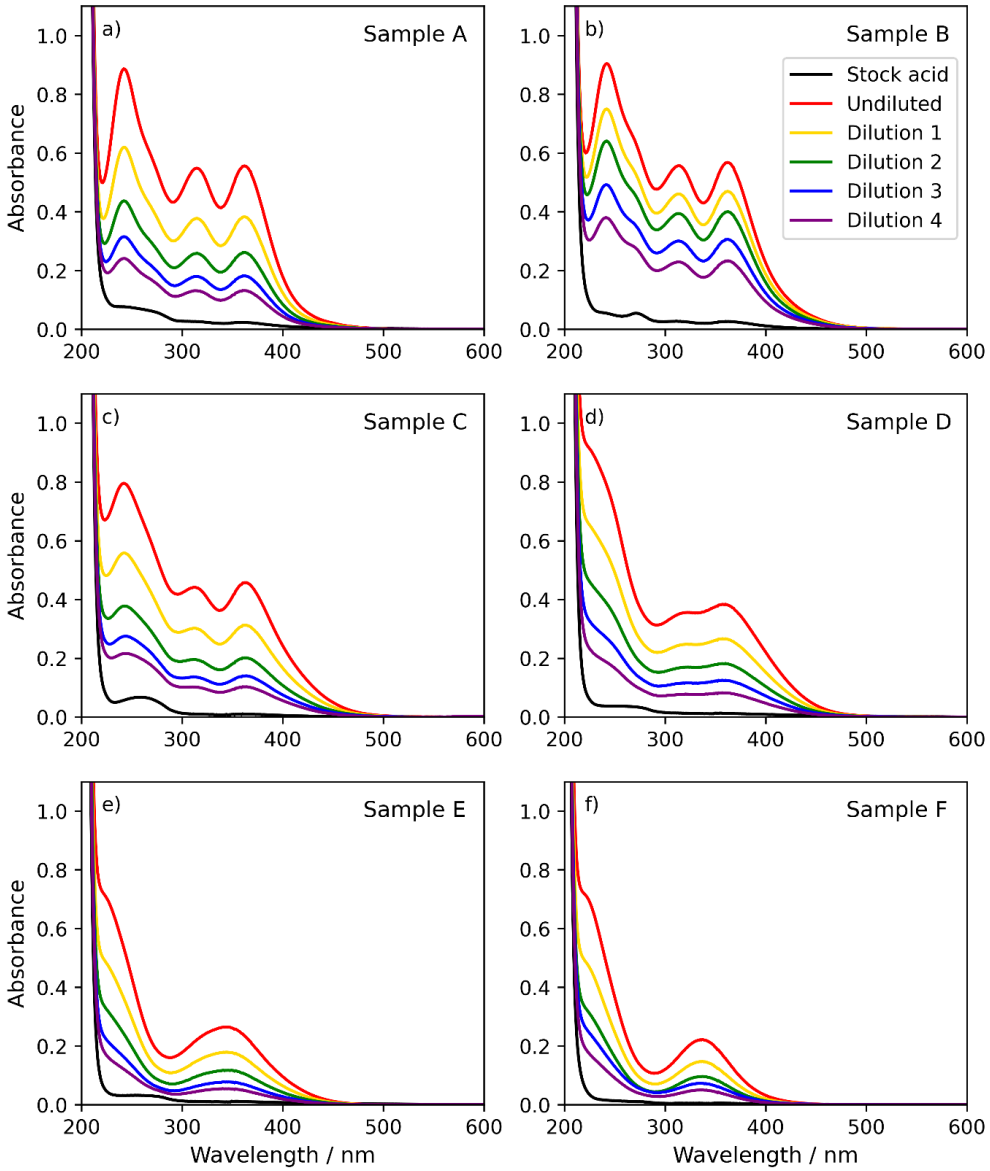

Figure 4.17. All measured spectra of $FeCl_3$ in HCl. For concentrations of samples and dilutions, the reader is referred to Table 4.5 (page 176).

4.6.2.2 Molar absorptivity

Figure 4.18 shows, for each of the six chloride samples, the absorbance spectra with the acid spectrum removed (Figure 4.18, columns 1 and 3) and linearity confirmation for each sample (columns 2 and 4).

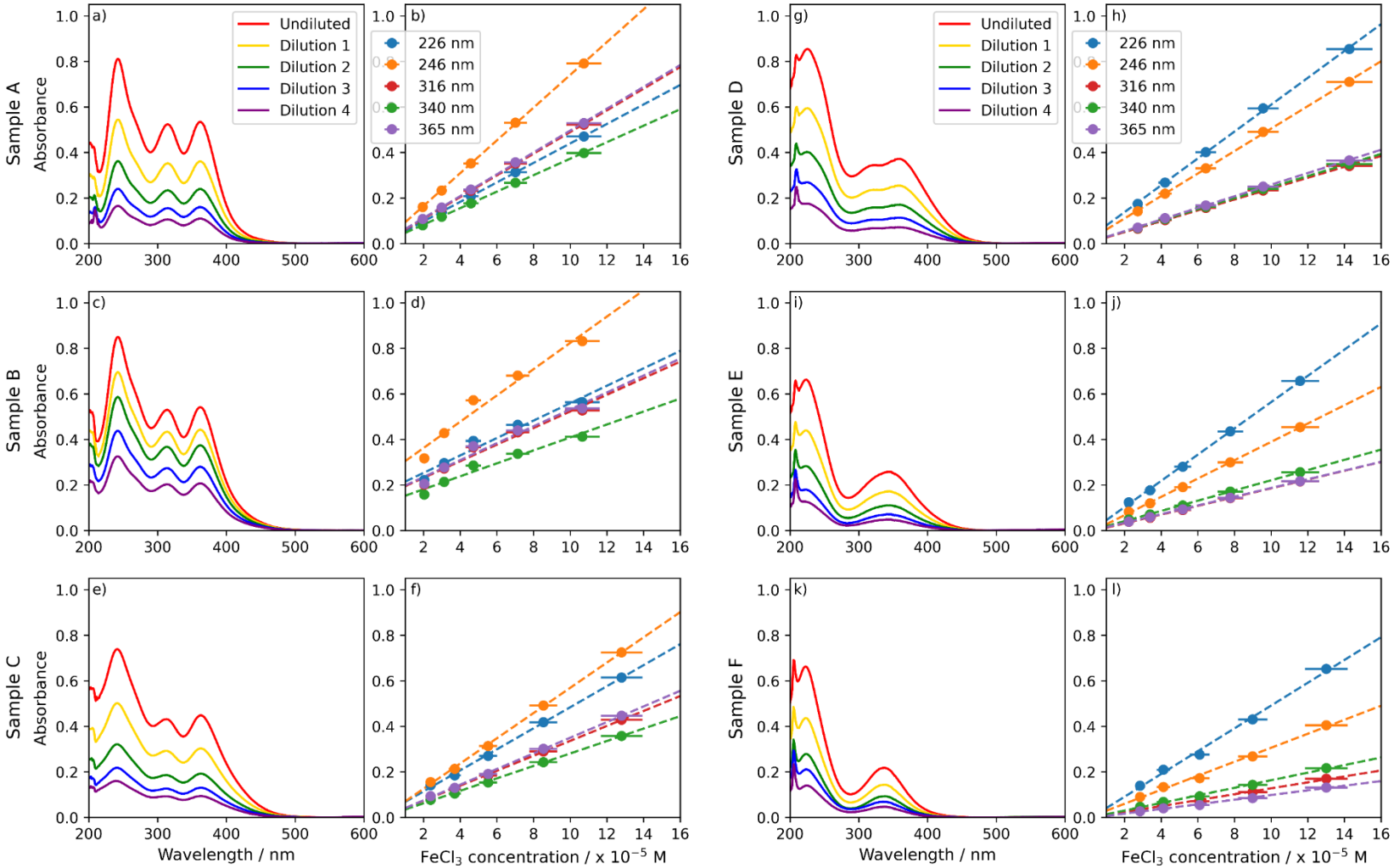

Figure 4.18. 1st and 3rd columns: measured absorbance spectra with stock acid spectrum removed. 2nd and 4th columns: concentration against absorbance for each sample, with a linear regression line fitted through the points. $FeCl_3$ concentrations of samples are as shown in Table 4.5 (page 176).

The sharp spikes occurring in the samples below 210 nm are due to incomplete removal of the HCl spectrum. This occurs because the strong absorption exceeded the detector's range, producing a large, noisy signal. It is therefore not exactly the same shape and height in the stock acid and sample spectra, and so artefacts remain when it is removed. These features are not iron concentration-dependent and so are mostly removed when the molar absorptivity is calculated.

With the exception of sample B (10.44 M HCl, see Table 4.5, page 176 for all concentrations) all samples obey linearity to within the experimental uncertainty in their concentrations. The calculated molar absorptivities are presented in Figure 4.19. Sample B is very similar to sample A, but with small differences, especially above 400 nm and below 300 nm. It is likely that the other samples contain mostly one complex ion, while sample B may contain comparable contributions from two with different absorptivities, producing agreement with sample A in some regions but not others. The findings by Liu et al. (2006) support this hypothesis: At 25 °C, the closest reported temperature to the room temperature (~20 °C) used in this study, Liu et al. estimated the ratio of complex ions $FeCl_2^+$, $FeCl_3$ (aq) and $FeCl_4^-$ at the concentration of sample B (~10.4 M) to be 10:50:39%; Their calculated absorptivity of the $FeCl_4^-$ ion is stronger than that of $FeCl_3$ except below 250 nm and above 400 nm, the regions where samples A and B differ.

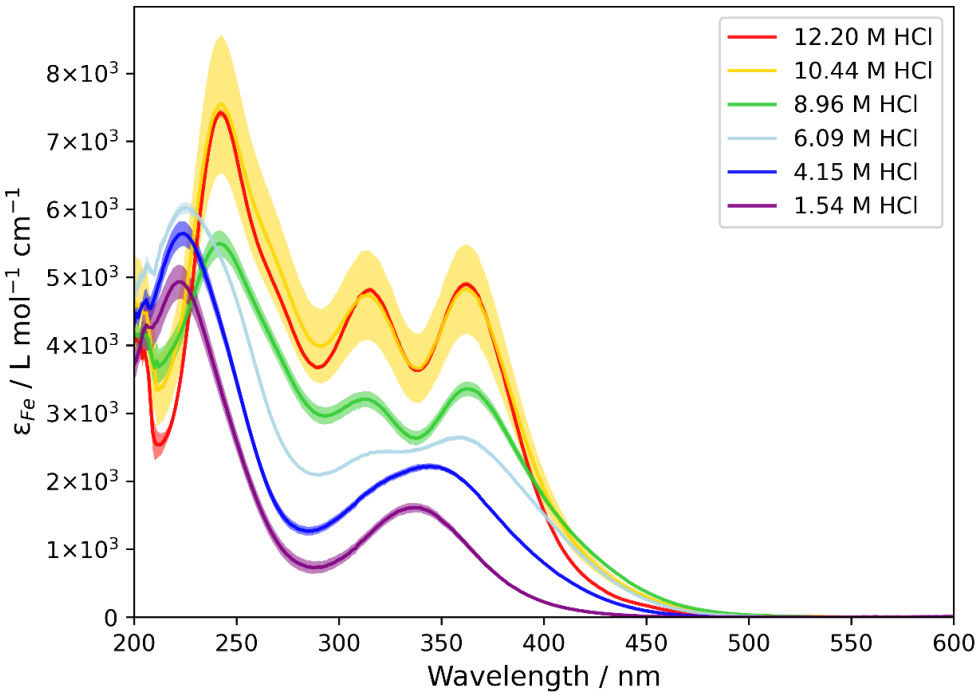

Figure 4.19. Calculated absorptivities of $FeCl_3$ in different concentrations of HCl. Shaded areas indicate the uncertainties in the absorptivity from the fitting process. The large uncertainty in the 10.44 M sample is due to non-linearity of absorbance with concentration (see Figure 4.18d).

The noisy regions near 200 nm are the effect of the artefacts arising from the HCl removal. These are not expected to bias the fitting as they will not correlate with any features of the

$FeCl_3$/HCl/H_2SO_4 spectra they will be used to fit. In addition, an HCl spectrum is included in the fitting to help counteract the higher absorption from the artefacts.

4.6.2.3 Interpretation

The shapes of the chloride absorptivity spectra vary significantly with HCl concentration. The general trends are similar to those reported by Liu et al. (2006), who measured UV-Vis spectra of $FeCl_3$ in ultra-saline solutions of HCl and LiCl. They identified five absorbing iron and iron chloride ion complexes (which they identify as Fe^{3+}, $FeCl^{2+}$, $FeCl_2^{+}$, $FeCl_3$ (aq), and $FeCl_4^{-}$) by principal component and "model-free" analysis and reported that the variety in shape with chloride concentration (HCl concentration in this case) is due to the dominance of different complexes at different chloride concentrations.

Liu et al. (2006) found the change in dominance of each complex ion with total chloride concentration and the shapes of the absorption spectra for each component to be temperature dependent, so this experiment would not be expected to agree exactly with their results. Nevertheless, there is a qualitative similarity in the change in shape, from a single peak above 300 nm at low chloride concentration ($FeCl^{2+}$), becoming broader and stronger with increasing chloride concentration ($FeCl_2^{+}$), followed by the formation of two separate peaks ($FeCl_3$), which then develop a more pronounced minimum and overall higher absorbance ($FeCl_4^{-}$) at the highest chloride concentrations.

Principal component analysis of the measured spectra was unable to separate the species as Liu et al. (2006) did, and linear combinations of the spectra reported by Liu et al. could approximate the measured spectra, but not fully reproduce them. This is assumed to be due to the temperature dependence of the exact shapes of the absorption spectra. Instead, all measured spectra were used in the fitting programme (Section 4.7). By selecting combinations of the measured spectra, a broader range of complex ion ratios can be modelled. This is not exact, as not all ratios of ions are achievable with this method, but it is expected to provide a reasonable approximation of the concentration of iron chlorides, though individual iron chloride complex ion concentrations are not quantitatively reliable.

4.6.3 $Fe_2(SO_4)_3$ + H_2SO_4

4.6.3.1 Measured spectra

All measured sulphate spectra relative to the stock acids are presented in Figure 4.20. All spectra are broadly similar, but there is a change in the height and location of the second peak with sulphuric acid concentration, as seen in Figure 4.15.

4.6.3.2 Molar absorptivity

Figure 4.20 also shows linearity tests of the sulphate samples. Figure 4.21 shows the calculated absorption spectra of the five different samples.

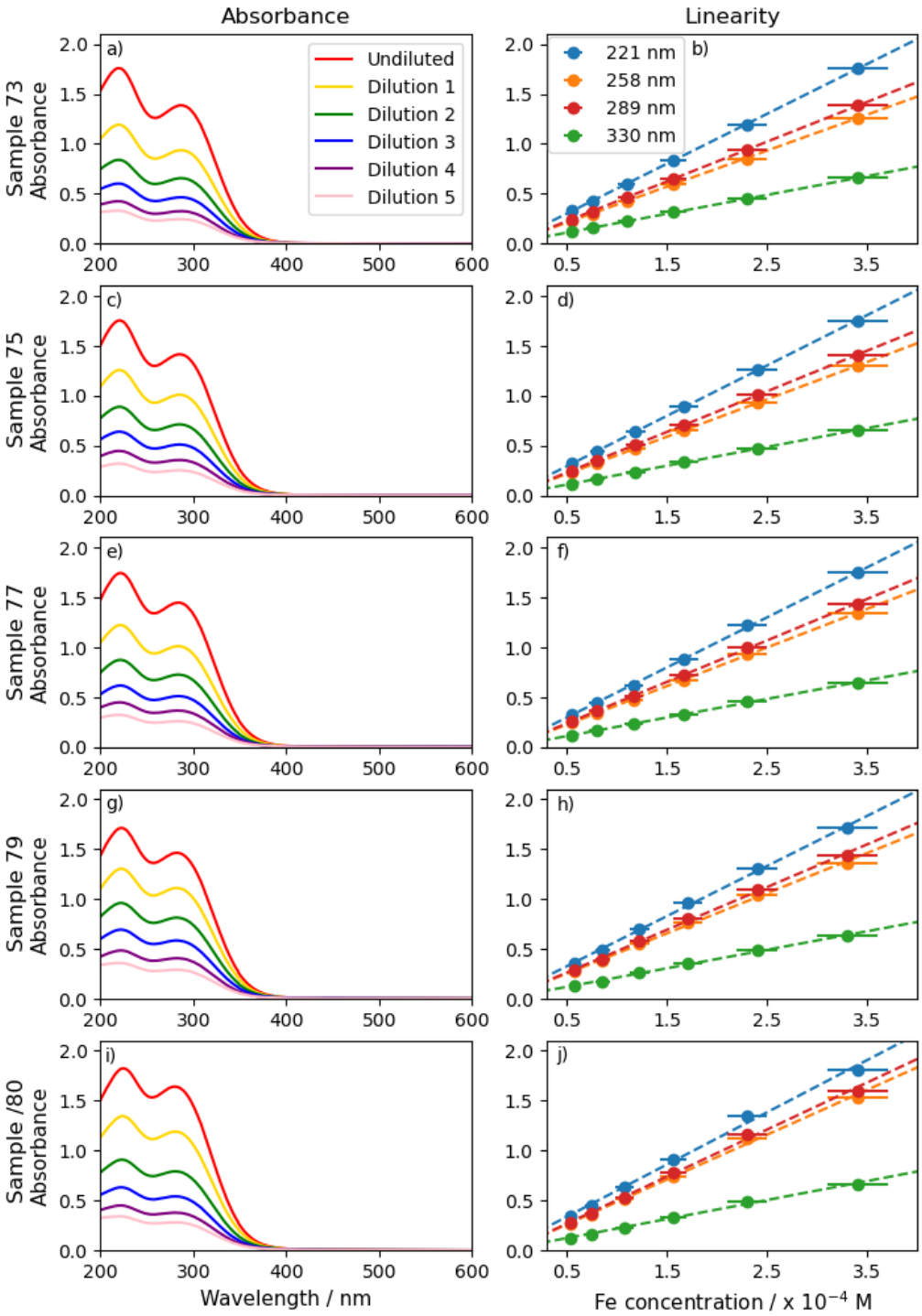

Figure 4.20. All spectra with stock H_2SO_4 spectra removed. The absorbances of samples at particular wavelengths are plotted in the right-hand column, with a linear regression fitted to the points.

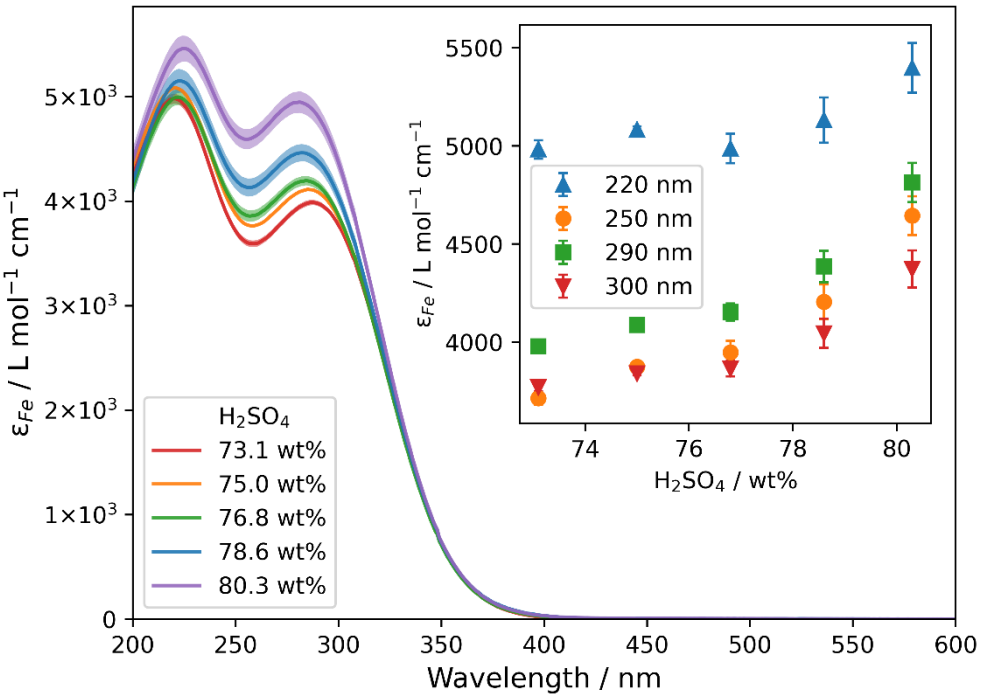

Figure 4.21. Calculated molar absorptivities of $Fe_2(SO_4)_3$ in different concentrations of H_2SO_4. Shaded regions show uncertainties. Inset: absorptivity at given wavelengths against sulphuric acid concentration.

Overall, the trend with sulphuric acid concentration is consistent with Figure 4.15. The inset in Figure 4.21 shows that there is a non-linear increase in absorptivity with sulphuric acid concentration. A change in shape is also evident as absorption at 300 nm is higher than at 250 nm at 73.1 wt%, comparable at 75.0 wt%, and lower than at 250 nm above this. This is due to displacement of the second peak to shorter wavelengths with increasing sulphuric acid concentration.

The spectra closest to the sulphuric acid concentration in the N23 and A24 sample sets of $FeCl_3$/HCl/H_2SO_4 were used for the fitting.

4.7 Concentration calculations using non-linear fitting

4.7.1 The fitting routine

The measured molar absorptivities of the six $FeCl_3$/HCl samples, the absorptivity of the $Fe_2(SO_4)_3$/H_2SO_4 sample closest in concentration to the $FeCl_3$/HCl/H_2SO_4 samples (76.8 wt% for the N23 sample set and 78.6 wt% for the A24 sample set), and average samples of H_2SO_4 and HCl (and a baseline correction if required) were fitted to the $FeCl_3$/HCl/H_2SO_4 sample absorption. The Beer-Lambert law for multiple absorbing species is written:

$$A(\lambda) = \sum_i \varepsilon_i(\lambda) c_i l \qquad (4.2)$$

where i are the absorbing species and (λ) indicates variables that are a function of wavelength. The fitting programme therefore fitted with 1 nm resolution from 200 – 600 nm to a function of the form

$$y(\lambda) = b + \sum_i c_i y_i(\lambda) \tag{4.3}$$

where c_i are the fitting parameters and $y_i(\lambda)$ are the functions being fitted: the average absorbances of HCl, and H_2SO_4, molar absorptivities of the Fe sulphate (Figure 4.21) and chloride species (Figure 4.19), and b is a wavelength-independent baseline. The fitting parameters c_i were constrained to be strictly positive with two exceptions: the baseline and HCl concentration were constrained to be strictly negative. The baseline takes a negative value to allow for zero values where necessary (as all spectra $y_i(\lambda)$ and fitting parameters c_i are positive, except HCl). The HCl is strictly negative to offset the HCl contribution that could not be fully removed in the chloride reference spectra (Figure 4.19).

When the functions are the absorptivities of each species (multiplied by a path length of 1 cm), the fitting parameters are their concentrations in the mixture. Uncertainties were calculated using python's non-linear least squares minimization ("lmfit") module. The change in concentration over time was used to estimate the rate of the reaction, which is affected by the concentration of HCl in the solutions.

As there are 306 spectra in total measured for the N23 batch and 234 for A24, only a small number of representative fitted spectra are presented in Figure 4.22.

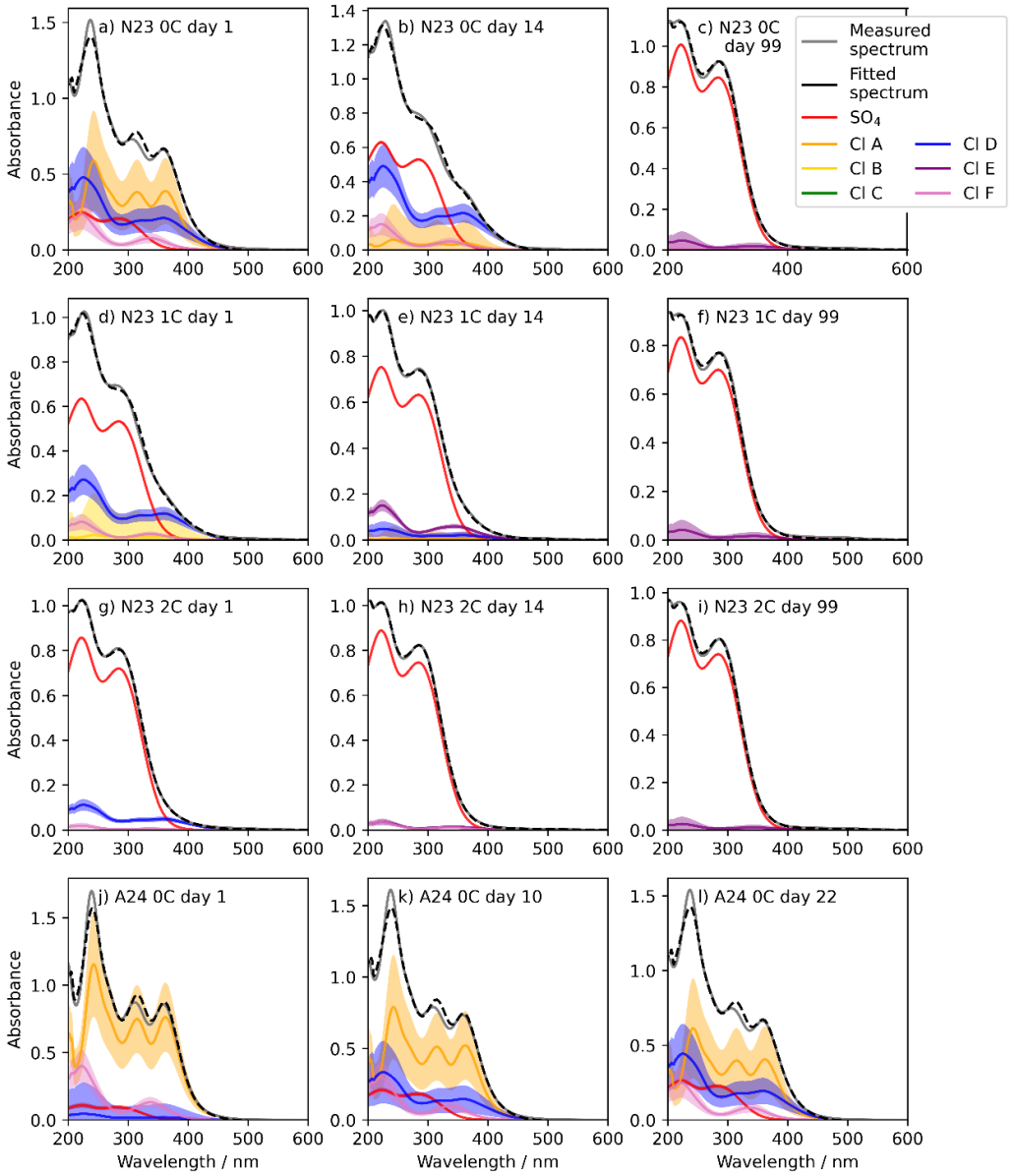

Figure 4.22. Example fitting programme results. The measured spectrum (grey line) is fitted by least squared minimisation to produce a total spectrum (black, dashed line). Components fitted to the spectrum with concentrations of $>10^{-8}$ M are plotted (different colours) with uncertainties from the fitting programme (shaded regions). The reader is referred to Table 4.5 (page 176) for interpretation of the Cl spectrum names. The SO_4 spectrum is the $Fe_2(SO_4)_3$ spectrum at the closest available H_2SO_4 concentration (Samples 77 and 79 for N23 and A24 samples respectively, see Table 4.6, page 176).

The agreement of the fitted spectrum with the measured spectrum is generally very satisfactory, although somewhat less so when the spectrum is dominated by chlorides (see, for example, the ~240 nm peak in Figures 4.22a, j, k, and l). This is presumably due to both the combination of multiple absorbing species in the chloride reference spectra and the simplified model of the reaction used: it is highly unlikely that the iron directly forms pure sulphate complex ions from pure chloride complex ions. It will almost certainly form some intermediate combined iron-chloride-sulphate complex. The absorption spectrum of this is expected to be similar to both

the chloride and sulphate spectra but will not agree exactly with the spectra used to fit it. This is unavoidable with the methods available. The overall shape and trends of the spectra over time can be reproduced with this method, which confirms that the iron is forming sulphates over time.

4.7.2 Fitted concentrations

The uncertainties shown in Figure 4.22 are only those reported by the fitting programme. The programme does not have the capability to include uncertainties of the reference spectra in the fit, so the uncertainties shown are an underestimate. To calculate the total uncertainties, the uncertainty of the fitted concentration and the average uncertainty in absorptivity for each reference spectrum from 200 – 500 nm (avoiding the region from 500 – 600 nm where the signal is smallest and the percentage error therefore artificially large) were propagated to produce an overall uncertainty in the fitted concentration.

The total concentration of the six fitted chloride spectra were combined to estimate the total iron present as chlorides in the samples. Figure 4.23 shows the fitted sulphate and total chloride concentrations and therefore the total iron calculated by the fitting programme compared to the initial $FeCl_3$ concentration for each sample.

In general, samples show the expected decrease in iron chlorides over time and increase in sulphates, with the total iron fairly constant and almost always within error of the initial iron concentration in the samples (though the uncertainty in the concentrations is large due to the limitations of the fitting method).

The A samples are expected to contain no iron and therefore act as a test of the fitting programme. However, spectrum N23 0A and 1A have non-zero iron concentrations, even with the large fitting errors. They approximately follow the general trends of the other samples, with higher chlorides at the start of the experiment and higher sulphates at the end, so it seems likely that these samples were contaminated with ferric chloride during their production.

All N23 D samples significantly underestimate the total Fe concentration compared to the initial concentrations. As it occurs in all D samples, this suggests a systematic error in the initial concentration. The D samples were intended to be more concentrated than C samples and less than E, but were generally calculated to be comparable to or more concentrated than the E samples. The fitted concentrations are broadly consistent with the C samples. As the issue is thought to be with the sample concentration, not the fitted concentration, these spectra will still be used in calculations of the rate of the reaction (Section 4.7.3).

All N23 samples show an odd increase in fitted chloride concentrations between days 73 and 81. As it affects all samples, this is assumed to be an issue with the baseline of the instrument on one or both of those days. When rates are calculated from the concentration (Section 4.7.3), only the earlier days will be used so as to reduce the effect of noise at low fitted chloride concentrations. This means the increase from day 73 to 81 will not affect the calculated rate.

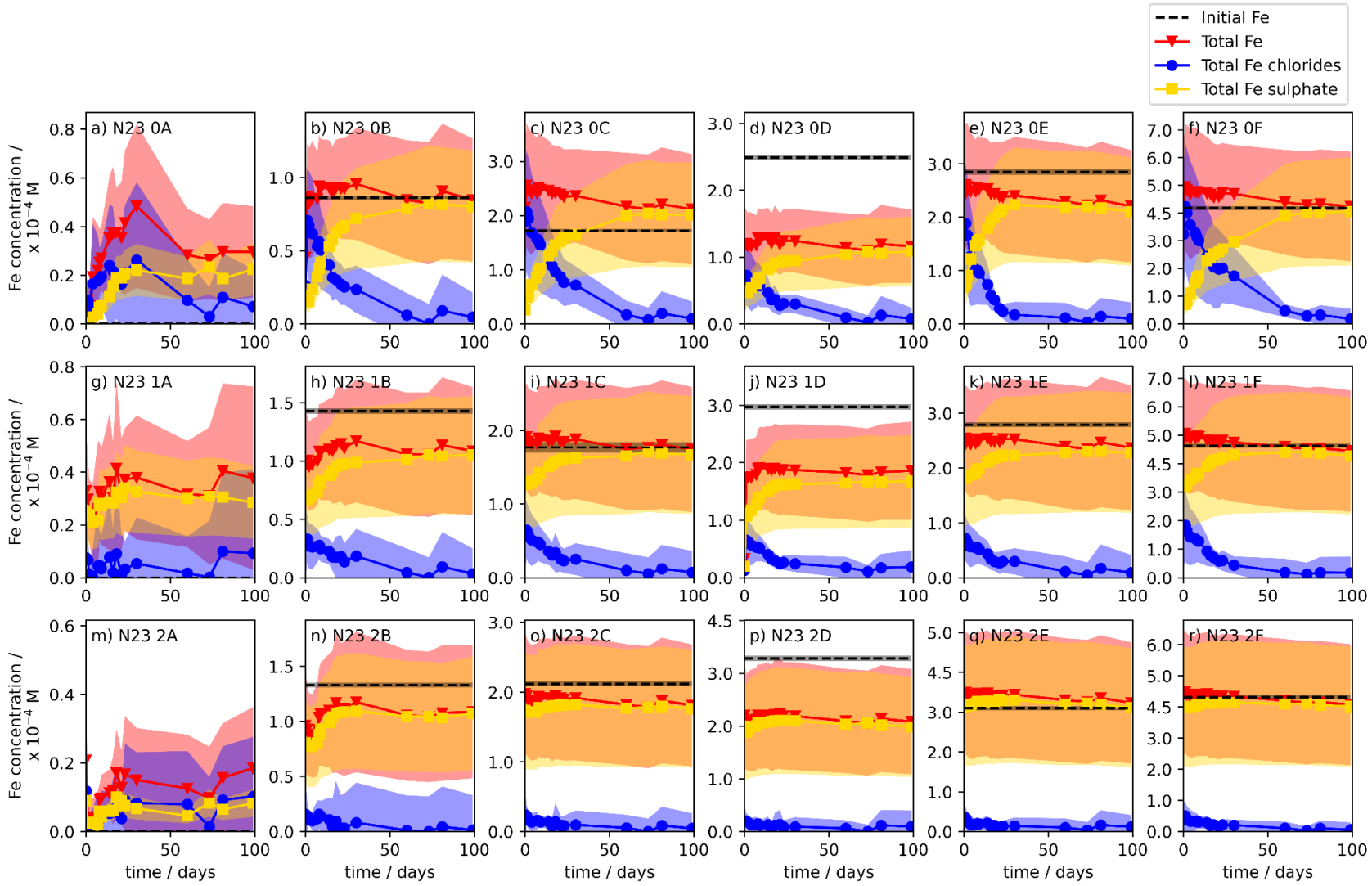
Initial Fe
Total Fe
Total Fe chlorides
Total Fe sulphate
a) N23 0A
b) N23 0B
c) N23 0C
d) N23 0D
e) N23 0E
f) N23 0F
g) N23 1A
h) N23 1B
i) N23 1C
j) N23 1D
k) N23 1E
l) N23 1F
m) N23 2A
n) N23 2B
o) N23 2C
p) N23 2D
q) N23 2E
r) N23 2F
Fe concentration / x 10⁻⁴ M
time / days

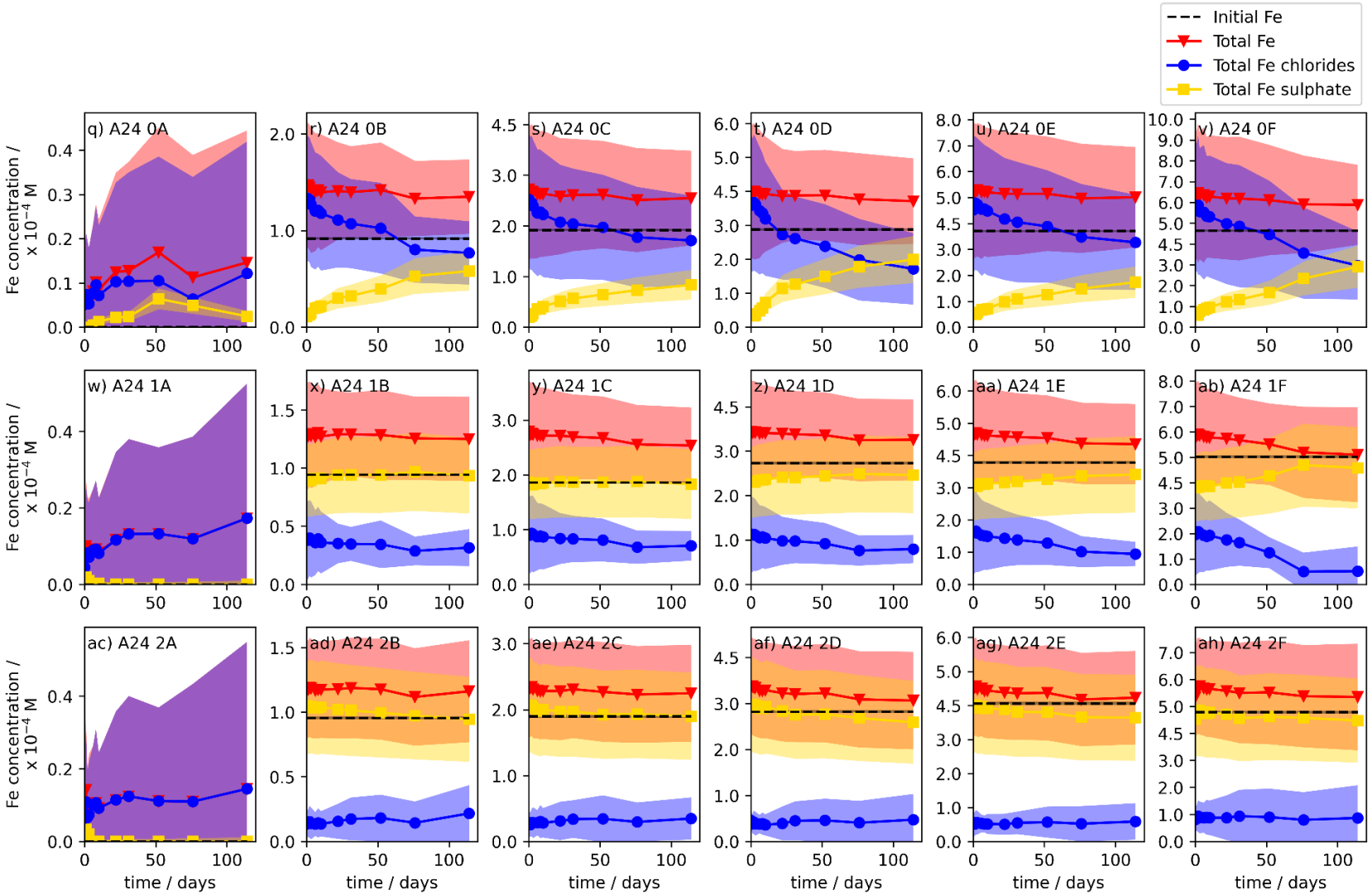

Figure 4.23. Fitted concentration of iron chlorides and sulphate over time for all samples. Shaded areas show uncertainties.

4.7.3 Rate of reaction

For Reaction R4.1, assuming that the rate-determining step involves both $FeCl_3$ and H_2SO_4, the rate of loss of reactants is given by

$$rate = k[FeCl_3]^x[H_2SO_4]^y \tag{4.4}$$

where k is the rate constant and [$FeCl_3$] and [H_2SO_4] indicate concentrations. As H_2SO_4 is in large excess compared to the $FeCl_3$, the concentration of H_2SO_4 is approximately constant across the experiment and the reaction is therefore pseudo-first order in $FeCl_3$. The rate is therefore only dependent on the $FeCl_3$ concentration and can be rewritten as

$$observed\ rate\ of\ loss\ of\ FeCl_3 = -\frac{d[FeCl_3]}{dt} = k_{obs}[FeCl_3]^x \tag{4.5}$$

where x is the order of the reaction for the rate determining step with respect to $FeCl_3$. Rearranging and integrating the equation over time *t*,

$$\int_{[FeCl_3]_0}^{[FeCl_3]} \frac{1}{[FeCl_3]^x} d[FeCl_3] = \int_0^t -k_{obs}\, dt = -k_{obs}t \tag{4.6}$$

where $[FeCl_3]_0$ is the initial concentration of $FeCl_3$. The value of this integral depends on the order of the reaction. If the reaction is zero-order, the left-hand side has no dependence on [$FeCl_3$], so

$$[FeCl_3] = [FeCl_3]_0 - k_{obs}t \tag{4.7}$$

A plot of $FeCl_3$ concentration against time would therefore be a straight line, which is clearly not the case by inspection of Figure 4.23. If the reaction is either first- or second-order, Equation 4.6 becomes

$$\ln[FeCl_3] = \ln[FeCl_3]_0 - k_{obs}t \tag{4.8}$$

or

$$\frac{1}{[FeCl_3]} = k_{obs}t - \frac{1}{[FeCl_3]_0} \tag{4.9}$$

respectively. Figure 4.24 shows ln[$FeCl_3$] (primary axis, blue) and [$FeCl_3$]$^{-1}$ (secondary axis, green) against time. The first-order case produces a better straight line fit. This can be seen most clearly in HCl concentration batches 0 and 1, particularly 0E and 1C of the N23 sample set, where the second-order case is clearly non-linear. The small change in $FeCl_3$ concentration in batches 1 and 2 mean that the variation in the concentrations calculated by the fitting programme is large compared to the overall change, producing a large amount of scatter in the data. This is exacerbated by the minimal change in the concentrations in the A24 batch.

The average R^2 value of the fit for all data is 0.776 for the first order fit and 0.753 for the second order fit. These are skewed by the low fitting quality for HCl batch 2 in the A24 set. When batch

2 is neglected, the average R^2 values are 0.947 and 0.923 respectively, and when only N23 batches 0 and 1 are considered, the average R^2 values are 0.965 and 0.929. In each case, first-order kinetics produce a better fit.

In batch 2 of the A24 sample set, the sample is dominated by noise. From Figure 4.23ac) to 4.23ah), it is clear that there is no measurable change in concentration with time in these samples. The fitted rates for these samples are therefore neglected.

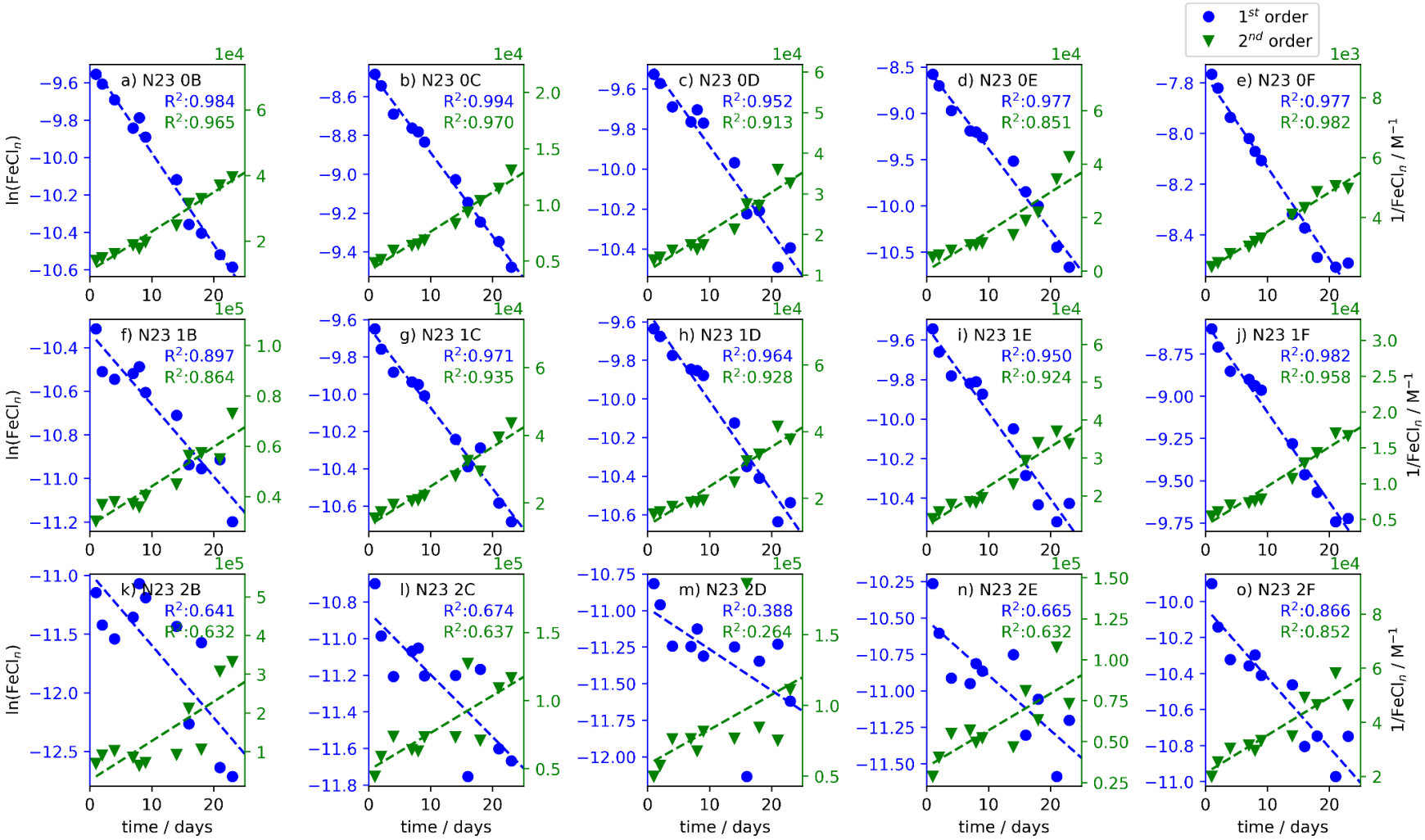
1st order
2nd order
a) N23 0B
R²:0.984
R²:0.965
b) N23 0C
R²:0.994
R²:0.970
c) N23 0D
R²:0.952
R²:0.913
d) N23 0E
R²:0.977
R²:0.851
e) N23 0F
R²:0.977
R²:0.982
f) N23 1B
R²:0.897
R²:0.864
g) N23 1C
R²:0.971
R²:0.935
h) N23 1D
R²:0.964
R²:0.928
i) N23 1E
R²:0.950
R²:0.924
j) N23 1F
R²:0.982
R²:0.958
k) N23 2B
R²:0.641
R²:0.632
l) N23 2C
R²:0.674
R²:0.637
m) N23 2D
R²:0.388
R²:0.264
n) N23 2E
R²:0.665
R²:0.632
o) N23 2F
R²:0.866
R²:0.852
ln(FeCl$_n$)
1/FeCl$_n$ / M^{-1}
time / days

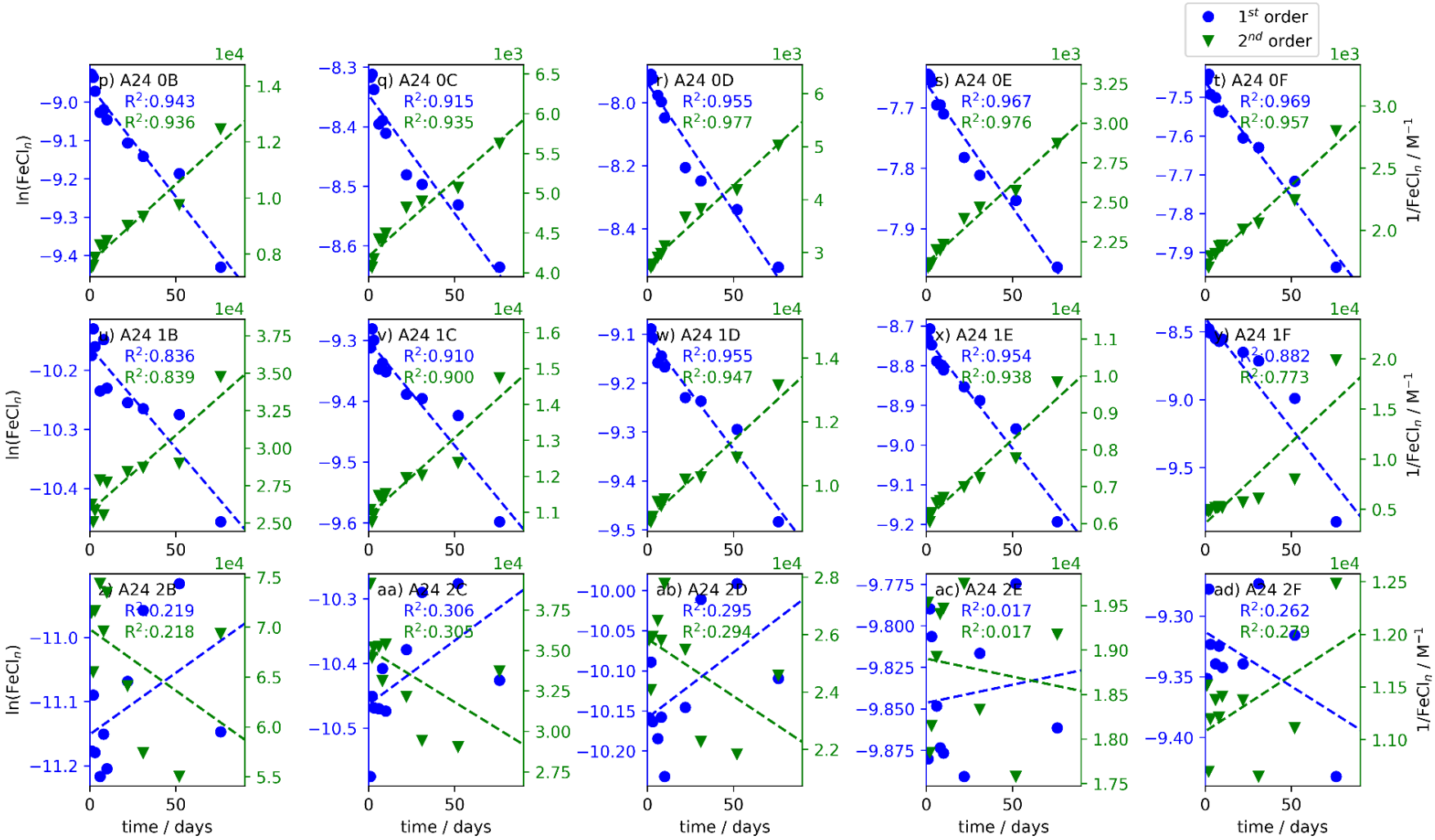

Figure 4.24. Calculated rate of reaction of $FeCl_3$ for first-order (blue) and second-order (green) kinetics for each sample. The A samples are not shown due to their low Fe concentration. The first-order plots show better agreement, so the reaction is concluded to be first-order in $FeCl_3$.

There is no significant change in the rate of the reaction with the concentration of HCl. Within each set of samples, N23 and A24, there is no significant variation with batch compared to the standard deviation of the rates at a given batch ($(6.0 \pm 2.1) \times 10^{-7}$, $(5.1 \pm 0.8) \times 10^{-7}$, and $(4.6 \pm 1.3) \times 10^{-7}$ s^{-1} for sample set N23 batches 0 – 2, respectively, and $(6.4 \pm 1.7) \times 10^{-8}$ and $(7.7 \pm 5.6) \times 10^{-8}$ s^{-1} for A24 batches 0 and 1). However, there is a significant difference between the rates of the two sets, which change by an order of magnitude. This is unlikely to be due to the difference in concentration in the sulphuric acid (Table 4.1) – a difference of 0.5 M in the H_2SO_4 concentration would not account for an order of magnitude change in the rate and, in particular, the higher H_2SO_4 concentration (A24) would be expected to increase the rate, not decrease it. Variation in temperature would also be expected to affect the rate, but not to the extent observed.

It seems more likely that the change in rate is due to the preparation of the samples. For example, the amount of time the $FeCl_3$ was in the HCl stock solutions varied between the two experiments. For N23, the samples were made up from scratch and measurements started within an hour, whereas for A24, the H_2SO_4, HCl, and $FeCl_3$/HCl stock solutions were made up ~18 hours before the final samples were made up and measurements started. The difference is unlikely to be due to HCl escaping from the solution at different rates between the two sample sets, as this would be expected to produce a distinct difference in rate at high HCl concentrations, and less difference at lower concentrations when the HCl evaporation is low, which was not the case. It is therefore possible that in the A24 set, where the $FeCl_3$/HCl stock solutions were left for several hours before being added to the sulphuric acid, the $FeCl_3$ formed $FeCl_4^-$ in the solutions more completely than in the N23 batch. The binding of chloride ions to the $FeCl_3$ may have prevented as much HCl from escaping from the solutions in the A24 set as the N23 set.

The possibility that the rate of the reaction depends on the initial complex ions formed should also be considered, as $FeCl_4^-$ may react more slowly than $FeCl_3$. However, this does not seem sufficient to explain the order of magnitude difference in observed rates. In Figure 4.22, Samples 0C from N23 and A24 on days 1 and 10 respectively (Figures 4.22a and 4.22k) are reproduced by the fitting programme by similar sets of chloride spectra – mostly chloride spectrum A, with smaller contributions from B, C, and E. While exact concentrations of the different species cannot be reliable ascertained, both samples are qualitatively expected to be mostly $FeCl_4^-$ with some $FeCl_3$ and other complex ions. However, the change in composition of N23 0C day 1 to day 14 (Figure 4.22b, 13 days) and A24 0C day 10 to day 22 (Figure 4.22l, 12 days) are very different. For the N23 sample, the sulphate becomes a significant species and contributes comparably to the chlorides, while the A24 sample is still dominated by the chloride A spectrum, with only a minor sulphate contribution. If the difference in rate were due to the chloride complex ion ratios, there would not be this discrepancy.

As it is likely that the reaction depends on HCl concentration in the solution, which cannot be measured or controlled with the present experimental setup, further repeats are expected to show

further variation, but would not help identify the cause. In future, experiments with control of the headspace above the samples would allow for measurement of the HCl coming out of the solution, and therefore estimates of the Cl^- concentration in the solution.

4.8 Temperature-dependent rates

4.8.1 Methods

To measure the effect of temperature on the rate of reaction, samples consisting of approximately the same concentration of sulphuric acid, HCl, and $FeCl_3$ were stored at different temperatures and the absorption spectrum was measured over 10 days (days 0 – 9). A stock $FeCl_3$/HCl solution was made up at least a day in advance of sample preparation. The concentrations of four different batches of samples are presented in Table 4.7.

Table 4.7. Concentration of solutions for temperature-dependent experiments.

Batch	H_2SO_4 concentration		HCl concentration / M	$FeCl_3$ concentration / M
	/ M	/ wt%		
1	13.17(2)	77.278(8)	$1.374(6) \times 10^{-2}$	$3.5(5) \times 10^{-4}$
2	13.13(2)	77.47(3)	$1.341(6) \times 10^{-2}$	$3.4(5) \times 10^{-4}$
3	13.18(2)	77.44(5)	$1.405(6) \times 10^{-2}$	$3.2(4) \times 10^{-4}$
4	13.09(2)	76.935(11)	$1.310(4) \times 10^{-2}$	$3.0(4) \times 10^{-4}$

Each batch solution was made up and pipetted into separate cuvettes. An extra cuvette was filled, and its spectrum measured immediately and then the sample discarded ("day 0") to avoid measuring one sample more than others in case the UV-Vis light incident upon the samples during measurements affected the sample in any way. Due to the high viscosity of sulphuric acid at low temperatures, it was not feasible to keep a large stock solution and take small samples for spectroscopy when needed. To treat all samples the same, all samples were pipetted into cuvettes on day 0 and then stored in different locations at different temperatures. In most cases, the samples were simply stored in chemical cupboards and the temperature monitored over the 10 days. Air conditioning maintained a broadly consistent temperature for the samples. For temperatures of 0 °C and lower, a Labplant RP100CD immersion cooling probe and a bath of propylene glycol were used (Figure 4.25). To avoid risk of damaging the cuvettes by rapid cooling, the samples were placed in the bath at room temperature, and the temperature lowered to the set point. By necessity this means the samples did not spend the full time they were stored at their target temperatures. However, set point temperatures were generally achieved in under an hour, so the effect of the temperature ramp should not be the most significant source of error.

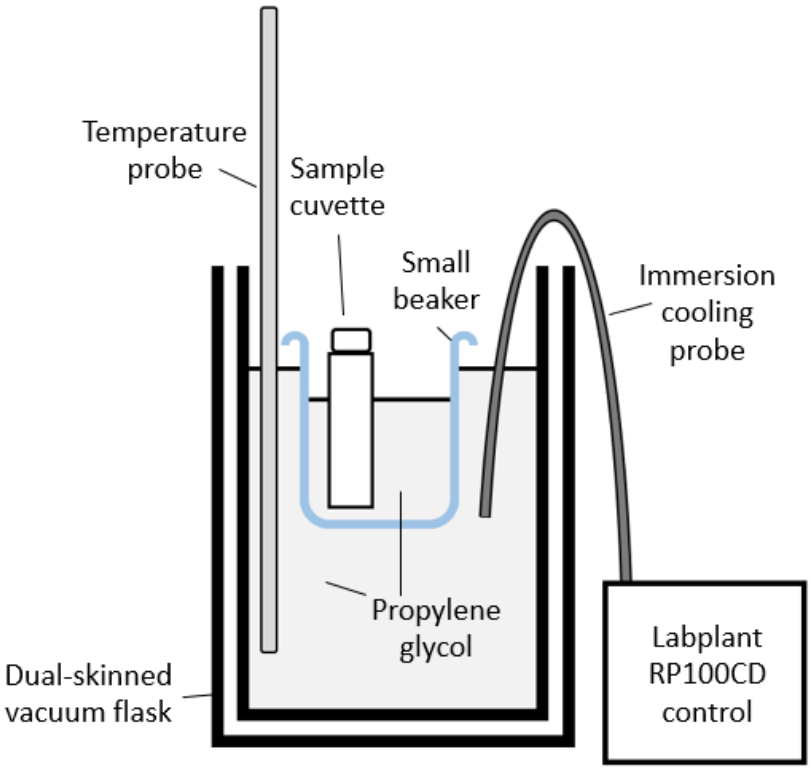

Figure 4.25. Diagram of low temperature apparatus. The Labplant control box is connected to the immersion probe and temperature probe (this connection is not shown for clarity). Cooling is turned on and off automatically to maintain the set point temperature. The Labplant RP100CD cools a bath of propylene glycol in a dual-skinned vacuum flask. A small beaker is suspended from the rim of the flask using a clamp (not shown for clarity). The beaker and flask both contain propylene glycol. The sample cuvette(s) are placed within the small beaker. The beaker can be removed easily to access the samples, then lowered back into the flask.

The temperature of the room/bath was recorded when samples were taken and used to calculate the uncertainty in the temperature. The sides of the cuvettes were rinsed with acetone to dry them, which was then allowed to evaporate before spectra were measured. The samples from the propylene glycol were rinsed thoroughly with deionised water and cleaned and dried with lens tissues and acetone. A spectrum was measured of pure propylene glycol, which showed very little absorbance, so there is no risk of contamination of the samples with propylene glycol absorbance from the outside of the cuvettes. However, the low temperature of the cuvettes meant that condensation would periodically form on the cuvettes in the spectrometer. Any spectra where this appeared to be the case during sampling were immediately stopped, the cuvettes dried again with lens tissue, and the sample rerun. However, this does not guarantee that no small amounts of condensation went unnoticed. In addition, the effect of the condensation was only apparent at large wavelengths where absorption from the spectrum was negligible. Any condensation that formed later in data acquisition (i.e., only began to appear when the spectrometer was measuring at above ~450 nm) will not have been detectable.

In some cases, stoppered (Agilent) and unstoppered (Thermo Fisher Scientific) cuvettes were used in the same locations to test whether the rapid rate of reaction was due to HCl escaping from the solution. It was hypothesised that the solutions would not remain saturated with HCl if it could escape from the liquid into the headspace in the cuvette and then out of the unstoppered cuvettes. Figure 4.26 shows an unsealed sample at room temperature after one day. Large numbers of bubbles, assumed to be HCl, have nucleated in the solution. The sample was inverted before measurements were taken, and the bubbles disappeared. No significant difference in rate was found between the stoppered and unstoppered cuvettes. However, with the temperature changes the cuvettes were subjected to, there is no certainty that the stoppered cuvettes remained sealed at all times.

Figure 4.26. Room temperature sample in an unstoppeded cuvette after 1 day. Large numbers of bubbles, presumably HCl, have nucleated in the solution.

At -40 °C, the propylene glycol became viscous and sticky, and the cooling and temperature probes regularly became encased in ice. It is likely that the temperature readings for these samples are unreliable as the temperature probe will have been biased by the ice coating it and would therefore presumably read higher temperatures than were accurate, leading to the cooling running for longer than it should have done, decreasing the temperature further. The ice would regularly encase the samples in the bath, so they may not have been at the temperature of the bath either. Both the stoppered and unstoppered samples became unsealed when they were encased in ice, and it is likely that some of the samples were contaminated with water, propylene glycol, or both. Samples at –40 °C therefore have large temperature errors.

The absorbance of each sample was measured over time and the cuvette returned to its storage location immediately after recording. The spectra were then analysed using the fitting programme (Section 4.7) to calculate the iron chloride concentration. The overall change in the spectra was

low, so fractional uncertainty in the change is high. In addition, Liu et al. (2006) found temperature dependence of the shape of their spectra at higher temperatures, so it is likely that the spectra will differ somewhat from the reference spectra at room temperature. This will introduce additional uncertainty in the concentrations of chlorides from the fitting programme.

4.8.2 Temperature dependent rates

The pseudo first-order rate constant was calculated for each sample using Equation 4.8. The dependence of the rate of the reaction on temperature is expected to follow the Arrhenius equation:

$$k_{obs} = A \exp\left(-\frac{E_a}{RT}\right) \tag{4.10}$$

where E_a is the activation energy, R the ideal gas constant, and A is an exponential pre-factor for a given reaction. Figure 4.27 shows the dependence of the rate on temperature. A linear fit to Equation 4.10 was performed for all batches of samples together.

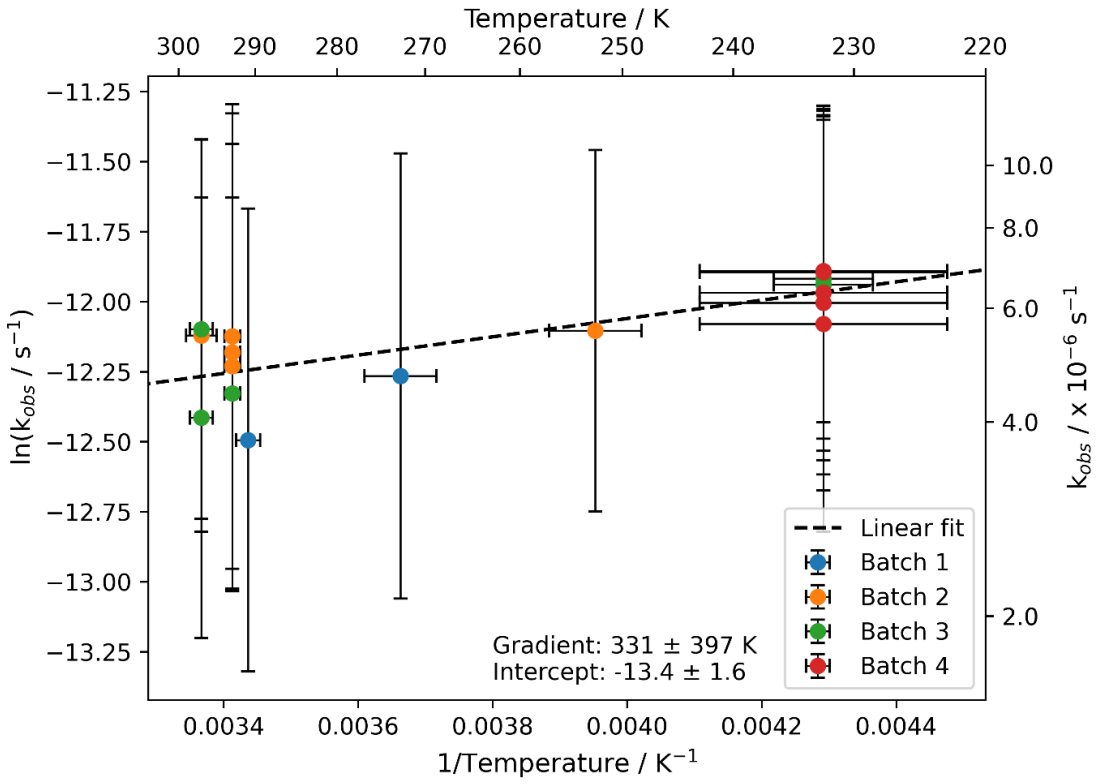

Figure 4.27. Arrhenius plot of the rate constant for the conversion of $FeCl_3$ to $Fe_2(SO_4)_3$. The reader is referred to Table 4.7 (page 193) for concentrations. For clarity, while $1/T$ and $\ln(k_{obs})$ are fitted, k_{obs} and T are shown on secondary axes).

The line of best fit in Figure 4.27 returns a pre-factor $A = 2 \pm 2 \times 10^{-6}$ s^{-1} and activation energy $E_a = -40 \pm 48$ J mol^{-1}. There is negligible temperature dependence measurable with this technique.

4.9 Conclusions

When ferric chloride is added to sulphuric acid, a yellow solution with dark and light particles, thought to be anhydrous and hydrated ferric chloride, respectively, was formed at room temperature. These particles dissolved and a pale precipitate of unknown composition formed over the next 24 hours. For application to Venus, ideally both the liquid phase and the particles would be considered, but the available techniques in this study were not sensitive to particles. Future work should consider the particles and make attempts to conclusively identify both the particles and the pale precipitate.

The iron concentration in the solutions was decreased to measure the absorbance due to ferric chloride in sulphuric acid. The shape of the resulting spectrum is very different compared to the spectrum of $FeCl_3$ used in the literature (Pérez-Hoyos et al., 2018). A fitting programme was developed to estimate the concentration of iron sulphate and chloride species in the solutions. This is an oversimplification: numerous different iron chloride complex ions form depending on the chloride concentration in the solution, and it seems unlikely that no intermediate iron-sulphate-chloride complexes would form during the conversion of $FeCl_3$ to $Fe_2(SO_4)_3$. This chemical system is clearly highly complex and further study is necessary. Nevertheless, despite the required simplifications to the model of the system, the fitting programme reproduced the initial iron concentrations well. The measured spectra and concentrations will be used to model $FeCl_3$ behaviour in the Venusian clouds and atmosphere in Chapter 5.

The rate of the reaction of the iron chlorides to form ferric sulphate is highly variable. No indication of further reaction of the sulphates was found. The rate has a very small dependence on temperature, but the uncertainty in the rate within a single batch of samples at a given temperature, and between batches of samples at similar temperatures is large and the measured rate differed significantly between samples which appeared to have the same approximate composition. The rate-limiting process in the reaction is unclear at present, but the concentration of free chloride ions in the solution may have a significant influence on the rate that cannot currently be quantified.

This chapter presents initial exploration of a highly complex system. The measured spectra and concentrations are a clear improvement on the existing literature spectra in terms of relevance to the Venusian clouds, but further exploration is necessary to produce reliable estimates of the lifetime of ferric chloride within the cloud droplets at Venusian temperatures. It is likely that the concentration and partitioning of iron between iron chloride and sulphate species will vary with time and location in the Venusian clouds, so an understanding of the factors affecting the rate must be understood to capture the variability in the reaction and therefore in predicted observations.

5. Photochemical and radiative transfer modelling of $FeCl_3$

5.1 Introduction

Zasova et al. (1981) proposed 1 wt% $FeCl_3$ in the mode 2 cloud droplets as the cause of the unknown UV absorption, and suggested meteoric iron as the source of the $FeCl_3$. Krasnopolsky (2017) proposed a surface source of $FeCl_3$, arguing that the surface colour observed by Venera landers indicated that the surface could contain ferric rocks. These, he argued, could react with volcanic HCl to produce ferric chloride. The Venusian surface is above the boiling point of $FeCl_3$, so $FeCl_3$ gas would therefore rapidly evaporate and be transported through the atmosphere to the upper clouds, where it would condense into particles to produce the observed absorption. However, vertical transport in the lower atmosphere is very slow (Cohen et al., 2024) and it therefore seems unlikely that the $FeCl_3$ would survive unreacted through the lower atmosphere and throughout the cloud deck to reach the upper clouds, where it could contribute to the observable absorption.

Between them, these two sources cover all possible sources of iron: entering from the surface or from the TOA. In this chapter, the feasibility of $FeCl_3$ production from the reaction of meteoric iron from ablated cosmic dust with chlorine from volcanic HCl is examined using the PCM and a 1D model of sedimentation and agglomeration (Frankland et al., 2017). The required concentrations of $FeCl_3$ in the different cloud modes are predicted using the measured absorption spectra reported in Chapter 4 in SOCRATES, and the required concentrations compared to the PCM predicted concentrations.

5.2 Chemical modelling

Photochemical modelling of meteoric iron was carried out using the Venus PCM up to ~250 km (including the ionosphere, Section 2.1.3.2). An initial source of iron (Fe and Fe^+) from ablated cosmic dust is injected in the model and the chemistry scheme run for 3.0 Venus days.

5.2.1 Meteoric Injection

An overview of meteoric injection and its implementation in the PCM is provided in Section 3.4. Meteoric iron is injected following the profile reported by Carrillo-Sánchez et al. (2020) as a mixture of neutral iron atoms (72%) and Fe^+ ions (28%).

As discussed in Section 3.4, the flux of meteoric material and Fe in particular is not well constrained on Venus because the metallic species have not yet been observed; however, the flux into the terrestrial atmosphere is now reasonably well constrained (Carrillo-Sánchez et al., 2020) and the same Zodiacal Dust Cloud model was employed for Venus. Development of sodium and magnesium chemistry for comparison with future observations is underway, and will be able to provide indirect validation of the iron injection rate when observations are available.

5.2.2 PCM Chemistry

A system of iron chemistry was developed by J.M.C Plane and implemented in the PCM. Descriptions of the predictions of the rate coefficients are available in Appendix A. Table 5.1 and Figure 5.1 detail the reactions and rate coefficients of the iron chemistry added to PCM Venus.

Table 5.1. Fe chemistry in the Venus PCM.

No.	Reaction	Rate Coefficient[a]	Note
Neutral reactions			
1	$Fe + O_3 \rightarrow FeO + O_2$	$3.4 \times 10^{-10} \exp(-146/T)$	1
2	$FeO + O \rightarrow Fe + O_2$	$4.6 \times 10^{-10} \exp(-350/T)$	2
3	$FeO + CO \rightarrow Fe + CO_2$	$1.2 \times 10^{-13}(T/300)^{2.307} \exp(-820/T)$	3
4	$FeO + O_3 \rightarrow FeO_2 + O_2$	$3.0 \times 10^{-10} \exp(-177/T)$	4
5	$FeO + CO_2 (+ M) \rightarrow FeCO_3$	$\log_{10}(k_{rec,0}) = \log(2) + (-37.87+7.074\log T-1.649(\log T)^2)$	4
6	$FeO_2 + O \rightarrow FeO + O_2$	$1.4 \times 10^{-10} \exp(-580/T)$	2
7	$FeO_2 + CO_2 (+M) \rightarrow OFeCO_3$	$1.3 \times 10^{-30} (T/300)^{-4.06}$	5
8	$OFeCO_3 + O \rightarrow FeCO_3 + O_2$	$2.0 \times 10^{-10} (T/300)^{0.167}$	5
9	$FeCO_3 + CO_2 (+M) \rightarrow FeCO_3.CO_2$	$\log_{10}(k_{rec,0}) = \log(2) + (-51.8343 + 26.43\log(T) - 6.335(\log(T)^{2,})$	5
10	$FeCO_3.CO_2 + O \rightarrow OFeCO_3 + CO_2$	$2.0 \times 10^{-10} (T/200)^{0.167}$	5
11	$FeCO_3.CO_2 (+M) \rightarrow FeCO_3 + CO_2$	$k_9/(6.78 \times 10^{-25} \exp(13387/T))$	5
12	$FeCO_3 + HCl \rightarrow HOFeCl + CO_2$	$2.0 \times 10^{-10} (T/200)^{0.167}$	5
13	$FeCO_3.CO_2 + HCl \rightarrow HOFeCl + 2CO_2$	$2.0 \times 10^{-10} (T/200)^{0.167}$	5
14	$HOFeCl + HCl \rightarrow FeCl_2 + H_2O$	$2.0 \times 10^{-10} (T/200)^{0.167}$	5
15	$FeCO_3 + Cl \rightarrow OFeCl + CO_2$	$2.0 \times 10^{-10} (T/200)^{0.167}$	5
16	$FeCO_3.CO_2 + Cl \rightarrow OFeCl + 2CO_2$	$2.0 \times 10^{-10} (T/200)^{0.167}$	5
17	$OFeCl + Cl \rightarrow FeCl_2 + O$	$2.0 \times 10^{-10} (T/200)^{0.167}$	5
18	$FeCl + O_3 \rightarrow OFeCl + O_2$	$2.0 \times 10^{-10} (T/200)^{0.167}$	5
19	$FeCl_2\text{-}H_2O + Cl \rightarrow FeCl_3 + H_2O$	$2.0 \times 10^{-10} (T/200)^{0.167}$	5
20	$FeCl_2 + H_2O (+ M) \rightarrow FeCl_2.H_2O$	$8.6 \times 10^{-26} (T/200)^{-5.06}$	5
21	$FeCl_3 + CO_2 (+M) \rightarrow FeCl_3.CO_2$	$1.2 \times 10^{-28} (T/200)^{-6.53}$	5
22	$FeCl_3.CO_2 (+M) \rightarrow FeCl_3 + CO_2$	$5.1 \times 10^{-8} (\exp(-3012/T)$	5
Ion-molecule reactions			
30	$Fe^+ + O_3 \rightarrow FeO^+ + O_2$	$7.1 \times 10^{-10} \exp(-129/T)$	6
31	$FeO^+ + O \rightarrow Fe^+ + O_2$	3.2×10^{-11}	7
32	$FeO^+ + CO \rightarrow Fe^+ + CO_2$	1.6×10^{-10}	7
33	$FeO^+ + CO_2 (+M) \rightarrow FeO^+.CO_2$	$3.2 \times 10^{-27} (T/300)^{-3.11}$	5
34	$Fe^+ + CO_2 (+M) \rightarrow Fe^+.CO_2$	$8.1 \times 10^{-29} (T/300)^{-2.31}$	8
35	$Fe^+.CO_2 + CO_2 (+M) \rightarrow Fe^+.(CO_2)_2$	$4.6 \times 10^{-28} (T/300)^{-5.38}$	5
36	$Fe^+.CO_2 + O \rightarrow FeO^+ + CO_2$	4.6×10^{-10}	5
37	$Fe^+.(CO_2)_2 + O \rightarrow FeO^+.CO_2 + CO_2$	5.0×10^{-10}	5
38	$FeO^+.CO_2 + CO_2 (+M) \rightarrow FeO^+.(CO_2)_2$	$2.3 \times 10^{-26} (T/300)^{-5.52}$	5

39a	$FeO^+.CO_2 + O \rightarrow FeO_2^+ + CO_2$	$7.0 \times 10^{-11} (T/300)^{-0.33}$	5
39b	$FeO^+.CO_2 + O \rightarrow Fe^+.CO_2 + O_2$	$3.1 \times 10^{-10} (T/300)^{0.03}$	5
40	$FeO_2^+ + O \rightarrow FeO^+ + O_2$	6.3×10^{-11}	7
41	$FeO^+ + e^- \rightarrow Fe + O$	$5.5 \times 10^{-7} (T300)^{-0.5}$	9
42	$FeO_2^+ + e^- \rightarrow Fe + O_2$	$5.5 \times 10^{-7} (T300)^{-0.5}$	10
43	$Fe^+.CO_2 + e^- \rightarrow Fe + CO_2$	$5.5 \times 10^{-7} (T300)^{-0.5}$	10
44	$Fe^+.(CO_2)_2 + e^- \rightarrow Fe + CO_2 + CO_2$	$5.5 \times 10^{-7} (T300)^{-0.5}$	10
45	$FeO^+.CO_2 + e^- \rightarrow FeO + CO_2$	$5.5 \times 10^{-7} (T300)^{-0.5}$	10
46	$FeO^+.(CO_2)_2 + e^- \rightarrow FeCO_3 + CO_2$	$5.5 \times 10^{-7} (T300)^{-0.5}$	10
47	$FeO_2^+.CO_2 + e^- \rightarrow FeO_2 + CO_2$	$5.5 \times 10^{-7} (T300)^{-0.5}$	10
48	$FeO^+.(CO_2)_2 + O \rightarrow FeO_2^+.CO_2 + CO_2$	$3.1 \times 10^{-10} (T/300)^{0.03}$	5
49	$Fe + O_2^+ \rightarrow Fe^+ + O_2$	1.1×10^{-9}	11
50	$Fe + NO^+ \rightarrow Fe^+ + NO$	9.2×10^{-10}	11
51	$FeCO_3 + O_2^+ \rightarrow FeO^+.CO_2 + O_2$	1.0×10^{-9}	12
52	$FeCO_3 + NO^+ \rightarrow FeO^+.CO_2 + NO$	1.0×10^{-9}	12
53	$FeCO_3.CO_2 + O_2^+ \rightarrow FeO^+.(CO_2)_2 + O_2$	1.0×10^{-9}	12
54	$FeCO_3.CO_2 + NO^+ \rightarrow FeO^+.(CO_2)_2 + NO$	1.0×10^{-9}	12
55	$Fe^+ + e^- \rightarrow Fe$	$6.5 \times 10^{-12} (T/300)^{-0.51}$	13
Photochemical reactions			
60	$Fe + h\nu \rightarrow Fe^+ + e^-$	3.2×10^{-6}	14
61	$FeCl + h\nu \rightarrow Fe + Cl$	0.15	5
62	$FeCl_2 + h\nu \rightarrow FeCl + Cl$	2.0×10^{-3}	5
63	$FeCl_3 + h\nu \rightarrow FeCl_2 + Cl$	2.3×10^{-2}	5
64	$FeCO_3 + h\nu \rightarrow FeO + CO_2$	0.17	5
65	$FeCl_3.CO_2 + h\nu \rightarrow FeCl_3 + CO_2$	0.41	5
66	$FeCO_3.CO_2 + h\nu \rightarrow FeO + 2CO_2$	0.20	5
67	$OFeCO_3 + h\nu \rightarrow FeO_2 + CO_2$	0.34	5

[a] Units: photolysis reactions, s^{-1}; bimolecular reactions, cm^3 $molecule^{-1}$ s^{-1}; termolecular, cm^6 $molecule^{-2}$ s^{-1}.

1. Helmer and Plane (1994). 2. Self and Plane (2003). 3. A best fit using Transition State Theory to the literature rate coefficients for the reverse reaction, $Fe + CO_2 \rightarrow FeO + CO$ (Giesen et al., 2002; Smirnov, 2008). 4. Rollason and Plane (2000). 5. This work (see Appendix A). 6. Rollason and Plane (1998). 7. Woodcock et al. (2006). 8. Vondrak et al. (2006). 9. Bones et al. (2016). 10. Set to the measured rate coefficient for $FeO^+ + e^-$ (Bones et al., 2016). 11. Rutherford and Vroom (1972). 12. Set to a typical charge transfer rate coefficient cf. reactions 49 and 50. 13. Nahar et al. (1997). 14. Whalley and Plane (2010), rescaled for Venus.

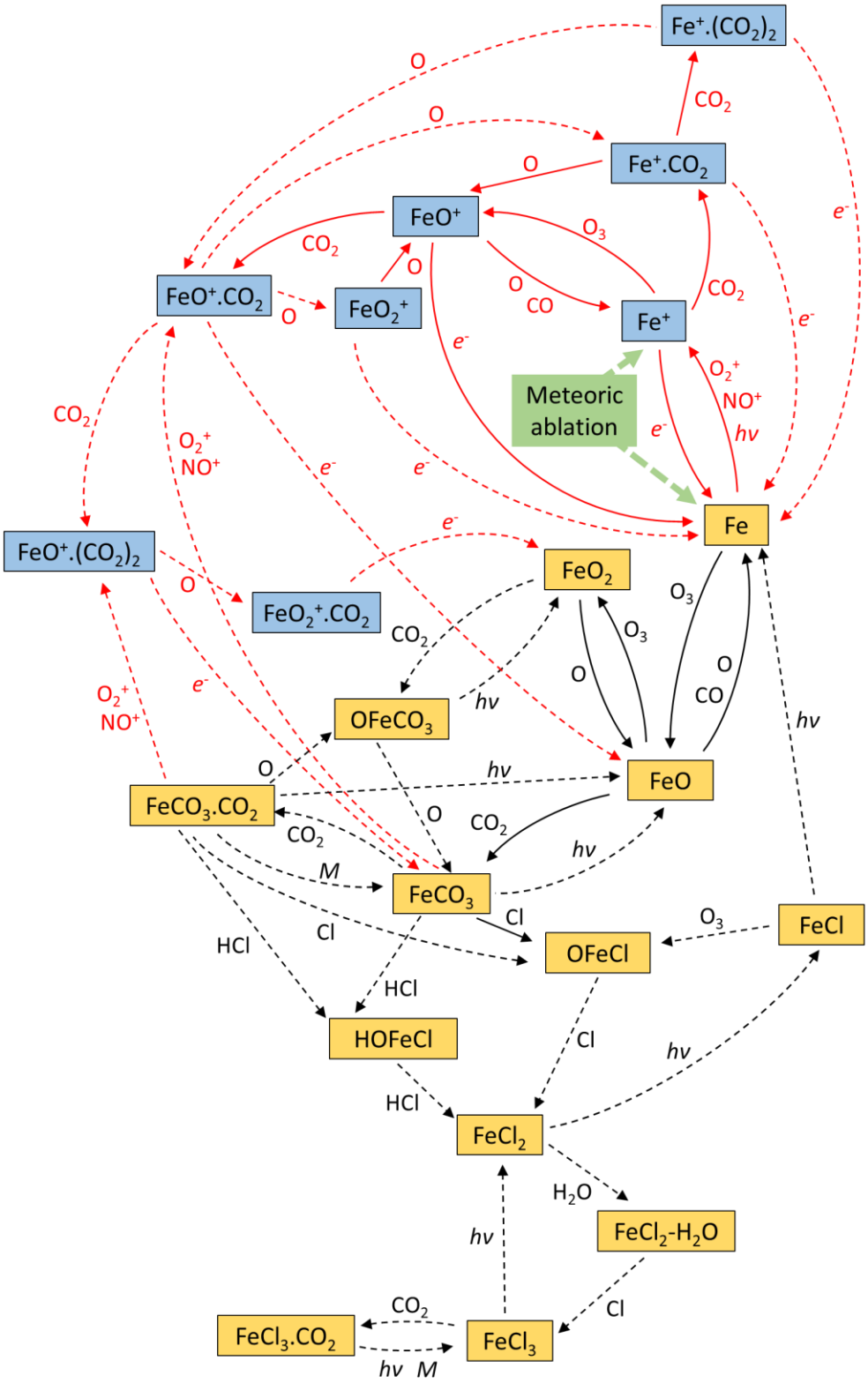

Figure 5.1. Reactions of neutral (gold) and charged (blue) Fe-containing species added to the PCM (Table 5.1). Meteoric ablation (green) provides a source of Fe and Fe^+. Black lines and reactants indicate neutral chemistry, red lines and reactants indicate reactions involving charged species. Collision partners are indicated on arrows. *M* indicates thermal decomposition after collision with CO_2, e^- is electron uptake, and *hv* indicates absorption of a photon. Solid lines indicate reactions that have been measured experimentally, dashed lines indicate predicted reaction rates.

Figure 5.2 shows the global mean profiles of charged (Figure 5.2a) and neutral (Figure 5.2b) iron species after 3.0 Venus solar days resulting from the added iron chemistry. The dominant species above 110 km remain Fe and Fe^+ by 1 – 2 orders of magnitude. The majority of the charged species are limited to altitudes above 100 km, with only small amounts of $Fe^+.(CO_2)_2$ and $FeO_2^+.CO_2$ present below this region. Similarly, the majority of the neutral iron species are constrained above the cloud deck. Only the $FeCl_3$, $FeCl_2.H_2O$ and $FeCl_3.CO_2$ persist for sufficiently long periods to reach the cloud deck and below. In the upper haze and cloud layer, it is therefore acceptable to consider only iron chloride species. Note that the interaction of Fe species with the haze/cloud droplets is not considered in the model.

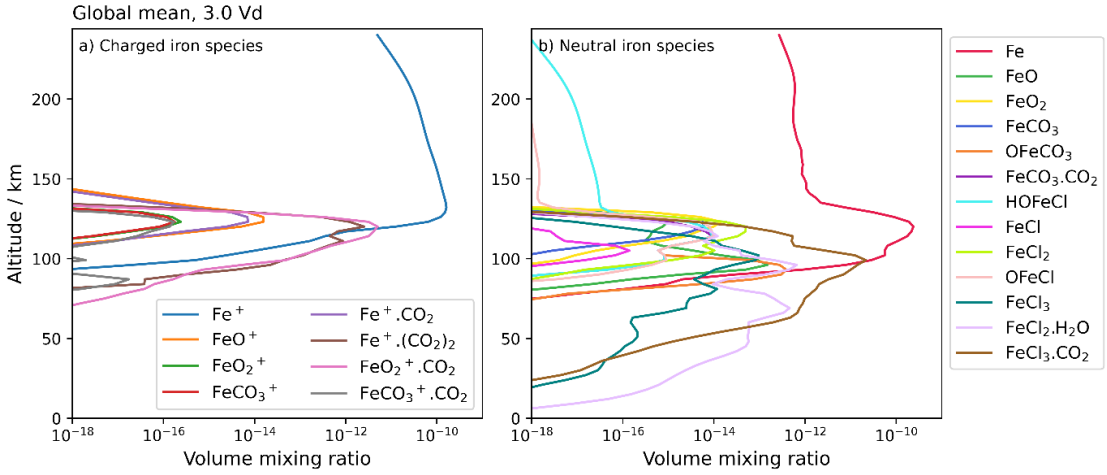

Figure 5.2. Global mean vmrs of all a) charged and b) neutral iron species after 3.0 Venus days.

The dominant form of $FeCl_3$ throughout most of the atmosphere is $FeCl_3.CO_2$. Comparison of predicted gas phase absorption spectra showed negligible change to the absorption cross-section of $FeCl_3$ due to the binding of the CO_2 molecule (Figure 5.3, see Appendix Section A1.2 for details of the calculation of these spectra). It is not expected to affect the absorption spectrum or uptake into cloud droplets, and the bound CO_2 should be readily lost when $FeCl_3.CO_2$ is dissolved in the droplets, or below the clouds when the temperature is high enough. All further consideration of the $FeCl_3$ concentration predicted by the PCM will consider the sum of the $FeCl_3$ and $FeCl_3.CO_2$.

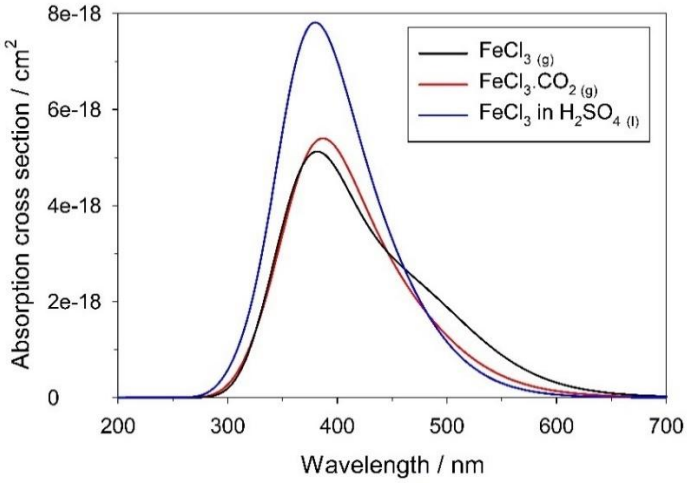

Figure 5.3. Calculated absorption cross-sections for the $FeCl_3.CO_2$ cluster and $FeCl_3$ in the gas phase, and $FeCl_3$ in liquid H_2SO_4 using Time-Dependent Density Functional Theory (Scalmani et al., 2006). See Appendix Section A1.2 for details of the calculation of these spectra.

There is little change in the absorption peak wavelength for $FeCl_3.CO_2$, $FeCl_3$ and $FeCl_3$ in H_2SO_4 (387, 382 and 380 nm, respectively), and the three spectra all have long wavelength tails to more than 600 nm. However, the shoulder between 460 and 560 nm in the $FeCl_3$ spectrum disappears when CO_2 clusters with it; and the H_2SO_4-solvated $FeCl_3$ peak absorption cross-section is 52% higher. These differ significantly from the absorption spectra measured experimentally, which found two absorption peaks at wavelengths of ~320 and ~365 nm. Given the marked differences between the predicted and measured spectra (discussed further in Section 5.4), the predicted spectra are not used for comparison with the observed Venusian spectrum. However, the similarity between the three predicted spectra are taken as an indication that the spectra will not differ significantly between gas and droplet phases, and that the measured laboratory spectra are a reasonable representation of the gaseous $FeCl_3$ and $FeCl_3.CO_2$ absorption spectra.

5.2.3 Results

Figure 5.4 shows the total $FeCl_3$ (sum of $FeCl_3$ and $FeCl_3.CO_2$) column abundance (Figure 5.4a) over time, and the global mean number density profile after 1.0, 2.0, and 3.0 Vd (Figure 5.4b).

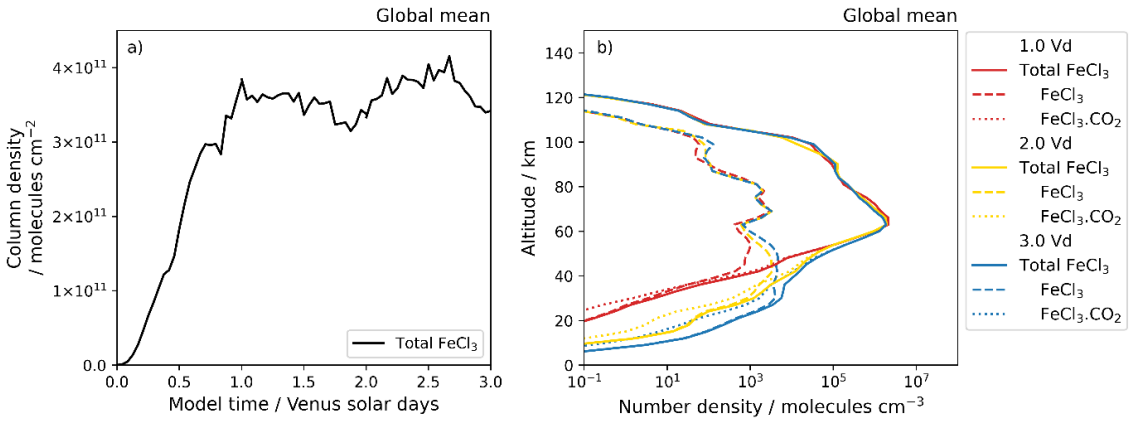

Figure 5.4. The change in global mean total $FeCl_3$ a) column density and b) number density with time over the 3.0 Venus days of model run.

As was seen in Figure 5.2, the dominant form of $FeCl_3$ (solid lines) is $FeCl_3.CO_2$ (dotted lines, mostly obscured by the solid lines) above ~30 km. At this point, the dissociation of $FeCl_3.CO_2$ to $FeCl_3$ and CO_2 makes $FeCl_3$ (dashed lines) the dominant form.

The number density remains approximately constant in the mesosphere above 95 km across the 3.0 Vd (due to rapid vertical mixing by eddy diffusion), but the concentration below the clouds increases with model time. The cause of this can be seen in Figure 5.5, which shows vertical slices through the atmosphere at local midday and midnight, and the morning and evening terminators.

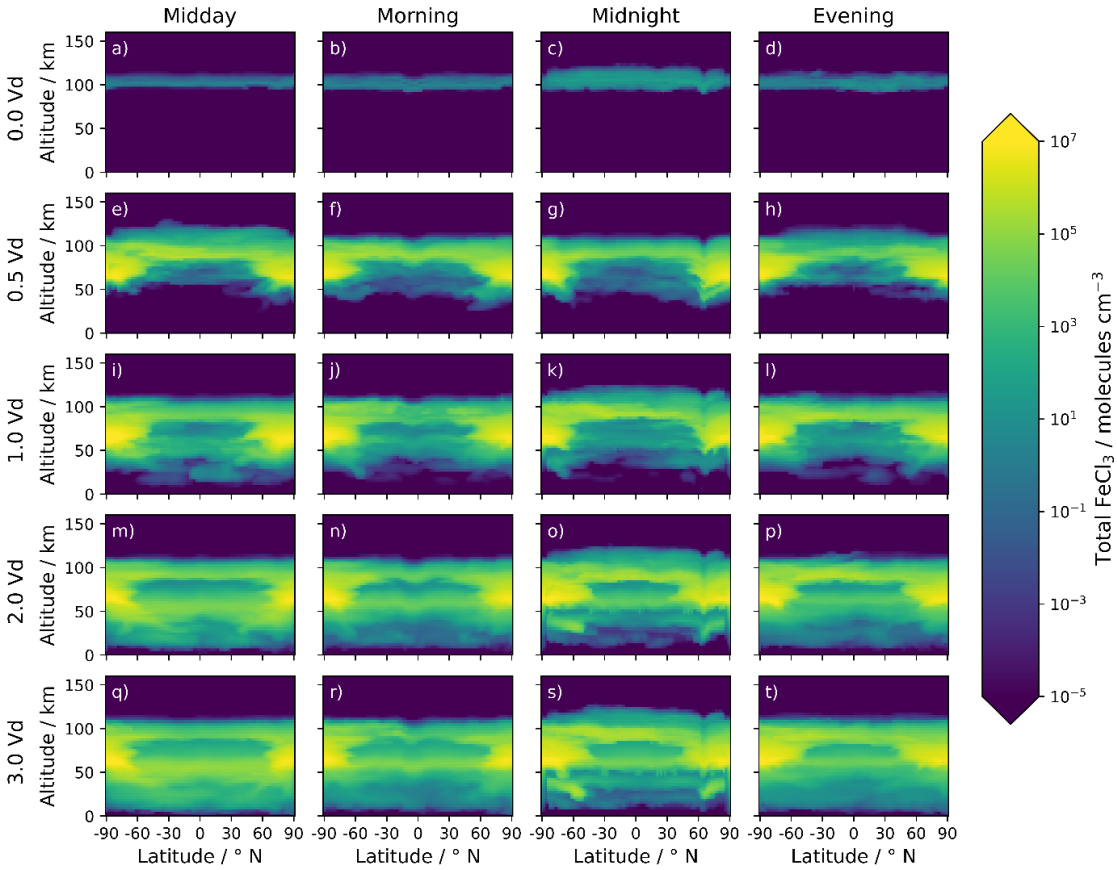

Figure 5.5. Vertical slices through the atmosphere at different local times and at the start, middle, and end of the first day of the model run, and after each subsequent day.

$FeCl_3$ is initially formed in a thin layer near the meteoric injection peak at 115 km (Figure 5.5a – d). The $FeCl_3$ is transported poleward in and above the upper haze, and downward in the polar regions (Figure 5.5e – h). The equatorward transport in the troposphere is weaker than the poleward transport in the mesosphere, and so the accumulation in the lower atmosphere is slow. Low concentrations in the low- to mid-latitude regions are not indicative of a strong loss process in this region, but simply illustrate slow accumulation following the dynamical transport. The concentration through and below the clouds increases with model time (Figure 5.5i – t) as the $FeCl_3$ is transported, and the low concentrations at low latitudes are not expected to persist after the model reaches steady state.

Figure 5.6 shows the column abundance of $FeCl_3$ with location. The highest concentrations occur in the polar regions, and the lowest at the evening terminator. The increase in concentration at low latitudes can be seen across the three days (all three subplots use the same colourbar) and the low concentration region at the morning terminator fills in over time. The high concentrations in polar regions are due to the limitations for the PCM dynamics. As illustrated in Section 2.1.2.3, the PCM meridional winds are unphysically strong at high latitudes and do not match observations. The high concentration in the polar regions seen in Figures 5.4 and 5.6 are due to the peak meridional winds occurring at ~80° in the PCM, rather than the ~60° seen in observations. The true $FeCl_3$ concentration distribution would therefore be expected to be higher in low- to mid-latitudes than is produced here.

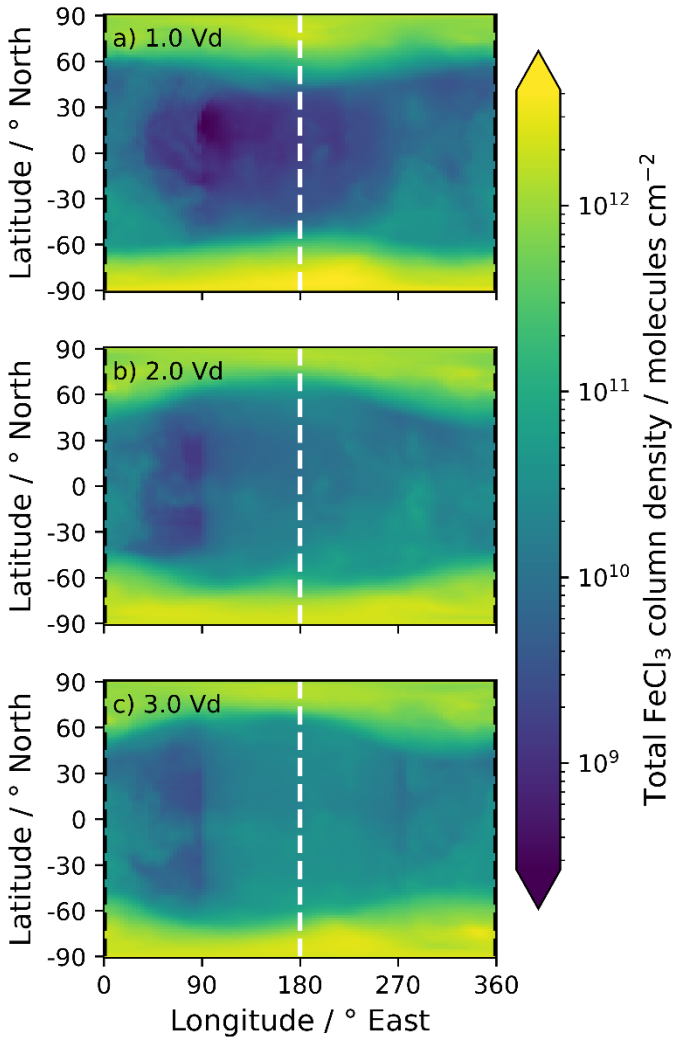

Figure 5.6. Total $FeCl_3$ column abundance across the model run. White dashed line indicates local midday, black lines indicate midnight, which is at the break of the map projection.

5.2.4 1D model extrapolation

The 1D model (described in Section 2.3) was initialised with injection rates of the different meteoric metals and the $FeCl_3$ concentration at 100 km constrained to the total diurnal average Fe modelled by the PCM at 100 km. J.M.C. Plane estimated total $FeCl_3$ abundance due to meteoric

injection and loss by agglomeration of MSPs and setting through the atmosphere. Meteoric metals were all assumed to form chlorides with an average monomer size of 0.27 nm as described in Section 2.3.

Two model runs were performed, each for 20 000 Earth days (~171 Venus solar days). In the first, the $FeCl_3$ was allowed to accumulate in the atmosphere with no coagulation. In the second, the particles were allowed to collide and coagulate with a collision efficiency (fraction of particle collisions that result in coagulation) of 1%. Figure 5.7 shows the particle size distribution with altitude. Particles grow through coagulation as they sediment and mix vertically through the atmosphere from 100 km. Most of the particle number is in the sub-nm size range above 80 km, and between 100 and 600 nm below 60 km. The rapid switchover is caused by the longer time the small particles (r < 20 nm) spend between 60 and 70 km, as the sedimentation rate slows down and the vertical eddy diffusion coefficient decreases (see Figure 2.31).

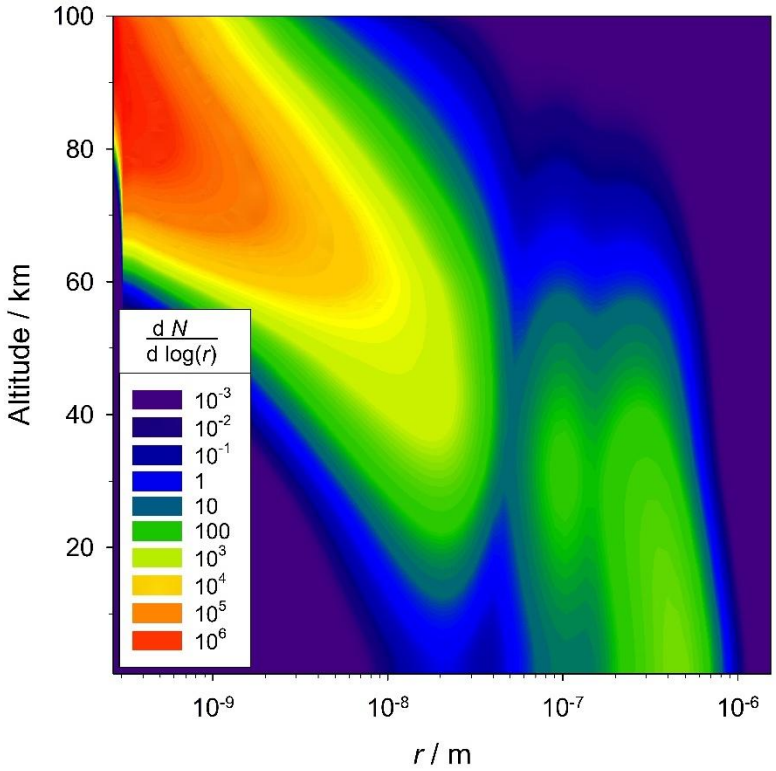

Figure 5.7. The size distribution (radius r) of MSP particle number density, N, as a function of altitude, after running the 1D model with coagulation for 20 000 Earth days.

Figure 5.8 shows the resulting $FeCl_3$ number density profiles below 100 km for the coagulating and non-coagulating cases. The modelling for 20 000 Earth days increases the number density significantly throughout the mesosphere and troposphere, with ~10^{11} molecules cm^{-3} in the upper clouds (compared to ~10^6 molecules cm^{-3} after 3.0 Vd in the PCM results), and a maximum number density near the surface of over 10^{12} molecules cm^{-3} without coagulation. The increase in particle size due to coagulation increases the sedimentation rate of the particles and decreases the number density of $FeCl_3$ by approximately an order of magnitude throughout the atmosphere.

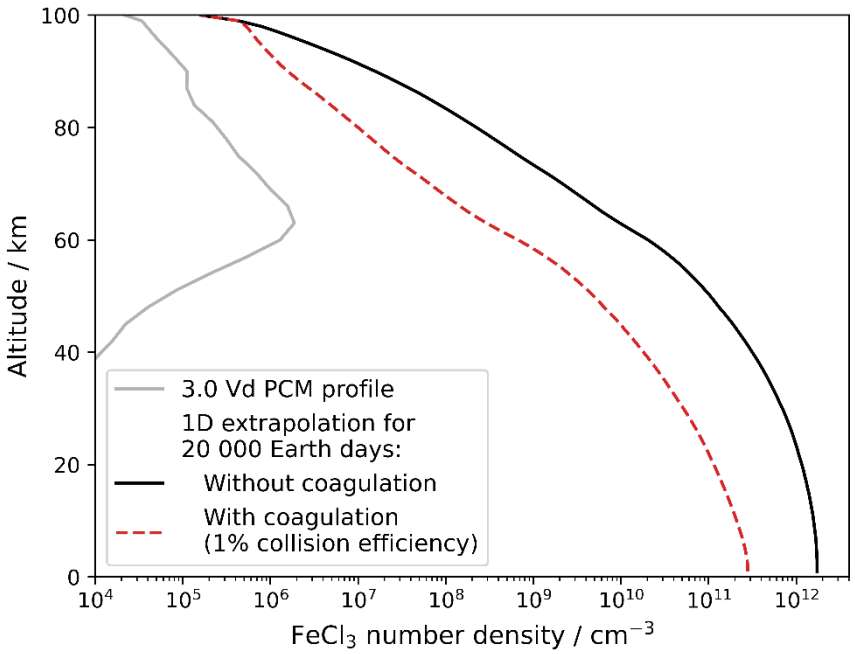

Figure 5.8. $FeCl_3$ number density in MSPs with and without coagulation of particles.

Integrating up to 100 km, the total column abundance of $FeCl_3$ in the MSPs is 4.7×10^{18} molecules cm^{-2} without coagulation, and 5.3×10^{17} molecules cm^{-2} with modelled coagulation. If only the region in and above the upper clouds (above 60 km, the location of the unknown UV absorber, see Section 1.4.3) is considered, there is a column abundance (without coagulation) of 9.8×10^{15} molecules cm^{-2} or (with coagulation) of 3.17×10^{14} molecules cm^{-2}.

5.3 SOCRATES reflectance calculations

5.3.1 Calculation of refractive index from absorptivity

The 1 wt% predicted concentration of $FeCl_3$ in the cloud droplets (Zasova et al., 1981) is significantly higher than the concentrations used to measure the molar absorptivity spectrum (Chapter 4), so the absorbance at higher concentrations must to be predicted from the absorptivity and converted to the imaginary refractive index, which is used (along with the real refractive index of sulphuric acid) for the Mie theory calculations of single particle extinction performed by SOCRATES.

The molar absorptivity, ε, of the sample of length l is related to absorbance by the Beer-Lambert law (Equation 4.1). The absorbance is a measure of the decrease in light intensity passing through a sample:

$$\log_{10}\left(\frac{I_0}{I}\right) = A = \varepsilon c l \qquad (5.1)$$

where I_0 is the intensity of light incident upon the sample and I is the intensity of light that passes through the sample.

The imaginary refractive index, k, describes the attenuation of light as it passes through a sample:

$$I(x) = I_0 exp\left(\frac{-4\pi kx}{\lambda_0}\right) \tag{5.2}$$

where I_0 is the intensity of light incident upon the sample, $I(x)$ is the intensity at a distance x through the sample, and λ_0 is the vacuum wavelength of the light.

Rearranging Equation 5.2 and setting the distance through the sample $x = l$,

$$\frac{I_0}{I} = exp\left(\frac{4\pi kl}{\lambda_0}\right) \tag{5.3}$$

Using the logarithm change of base rule:

$$\log_a(x) = \frac{\log_b(x)}{\log_b(a)} \tag{5.4}$$

Equation 5.3 can be rewritten as

$$ln\left(\frac{I_0}{I}\right) = \frac{\log_{10}\left(\frac{I_0}{I}\right)}{\log_{10}(e)} = \frac{4\pi kl}{\lambda_0} \tag{5.5}$$

By comparison with Equation 5.1,

$$\frac{4\pi kl}{\lambda_0} = \frac{\varepsilon cl}{\log_{10}(e)}$$

$$k = \frac{\varepsilon c\lambda_0}{4\pi \log_{10}(e)} \tag{5.6}$$

The imaginary refractive index of the iron solutions can therefore be calculated for different concentrations of iron by scaling the molar absorptivity measured in the experimental work to higher concentrations. The real refractive index of the cloud modes is taken to be that of 75 wt% sulphuric (Figure 2.30) acid due to the small change measured (Section 4.2.1) upon addition of $FeCl_3$ to the sulphuric acid. Outside the region of absorption measured experimentally, the imaginary refractive index is taken to be that of sulphuric acid.

5.3.2 Effect in droplets using measured $FeCl_3$ spectra

Initial tests were carried out with a coarse refractive index (Figure 5.9) estimated from the molar absorptivity calculated by a linear fit to preliminary $FeCl_3$ measurements at concentrations between 2×10^{-3} and 10×10^{-3} wt% (not shown).

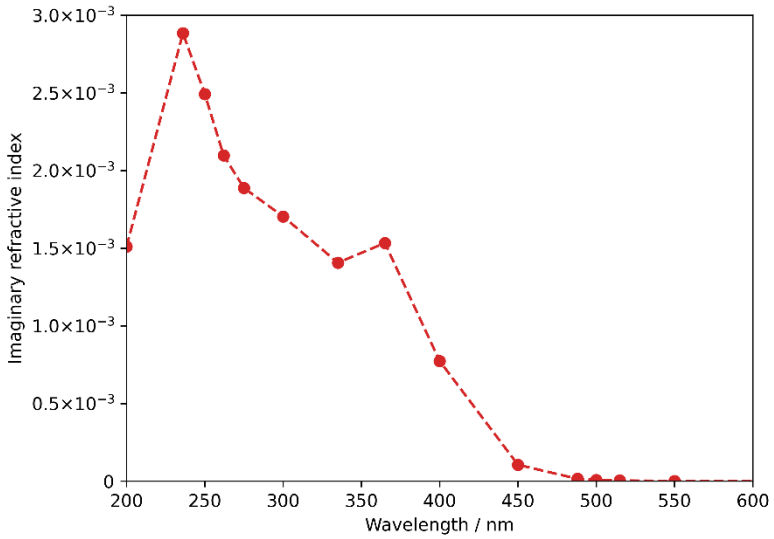

Figure 5.9. The calculated imaginary refractive index of a solution of an initial concentration of 1 wt% $FeCl_3$, based on measurements of 2×10^{-3} to 10×10^{-3} wt%.

5.3.2.1 Initial tests

Initial tests were carried out with the coarse refractive index spectrum. Different concentrations of $FeCl_3$ were tested. In initial tests, the same concentration of $FeCl_3$ was modelled in all cloud droplets (Figure 5.10). The concentrations refer to the initial $FeCl_3$ added to the solutions, not the unreacted $FeCl_3$ remaining in the solution at the time the spectrum was measured. It would be more unambiguous to refer to Fe concentrations in the droplets; however, as previous work (Krasnopolsky, 2017; Zasova et al., 1981) reported concentrations in $FeCl_3$ wt%, the same convention is used here. The cloud particle distribution is taken from the PCM and converted to separate modes as outlined in Section 2.2.2.7. The SO_2 profile used is an artificial profile constructed to broadly match observations, as in Figure 3.18 The measured spectrum can be matched well by an initial concentration of approximately 2 – 3 wt% $FeCl_3$ in the cloud droplets.

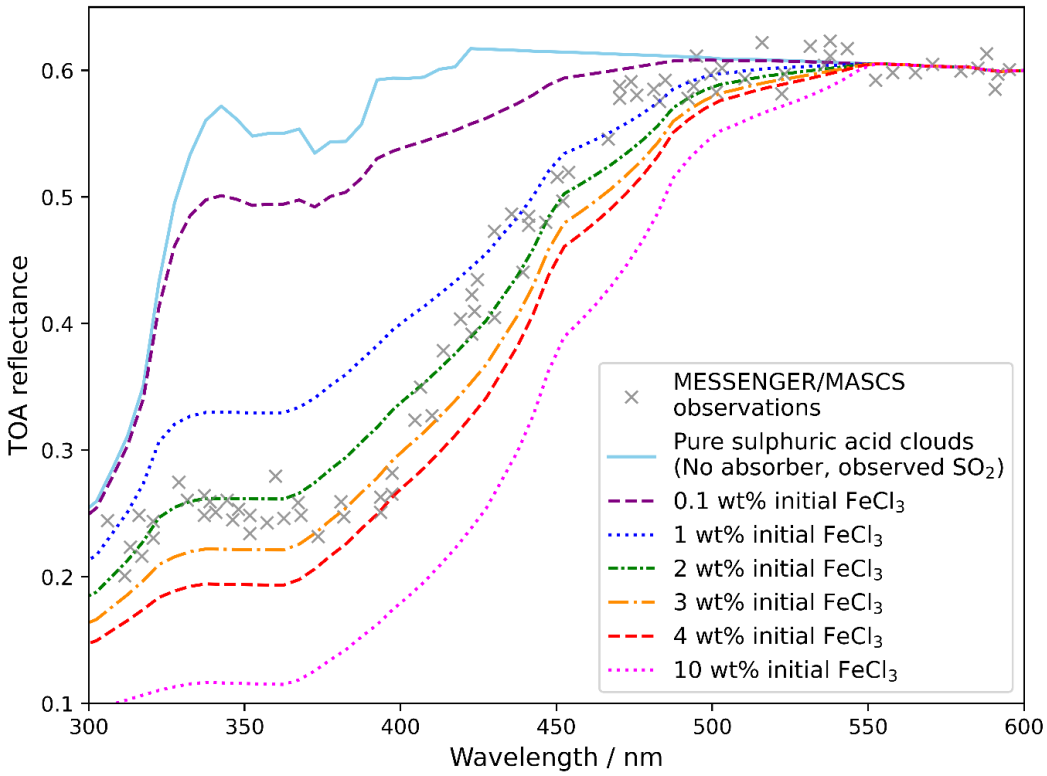

Figure 5.10. SOCRATES modelled reflectance for different initial concentrations of $FeCl_3$ in all cloud modes.

5.3.2.2 Individual cloud modes

Figure 5.11 shows the modelled TOA reflectance when the iron is modelled in one cloud mode at a time. The refractive indices of the other cloud modes are those of 75 wt% sulphuric acid.

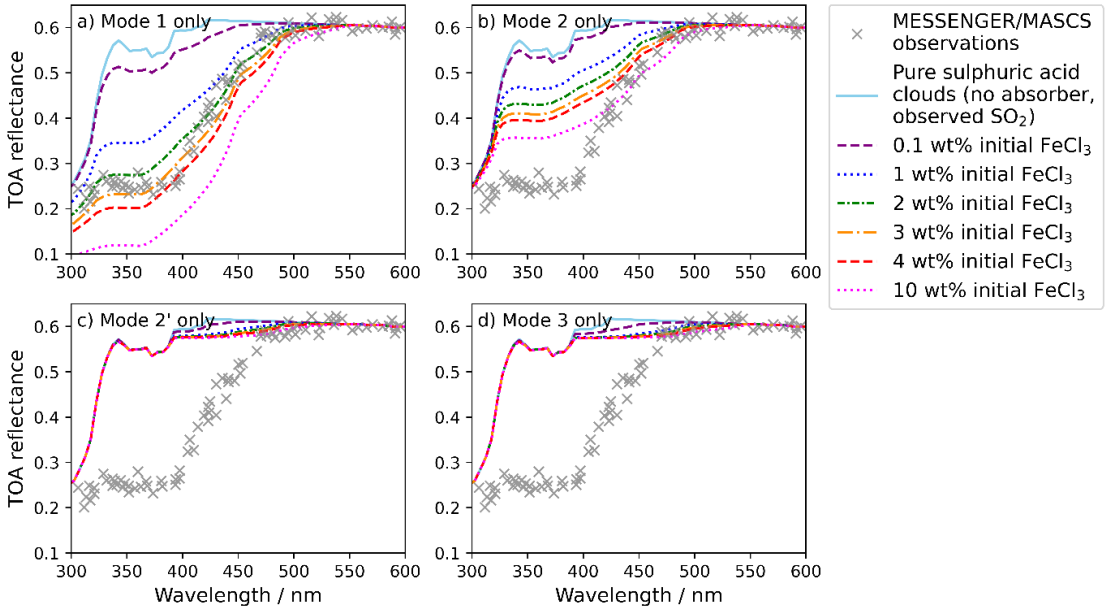

Figure 5.11. SOCRATES modelled reflectance for different concentration of $FeCl_3$ in a) mode 1, b) mode 2, c) mode 2', and d) mode 3 cloud droplets only. In each case, all other cloud modes are sulphuric acid.

The $FeCl_3$ produces a similar spectral shape in mode 1 as when it was included in all of the cloud modes (Figure 5.10), indicating that mode 1 is the dominant source of absorption when $FeCl_3$ is in all cloud modes.

Figure 5.11b shows that higher concentrations of $FeCl_3$ are required in mode 2 than in mode 1: 10 wt% $FeCl_3$ in mode 2 produces a similar predicted reflectance near 350 nm to 1 wt% $FeCl_3$ in mode 1. The required $FeCl_3$ mass fraction in mode 2 would be impossibly high to reproduce the observed absorption, so even at higher concentrations than modelled, the $FeCl_3$ cannot be in mode 2 particles alone. The absorption at 450 – 500 nm is less dependent on the choice of cloud mode than near 350 nm, with only a factor of 2 to 3 times the $FeCl_3$ required in mode 2 to reproduce the absorption seen in mode 1. The same effect is seen for modes 2' and 3 (Figures 5.11c and d, respectively): while the long wavelength 'tail' of the absorption can be reproduced by high $FeCl_3$ concentrations, the strength of the absorption below 400 nm is not reproduced.

The inability of the larger cloud modes to reproduce the required absorption is due to the depth of these modes below the cloud top. The highly refractive pure sulphuric acid droplets that make up mode 1 scatter most efficiently at UV wavelengths (Figure 2.29). When only the large modes contain $FeCl_3$, the bright mode 1 haze and cloud overlying the absorber deeper within the main cloud deck efficiently scatters light before it penetrates the middle and lower clouds. It should, however, be noted that as the clouds are based on the PCM cloud treatment, which is itself prescribed based on the Pioneer Venus LCPS measurements (Knollenberg & Hunten, 1980; Stolzenbach et al., 2023), the upper haze is therefore purely mode 1, with a low number concentration of mode 2 particles within the upper clouds (the layers that reflectivity is most sensitive to). This does not reflect the bimodality in the upper haze and larger mode 2' or mode 3 particles in the upper clouds reported to be required to reproduce observations by Luginin et al. (2016) and Satoh et al. (2015).

Given the dominance of the mode 1 contribution to the absorber, the model is not sensitive to the concentration of $FeCl_3$ in the larger size modes. The concentration of the absorber in these modes is therefore unconstrained by the model. However, a high concentration of $FeCl_3$ in mode 1 would be consistent with observations of two modes of populations of particles within mode 1 (which Knollenberg and Hunten (1980) proposed were uncoated CCN, in this case assumed to be ferric chloride particles which cannot be reliably studied with the experimental work presented in Chapter 4), and the less refractive sulphuric acid droplets where the particles have nucleated droplets but not reached the Kelvin threshold to grow freely. Lower concentrations of $FeCl_3$ in the larger modes would be expected if the mode 1 cloud particles grow into the larger cloud modes by deposition of water and sulphuric acid. The volume increase from mode 1 to mode 2 alone would decrease the concentration of $FeCl_3$ in the newly grown mode 2 particles by a factor of 20. A concentration of ~0.1 wt% in mode 2, and lower concentrations still in modes 2' and 3 would,

by comparison with the low absorption predicted in Figures 5.11b – d, have a negligible effect on the spectrum.

5.3.3 Effect of change in ferric chloride and sulphate concentrations

5.3.3.1 Comparison of different times in the reaction

As the model is most sensitive to the concentration of $FeCl_3$ in mode 1, the effect of the choice of spectral shape is investigated in this single mode only. Four high-resolution spectra are used (Figure 5.12). Each of these is the same sample (N23 0C, see Table 4.1, page 164) on different days – 1, 4, 9, and 18. Different concentrations of each were tested in mode 1.

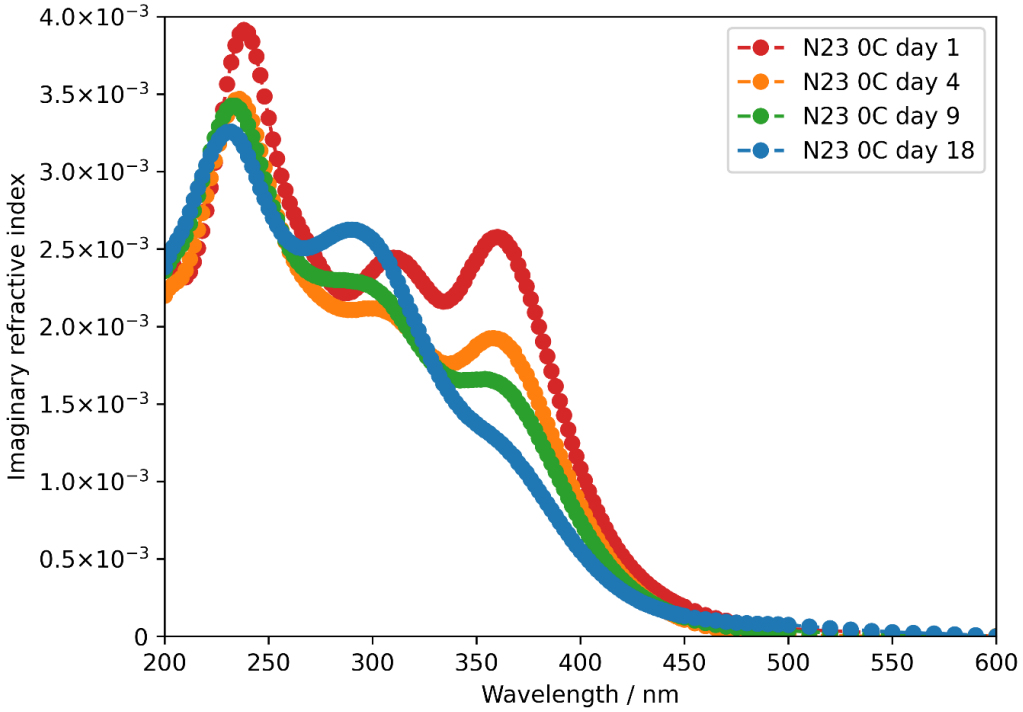

Figure 5.12. 2 nm resolution imaginary refractive index spectra of solutions of 1 wt% initial $FeCl_3$ concentration calculated from the measured absorption spectra of sample N23 0C (see Table 4.1 (page 164) for initial concentrations) on different days.

Figures 5.13 shows a range of initial $FeCl_3$ concentrations for the different sample spectra in mode 1. The initial iron concentration required to reproduce the absorption increases with the time the samples were taken at. This is to be expected: the higher fraction of ferric chloride at earlier times means that a lower overall iron concentration (and therefore initial $FeCl_3$ concentration) is required to produce the same instantaneous ferric chloride concentration.

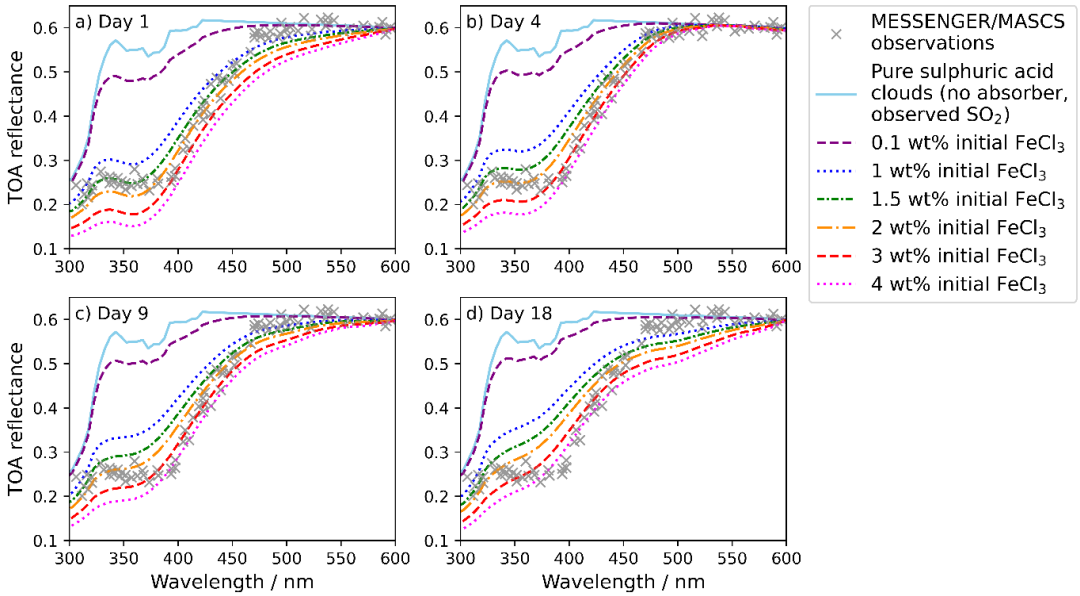

Figure 5.13. SOCRATES modelled reflectance for different modelled initial concentrations of $FeCl_3$ for spectra measured after a) 1 day, b) 4 days, c) 9 days, and d) 18 days in mode 1 cloud droplets. In each case, all other cloud modes are modelled as sulphuric acid.

The strength of the absorption in the NUV region is best reproduced by 1.5 – 2 wt% $FeCl_3$ using the day 1 spectrum, 2 – 3 wt% with days 4 and 9, and 3 – 4 wt% on day 18. For direct comparison between the spectra, the lower end of these best fit predicted reflectances are shown in Figure 5.14. The shape is best reproduced by the spectrum from day 4, particularly at long wavelengths, where all other spectra over-predict absorption. All spectra marginally over-predict absorption near 300 nm, where the SO_2 absorption is dominant.

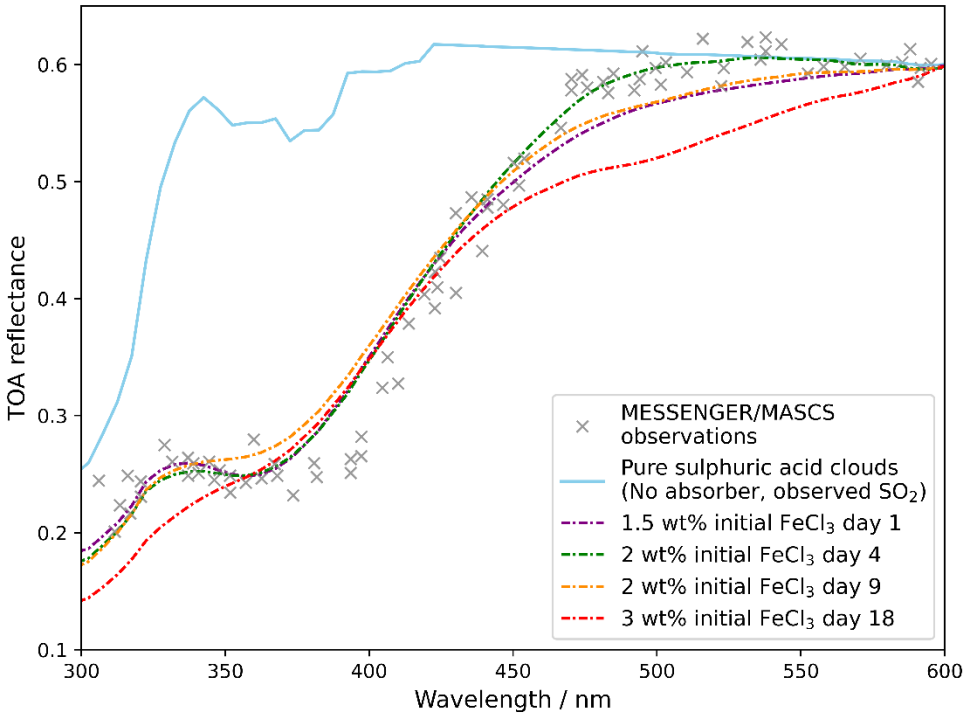

Figure 5.14. Best fit initial $FeCl_3$ concentrations for the four spectra in mode 1 from comparison of SOCRATES model results to observations.

On day 4, the fitting algorithm (Section 4.7) estimated that 71 % of the total iron in the solution existed as ferric chloride species and 29 % ferric sulphate (1.7×10^{-4} M ferric chlorides and 7.2×10^{-5} M ferric sulphate. Applying this correction to the best fit concentrations for the day 4 spectrum, the absorption would be well matched by 1.4 – 2.1 wt% $FeCl_3$ in the cloud droplets.

5.3.3.2 Identification of best-fit $FeCl_n^{3-n}$ species

To estimate the specific form of ferric chloride producing the absorption, and the expected absorption in the absence of ferric sulphate, the specific concentrations of the different components estimated by the fitting algorithm can be inspected (Figure 5.15). The dominant chloride spectrum ("Cl D") is that measured in 6.09 M HCl. By comparison with Liu et al. (2006), the dominant chloride species in this spectrum is $FeCl_2^+$. Additional contributions are from spectra Cl A (12.2 M HCl, containing by $FeCl_3$ (aq) and $FeCl_4^-$) and Cl F (1.54 M HCl, dominated by $FeCl^{2+}$).

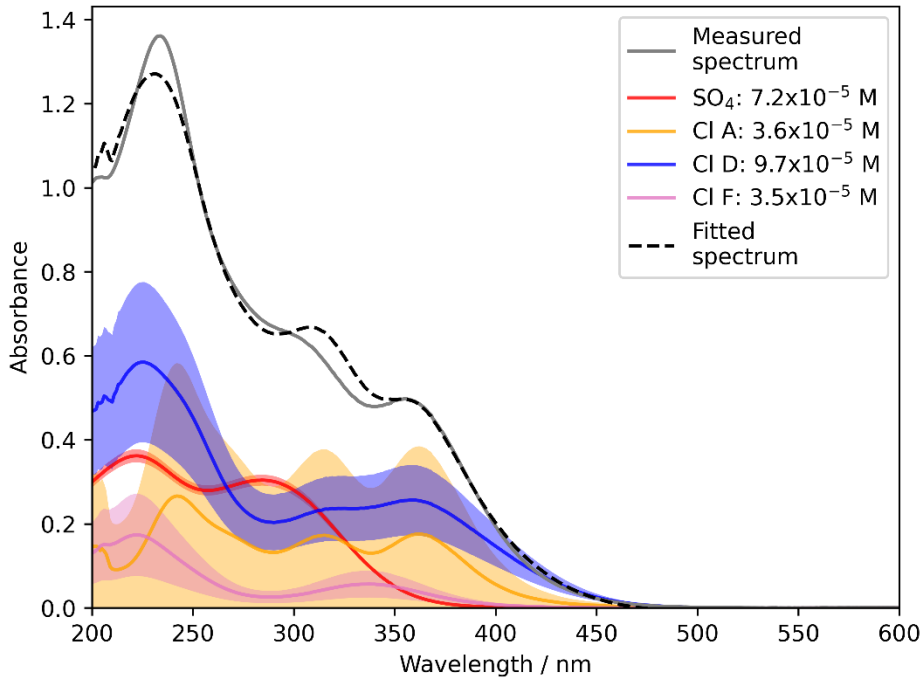

Figure 5.15. Dominant fitted components in sample N23 0C day 4 calculated using the fitting algorithm described in Section 4.7.

The absorption spectrum due to the ferric chloride species with no ferric sulphate contribution can be estimated by combining the fitted chloride spectra alone to produce an estimated absorbance. This spectrum can then be converted to the expected imaginary refractive index at higher concentrations as before and used to model the TOA reflectance of ferric chloride in the limiting case of such a slow rate of reaction that ferric sulphate concentration is negligible (Figure 5.16).

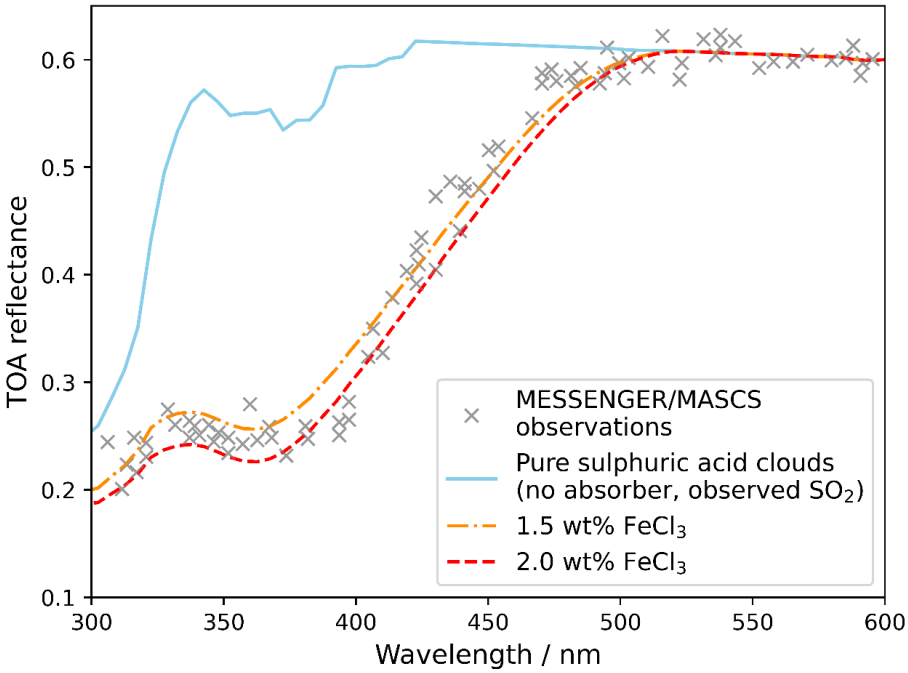

Figure 5.16. The SOCRATES model results using spectral fit results for ferric chloride species only.

The resulting spectra from the predicted spectrum of only ferric chloride species show excellent agreement with the observed spectrum, including the region near 300 nm that was previously higher than observations due to the presence of the ferric sulphate ions.

5.4 Validation of $FeCl_3$ absorbance cross-section

Comparison of the measured and calculated $FeCl_3$ spectra in sulphuric acid (Figure 5.17) shows that the calculated spectrum is broadly consistent in strength with the measured spectrum, differing only in the location and width of the peak. The cross-section, σ, for the measured spectrum is calculated from the molar absorptivity (as explained in Section 4.4.2). As iron and chlorine are large, heavy atoms, and $FeCl_3$ is in a state of high (quintet) spin multiplicity, the calculated cross-sections (see Appendix Section A1.2) are not expected to reproduce the experimental spectra very accurately. That the two methods produce reasonable agreement above 350 nm supports the identification of the measured spectrum as ferric chloride and validates the use of the calculated spectrum in the photolysis calculations in the PCM.

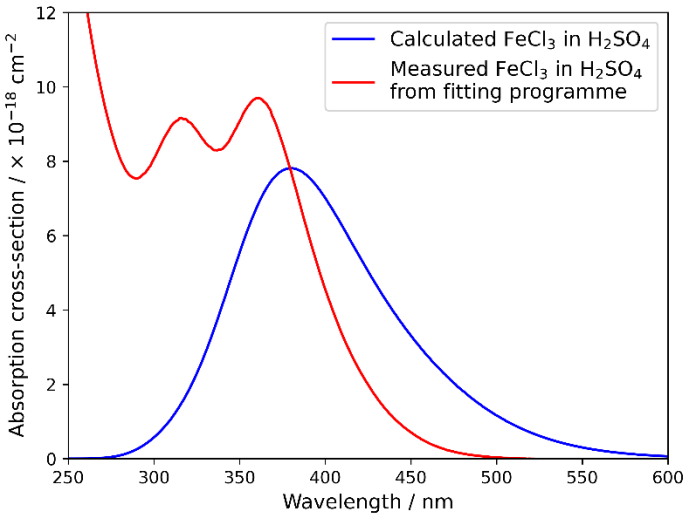

Figure 5.17. Comparison of the calculated $FeCl_3$ absorption cross-section in sulphuric acid (Figure 5.3) and the best fit pure chloride contribution to the measured absorption (sample N23 0C day 4, as used in Figures 5.15 and 5.16).

5.5 Estimated meteoric sources of $FeCl_3$

The total number density and column abundance required to produce the $FeCl_3$ concentrations predicted from comparison of SOCRATES-predicted spectra to the MASCS/MESSGENGER-retrieved spectrum of the NUV absorber are estimated from the cloud mass loading in the PCM in four different cases. As an upper limit on the $FeCl_3$ required, the $FeCl_3$ concentration required to form 2.5 wt% of all cloud modes is predicted, representing the 2 – 3 wt% initial $FeCl_3$ to produce the best fit in all cloud modes (Figure 5.10). As a lower limit, 1.75 wt% $FeCl_3$ in mode 1 in the upper clouds and haze is calculated, representing the 1.5 – 2.0 wt% best fit in the absence of ferric sulphate (Figure 5.16). The dominance of the upper clouds in the reflectance spectrum means the absence of the absorber from the lower clouds would have a negligible effect. Two intermediate values are also estimated: 2.5 wt% of mode 1 (Figure 5.14) throughout the cloud deck, or in the upper clouds and haze alone. Figure 5.18 shows the predicted number density for each case compared to the 1D model extrapolation of the number density after ~171 Venus days (20 000 Earth days).

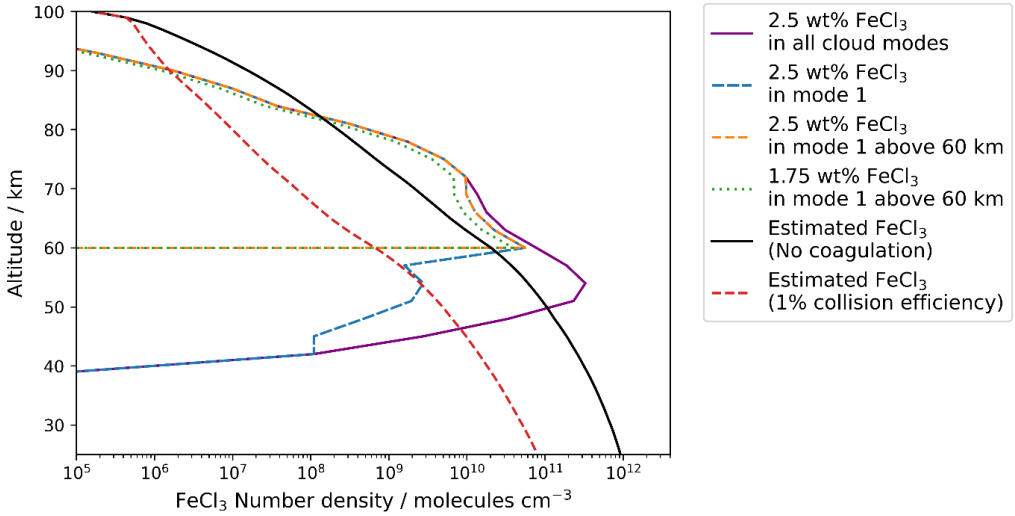

Figure 5.18. Global average number density of $FeCl_3$ equal to 2.5 wt% of the total cloud particles (purple); 2.5 wt% of mode 1 throughout the clouds (blue), or only above 60 km (orange); and 1.75 wt% of mode 1 above 60 km (green); compared to 1D model (Figure 5.8), with (red) and without (black) coagulation and sedimentation.

The total predicted column of $FeCl_3$ from the 1D model (with or without coagulation) is sufficient to provide all of the required $FeCl_3$ in the clouds. However, as the highest $FeCl_3$ concentration in the 1D model occurs below the clouds, much of this would not be available for uptake into the cloud droplets. The effect of $FeCl_3$ uptake into the cloud and haze on the available column of $FeCl_3$ is beyond the scope of this study. Instead, the partial column of $FeCl_3$ within either the full cloud layer or the upper cloud layer is compared to the required $FeCl_3$ to explain the absorption.

The available (1D modelled) and required (SOCRATES-predicted) $FeCl_3$ column abundances are listed in Table 5.2 for each of the four choices of $FeCl_3$ concentration in the cloud modes and three different regions of available $FeCl_3$. The predicted partial column of $FeCl_3$ in and above the cloud layer (above 40 km) is 2.8×10^{17} cm^{-2} without coagulation, or 1.4×10^{16} cm^{-2} with coagulation. The non-coagulating modelled $FeCl_3$ can provide 97% of the required $FeCl_3$ in all cloud modes and more than 100% of the required $FeCl_3$ in all other cases. The coagulating modelled $FeCl_3$ can account for 5% of the $FeCl_3$ in all cloud modes, 37% (39%) of $FeCl_3$ in mode 1 throughout the clouds (in the upper clouds and haze), or 56 % of the $FeCl_3$ in the upper clouds if reaction to form sulphates is neglected. If only the region in and above the upper clouds is considered, the majority of the $FeCl_3$ exists in monomers before droplet uptake occurs, so the non-coagulating case should be used. In this case, the available $FeCl_3$ in and above the upper clouds can provide 28% of the required $FeCl_3$ in mode 1 or 39% if formation of iron sulphates is neglected. The comparison of the available upper cloud and haze $FeCl_3$ with total required $FeCl_3$ through the clouds is physically unjustified (as it assumes that $FeCl_3$ uptake into the clouds could only occur in the upper clouds, but $FeCl_3$ particles could somehow persist into the middle and lower clouds without interacting with the cloud droplets), but values are included in Table 5.2 for completeness.

Table 5.2. Percentage of required $FeCl_3$ to account for all absorption in the four test cases (Figure 5.18, rows) available from meteoric iron in the different regions and with and without coagulation (columns).

			$FeCl_3$ available (1D model)		
			Non-coagulating case (full cloud)	Coagulating case (1% collision efficiency, full cloud)	Non-coagulating case (upper cloud and haze)
		Column abundance / cm^{-2}	2.8×10^{17}	1.4×10^{16}	9.8×10^{15}
$FeCl_3$ required (PCM)	2.5 wt% $FeCl_3$ in all cloud modes	2.8×10^{17}	97 %	5 %	0.4 %
	2.5 wt% $FeCl_3$ in mode 1 (all cloud layers)	3.8×10^{16}	> 100 %	37 %	26 %
	2.5 wt% $FeCl_3$ in mode 1 (upper clouds and haze)	3.5×10^{16}	> 100 %	39 %	28 %
	1.75 wt% $FeCl_3$ in mode 1 (upper clouds and haze)	2.5×10^{16}	> 100 %	56 %	39 %

5.6 Conclusions

The best fit to Venusian observations is found for approximately 1.5 – 2 wt% $FeCl_3$ in the mode 1 cloud droplets. The model is most sensitive to the $FeCl_3$ in the upper clouds and haze. The best fit spectrum was that measured in 76.5 wt% H_2SO_4 after four days. The sample had initial concentrations of approximately 9.3×10^{-2} M HCl and 1.7×10^{-4} M (1.7×10^{-3} wt%) $FeCl_3$ added. The $FeCl_3$ concentration was scaled to higher concentrations for modelling. By comparison to the reported dominance of $FeCl_n^{3-n}$ ions in hypersaline solutions by Liu et al. (2006), the dominant ferric chloride species is identified as $FeCl_2^+$, with additional contributions from other ferric chloride species.

For reasonable assumptions about the concentration and location of the $FeCl_3$ ($FeCl_3$ makes up 2.5 wt% of mode 1 particles in the upper clouds), meteoric injection of iron can explain approximately 37% of the $FeCl_3$ required to match observations. If the $FeCl_3$ is absent from (or only present in lower concentrations in) the middle and lower clouds, or if the reaction of $FeCl_3$ with sulphuric acid is slow under Venusian conditions, this value may be higher. It should also be noted that the uncertainty on the Venusian meteoric iron flux is approximately 50% (Carrillo-Sánchez et al., 2020), so it is possible that the meteoric contribution may differ significantly from the values used in this work.

It is also possible that, if additional mineral phases form, as reported by Jiang et al. (2024), the required concentration may be lower than predicted, as the same concentration of $FeCl_3$ contributes to the absorption "twice": once as unreacted ferric chloride, which then forms ferric sulphate ions, and then again as the mineral phases (copiapite, rhomboclase, and acid ferric sulphate) they reported. It is currently unclear why these mineral phases were not observed in this work.

At present, uptake of $FeCl_3$ into droplets and reaction with the sulphuric acid is not modelled. In addition, the production of $FeCl_3$ and the long-term transport and removal by settling of $FeCl_3$ are modelled separately, by the PCM and 1D model, respectively. The development of a comprehensive treatment of $FeCl_3$ formation, transport, uptake and agglomeration, and reaction is required. In particular, the droplet chemistry is of particular interest as this is the likely location of the unknown absorber. The limitations of the aerosol treatment in SOCRATES mean that the absorber must be tied to the entirety of a cloud mode – there is no way to vary the concentration of the $FeCl_3$ within a cloud mode (for example, higher concentrations in smaller particles within a mode to represent a concentrated core that grows by deposition of sulphuric acid; or varying concentrations with altitude). Other choices of $FeCl_3$ concentration in different regions or subsets of the cloud modes may produce better fits to observations. The development of a comprehensive cloud model with heterogeneous chemistry would permit further detailed study and decrease uncertainties in the estimate of the contribution that meteoric iron can make to the observations.

6. Conclusions and future work

6.1 Conclusions

In this work, two possible causes for the Venusian unknown UV absorber have been considered: OSSO (Chapter 3) and $FeCl_3$ (Chapters 4 and 5). Both candidates had previously been proposed in the literature (e.g., Frandsen et al., 2016; Zasova et al., 1981), but significant issues precluded the identification of either as the absorber: 1D modelling of OSSO predicted concentrations were too low to explain the observed absorption, and the available $FeCl_3$ spectrum in the literature showed poor agreement with the shape of the observed absorption.

6.1.1 Summary

In this work, the 3D chemical and dynamical modelling of OSSO has been carried out, using the Venus PCM, and an additional source of SO from ablation of meteoric material included in the model. Despite this, the concentrations of OSSO in the atmosphere are such that OSSO is expected to be able to explain much less than 1% of the observed absorption.

Laboratory measurements of the absorbance of ferric chloride in sulphuric acid were performed, and the contribution of ferric chloride ions and molecules and ferric sulphate ions to the total absorption have been quantified using a fitting algorithm and spectra of ferric sulphate ions with no chloride components, and ferric chloride ions with no sulphate components. The resulting spectra were compared to observations using the 1D radiative transfer model SOCRATES, which was adapted to study Venus. The best fit was found for an initial $FeCl_3$ concentration of ~2.5 wt% in the mode 1 cloud droplets, of which ~1.75 wt% remains as unreacted ferric chloride (the rest of the iron having formed ferric sulphate by reaction with the sulphuric acid of the droplets). The absorbance spectra that produced the best fits are presented in Figure 6.1.

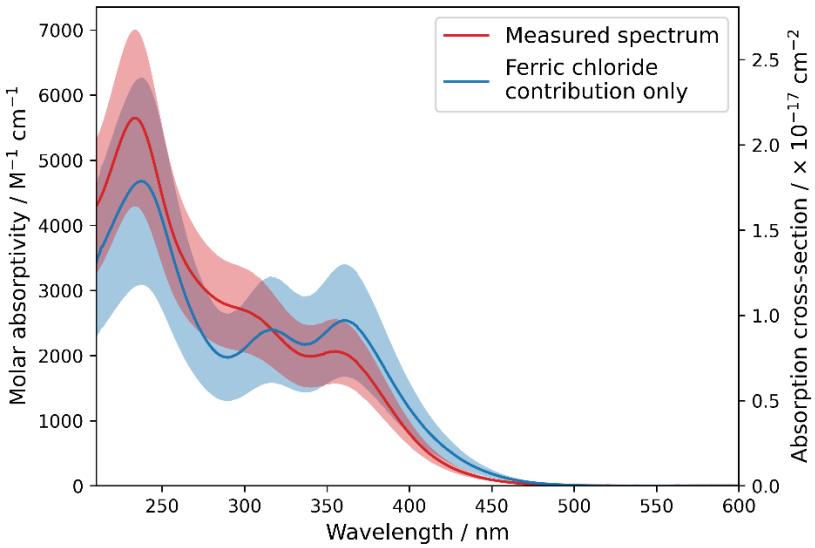

Figure 6.1. Measured molar absorptivity spectrum (per total fitted concentration of Fe, red) of a solution of $FeCl_3$ in 76.5(5) wt% H_2SO_4 with small amounts of HCl. Best fit to MESSENGER observations was for an initial 2 – 3 wt% $FeCl_3$ in the cloud droplets. Partial reaction to form ferric sulphate ions has occurred. When the ferric sulphate contribution is removed by the fitting algorithm, the absorptivity of the chloride contribution only can be calculated (blue). The best fit to MESSENGER observations was for 1.5 – 2 wt% $FeCl_3$. Spectra are reported in both molar absorptivity (primary axis) and cross-section (secondary axis).

By inclusion of iron chemistry in the Venus PCM, the formation of $FeCl_3$ from meteoric iron and atmospheric HCl and Cl has been modelled, and the accumulation of $FeCl_3$ over long times estimated in 1D with a coagulation and sedimentation model of the atmosphere. By comparison of the three models, ~40% of the observed absorption can be explained by the meteoric source of iron. It should be noted that there are significant and unconstrained uncertainties in this estimate relating to the sedimentation rate of the particles, the chemical lifetime of the $FeCl_3$ in the cloud droplets, and the uncertainty in input flux of meteoric iron on Venus. These uncertainties may increase or decrease the $FeCl_3$ by more than a factor of two, so it is possible that a purely meteoric source of $FeCl_3$ could fully explain the Venusian unknown UV absorption.

6.1.2 Broader implications

Sulphur chemistry in the Venusian atmosphere remains a significant unsolved problem for the field. In particular, observations show a decrease of SO_2 concentration with altitude by at least three orders of magnitude (from ~150 ppm below the clouds to ~10 – 100 ppb above the clouds, see Figure 3.13). The major loss process of SO_2 through the clouds is thought to be oxidation and reaction with water to form sulphuric acid, which condenses to form cloud droplets with additional water. This process requires an equivalent amount of H_2O to be destroyed as SO_2, but the observed water decrease is significantly smaller. An additional SO_2 sink in the cloud layer is therefore required.

One possible sink is a sulphur-containing species: polysulphur, polysulphur oxides, and OSSO have all been proposed as candidates. However, even with artificially low SO_2 concentrations below the clouds, the modelled OSSO cannot provide a significant sink of sulphur through the clouds, and modelled SO_2 concentrations above the cloud layer exceed observations. The reaction of OSSO to form polysulphur or polysulphur oxides is beyond the scope of this work, but OSSO alone cannot provide the required sulphur sink, and other mechanisms must be considered.

Increased uptake of SO_2 into the cloud droplets has been proposed if the droplets are somehow buffered or decreased below the saturation ratio of SO_2. Rimmer et al. (2021) proposed the inclusion of hydroxide salts in the cloud droplets as a potential buffering method. An alternative could be iron ions, which could increase uptake of sulphur by, for example, formation of ferric sulphate in the middle and lower clouds, permitting additional SO_2 uptake into the droplets. The role of heterogeneous chemistry on the surface of the droplets and reactions within the bulk must be considered, and further study is necessary to explore these possibilities.

In addition to the potential increase in SO_2 uptake, the inclusion of $FeCl_3$ particles in the cloud droplets has been proposed to solve other open questions regarding Venus, such as the refractive indices measured from glory patterns observed near opposition (Markiewicz et al., 2014; Petrova, 2018; Petrova et al., 2015) if it is also present in the mode 2 particles. This could be achieved if chloride-containing MSPs act as CCN – as proposed by Knollenberg and Hunten (1980) – providing either refractive inclusions (undissolved MSPs) or an absorbing homogeneous liquid (ferric chloride ions), the two possibilities proposed for the cause of the glory measurements by Petrova (2018), or a mixture of the two if some components of the MSPs do not dissolve.

6.2 Future work

The study of the Venusian atmosphere is best carried out through a combination of laboratory measurements, modelling work, and observations. Future work based in the findings of this study in each of those three areas is outlined here.

6.2.1 Laboratory work

6.2.1.1 Iron chemistry

Initial measurements of the $FeCl_3 + H_2SO_4$ reaction reveal a highly complex system. The reaction is clearly affected by the concentrations of the reagents, and in particular by the chloride concentration in the solution. In this work, the chloride concentration has been varied by the addition of HCl. However, the concentrations added clearly exceeded the saturation of the solution, leading to visible escape of gas (presumably HCl) from the samples. As such, the HCl concentration and therefore the total Cl concentration in the solutions, could not be reliably ascertained throughout the course of an experiment. If the HCl concentration in the headspace above the sample could be measured, the HCl concentration within the liquid phase could be calculated. This technique was not possible with the equipment available for this study, but would provide a better understanding of the concentration of chloride in the solution. As the chloride

concentration seems likely to be the rate-limiting factor in the reaction, its study is vital for more robust estimates of the instantaneous $FeCl_3$ concentration in the cloud droplets in the Venusian atmosphere.

In addition, the identification of the species formed during the reaction would be beneficial in understanding the observed behaviour. In this work, ferric chloride ions are assumed to form ferric sulphate completely – that is to say, that no intermediate iron-chloride-sulphate complexes are formed. This seems unlikely, and may account for the uncertainties in the concentrations produced by the fitting algorithm (Chapter 4). The combination of multiple spectroscopy techniques, such as Raman or infrared spectroscopy simultaneously with UV-Vis spectroscopy, may be able to identify intermediate species formed during the reaction, or otherwise help constrain the rate of reaction and decrease the uncertainties in concentration and rate reported in Chapter 4.

Finally, comparison of this work with that of Jiang et al. (2024) shows clear differences: they report the formation of copiapite, rhomboclase and acid ferric sulphate from ferric chloride, but no further reaction is observed in this work after ferric sulphate ions form, even after months. The reason for this difference is unclear, but is likely due to the low concentrations of $FeCl_3$ used (i.e., the minerals form in undetectably low concentrations and do not sediment out of solution) or the high concentrations of chlorides in this study, which may be preventing the formation of the minerals. Further study of the iron-sulphur-chlorine system is clearly required to better understand the chemistry and formation of the different species.

6.2.1.2 OSSO measurements

While calculations of OSSO absorbance spectra have been reported (this work; Frandsen et al., 2020; Frandsen et al., 2016, see Figure 3.2), experimental measurements are scarce. Wu et al. (2018) measured spectra they identified as the OSSO isomers (combined with other species), but their reported spectra, made in a matrix isolation experiment, are very different from the predicted spectra. While some differences are to be expected (as seen, for example, with the measured and calculated $FeCl_3$ spectra presented in Figure 5.17), the absorption spectra reported by Wu et al. show significant differences, including strong absorption at wavelengths far too long to be consistent with the Venusian unknown UV absorber (Figure 3.2). Two possibilities for this discrepancy exist: the spectra measured by Wu et al. are not of the OSSO isomers, as they reported, but for other products formed during the reaction; or the measured spectra are of OSSO, and the calculated spectra are unreliable, meaning that the OSSO absorption spectrum is inconsistent with the Venusian absorber. To distinguish these two cases, experimental measurements of gas phase OSSO are required. These measurements are challenging due to the short lifetime of both OSSO and the SO it is produced from under achievable laboratory conditions, but gas-phase measurements are the only way to remove the uncertainty associated with the matrix isolation method used by Wu et al.

However, while the accurate quantification of OSSO absorption spectra is necessary for atmospheric modelling – OSSO will be produced in the Venusian atmosphere by the known sulphur chemistry that takes place there – it is extremely unlikely that the "true" absorption spectrum of the isomers would be sufficiently strong to overcome the two to three orders-of-magnitude discrepancy in the current modelled OSSO concentrations. Therefore, no matter what the absorption spectrum of OSSO is measured to be, it does not seem to be a viable candidate for the unknown UV absorber.

6.2.2 Modelling work

The chemistry and microphysics in the clouds of Venus are clearly areas in need of further study. The current PCM cloud model is simplistic, with mass ratios of the different cloud modes prescribed and the system forced to be in equilibrium at all times, with no sub- or super-saturation of condensing gases (limited to H_2O and H_2SO_4) permitted. Development of a more sophisticated cloud model, taking account of the non-equilibrium conditions that could occur in the clouds, and modelling the condensation, evaporation, and settling of the cloud droplets and their coagulation with other droplets or MSPs, would allow for more robust study of the cloud system. The uptake of MSPs (and $FeCl_3$ specifically) into the cloud droplets could then be comprehensively modelled to more directly predict the $FeCl_3$ absorbance that can be provided by meteoric ablation. The rates of uptake of $FeCl_3$ into the cloud droplets and of the growth and settling of cloud particles would provide an estimate of the lifetime of iron in the atmosphere to improve the estimated iron flux that would be required to maintain the observed absorption.

Within the droplets, complex chemistry is expected between the meteoric iron (and other metals), sulphur, and chlorine, as well as any other gases that may interact with the droplets. Some degree of modelling will therefore be required (in addition to laboratory measurements) to fully understand the system. If the rate of reaction of the $FeCl_3$ in sulphuric acid can be reliably measured, the reaction in the cloud droplets will further constrain the required $FeCl_3$ concentration in the atmosphere to explain the absorption. Furthermore, the addition of liquid phase chemistry to atmospheric models would provide a means to test SO_2 uptake into droplets as an additional SO_2 sink through the clouds.

6.2.3 Missions and observations

Variations have been seen in the observed NUV absorption by different spacecraft-based instruments and ground-based observations over decades (Lee et al., 2022; Pérez-Hoyos et al., 2018; Pollack et al., 1980, Figures 1.2 and 1.31). However, the available spectra were measured many years apart by different instruments, so the effects of variation between different spectrometers cannot be separated out from the short- or long-term variability of the shape of the absorption. A period of sustained observation by a single spectrometer would allow the change in shape over time to be studied reliably. If the variation in shape can be quantified, the cause can

be considered: it may be either the same species which varies in location, or a combination of different species which vary in ratio.

This may be measurable with the low resolution channel of the VenSpec-U instrument on the proposed upcoming ESA EnVision mission (Lustrement et al., 2024). The low-resolution channel of the UV spectrometer (spectral range 190 – 380 nm) will only be sensitive to the shorter wavelengths of the absorption, but may provide the best available continuous spectral dataset over time for the study of the variation of the unknown UV absorber.

A. Iron chemistry predictions – J.M.C.Plane

A1 Iron chemistry in the Venus PCM

A list of all iron chemistry added to the Venus PCM in this work can be found in Table 5.1. Many reactions in the table have been included in previous models (see Table 5.1 footnotes). Novel reactions, which have not been included previously in models of Fe in the upper atmospheres of Earth (Feng et al., 2013) or Mars (Whalley & Plane, 2010), are identified with footnote 5 in Table 5.1. The calculation of these rate constants is detailed below.

A1.1 Additional reactions of Fe species included in the Venus PCM

The reaction enthalpies of the new chemistry reactions were calculated at the complete basis set CBS-QB3 level of theory (Montgomery et al., 2000) within the Gaussian 16 suite of programs (Frisch et al., 2016), and are listed in Table A.1. Table A.2 contains the molecular parameters (geometry co-ordinates, rotational constants and vibrational frequencies) of the reactants and products, calculated at the B3LYP/6-311+g(2d,p) level of theory (Frisch et al., 2016). The molecular geometries are illustrated in Figures A.1 and A.2.

Table A.1. Reaction enthalpies (at 0 K) for the additional reactions of Fe species predicted in this work that are included in the Venus PCM. The reader is referred to Table 5.1 (page 200) for a full list of reactions and references.

No.	Reaction	ΔH_r^o (0 K) / kJ mol^{-1}
7	$FeO_2 + CO_2$ (+M) $\rightarrow OFeCO_3$	-71.9
8	$OFeCO_3 + O \rightarrow FeCO_3 + O_2$	-111.1
9	$FeCO_3 + CO_2$ (+M) $\rightarrow FeCO_3.CO_2$	-111.4
10	$FeCO_3.CO_2 + O \rightarrow OFeCO_3 + CO_2$	-274.8
11	$FeCO_3.CO_2$ (+M) $\rightarrow FeCO_3 + CO_2$	+111.4
12	$FeCO_3 + HCl \rightarrow HOFeCl + CO_2$	-332.8
13	$FeCO_3.CO_2 + HCl \rightarrow HOFeCl + 2CO_2$	-221.5
14	$HOFeCl + HCl \rightarrow FeCl_2 + H_2O$	-71.8
15	$FeCO_3 + Cl \rightarrow OFeCl + CO_2$	-330.4
16	$FeCO_3.CO_2 + Cl \rightarrow OFeCl + 2CO_2$	-219.0
17	$OFeCl + Cl \rightarrow FeCl_2 + O$	-20.0
18	$FeCl_2$-$H_2O + Cl \rightarrow FeCl_3 + H_2O$	-141.8
19	$FeCl_2 + H_2O$ (+ M) $\rightarrow FeCl_2.H_2O$	-79.5
20	$FeCl_3 + CO_2$ (+M) $\rightarrow FeCl_3.CO_2$	-42.3
21	$FeCl_3.CO_2$ (+M) $\rightarrow FeCl_3 + CO_2$	+42.3
33	$FeO^+ + CO_2$ (+M) $\rightarrow FeO^+.CO_2$	-126.3
35	$Fe^+.CO_2 + CO_2$ (+M) $\rightarrow Fe^+.(CO_2)_2$	-49.8
36	$Fe^+.CO_2 + O \rightarrow FeO^+ + CO_2$	-270.8
37	$Fe^+.(CO_2)_2 + O \rightarrow FeO^+.CO_2 + CO_2$	-347.3
38	$FeO^+.CO_2 + CO_2$ (+M) $\rightarrow FeO^+.(CO_2)_2$	-78.7
39a	$FeO^+.CO_2 + O \rightarrow FeO_2^+ + CO_2$	-134.1
39b	$FeO^+.CO_2 + O \rightarrow Fe^+.CO_2 + O_2$	-100.0

The neutral bimolecular reactions 8, 10, and 12 – 18 are significantly exothermic and do not have raised barriers on their potential energy surfaces. These reactions were therefore assigned a typical capture rate coefficient with a small temperature dependence (Smith, 1980). The ion-molecule reactions 36 and 37 were assigned somewhat higher capture rate coefficients with no temperature dependence, consistent with Langevin theory (Smith, 1980).

Reactions 7, 9, 19, 20, 33, 35 and 38 are recombination reactions. Their rate coefficients were estimated using electronic structure theory within the Gaussian 16 suite of programs (Frisch et al., 2016) to determine reaction energies and molecular parameters, combined with RRKM theory using the MESMER program (Glowacki et al., 2012). MESMER assumes that the reaction initially forms an excited adduct, which can either dissociate back to the reactants or be stabilized by collision with the third body, into any minimum on the potential energy surface. The internal energy of the adduct was divided into a contiguous set of grains (width typically 40 cm^{-1}). Each grain, which contains a bundle of rovibrational states, is then assigned a set of microcanonical rate coefficients for dissociation back to the reactants. In this study these microcanonical rate coefficients were linked by inverse Laplace transformation to the high-pressure limiting recombination coefficients, set to the capture rate determined using long-range transition state theory (Georgievskii & Klippenstein, 2005). The rovibrational densities of states were calculated from the molecular parameters in Table A.2.

The exponential-down model (Gilbert & Smith, 1990) was used to estimate the probability of collisional transfer between grains. The average energy for downward transitions $\langle \Delta E \rangle_{down}$ was set to 300 cm^{-1} for N_2 at 300 K, with no temperature dependence. The resulting temperature-dependent rate coefficients were then multiplied by a factor of 2.5 to account for the increased efficiency of CO_2 (the major component of the Venusian atmosphere), compared with N_2 (Gilbert & Smith, 1990). The rate coefficients for the thermal dissociation of $FeCO_3.CO_2$ and $FeCl_3.CO_2$ (reactions 11 and 21), which are weakly bound clusters and hence prone to dissociation at temperatures below 300 K, were then determined by detailed balance. These rate coefficients are listed in Table 5.1.

Table A.2. Molecular properties of the Fe-containing molecules illustrated in Figures A.1 and A.2, calculated at the B3LYP/6-311+g(2d,p) level of theory.

Molecule (spin multiplicity)	**Geometry (Cartesian co-ordinates in Å)** [a]	**Rotational constants (GHz)** [a]	**Vibrational frequencies (cm^{-1})** [a]
Neutral molecules			
FeCl (quartet)	Fe, 0., 0., -0.116 Cl, 0., 0., 2.016	5.1619	406
$FeCl_2$ (quintet)	Fe, 0., 0., 0. Cl, 0., 0., 2.150 Cl, 0., 0., -2.150	1.5632	82 (×2), 344 493

$FeCl_2.H_2O$ (quintet)	Fe, -0.002, 0.123, -0.033 Cl, 2.149, 0.501, 0.022 Cl, -2.152, 0.504, 0.021 O, 0.000, -2.054, -0.201 H, 0.785, -2.532, 0.093 H, -0.781, -2.536, 0.096	5.0752 1.5541 1.1910	68, 91, 94, 187, 291, 318, 330, 444, 535, 1612, 3781, 3886
$FeCl_3$ (sextet)	Fe, 0., 0., 0. Cl, -0.0, 2.147, 0. Cl, 1.859, -1.073, 0. Cl, -1.859, -1.073, 0.	2.0887 2.0887 1.0443	89, 102 (×2), 356, 457 (×2)
$FeCl_3.CO_2$ (sextet)	Fe, 0.076, 0.097, 0.047 Cl, -0.124, 0.079, 2.198 Cl, -0.264, 1.962, -0.988 Cl, -0.405, -1.735, -1.013 C, 3.047, -0.867, -0.649 O, 2.325, -0.0857, -0.159 O, 3.776, -1.618, -1.122	1.1371 0.7345 0.6985	16, 36, 90, 90, 106, 117, 132, 178, 353, 435, 443, 654, 662, 1365, 2409
$FeCO_3$ (quintet)	Fe, 0., 0., 1.178 O, 0., 1.110, -0.333 C, 0., 0., -1.134 O, 0., 0., -2.330 O, 0., -1.110, -0.333	12.817 2.7548 2.2674	157, 388, 465, 636, 793, 827, 915, 1024, 1799
$FeCO_3.CO_2$ (quintet)	Fe, 0.235, 0.122 0.007 O, 1.937, 0.997, 0.006 C, 2.521, -0.221, 0.009 O, 3.697, -0.452, 0.010 O, 1.535, -1.174, 0.011 C, -0.296, 3.012, -0.002 O, -0.799, 1.946, 0.001 O, 0.141, 4.069, -0.006	3.3662 1.0016 0.7719	21, 25, 80, 130, 158, 260, 382, 453, 643, 651, 657, 794, 803, 927, 1066, 1353, 1795, 2411
FeO_2 (quintet)	Fe, 0.005, 0., 0.003 O, -0.001, 0., 1.611 O, 1.430, 0., -0.739	35.974 8.3452 6.7738	289, 919, 960
HOFeCl (quintet)	Fe, 0.014, 0.007, -0.212 Cl, 0.036, 0.020, 1.949 O, -0.055, -0.030, -1.993 H, 0.542, 0.299, -2.667	1105.8 2.5042 2.4986	105, 107, 395, 446, 718,3908

$OFeCO_3$ (quintet)	Fe, 0.742, -0.283, -0.003 O, -0.605, 1.002, -0.003 C, -1.541, 0.040, 0.001 O, -2.723, 0.140, 0.003 O, -0.842, -1.153, 0.002 O, 2.227, -0.940, -0.004	12.839 1.7797 1.5631	66, 90, 179, 400, 453, 638, 741, 788, 905, 955, 1045, 1832
OFeCl (sextet)	Fe, -0.0, 0.465, 0. O, 0.001, 2.118, 0. Cl, -0.001, -1.709, 0.	2.7157	44 (×2), 401, 882
Ionized molecules			
FeO^+ (sextet)	Fe, 0., 0., 0.084 O, 0., 0., 1.725	15.0963	830
FeO_2^+ (sextet)	O, 1.778, 0.255, 0. O, 1.767, -1.069, 0. Fe, -0.037, -0.393, 0.	36.004 7.5765 6.2593	400, 451, 1165
$FeO^+.CO_2$ (sextet)	Fe, 1.022, 0.0, 0.0 O, 2.661, -0.001, 0.0 C, -2.191, 0.002, 0.0 O, -1.009, 0.001, 0.0 O, -3.328, 0.002, 0.0	1.1955	42 (×2), 101 (×2), 265, 628 (×2), 854, 1382, 2449
$Fe^+.CO_2$ (sextet)	Fe, 0.054, -1.638, 0.002 O, 1.470, 0.001, -0.001 C, 2.398, 0.733, 0.0 O, 3.291, 1.441, 0.0	895.52 1.6097 1.6068	38, 196, 636, 637, 1357, 2424
$Fe^+.(CO_2)_2$ (sextet)	Fe, -0.006, -1.436, 0.001 O, 1.467, 0.258, 0.001 C, 2.557, 0.706, -0.0 O, 3.612, 1.145, -0.001 O, -1.496, 0.236, 0.005 O, -3.651, 1.101, -0.003 C, -2.591, 0.672, 0.001	3.0364 0.7759 0.6180	30, 34, 44, 59, 90, 133, 190, 643, 644, 645, 647, 1352, 1359, 2390, 2426

$FeO^{+}.(CO_2)_2$ (sextet)	Fe, -0.164, -0.157, -0.239 O, -0.173, -0.060, 1.410 C, 2.613, 0.207, -1.792 O, 1.469, 0.034, -1.550 O, 3.712, 0.371, -2.045 C, -3.023, -0.714, -1.553 O, -4.138, -0.908, -1.691 O, -1.865, -0.512, -1.432	3.0486 0.6359 0.5261	22, 24, 33, 67, 91, 95, 108, 236, 248, 640, 641, 644, 646, 842, 1362, 1365, 2422, 2436

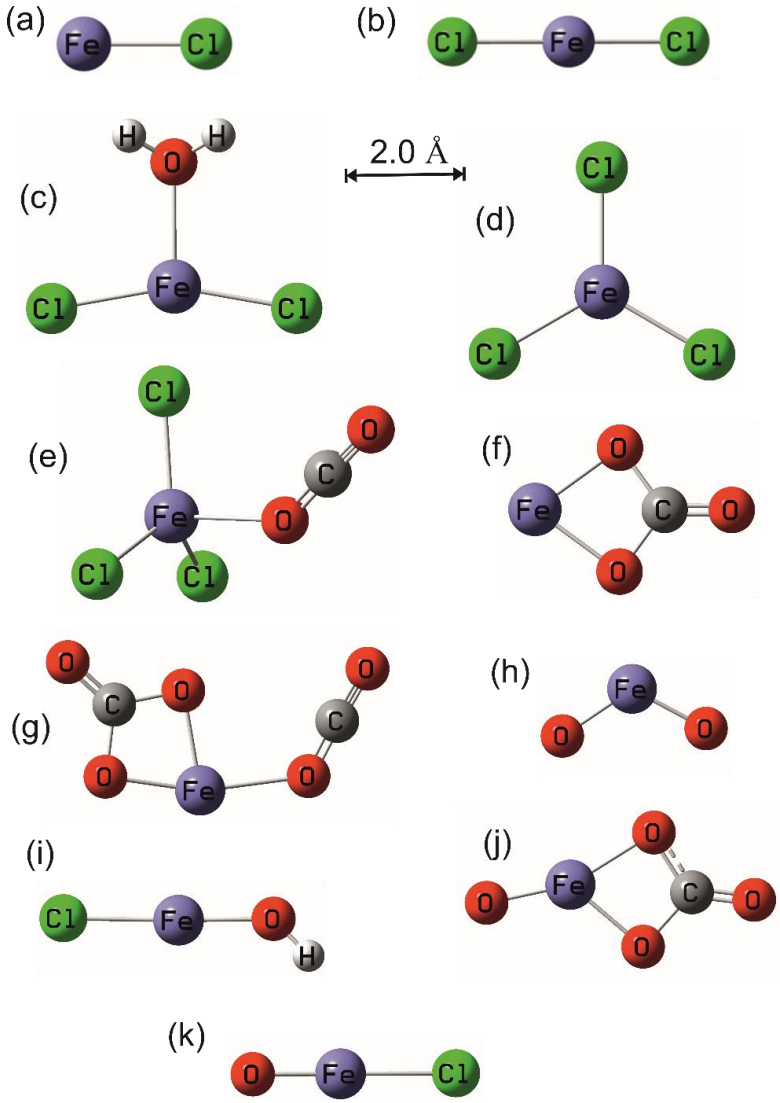

Figure A.1. Molecular geometries calculated at the b3lyp/6-311+g(2d,p) level of theory: (a) FeCl; (b) $FeCl_2$; (c) $FeCl_2.H_2O$; (d) $FeCl_3$; (e) $FeCl_3.CO_2$; (f) $FeCO_3$; (g) $FeCO_3.CO_2$; (h) FeO_2; (i) HOFeCl; (j) $OFeCO_3$; (k) OFeCl.

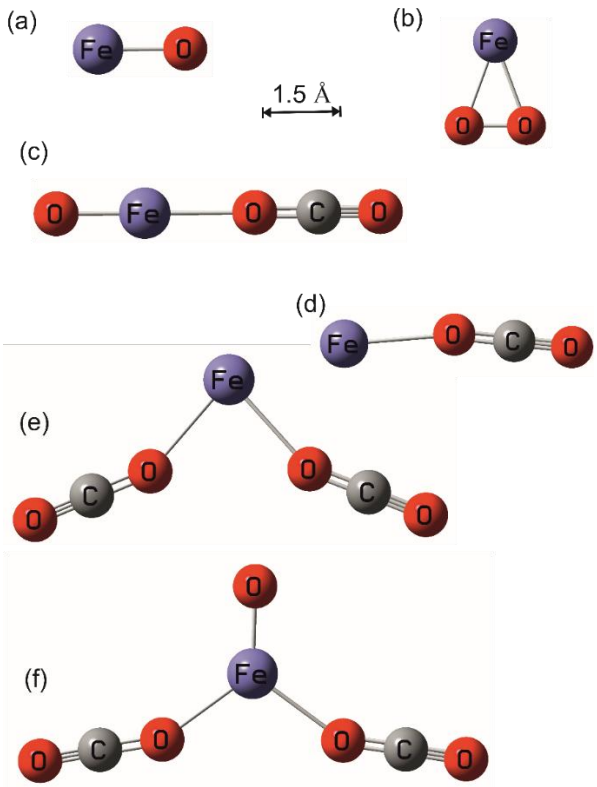

Figure A.2. Molecular geometries calculated at the b3lyp/6-311+g(2d,p) level of theory: (a) FeO^+; (b) FeO_2^+; (c) $FeO^+.CO_2$; (d) $Fe^+.CO_2$; (e) $Fe^+.(CO_2)_2$; (f) $FeO^+.(CO_2)_2$

A1.2 Photochemical reactions

The absorption cross-section of each molecule was calculated for its first 30 excited states, using Time-Dependent Density Functional Theory (Scalmani et al., 2006) with the 6-311+g(2d,p) basis set from the Gaussian 16 suite of programs (Frisch et al., 2016). The resulting cross-sections are illustrated in Figure A.3 (see Figure 5.3 for the cross-sections of $FeCl_3$ and $FeCl_3.CO_2$). The cross-section was then convolved with the solar actinic flux taken from the semi-empirical SOLAR2000 model (Tobiska et al., 2000) (averaged over a solar cycle), and adjusted to the orbit of Venus. The photodissociation threshold was set to be the wavelength corresponding to the lowest energy dissociation pathway: FeCl (340 nm); $FeCl_2$ (257 nm); and $FeCl_3$ (379 nm). For $FeCO_3.CO_2$, $FeCl_3.CO_2$ and $OFeCO_3$, these thresholds are beyond 1000 nm.

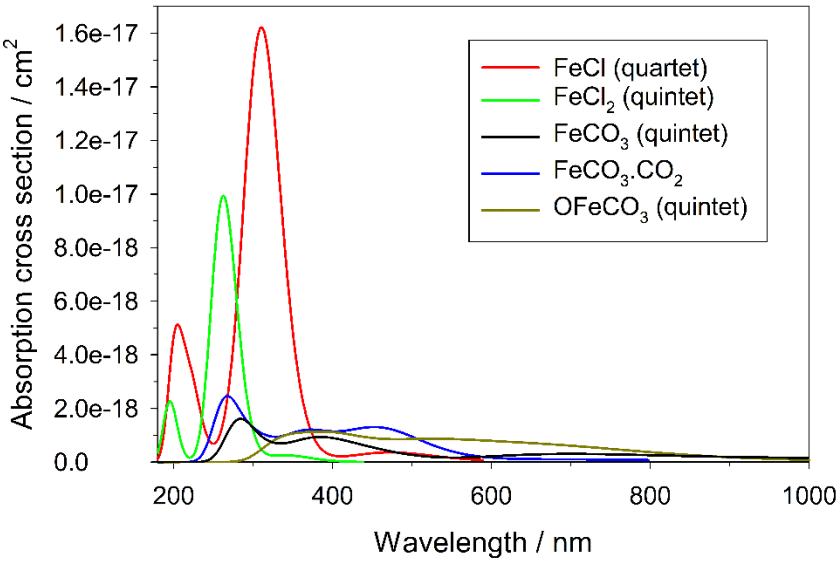

Figure A.3. Absorption cross-sections of FeCl, $FeCl_2$, $FeCO_3$, $FeCO_3.CO_2$ and $OFeCO_3$, calculated using Time-Dependent Density Functional Theory with the 6-311+g(2d,p) basis set.

References

Allen, D. A., & Crawford, J. W. (1984). Cloud structure on the dark side of Venus. *Nature, 307*(5948), 222-224. http://doi.org/10.1038/307222a0

Ando, H., Imamura, T., Tellmann, S., Pätzold, M., Häusler, B., Sugimoto, N., et al. (2020). Thermal structure of the Venusian atmosphere from the sub-cloud region to the mesosphere as observed by radio occultation. *Scientific Reports, 10*(1), 3448. https://doi.org/10.1038/s41598-020-59278-8

Aoshima, H., Satoh, K., Umemura, T., & Kamigaito, M. (2013). A simple combination of higher-oxidation-state FeX_3 and phosphine or amine ligand for living radical polymerization of styrene, methacrylate, and acrylate. *Polymer Chemistry, 4*(12), 3554-3562. http://doi.org/10.1039/C3PY00352C

Avduevsky, V. S., Marov, M. Y., & Rozhdestvensky, M. K. (1970). Preliminary results of measurements by space probes Venera 5 and Venera 6 in the atmosphere of Venus—summary. *Radio Science, 5*(2), 333-337. https://doi.org/10.1029/RS005i002p00333

Avduevsky, V. S., Marov, M. Y., Rozhdestvensky, M. K., Borodin, N. F., & Kerzhanovich, V. V. (1971). Soft landing of Venera 7 on the Venus surface and preliminary results of investigations of the Venus atmosphere. *Journal of the Atmospheric Sciences, 28*(2), 263-269. http://doi.org/10.1175/1520-0469(1971)028%3C0263:Slovot%3E2.0.Co;2

Barnes, E. C., Petersson, G. A., Montgomery, J. A., Frisch, M. J., & Martin, J. M. L. (2009). Unrestricted coupled cluster and Brueckner doubles variations of W1 theory. *Journal of Chemical Theory and Computation, 5*(10), 2687-2693. https://doi.org/10.1021/ct900260g

Belton, M. J. S., Gierasch, P. J., Smith, M. D., Helfenstein, P., Schinder, P. J., Pollack, J. B., et al. (1991). Images from Galileo of the Venus cloud deck. *Science, 253*(5027), 1531-1536. http://doi.org/10.1126/science.253.5027.1531

Belyaev, D. A., Montmessin, F., Bertaux, J.-L., Mahieux, A., Fedorova, A. A., Korablev, O. I., et al. (2012). Vertical profiling of SO_2 and SO above Venus' clouds by SPICAV/SOIR solar occultations. *Icarus, 217*(2), 740-751. https://doi.org/10.1016/j.icarus.2011.09.025

Bertaux, J.-L., Vandaele, A.-C., Korablev, O., Villard, E., Fedorova, A., Fussen, D., et al. (2007). A warm layer in Venus' cryosphere and high-altitude measurements of HF, HCl, H_2O and HDO. *Nature, 450*(7170), 646-649. https://doi.org/10.1038/nature05974

Bertaux, J.-L., Widemann, T., Hauchecorne, A., Moroz, V. I., & Ekonomov, A. P. (1996). VEGA 1 and VEGA 2 entry probes: An investigation of local UV absorption (220 – 400 nm) in the atmosphere of Venus (SO_2 aerosols, cloud structure). *Journal of Geophysical Research: Planets, 101*(E5), 12709-12745. https://doi.org/10.1029/96JE00466

Bézard, B., Bergh, C., Fegley, B., Maillard, J.-P., Crisp, D., Owen, T., et al. (1993). The abundance of sulfur dioxide below the clouds of Venus. *Geophysical Research Letters, 20*. https://doi.org/10.1029/93GL01338

Bézard, B., de Bergh, C., Crisp, D., & Maillard, J.-P. (1990). The deep atmosphere of Venus revealed by high-resolution nightside spectra. *Nature, 345*(6275), 508-511. https://doi.org/10.1038/345508a0

Bierson, C. J., & Zhang, X. (2020). Chemical cycling in the Venusian atmosphere: a full photochemical model from the surface to 110 km. *Journal of Geophysical Research: Planets, 125*(7), e2019JE006159. https://doi.org/10.1029/2019JE006159

Bjoraker, G., Larson, H., Mumma, M., Timmermann, R., & Montani, J. (1992). Airborne observations of the gas composition of Venus above the cloud tops: measurements of H_2O, HDO, HF, and the D/H and $^{18}O/^{16}O$ isotopic ratios. *Bull. Am. Astron. Soc., 24*, 995. Retrieved from https://ui.adsabs.harvard.edu/abs/1992DPS....24.3004B

Blamont, J., & Ragent, B. (1979). Further results of the Pioneer Venus nephelometer experiment. *Science, 205*(4401), 67-70. http://doi.org/10.1126/science.205.4401.67

Bones, D. L., Plane, J. M. C., & Feng, W. (2016). Dissociative recombination of FeO^+ with electrons: implications for plasma layers in the ionosphere. *J. Phys. Chem. A, 120*(9), 1369-1376. https://doi.org/10.1021/acs.jpca.5b04947

Boyer, C. (1973). The 4-day rotation of the upper atmosphere of venus. *Planetary and Space Science, 21*(9), 1559-1561. https://doi.org/10.1016/0032-0633(73)90062-7

Brooke, J. S. A., Feng, W., Carrillo-Sánchez, J. D., Mann, G. W., James, A. D., Bardeen, C. G., et al. (2017). Meteoric smoke deposition in the polar regions: a comparison of measurements with global atmospheric models. *Journal of Geophysical Research: Atmospheres, 122*(20), 11,112-111,130. https://doi.org/10.1002/2017JD027143

Burkholder, J. B., Sander, S. P., Abbatt, J., Barker, J. R., Cappa, C., Crounse, J. D., et al. (2019). *Chemical kinetics and photochemical data for use in atmospheric studies, evaluation no. 19*. Pasadena: Jet Propulsion Laboratory.

Carrillo-Sánchez, J. D., Gómez-Martín, J. C., Bones, D. L., Nesvorný, D., Pokorný, P., Benna, M., et al. (2020). Cosmic dust fluxes in the atmospheres of Earth, Mars, and Venus. *Icarus, 335*, 113395. https://doi.org/10.1016/j.icarus.2019.113395

Chase, M. W., Davies, C. A., Downey, J. R., Frurip, D. J., McDonald, R. A., & Syverud, A. N. (1985). *NIST-JANAF thermochemical tables version 1.0*. Gaithersburg, MD: National Institute of Standards and Technology.

Cohen, M., Holmes, J., Lewis, S., & Patel, M. (2024). Planetary waves drive horizontal variations in trace species in the Venus deep atmosphere. *The Planetary Science Journal, 5*(10), 219. https://doi.org/10.3847/PSJ/ad76a8

Colin, L. (1979). Encounter with Venus: an update. *Science, 205*(4401), 44-46. http://doi.org/10.1126/science.205.4401.44

Collinson, G. A., Ramstad, R., Glocer, A., Wilson III, L., & Brosius, A. (2021). Depleted plasma densities in the ionosphere of Venus near solar minimum from Parker Solar Probe observations of upper hybrid resonance emission. *Geophysical Research Letters, 48*(9), e2020GL092243. https://doi.org/10.1029/2020GL092243

Connes, P., Connes, J., Kaplan, L. D., & Benedict, W. S. (1968). Carbon monoxide in the Venus atmosphere. *Astrophysical Journal, 152*, 731-743. https://doi.org/10.1086/149590

Cottini, V., Ignatiev, N. I., Piccioni, G., Drossart, P., Grassi, D., & Markiewicz, W. J. (2012). Water vapor near the cloud tops of Venus from Venus Express/VIRTIS dayside data. *Icarus, 217*(2), 561-569. https://doi.org/10.1016/j.icarus.2011.06.018

Counselman, C. C., Gourevitch, S. A., King, R. W., Loriot, G. B., & Ginsberg, E. S. (1980). Zonal and meridional circulation of the lower atmosphere of Venus determined by radio interferometry. *Journal of Geophysical Research: Space Physics, 85*(A13), 8026-8030. https://doi.org/10.1029/JA085iA13p08026

Counselman, C. C., Gourevitch, S. A., King, R. W., Loriot, G. B., & Prinn, R. G. (1979). Venus winds are zonal and retrograde below the clouds. *Science, 205*(4401), 85-87. https://doi.org/10.1126/science.205.4401.85

Crismani, M. M. J., Deighan, J., Schneider, N. M., Plane, J. M. C., Withers, P., Halekas, J., et al. (2019). Localized ionization hypothesis for transient ionospheric layers. *Journal of Geophysical Research: Space Physics, 124*(6), 4870-4880. https://doi.org/10.1029/2018JA026251

Crismani, M. M. J., Schneider, N. M., Plane, J. M. C., Evans, J. S., Jain, S. K., Chaffin, M. S., et al. (2017). Detection of a persistent meteoric metal layer in the Martian atmosphere. *Nature Geoscience, 10*(6), 401-404. https://doi.org/10.1038/ngeo2958

Crisp, D. (1986). Radiative forcing of the Venus mesosphere: I. Solar fluxes and heating rates. *Icarus, 67*(3), 484-514. https://doi.org/10.1016/0019-1035(86)90126-0

Crisp, D., Allen, D. A., Grinspoon, D. H., & Pollack, J. B. (1991). The dark side of Venus: near-infrared images and spectra from the Anglo-Australian Observatory. *Science, 253*(5025), 1263-1266. https://doi.org/10.1126/science.11538493

Crisp, D., & Young, A. T. (1978). Vertical extent of zonal winds on Venus. *Icarus, 35*(2), 182-188. https://doi.org/10.1016/0019-1035(78)90003-9

Davies, M. E., Abalakin, V. K., Cross, C. A., Duncombe, R. L., Masursky, H., Morando, B., et al. (1980). Report of the IAU Working Group on cartographic coordinates and rotational elements of the planets and satellites. *Celestial mechanics, 22*(3), 205-230. https://doi.org/10.1007/BF01229508

de Bergh, C., Bézard, B., Owen, T., Crisp, D., Maillard, J.-P., & Lutz, B. L. (1991). Deuterium on Venus: observations from Earth. *Science, 251*(4993), 547-549. https://doi.org/10.1126/science.251.4993.547

Donahue, T. M. (1979). Pioneer Venus results: an overview. *Science, 205*(4401), 41-44. https://doi.org/10.1126/science.205.4401.41

Donahue, T. M., Hoffman, J. H., Hodges, R. R., & Watson, A. J. (1982). Venus was wet: a measurement of the ratio of deuterium to hydrogen. *Science, 216*(4546), 630-633. https://doi.org/10.1126/science.216.4546.630

Drossart, P., Bézard, B., Encrenaz, T., Lellouch, E., Roos, M., Taylor, F. W., et al. (1993). Search for spatial variations of the H_2O abundance in the lower atmosphere of Venus from NIMS-Galileo. *Planetary and Space Science, 41*(7), 495-504. https://doi.org/10.1016/0032-0633(93)90032-W

Dunne, J. A., & Burgess, E. (1978). Best seen in black light. In *The voyage of Mariner 10 : mission to Venus and Mercury* (Vol. 424).

Edwards, J. M., & Slingo, A. (1996). Studies with a flexible new radiation code. I: Choosing a configuration for a large-scale model. *Quarterly Journal of the Royal Meteorological Society, 122*(531), 689-719. https://doi.org/10.1002/qj.49712253107

Ekonomov, A. P., Golovin, Y. M., & Moshkin, B. E. (1980). Visible radiation observed near the surface of Venus: Results and their interpretation. *Icarus, 41*(1), 65-75. https://doi.org/10.1016/0019-1035(80)90159-1

Ekonomov, A. P., Moroz, V. I., Moshkin, B. E., Gnedykh, V. I., Golovin, Y. M., & Crigoryev, A. V. (1984). Scattered UV solar radiation within the clouds of Venus. *Nature, 307*(5949), 345-347. https://doi.org/10.1038/307345a0

Encrenaz, T., Greathouse, T. K., Roe, H., Richter, M., Lacy, J., Bézard, B., et al. (2012). HDO and SO_2 thermal mapping on Venus: evidence for strong SO_2 variability. *Astronomy & Astrophysics, 543*, A153. https://doi.org/10.1051/0004-6361/201219419

ESA. (2014a, 1 September 2019). Major discoveries by Venus Express: 2006-2014: 1. Shape-shifting polar vorticies. Retrieved from https://sci.esa.int/s/8J4qpKw

ESA. (2014b, 1 September 2019). Major discoveries by Venus Express: 2006-2014: 4. Super-rotation is speeding up. Retrieved from https://sci.esa.int/s/AM9KzXA

ESA. (2018, 09/10/2018). BepiColombo Venus flyby science. Retrieved from https://www.esa.int/ESA_Multimedia/Images/2018/10/BepiColombo_Venus_flyby_science

ESA. (2019, 1st September 2019). Venus. Retrieved from https://sci.esa.int/s/wNVr6jw

ESA. (2020a, 30 March 2020). BepiColombo fact sheet. Retrieved from https://sci.esa.int/s/WLZPlbA

ESA. (2020b, 12th February 2020). Solar Orbiter summary. Retrieved from https://sci.esa.int/s/W3gmGyW

ESA. (2022). Solar Orbiter perihelia and flybys. Retrieved from https://www.esa.int/Science_Exploration/Space_Science/Solar_Orbiter/Solar_Orbiter_perihelia_and_flybys

ESA/MPS/DLR/IDA. (2008). Venus, as seen by Venus Express on 24 July 2007. Retrieved from https://www.esa.int/ESA_Multimedia/Search?SearchText=ultraviolet+venus+express&result_type=images

Esposito, L. W., Knollenberg, R. G., Marov, M. Y., Toon, O. B., & Turco, R. P. (1983). The clouds and hazes of Venus. In *Venus* (pp. 484).

Esposito, L. W., Winick, J. R., & Stewart, A. I. (1979). Sulfur dioxide in the Venus atmosphere: distribution and implications. *Geophysical Research Letters, 6*(7), 601-604. https://doi.org/10.1029/GL006i007p00601

Eymet, V., Fournier, R., Dufresne, J.-L., Lebonnois, S., Hourdin, F., & Bullock, M. A. (2009). Net exchange parameterization of thermal infrared radiative transfer in Venus' atmosphere. *Journal of Geophysical Research: Planets, 114*(E11). https://doi.org/10.1029/2008JE003276

Fedorova, A., Korablev, O., Vandaele, A.-C., Bertaux, J.-L., Belyaev, D., Mahieux, A., et al. (2008). HDO and H_2O vertical distributions and isotopic ratio in the Venus mesosphere by Solar Occultation at InfraRed spectrometer on board Venus Express. *Journal of Geophysical Research: Planets, 113*(E5). https://doi.org/10.1029/2008JE003146

Feng, W., Marsh, D. R., Chipperfield, M. P., Janches, D., Hoeffner, J., Yi, F., & Plane, J. M. C. (2013). A global atmospheric model of meteoric iron. *J. Geophys. Res., 118*(16), 9456-9474. https://doi.org/10.1002/jgrd.50708

Francés-Monerris, A., Carmona-García, J., Trabelsi, T., Saiz-Lopez, A., Lyons, J. R., Francisco, J. S., & Roca-Sanjuán, D. (2022). Photochemical and thermochemical pathways to S_2 and polysulfur formation in the atmosphere of Venus. *Nature Communications, 13*(1), art. no.: 4425. https://doi.org/10.1038/s41467-022-32170-x

Frandsen, B. N., Farahani, S., Vogt, E., Lane, J. R., & Kjaergaard, H. G. (2020). Spectroscopy of OSSO and other sulfur compounds thought to be present in the Venus atmosphere. *The Journal of Physical Chemistry A, 124*(35), 7047-7059. https://doi.org/10.1021/acs.jpca.0c04388

Frandsen, B. N., Wennberg, P. O., & Kjaergaard, H. G. (2016). Identification of OSSO as a near-UV absorber in the Venusian atmosphere. *Geophysical Research Letters, 43*(21), 11,146-111,155. https://doi.org/10.1002/2016GL070916

Frankland, V. L., James, A. D., Carrillo-Sánchez, J. D., Nesvorný, D., Pokorný, P., & Plane, J. M. C. (2017). CO oxidation and O_2 removal on meteoric material in Venus' atmosphere. *Icarus, 296*, 150-162. https://doi.org/10.1016/j.icarus.2017.06.005

Frisch, M. J., Trucks, G. W., Schlegel, H. B., Scuseria, G. E., Robb, M. A., Cheeseman, J. R., et al. (2016). Gaussian 16 Rev. C.01. Wallingford, CT: Gaussian Inc. Retrieved from https://gaussian.com/gaussian16/

Fuchs, N. A. (1964). *Mechanics of aerosols*. New York: Pergamon.

Fukuhara, T., Futaguchi, M., Hashimoto, George L., Horinouchi, T., Imamura, T., Iwagaimi, N., et al. (2017). Large stationary gravity wave in the atmosphere of Venus. *Nature Geoscience, 10*(2), 85-88. http://doi.org/10.1038/ngeo2873

Garate-Lopez, I., & Lebonnois, S. (2018). Latitudinal variation of clouds' structure responsible for Venus' cold collar. *Icarus, 314*, 1-11. https://doi.org/10.1016/j.icarus.2018.05.011

Gary, D. E. (2003). Radio astronomy: lecture 3. Retrieved from https://web.njit.edu/~gary/728/Lecture3.html

Gel'man, B. G., Zolotukhin, V. G., Lamonivm, N. I., Levchuk, B. V., Mukhin, L. M., Nenarokov, D. F., et al. (1979). *Analiz khimicheskogo sostava atmosfery venery na AMS Venera-12 gazovym khromatografom*. Retrieved from https://ntrs.nasa.gov/citations/19790017793

George, H., Malaspina, D. M., Goodrich, K., Ma, Y., Ramstad, R., Conner, D., et al. (2023). Non-lightning-generated Whistler waves in near-Venus space. *Geophysical Research Letters, 50*(19), e2023GL105426. https://doi.org/10.1029/2023GL105426

Georgievskii, Y., & Klippenstein, S. J. (2005). Long-range transition state theory. *Journal of Chemical Physics, 122*, art. no. 194103. https://doi.org/10.1063/1.1899603

Giesen, A., Herzler, J., & Roth, P. (2002). High temperature oxidation of iron atoms by CO_2. *Phys. Chem. Chem. Phys., 4*, 3665-3668. https://doi.org/10.1039/B201822E

Gilbert, R. G., & Smith, S. C. (1990). *Theory of unimolecular and recombination reactions*. Oxford: Blackwell.

Gilli, G., Navarro, T., Lebonnois, S., Quirino, D., Silva, V., Stolzenbach, A., et al. (2021). Venus upper atmosphere revealed by a GCM: II. Model validation with temperature and density measurements. *Icarus, 366*, 114432. https://doi.org/10.1016/j.icarus.2021.114432

Glowacki, D. R., Liang, C.-H., Morley, C., Pilling, M. J., & Robertson, S. H. (2012). MESMER: An open-source Master Equation Solver for Multi-Energy well Reactions. *The Journal of Physical Chemistry A, 116*(38), 9545-9560. https://doi.org/10.1021/jp3051033

Goings, J., Caricato, M., Frisch, M. J., & Li, X. (2014). Assessment of low-scaling approximations to the equation of motion coupled-cluster singles and doubles equations. *Journal of Chemical Physics, 141*, art. no.: 164116. https://doi.org/10.1063/1.4898709

Gómez Martín, J. C., Brooke, J. S. A., Feng, W., Höpfner, M., Mills, M. J., & Plane, J. M. C. (2017). Impacts of meteoric sulfur in the Earth's atmosphere. *Journal of Geophysical Research: Atmospheres, 122*(14), 7678-7701. https://doi.org/10.1002/2017JD027218

Goody, R., West, R., Chen, L., & Crisp, D. (1989). The correlated-k method for radiation calculations in nonhomogeneous atmospheres. *Journal of Quantitative Spectroscopy and Radiative Transfer, 42*(6), 539-550. https://doi.org/10.1016/0022-4073(89)90044-7

Gordon, I. E., Rothman, L. S., Hargreaves, R. J., Hashemi, R., Karlovets, E. V., Skinner, F. M., et al. (2022). The HITRAN2020 molecular spectroscopic database. *Journal of Quantitative Spectroscopy and Radiative Transfer, 277*, 107949. https://doi.org/10.1016/j.jqsrt.2021.107949

Grebowsky, J. M., Benna, M., Plane, J. M. C., Collinson, G. A., Mahaffy, P. R., & Jakosky, B. M. (2017). Unique, non-Earthlike, meteoritic ion behavior in upper atmosphere of Mars. *Geophysical Research Letters, 44*(7), 3066-3072. https://doi.org/10.1002/2017GL072635

Gurnett, D. A., Zarka, P., Manning, R., Kurth, W. S., Hospodarsky, G. B., Averkamp, T. F., et al. (2001). Non-detection at Venus of high-frequency radio signals characteristic of terrestrial lightning. *Nature, 409*(6818), 313-315. https://doi.org/10.1038/35053009

Hadid, L. Z., Delcourt, D., Saito, Y., Fränz, M., Yokota, S., Fiethe, B., et al. (2024). BepiColombo observations of cold oxygen and carbon ions in the flank of the induced magnetosphere of Venus. *Nature Astronomy, 8*(6), 716-724. https://doi.org/10.1038/s41550-024-02247-2

Hall, J. S. (1971). Commission 16: physical study of planets and satellites. *Transactions of the International Astronomical Union, 14*(2), 128-130. Retrieved from https://ui.adsabs.harvard.edu/abs/1971IAUTB..14..128H

Hapke, B., & Graham, F. (1989). Spectral properties of condensed phases of disulfur monoxide, polysulfur oxide, and irradiated sulfur. *Icarus, 79*(1), 47-55. https://doi.org/10.1016/0019-1035(89)90107-3

Hapke, B., & Nelson, R. (1975). Evidence for an elemental sulfur component of the clouds from Venus spectrophotometry. *Journal of the Atmospheric Sciences, 32*(6), 1212-1218. http://doi.org/10.1175/1520-0469(1975)032%3C1212:Efaesc%3E2.0.Co;2

Hartle, R. E., & Taylor, H. A. J. (1983). Identification of deuterium ions in the ionosphere of Venus. *Geophysical Research Letters, 10*(10), 965-968. https://doi.org/10.1029/GL010i010p00965

Harvey, B. (2007a). First landfall on Venus, Mars. In J. Mason (Ed.), *Russian Planetary Exploration* (1 ed.). Chichester, UK: Praxis Publishing Ltd.

Harvey, B. (2007b). The high summer of Soviet planetary exploration, 1975 - 1986. In J. Mason (Ed.), *Russian Planetary Exploration* (1 ed.). Chichester, UK: Praxis Publishing Ltd.

Harvey, B. (2007c). OKB Lavochkin. In J. Mason (Ed.), *Russian Planetary Exploration* (1 ed.). Chichester, UK: Praxis Publishing Ltd.

Haus, R., Kappel, D., & Arnold, G. (2014). Atmospheric thermal structure and cloud features in the southern hemisphere of Venus as retrieved from VIRTIS/VEX radiation measurements. *Icarus, 232*, 232-248. https://doi.org/10.1016/j.icarus.2014.01.020

Haus, R., Kappel, D., Tellmann, S., Arnold, G., Piccioni, G., Drossart, P., & Häusler, B. (2016). Radiative energy balance of Venus based on improved models of the middle and lower atmosphere. *Icarus, 272*, 178-205. https://doi.org/10.1016/j.icarus.2016.02.048

Helbert, J., Haus, R., Arnold, G., D'Amore, M., Maturilli, A., Säuberlich, T., & Hiesinger, H. (2023). The second Venus flyby of BepiColombo mission reveals stable atmosphere over decades. *Nature Communications, 14*(1), 8225. https://doi.org/10.1038/s41467-023-43888-7

Helmer, M., & Plane, J. M. C. (1994). Kinetic study of the reaction between Fe and O_3 under mesospheric conditions. *J. Chem. Soc., Faraday Trans., 90*, 31-37 https://doi.org/10.1039/FT9949000031

Hochlaf, M., Linguerri, R., Cheraki, M., Ayari, T., Ben Said, R., Feifel, R., & Chambaud, G. (2021). $S_2O_2^{q+}$ (q = 0, 1, and 2) molecular systems: characterization and atmospheric planetary implications. *The Journal of Physical Chemistry A, 125*(9), 1958-1971. https://doi.org/10.1021/acs.jpca.0c11407

Hoffman, J. H., Hodges, R. R., McElroy, M. B., Donahue, T. M., & Kolpin, M. (1979). Composition and Structure of the Venus Atmosphere: Results from Pioneer Venus. *Science, 205*(4401), 49-52. https://doi.org/10.1126/science.205.4401.49

Horinouchi, T., Hayashi, Y.-Y., Watanabe, S., Yamada, M., Yamazaki, A., Kouyama, T., et al. (2020). How waves and turbulence maintain the super-rotation of Venus' atmosphere. *Science, 368*(6489), 405-409. https://doi.org/10.1126/science.aaz4439

Hübers, H.-W., Richter, H., Graf, U. U., Güsten, R., Klein, B., Stutzki, J., & Wiesemeyer, H. (2023). Direct detection of atomic oxygen on the dayside and nightside of Venus. *Nature Communications, 14*(1), 6812. https://doi.org/10.1038/s41467-023-42389-x

Ignatiev, N. I., Titov, D. V., Piccioni, G., Drossart, P., Markiewicz, W. J., Cottini, V., et al. (2009). Altimetry of the Venus cloud tops from the Venus Express observations. *Journal of Geophysical Research: Planets, 114*(E9). https://doi.org/10.1029/2008JE003320

Imamura, T., Mitchell, J., Lebonnois, S., Kaspi, Y., Showman, A. P., & Korablev, O. (2020). Superrotation in planetary atmospheres. *Space Science Reviews, 216*(5), 87. https://doi.org/10.1007/s11214-020-00703-9

Irwin, P. G. J., de Kok, R., Negrão, A., Tsang, C. C. C., Wilson, C. F., Drossart, P., et al. (2008). Spatial variability of carbon monoxide in Venus' mesosphere from Venus Express/Visible and InfraRed Thermal Imaging Spectrometer measurements. *Journal of Geophysical Research: Planets, 113*(E5). https://doi.org/10.1029/2008JE003093

Jacobson, M. Z. (2005). *Fundamentals of atmospheric modeling* (2nd ed.). New York: Cambridge Univ. Press.

Jastrow, R. (1968). The planet Venus. *Science, 160*(3835), 1403-1410. Retrieved from http://www.jstor.org/stable/1723646

Jenkins, J. M. (1995). *Reduction and analysis of seasons 15 and 16 (1991-1992) Pioneer Venus radio occultation data and correlation studies with observations of the near infra-red emission of Venus* (NASA-CR-199071). Retrieved from https://ntrs.nasa.gov/api/citations/19950026279/downloads/19950026279.pdf

Jessup, K. L., Marcq, E., Mills, F., Mahieux, A., Limaye, S., Wilson, C., et al. (2015). Coordinated Hubble Space Telescope and Venus Express observations of Venus' upper cloud deck. *Icarus, 258*, 309-336. https://doi.org/10.1016/j.icarus.2015.05.027

Jiang, C. Z., Rimmer, P. B., Lozano, G. G., Tosca, N. J., Kufner, C. L., Sasselov, D. D., & Thompson, S. J. (2024). Iron-sulfur chemistry can explain the ultraviolet absorber in the clouds of Venus. *Science Advances, 10*(1), eadg8826. https://doi.org/10.1126/sciadv.adg8826

Johnson-Groh, M. (2022). Parker Solar Probe captures its first images of Venus' surface in visible light, confirmed. Retrieved from https://www.nasa.gov/general/parker-solar-probe-captures-its-first-images-of-venus-surface-in-visible-light-confirmed/

Johnson, T. V., Yeates, C. M., Young, R., & Dunne, J. (1991). The Galileo Venus encounter. *Science, 253*(5027), 1516-1518. https://doi.org/10.1126/science.253.5027.1516

Jones, A. (2024, 30/05/2024). Japan loses contact with Akatsuki, humanity's only active Venus probe. *space.com*. Retrieved from https://www.space.com/jaxa-loses-contact-akatsuki-venus-probe

JPL. (1965). *Mariner-Venus 1962 final project report*. Retrieved from https://history.nasa.gov/SP-59.pdf

Kawabata, K., Coffeen, D. L., Hansen, J. E., Lane, W. A., Sato, M., & Travis, L. D. (1980). Cloud and haze properties from Pioneer Venus polarimetry. *Journal of Geophysical Research: Space Physics, 85*(A13), 8129-8140. https://doi.org/10.1029/JA085iA13p08129

Keating, G. M., Bertaux, J. L., Bougher, S. W., Dickinson, R. E., Cravens, T. E., Nagy, A. F., et al. (1985). Models of Venus neutral upper atmosphere: structure and composition. *Advances in Space Research, 5*(11), 117-171. https://doi.org/10.1016/0273-1177(85)90200-5

Kerzhanovich, V. V., & Limaye, S. S. (1985). Circulation of the atmosphere from the surface to 100 km. *Advances in Space Research, 5*(11), 59-83. https://doi.org/10.1016/0273-1177(85)90198-X

Kerzhanovich, V. V., Marov, M. Y., & Rozhdestvensky, M. K. (1972). Data on dynamics of the subcloud Venus atmosphere from Venera spaceprobe measurements. *Icarus, 17*(3), 659-674. https://doi.org/10.1016/0019-1035(72)90030-9

Khatuntsev, I. V., Patsaeva, M. V., Titov, D. V., Ignatiev, N. I., Turin, A. V., Fedorova, A. A., & Markiewicz, W. J. (2017). Winds in the middle cloud deck from the near-IR imaging by the Venus Monitoring Camera onboard Venus Express. *Journal of Geophysical Research: Planets, 122*(11), 2312-2327. https://doi.org/10.1002/2017JE005355

Knollenberg, R. G., & Hunten, D. M. (1979a). Clouds of Venus: a preliminary assessment of microstructure. *Science, 205*(4401), 70-74. https://doi.org/10.1126/science.205.4401.70

Knollenberg, R. G., & Hunten, D. M. (1979b). Clouds of Venus: particle size distribution measurements. *Science, 203*(4382), 792-795. https://doi.org/10.1126/science.203.4382.792

Knollenberg, R. G., & Hunten, D. M. (1980). The microphysics of the clouds of Venus: results of the Pioneer Venus Particle Size Spectrometer experiment. *Journal of Geophysical Research: Space Physics, 85*(A13), 8039-8058. https://doi.org/10.1029/JA085iA13p08039

Krasnopolsky, V. A. (1989). Vega mission results and chemical composition of Venusian clouds. *Icarus, 80*(1), 202-210. https://doi.org/10.1016/0019-1035(89)90168-1

Krasnopolsky, V. A. (2007). Chemical kinetic model for the lower atmosphere of Venus. *Icarus, 191*(1), 25-37. https://doi.org/10.1016/j.icarus.2007.04.028

Krasnopolsky, V. A. (2008). High-resolution spectroscopy of Venus: detection of OCS, upper limit to H_2S, and latitudinal variations of CO and HF in the upper cloud layer. *Icarus, 197*(2), 377-385. https://doi.org/10.1016/j.icarus.2008.05.020

Krasnopolsky, V. A. (2010a). Spatially-resolved high-resolution spectroscopy of Venus 1. Variations of CO_2, CO, HF, and HCl at the cloud tops. *Icarus, 208*(2), 539-547. https://doi.org/10.1016/j.icarus.2010.02.012

Krasnopolsky, V. A. (2010b). Spatially-resolved high-resolution spectroscopy of Venus 2. Variations of HDO, OCS, and SO_2 at the cloud tops. *Icarus, 209*(2), 314-322. https://doi.org/10.1016/j.icarus.2010.05.008

Krasnopolsky, V. A. (2012). A photochemical model for the Venus atmosphere at 47–112km. *Icarus, 218*(1), 230-246. https://doi.org/10.1016/j.icarus.2011.11.012

Krasnopolsky, V. A. (2016). Sulfur aerosol in the clouds of Venus. *Icarus, 274*, 33-36. https://doi.org/10.1016/j.icarus.2016.03.010

Krasnopolsky, V. A. (2017). On the iron chloride aerosol in the clouds of Venus. *Icarus, 286*, 134-137. https://doi.org/10.1016/j.icarus.2016.10.003

Krasnopolsky, V. A. (2018). Disulfur dioxide and its near-UV absorption in the photochemical model of Venus atmosphere. *Icarus, 299*, 294-299. https://doi.org/10.1016/j.icarus.2017.08.013

Kuiper, G. P. (1969). The identification of the Venus cloud layers. *Communications of the Lunar and Planetary Laboratory, 6*, 229-248. Retrieved from https://ntrs.nasa.gov/citations/19700004516

Lakowicz, J. R. (2006). *Principles of fluorescence spectroscopy* (Third edition. ed.). New York: Springer.

Laven, P. (2005). How are glories formed? *Applied Optics, 44*(27), 5675-5683. https://doi.org/10.1364/AO.44.005675

Lebonnois, S., Hourdin, F., Eymet, V., Crespin, A., Fournier, R., & Forget, F. (2010). Superrotation of Venus' atmosphere analyzed with a full general circulation model. *Journal of Geophysical Research: Planets, 115*(E6). https://doi.org/10.1029/2009JE003458

Lebonnois, S., Sugimoto, N., & Gilli, G. (2016). Wave analysis in the atmosphere of Venus below 100-km altitude, simulated by the LMD Venus GCM. *Icarus, 278*, 38-51. https://doi.org/10.1016/j.icarus.2016.06.004

Lee, Y. J., Muñoz, A. G., Yamazaki, A., Quémerais, E., Mottola, S., Hellmich, S., et al. (2022). Reflectivity of Venus's dayside disk during the 2020 observation campaign: outcomes and future perspectives. *The Planetary Science Journal, 3*(9), 209. https://doi.org/10.3847/PSJ/ac84d1

Lee, Y. J., Muñoz, A. G., Yamazaki, A., Yamada, M., Watanabe, S., & Encrenaz, T. (2021). Investigation of UV absorbers on Venus using the 283 and 365 nm phase curves obtained from Akatsuki. *Geophysical Research Letters, 48*(7), e2020GL090577. https://doi.org/10.1029/2020GL090577

Limaye, S. S. (1985). Venus atmospheric circulation: observations and implications of the thermal structure. *Advances in Space Research, 5*(9), 51-62. https://doi.org/10.1016/0273-1177(85)90270-4

Limaye, S. S., Grund, C. J., & Burre, S. P. (1982). Zonal mean circulation at the cloud level on Venus: spring and fall 1979 OCPP observations. *Icarus, 51*(2), 416-439. https://doi.org/10.1016/0019-1035(82)90092-6

Limaye, S. S., Mogul, R., Smith, D. J., Ansari, A. H., Słowik, G. P., & Vaishampayan, P. (2018). Venus' spectral signatures and the potential for life in the clouds. *Astrobiology, 18*(9), 1181-1198. https://doi.org/10.1089/ast.2017.1783

Limaye, S. S., & Suomi, V. E. (1981). Cloud motions on Venus: global structure and organization. *Journal of the Atmospheric Sciences, 38*(6), 1220-1235. https://doi.org/10.1175/1520-0469(1981)038%3C1220:CMOVGS%3E2.0.CO;2

Liu, W., Etschmann, B., Brugger, J., Spiccia, L., Foran, G., & McInnes, B. (2006). UV–Vis spectrophotometric and XAFS studies of ferric chloride complexes in hyper-saline LiCl solutions at 25–90 °C. *Chemical Geology, 231*(4), 326-349. https://doi.org/10.1016/j.chemgeo.2006.02.005

Luginin, M., Fedorova, A., Belyaev, D., Montmessin, F., Wilquet, V., Korablev, O., et al. (2016). Aerosol properties in the upper haze of Venus from SPICAV IR data. *Icarus, 277*, 154-170. https://doi.org/10.1016/j.icarus.2016.05.008

Lustrement, B., Bertran, S., Rouanet, N., Díaz Damián, A., Hassen-Khodja, R., Montaron, C., et al. (2024). *Design of the VenSpec-U instrument: a double UV imaging spectrometer to analyze sulfured gases in the Venus' atmosphere*. Paper presented at the Optical Engineering + Applications. https://doi.org/10.1117/12.3028252

Machado, P., Peralta, J., Silva, J. E., Brasil, F., Gonçalves, R., & Silva, M. (2022). Venus' cloud-tracked winds using ground- and space-based observations with TNG/NICS and VEx/VIRTIS. *Atmosphere, 13*(2), 337. https://doi.org/10.3390/atmos13020337

Mahieux, A., Robert, S., Mills, F. P., Jessup, K. L., Trompet, L., Aoki, S., et al. (2023a). Update on SO_2, detection of OCS, CS, CS_2, and SO_3, and upper limits of H_2S and HOCl in the Venus mesosphere using SOIR on board Venus Express. *Icarus, 399*, 115556. https://doi.org/10.1016/j.icarus.2023.115556

Mahieux, A., Robert, S., Piccialli, A., Trompet, L., & Vandaele, A. C. (2023b). The SOIR/Venus Express species concentration and temperature database: CO_2, CO, H_2O, HDO, $H^{35}Cl$, $H^{37}Cl$, HF individual and mean profiles. *Icarus, 405*, 115713. https://doi.org/10.1016/j.icarus.2023.115713

Manners, J., Edwards, J. M., Hill, P., & Thelen, J.-C. (2022a). *SOCRATES technical guide*. Retrieved from https://code.metoffice.gov.uk/trac/socrates

Manners, J., Edwards, J. M., Hill, P., & Thelen, J.-C. (2022b). *SOCRATES user guide*. Retrieved from https://code.metoffice.gov.uk/trac/socrates

Marcq, E., Bézard, B., Drossart, P., Piccioni, G., Reess, J. M., & Henry, F. (2008). A latitudinal survey of CO, OCS, H_2O, and SO_2 in the lower atmosphere of Venus: spectroscopic studies using VIRTIS-H. *Journal of Geophysical Research: Planets, 113*(E5). https://doi.org/10.1029/2008JE003074

Markiewicz, W. J., Petrova, E., Shalygina, O., Almeida, M., Titov, D. V., Limaye, S. S., et al. (2014). Glory on Venus cloud tops and the unknown UV absorber. *Icarus, 234*, 200-203. https://doi.org/10.1016/j.icarus.2014.01.030

Marov, M. Y., Avduevsky, V. S., Borodin, N. F., Ekonomov, A. P., Kerzhanovich, V. V., Lysov, V. P., et al. (1973). Preliminary results on the Venus atmosphere from the Venera 8 descent module. *Icarus, 20*(4), 407-421. https://doi.org/10.1016/0019-1035(73)90014-6

Marov, M. Y., Lystsev, V. E., Lebedev, V. N., Lukashevich, N. L., & Shari, V. P. (1980). The structure and microphysical properties of the Venus clouds: Venera 9, 10, and 11 data. *Icarus, 44*(3), 608-639. https://doi.org/10.1016/0019-1035(80)90131-1

Martinez, A., Chaufray, J.-Y., Lebonnois, S., Gonzàlez-Galindo, F., Lefèvre, F., & Gilli, G. (2024). Three-dimensional Venusian ionosphere model. *Icarus, 415*, 116035. https://doi.org/10.1016/j.icarus.2024.116035

Martinez, A., Lebonnois, S., Millour, E., Pierron, T., Moisan, E., Gilli, G., & Lefèvre, F. (2023). Exploring the variability of the venusian thermosphere with the IPSL Venus GCM. *Icarus, 389*, 115272. https://doi.org/10.1016/j.icarus.2022.115272

Miles, N. L., Verlinde, J., & Clothiaux, E. E. (2000). Cloud droplet size distributions in low-level stratiform clouds. *Journal of the Atmospheric Sciences, 57*(2), 295-311. https://doi.org/10.1175/1520-0469(2000)057%3C0295:CDSDIL%3E2.0.CO;2

Montgomery, J. A., Frisch, M. J., Ochterski, J. W., & Petersson, G. A. (2000). A complete basis set model chemistry. VII. Use of the minimum population localization method. *J. Chem. Phys., 112*, 6532-6542. https://doi.org/10.1063/1.481224

Moroz, V. I., Moshkin, B. E., Ekonomov, A. P., Golovin, Y. M., Gnedykh, V. I., & Grigorjev, A. V. (1982). Spectrophotometrical experiment on the Venera-13 and Venera-14 landers. *Soviet Astronomy Letters, 8*, 219. Retrieved from https://ui.adsabs.harvard.edu/abs/1982SvAL....8..219M

Moroz, V. I., Spänkuch, D., Linkin, V. M., Döhler, W., Matsygorin, I. A., Schäfer, K., et al. (1986). Venus spacecraft infrared radiance spectra and some aspects of their interpretation. *Applied Optics, 25*(10), 1710-1719. https://doi.org/10.1364/AO.25.001710

Murray, B. C., Belton, M. J. S., Danielson, G. E., Davies, M. E., Gault, D., Hapke, B., et al. (1974). Venus: atmospheric motion and structure from Mariner 10 pictures. *Science, 183*(4131), 1307-1315. https://doi.org/10.1126/science.183.4131.1307

Murray, B. J., Mangan, T. P., Määttänen, A., & Plane, J. M. C. (2023). Ephemeral ice clouds in the upper mesosphere of Venus. https://doi.org/10.22541/essoar.168881878.84423936/v1

Na, C. Y., Esposito, L. W., McClintock, W. E., & Barth, C. A. (1994). Sulfur dioxide in the atmosphere of Venus: II. modeling results. *Icarus, 112*(2), 389-395. https://doi.org/10.1006/icar.1994.1193

Nahar, S. N., Bautista, M. A., & Pradhan, A. K. (1997). Electron-ion recombination of neutral iron. *Astrophys. J., 479*(1), 497-503. https://doi.org/10.1086/303874

Nakamura, M., Titov, D., McGouldrick, K., Drossart, P., Bertaux, J.-L., & Liu, H. (2018). Akatsuki at Venus: the first year of scientific operation. *Earth, Planets and Space, 70*(1), 144. https://doi.org/10.1186/s40623-018-0916-3

NASA. (2018, 13 August 2018). Parker Solar Probe launches to 'touch the sun'. Retrieved from https://www.nasa.gov/image-feature/parker-solar-probe-launches-to-touch-the-sun

NASA Goddard Space Flight Centre. (2020). Solar Orbiter's orbit. Retrieved from https://svs.gsfc.nasa.gov/13532

NASA/JHU/APL. (2007a). PIA10124: Approaching Venus image #2. Retrieved from https://photojournal.jpl.nasa.gov/catalog/PIA10124

NASA/JHU/APL. (2007b). Venus 2 approach image. Retrieved from https://web.archive.org/web/20150919072003/http://messenger.jhuapl.edu/gallery/sciencePhotos/image.php?page=1&gallery_id=2&image_id=88

Newman, M., Schubert, G., Kliore, A. J., & Patel, I. R. (1984). Zonal winds in the middle atmosphere of Venus from Pioneer Venus radio occultation data. *Journal of the Atmospheric Sciences, 41*(12), 1901-1913. https://doi.org/10.1175/1520-0469(1984)041%3C1901:ZWITMA%3E2.0.CO;2

Oyama, V. I., Carle, G. C., Woeller, F., Pollack, J. B., Reynolds, R. T., & Craig, R. A. (1980). Pioneer Venus gas chromatography of the lower atmosphere of Venus. *Journal of Geophysical Research: Space Physics, 85*(A13), 7891-7902. https://doi.org/10.1029/JA085iA13p07891

Palmer, K. F., & Williams, D. (1975). Optical constants of sulfuric acid; application to the clouds of Venus? *Applied Optics, 14*(1), 208-219. https://doi.org/10.1364/AO.14.000208

Pätzold, M., Tellmann, S., Häusler, B., Bird, M. K., Tyler, G. L., Christou, A. A., & Withers, P. (2009). A sporadic layer in the Venus lower ionosphere of meteoric origin. *Geophysical Research Letters, 36*(5). https://doi.org/10.1029/2008GL035875

Peralta, J., Hueso, R., & Sánchez-Lavega, A. (2007). A reanalysis of Venus winds at two cloud levels from Galileo SSI images. *Icarus, 190*(2), 469-477. https://doi.org/10.1016/j.icarus.2007.03.028

Peralta, J., Iwagami, N., Sánchez-Lavega, A., Lee, Y. J., Hueso, R., Narita, M., et al. (2019). Morphology and dynamics of Venus's middle clouds with Akatsuki/IR1. *Geophysical Research Letters*, *46*(5), 2399-2407. https://doi.org/10.1029/2018GL081670

Peralta, J., Lee, Y. J., Hueso, R., Clancy, R. T., Sandor, B. J., Sánchez-Lavega, A., et al. (2017). Venus's winds and temperatures during the MESSENGER's flyby: An approximation to a three-dimensional instantaneous state of the atmosphere. *Geophysical Research Letters*, *44*(8), 3907-3915. https://doi.org/10.1002/2017GL072900

Peralta, J., Muto, K., Hueso, R., Horinouchi, T., Sánchez-Lavega, A., Murakami, S.-y., et al. (2018). Nightside winds at the lower clouds of Venus with Akatsuki/IR2: longitudinal, local time, and decadal variations from comparison with previous measurements. *The Astrophysical Journal Supplement Series*, *239*(2), 29. https://doi.org/10.3847/1538-4365/aae844

Pérez-Hoyos, S., Sánchez-Lavega, A., García-Muñoz, A., Irwin, P. G. J., Peralta, J., Holsclaw, G., et al. (2018). Venus upper clouds and the UV absorber from MESSENGER/MASCS observations. *Journal of Geophysical Research: Planets*, *123*(1), 145-162. https://doi.org/10.1002/2017JE005406

Petrova, E. V. (2018). Glory on Venus and selection among the unknown UV absorbers. *Icarus*, *306*, 163-170. https://doi.org/10.1016/j.icarus.2018.02.016

Petrova, E. V., Shalygina, O. S., & Markiewicz, W. J. (2015). The VMC/VEx photometry at small phase angles: glory and the physical properties of particles in the upper cloud layer of Venus. *Planetary and Space Science*, *113-114*, 120-134. https://doi.org/10.1016/j.pss.2014.11.013

Petryanov, I. V., Andreichikov, B. M., Korchuganov, B. N., Ovsyankin, E. I., Ogorodnikov, B. I., Skitovich, V. I., & Khristianov, V. K. (1981). Iron in Venus clouds. *Dokl. Akad. Naik. SSP*, *206*, 834-836. Retrieved from http://mi.mathnet.ru/eng/dan/v260/i4/p834

Petty, G. W., & Huang, W. (2011). The modified gamma size distribution applied to inhomogeneous and nonspherical particles: key relationships and conversions. *Journal of the Atmospheric Sciences*, *68*(7), 1460-1473. https://doi.org/10.1175/2011JAS3645.1

Pielke, R. A. (2024). Troposphere. In *Encyclopedia Britannica*.

Pinto, J. P., Li, J., Mills, F. P., Marcq, E., Evdokimova, D., Belyaev, D., & Yung, Y. L. (2021). Sulfur monoxide dimer chemistry as a possible source of polysulfur in the upper atmosphere of Venus. *Nature Communications*, *12*(1), 175. https://doi.org/10.1038/s41467-020-20451-2

Plane, J. M. C. (2003). Atmospheric chemistry of meteoric metals. *Chemical Reviews*, *103*(12), 4963-4984. https://doi.org/10.1021/cr0205309

Plane, J. M. C., Carrillo-Sanchez, J. D., Mangan, T. P., Crismani, M. M. J., Schneider, N. M., & Määttänen, A. (2018). Meteoric metal chemistry in the Martian atmosphere. *Journal of Geophysical Research: Planets*, *123*(3), 695-707. https://doi.org/10.1002/2017JE005510

Plane, J. M. C., Feng, W., & Dawkins, E. C. M. (2015). The mesosphere and metals: chemistry and changes. *Chemical Reviews*, *115*(10), 4497-4541. https://doi.org/10.1021/cr500501m

Pollack, J. B., Ragent, B., Boese, R., Tomasko, M. G., Blamont, J., Knollenberg, R. G., et al. (1979). Nature of the ultraviolet absorber in the Venus clouds: inferences based on Pioneer Venus data. *Science, 205*(4401), 76-79. https://doi.org/10.1126/science.205.4401.76

Pollack, J. B., Toon, O. B., Whitten, R. C., Boese, R., Ragent, B., Tomasko, M., et al. (1980). Distribution and source of the UV absorption in Venus' atmosphere. *Journal of Geophysical Research: Space Physics, 85*(A13), 8141-8150. https://doi.org/10.1029/JA085iA13p08141

Ragent, B., & Blamont, J. E. (1979). Preliminary results of the Pioneer Venus nephelometer experiment. *Science, 203*(4382), 790-792. https://doi.org/10.1126/science.203.4382.790

Ragent, B., & Blamont, J. E. (1980). The structure of the clouds of Venus: results of the Pioneer Venus nephelometer experiment. *Journal of Geophysical Research: Space Physics, 85*(A13), 8089-8105. https://doi.org/10.1029/JA085iA13p08089

Ragent, B., Esposito, L. W., Tomasko, M. G., Marov, M. Y., Shari, V. P., & Lebedev, V. N. (1985). Particulate matter in the Venus atmosphere. *Advances in Space Research, 5*(11), 85-115. https://doi.org/10.1016/0273-1177(85)90199-1

Rimmer, P. B., Jordan, S., Constantinou, T., Woitke, P., Shorttle, O., Hobbs, R., & Paschodimas, A. (2021). Hydroxide salts in the clouds of Venus: their effect on the sulfur cycle and cloud droplet pH. *The Planetary Science Journal, 2*(4), 133. https://doi.org/10.3847/PSJ/ac0156

Rollason, R. J., & Plane, J. M. C. (1998). A study of the reactions of Fe^{+}‘ with O_3 , O_2 and N_2. *J. Chem. Soc., Faraday Trans., 94*, 3067-3075. https://doi.org/10.1039/A805140B

Rollason, R. J., & Plane, J. M. C. (2000). The reactions of FeO with O_3, H_2, H_2O, O_2 and CO_2. *Phys. Chem. Chem. Phys, 2*(10), 2335-2343. https://doi.org/10.1039/B000877J

Ross, F. E. (1928). Photographs of Venus. *The Astrophysical Journal, 68*, 57. https://doi.org/10.1086/143130

Rossow, W. B., Del Genio, A. D., & Eichler, T. (1990). Cloud-tracked winds from Pioneer Venus OCPP images. *Journal of the Atmospheric Sciences, 47*(17), 2053-2084. https://doi.org/10.1175/1520-0469(1990)047%3C2053:CTWFVO%3E2.0.CO;2

Rossow, W. B., Del Genio, A. D., Limaye, S. S., Travis, L. D., & Stone, P. H. (1980). Cloud morphology and motions from Pioneer Venus images. *Journal of Geophysical Research: Space Physics, 85*(A13), 8107-8128. https://doi.org/10.1029/JA085iA13p08107

Rossow, W. B., & Williams, G. P. (1979). Large-scale motion in the Venus stratosphere. *Journal of the Atmospheric Sciences, 36*(3), 377-389. https://doi.org/10.1175/1520-0469(1979)036%3C0377:LSMITV%3E2.0.CO;2

Rutherford, J. A., & Vroom, D. A. (1972). Formation of iron ions by charge transfer. *J. Chem. Phys., 57*, 3091–3093. https://doi.org/10.1063/1.1678724

Sagan, C. (1969). The COSPAR meetings in Prague. *Icarus, 11*(2), 268-272. https://doi.org/10.1016/0019-1035(69)90052-9

Sagdeev, R. Z., Linkin, V. M., Blamont, J. E., & Preston, R. A. (1986a). The VEGA Venus balloon experiment. *Science, 231*(4744), 1407-1408. https://doi.org/10.1126/science.231.4744.1407

Sagdeev, R. Z., Linkin, V. M., Kerzhanovich, V. V., Lipatov, A. N., Shurupov, A. A., Blamont, J. E., et al. (1986b). Overview of VEGA Venus balloon in situ meteorological measurements. *Science, 231*(4744), 1411-1414. https://doi.org/10.1126/science.231.4744.1411

Sánchez-Lavega, A., Hueso, R., Piccioni, G., Drossart, P., Peralta, J., Pérez-Hoyos, S., et al. (2008). Variable winds on Venus mapped in three dimensions. *Geophysical Research Letters, 35*(13). https://doi.org/10.1029/2008GL033817

Sandor, B. J., Todd Clancy, R., Moriarty-Schieven, G., & Mills, F. P. (2010). Sulfur chemistry in the Venus mesosphere from SO_2 and SO microwave spectra. *Icarus, 208*(1), 49-60. https://doi.org/10.1016/j.icarus.2010.02.013

Satoh, T., Ohtsuki, S., Iwagami, N., Ueno, M., Uemizu, K., Suzuki, M., et al. (2015). Venus' clouds as inferred from the phase curves acquired by IR1 and IR2 on board Akatsuki. *Icarus, 248*, 213-220. https://doi.org/10.1016/j.icarus.2014.10.030

Saunders, R. W., Dhomse, S., Tian, W. S., Chipperfield, M. P., & Plane, J. M. C. (2012). Interactions of meteoric smoke particles with sulphuric acid in the Earth's stratosphere. *Atmos. Chem. Phys., 12*(10), 4387-4398. https://doi.org/10.5194/acp-12-4387-2012

Saunders, R. W., & Plane, J. M. C. (2006). A laboratory study of meteor smoke analogues: composition, optical properties and growth kinetics. *J. Atmos. Solar-Terr. Phys., 68*(18), 2182-2202. https://doi.org/10.1016/j.jastp.2006.09.006

Scalmani, G., Frisch, M. J., Mennucci, B., Tomasi, J., Cammi, R., & Barone, V. (2006). Geometries and properties of excited states in the gas phase and in solution: theory and application of a time-dependent density functional theory polarizable continuum model. *J. Chem. Phys., 124*, art. no.: 094107. https://doi.org/10.1063/1.2173258

Seiff, A. (1983). Thermal structure of the atmosphere of Venus. In D. M. Hunten, L. Colin, T. M. Donahue, & V. I. Moroz (Eds.), *Venus* (pp. 215-279). Tucson, Arizona: The Univeristy of Arizona Press.

Seiff, A., Kirk, D. B., Young, R. E., Sommer, S. C., Blanchard, R. C., Findlay, J. T., & Kelly, G. M. (1979). Thermal contrast in the atmosphere of Venus: initial appraisal from Pioneer Venus probe data. *Science, 205*(4401), 46-49. https://doi.org/10.1126/science.205.4401.46

Self, D. E., & Plane, J. M. C. (2003). A kinetic study of the reactions of iron oxides and hydroxides relevant to the chemistry of iron in the upper mesosphere. *Phys. Chem. Chem. Phys, 5*(7), 1407-1418. https://doi.org/10.1039/b211900e

Shimazaki, T. (1985). *Minor constituents in the middle atmosphere*. Dordrecht: D. Reidel Publishing Company.

Siddiqi, A. A. (2018). *Beyond Earth: a chronicle of deep space exploration, 1958-2016*. United States: NASA History Program Office.

Skog, R., Frandsen, B., & Kurtén, T. (2024). *Simulating UV-Vis spectra for polysulfur species in the Venusian atmosphere*. Paper presented at the EGU General Assembly 2024, Vienna, Austria.

Smirnov, V. N. (2008). Rate constant of the gas-phase reaction between Fe atoms and CO_2. *Kinet. Catal., 49*, 607-609. https://doi.org/10.1134/S0023158408050017

Smith, I. W. M. (1980). *Kinetics and dynamics of elementary gas reactions*. London: Butterworths.

Snyder, C. W. (1967). Mariner V flight past Venus. *Science, 158*(3809), 1665-1669. https://doi.org/10.1126/science.158.3809.1665

Sohn, R. (2024). Venus' atmosphere: composition, clouds, and weather. Retrieved from https://www.space.com/18527-venus-atmosphere.html

Sonett, C. P. (1963). A summary review of the scientific findings of the Mariner Venus mission. *Space Science Reviews, 2*(6), 751-777. https://doi.org/10.1007/BF00208814

Steudel, R., Holdt, G., & Young, A. T. (1986). On the colors of Jupiter's satellite Io: irradiation of solid sulfur at 77 K. *Journal of Geophysical Research: Solid Earth, 91*(B5), 4971-4977. https://doi.org/10.1029/JB091iB05p04971

Stolzenbach, A. (2016). *Étude de la photochimie de Vénus à l'aide d'un modèle de circulation générale.* (PhD thesis), l'Université Pierre et Marie Curie, Retrieved from https://web.lmd.jussieu.fr/~sllmd/Tmp/thesis_STOLZENBACH_24052016.pdf (In French)

Stolzenbach, A., Lefèvre, F., Lebonnois, S., & Määttänen, A. (2023). Three-dimensional modeling of Venus photochemistry and clouds. *Icarus, 395*, 115447. https://doi.org/10.1016/j.icarus.2023.115447

Svedhem, H., Titov, D. V., McCoy, D., Lebreton, J. P., Barabash, S., Bertaux, J. L., et al. (2007). Venus Express—the first European mission to Venus. *Planetary and Space Science, 55*(12), 1636-1652. https://doi.org/10.1016/j.pss.2007.01.013

Szafert, S., Lis, T., Drabent, K., & Sobota, P. (1994). Photochemical reduction of iron trichloride in ethyl acetate: synthesis, Mössbauer spectra and the crystal structure at 80 K of hexakis(ethyl acetate)iron(II) bis-tetrachloroironate(III). *Journal of Chemical Crystallography, 24*(3), 197-202. https://www.doi.org/10.1007/BF01672410

Taylor, F. W., Crisp, D., & Bézard, B. (1997). Near-infrared sounding of the lower atmosphere of Venus. In S. W. Bougher, D. M. Hunten, & R. J. Phillips (Eds.), *Venus II*. Tucson, Arizona: University of Arizona Press.

Taylor, F. W., Diner, D. J., Elson, L. S., McCleese, D. J., Martonchik, J. V., Delderfield, J., et al. (1979). Temperature, cloud structure, and dynamics of Venus middle atmosphere by infrared remote sensing from Pioneer Orbiter. *Science, 205*(4401), 65-67. https://doi.org/10.1126/science.205.4401.65

Tellmann, S., Pätzold, M., Häusler, B., Bird, M. K., & Tyler, G. L. (2009). Structure of the Venus neutral atmosphere as observed by the radio science experiment VeRa on Venus Express. *Journal of Geophysical Research: Planets, 114*(E9). https://doi.org/10.1029/2008JE003204

Titov, D. V., Ignatiev, N. I., McGouldrick, K., Wilquet, V., & Wilson, C. F. (2018). Clouds and hazes of Venus. *Space Science Reviews, 214*(8), 126. https://doi.org/10.1007/s11214-018-0552-z

Titov, D. V., Markiewicz, W. J., Ignatiev, N. I., Song, L., Limaye, S. S., Sanchez-Lavega, A., et al. (2012). Morphology of the cloud tops as observed by the Venus Express Monitoring Camera. *Icarus, 217*(2), 682-701. https://doi.org/10.1016/j.icarus.2011.06.020

Tobiska, W. K., Woods, T., Eparvier, F., Viereck, R., Floyd, L., Bouwer, D., et al. (2000). The SOLAR2000 empirical solar irradiance model and forecast tool. *Journal of Atmospheric and Solar-Terrestrial Physics*, *62*(14), 1233-1250. https://doi.org/10.1016/S1364-6826(00)00070-5

Tomasko, M. G., Doose, L. R., & Smith, P. H. (1979). Absorption of sunlight in the atmosphere of Venus. *Science*, *205*(4401), 80-82. https://doi.org/10.1126/science.205.4401.80

Tomasko, M. G., Doose, L. R., Smith, P. H., & Odell, A. P. (1980a). Measurements of the flux of sunlight in the atmosphere of Venus. *Journal of Geophysical Research: Space Physics*, *85*(A13), 8167-8186. https://doi.org/10.1029/JA085iA13p08167

Tomasko, M. G., Smith, P. H., Suomi, V. E., Sromovsky, L. A., Revercomb, H. E., Taylor, F. W., et al. (1980b). The thermal balance of Venus in light of the Pioneer Venus Mission. *Journal of Geophysical Research: Space Physics*, *85*(A13), 8187-8199. https://doi.org/10.1029/JA085iA13p08187

Toon, O. B., Ragent, B., Colburn, D., Blamont, J., & Cot, C. (1984). Large, solid particles in the clouds of Venus: do they exist? *Icarus*, *57*(2), 143-160. https://doi.org/10.1016/0019-1035(84)90063-0

Travis, L. D. (1978). Nature of the atmospheric dynamics on Venus from power spectrum analysis of Mariner 10 images. *Journal of the Atmospheric Sciences*, *35*(9), 1584-1595. https://doi.org/10.1175/1520-0469(1978)035%3C1584:NOTADO%3E2.0.CO;2

Travis, L. D., Coffeen, D. L., Genio, A. D. D., Hansen, J. E., Kawabata, K., Lacis, A. A., et al. (1979a). Cloud images from the Pioneer Venus Orbiter. *Science*, *205*(4401), 74-76. https://doi.org/10.1126/science.205.4401.74

Travis, L. D., Coffeen, D. L., Hansen, J. E., Kawabata, K., Lacis, A. A., Lane, W. A., et al. (1979b). Orbiter Cloud Photopolarimeter investigation. *Science*, *203*(4382), 781-785. https://doi.org/10.1126/science.203.4382.781

Vakhnin, V. M. (1968). A review of the Venera 4 flight and its scientific program. *Journal of the Atmospheric Sciences*, *25*(4), 533-534. https://doi.org/10.1175/1520-0469(1968)025%3C0533:Arotvf%3E2.0.Co;2

Vandaele, A. C., De Mazière, M., Drummond, R., Mahieux, A., Neefs, E., Wilquet, V., et al. (2008). Composition of the Venus mesosphere measured by solar occultation at infrared on board Venus Express. *Journal of Geophysical Research: Planets*, *113*(E5). https://doi.org/10.1029/2008JE003140

Vandaele, A. C., Korablev, O., Belyaev, D., Chamberlain, S., Evdokimova, D., Encrenaz, T., et al. (2017). Sulfur dioxide in the Venus atmosphere: I. Vertical distribution and variability. *Icarus*, *295*, 16-33. https://doi.org/10.1016/j.icarus.2017.05.003

Volwerk, M., Horbury, T. S., Woodham, L. D., Bale, S. D., Simon Wedlund, C., Schmid, D., et al. (2021). Solar Orbiter's first Venus flyby. *A&A*, *656*, A11. https://doi.org/10.1051/0004-6361/202140910

von Zahn, U., Kumar, S., Niemann, H., & Prinn, R. (1983). Composition of the Venus atmosphere. In *Venus* (pp. 299).

von Zahn, U., & Moroz, V. I. (1985). Composition of the Venus atmosphere below 100 km altitude. *Advances in Space Research, 5*(11), 173-195. https://doi.org/10.1016/0273-1177(85)90201-7

Vondrak, T., Woodcock, K. R. I., & Plane, J. M. C. (2006). A kinetic study of the reactions of Fe^+ with N_2O, N_2, O_2, CO_2 and H_2O, and the ligand-switching reactions $Fe^+.X + Y \rightarrow Fe^+.Y + X$ ($X = N_2$, O_2, CO_2; $Y = O_2$, H_2O). *Phys. Chem. Chem. Phys, 8*(4), 503-512. https://doi.org/10.1039/b508922k

Waterman, P. C. (1971). Symmetry, Unitarity, and Geometry in Electromagnetic Scattering. *Physical Review D, 3*(4), 825-839. https://doi.org/10.1103/PhysRevD.3.825

Whalley, C. L., & Plane, J. M. C. (2010). Meteoric ion layers in the Martian atmosphere. *Faraday Disc., 147*, 349-368. https://doi.org/10.1039/c003726e

Whiteker, R. A., & Davidson, N. (1953). Ion-exchange and spectrophotometric investigation of iron(III) sulfate complex ions. *Journal of the American Chemical Society, 75*, 3081-3085. https://doi.org/10.1021/ja01109a010

Williams, D. R. (2018). Pioneer Venus project information. Retrieved from https://nssdc.gsfc.nasa.gov/planetary/pioneer_venus.html

Williams, L. R., & Golden, D. M. (1993). Solubility of HCl in sulfuric acid at stratospheric temperatures. *Geophysical Research Letters, 20*(20), 2227-2230. https://doi.org/10.1029/93GL02607

Wood, B. E., Hess, P., Lustig-Yaeger, J., Gallagher, B., Korwan, D., Rich, N., et al. (2022). Parker Solar Probe imaging of the night side of Venus. *Geophysical Research Letters, 49*(3), e2021GL096302. https://doi.org/10.1029/2021GL096302

Woodcock, K. R. S., Vondrak, T., Meech, S. R., & Plane, J. M. C. (2006). A kinetic study of the reactions $FeO^+ + O$, $Fe^+.N_2 + O$, $Fe^+.O_2 + O$ and $FeO^+ + CO$: implications for sporadic E layers in the upper atmosphere. *Phys. Chem. Chem. Phys, 8*(15), 1812-1821. https://doi.org/10.1039/B518155K

Wright, W. H. (1927). Photographs of Venus made by infra-red and by violet light. *Publications of the Astronomical Society of the Pacific, 39*(230), 220-221. https://doi.org/10.1086/123718

Wu, Z., Wan, H., Xu, J., Lu, B., Lu, Y., Eckhardt, A. K., et al. (2018). The near-UV absorber OSSO and its isomers. *Chemical Communications, 54*(36), 4517-4520. https://doi.org/10.1039/C8CC00999F

Yamazaki, A., Yamada, M., Lee, Y. J., Watanabe, S., Horinouchi, T., Murakami, S.-y., et al. (2018). Ultraviolet imager on Venus orbiter Akatsuki and its initial results. *Earth, Planets and Space, 70*(1), 23. https://doi.org/10.1186/s40623-017-0772-6

Young, A. T. (1973). Are the clouds of Venus sulfuric acid? *Icarus, 18*(4), 564-582. https://doi.org/10.1016/0019-1035(73)90059-6

Young, A. T. (1977). An improved Venus cloud model. *Icarus, 32*(1), 1-26. https://doi.org/10.1016/0019-1035(77)90045-8

Young, A. T. (1983). Venus cloud microphysics. *Icarus, 56*(3), 568-577. https://doi.org/10.1016/0019-1035(83)90174-4

Young, L. D. G. (1972). High resolution spectra of Venus—a review. *Icarus, 17*(3), 632-658. https://doi.org/10.1016/0019-1035(72)90029-2

Yung, Y. L., & DeMore, W. B. (1982). Photochemistry of the stratosphere of Venus: implications for atmospheric evolution. *Icarus, 51*(2), 199-247. https://doi.org/10.1016/0019-1035(82)90080-X

Yung, Y. L., & DeMore, W. B. (1999). *Photochemistry of planetary atmospheres*. New York: Oxford University Press.

Zalach, J., von Savigny, C., Langenbach, A., Baumgarten, G., Lübken, F.-J., & Bourassa, A. (2020). A method for retrieving stratospheric aerosol extinction and particle size from ground-based Rayleigh-Mie-Raman lidar observations. *Atmosphere, 11*(8), 773. https://doi.org/10.3390/atmos11080773

Zasova, L. V., Krasnopolsky, V. A., & Moroz, V. I. (1981). Vertical distribution of SO_2 in upper cloud layer of Venus and origin of U.V.-absorption. *Advances in Space Research, 1*(9), 13-16. https://doi.org/10.1016/0273-1177(81)90213-1

Zhang, X., Liang, M. C., Mills, F. P., Belyaev, D. A., & Yung, Y. L. (2012). Sulfur chemistry in the middle atmosphere of Venus. *Icarus, 217*(2), 714-739. https://doi.org/10.1016/j.icarus.2011.06.016